Technical Physics, Vol. 50, No. 12, 2005, pp. 1535–1543. Translated from Zhurnal Tekhnicheskoĭ Fiziki, Vol. 75, No. 12, 2005, pp. 1–9.

THEORETICAL AND MATHEMATICAL PHYSICS

Discrete Model of Adsorption with a Finite Number of States

S. A. Kapliĭ, A. V. Prokaznikov, and N. A. Rud

Demidov State University, ul. Sovetskaya 14, Yaroslavl, 150000 Russia

Received October 21, 2004

Abstract—A discrete model of adsorption with allowance for recharge of the state and lateral interaction between molecules is constructed in the framework of the theory of probabilistic cellular automata. It is found that this model admits of the regular (ordered) behavior of the system accompanied by the global synchronization of the system's parameters. The turbulent (chaotic)–ordered transition takes place through the occurrence of local ordered areas due to the appearance of local leading centers (pacemakers) and helical waves. The ordered behavior originates from intrinsic instability in the system. The ordering is related to the collective behavior of the subsystems constituting the entire system. The model can be extended to the case of chemical reactions between an adsorbate and the surface. © *2005 Pleiades Publishing, Inc.*

INTRODUCTION

Material adsorption on the solid surface has long been a subject of much interest, because the surface is the only channel for penetration of impurities into the crystal [1]. In addition, surface processes specify the states of more complex systems consisting of bordering media, e.g., liquid–solid or gas–solid systems. Moreover, surface modification considerably affects the bulk properties of solids, especially, of fine-grain polycrystals, where the volume and surface area of features are commensurable. Material modification is also intimately related to surface processes, which control both the dynamic and physical properties of resulting structures.

During anodizing of silicon crystals in hydrofluoric acid, the dynamic characteristics of the process were found to periodically vary with time under certain conditions [2–9]. Oscillatory effects were also revealed at finish etching of porous silicon in water [10]. Similar phenomena were found in experiments with porous-silicon-based electroluminescent devices placed into a surface-active medium [11], which generally contains polar molecules [12, 13]. Finally, the periodic variation of dynamic variables was observed in recording the *I–V* characteristics of porous-silicon-based structures placed in a polar-molecule-containing medium [14].

Adsorption and/or desorption of atoms capable of changing their charge state are time-periodic. Self-oscillations were observed at the field desorption of potassium from the tungsten surface covered by gold and potassium adsorbates [15, 16]. Namely, the ionic current and desorption images periodically varied under invariable experimental conditions.

The observations listed above indicate the need for a theory that could explain the body of data gained in different fields of physics.

STATEMENT OF THE PROBLEM

The problem of adsorption with a change in the charge state, as applied to etching of silicon by atomic fluorine, was considered by Babanov *et al.* [17], who presented the energy diagrams of adsorbed fluorine atoms (ions), a system of kinetic equations, and their solutions. A continuous model that accounts for oscillations in the adsorption of surfactant molecules in terms of the averaged molecular surface density was developed in [13]. That model is in many ways based on the concepts put forward in [17].

Analysis of the problem stated is convenient to begin with writing the kinetic equations for molecules adsorbed on the surface in the same form as in [13], i.e., in the form suitable for describing the variation of surface concentration P of neutral and charged molecules (atoms). This system of equations sheds light on the physics of the phenomena accompanying molecular adsorption on the solid surface and clarifies the way of extending this model for the two-dimensional case with the method of probabilistic cellular automata [18],

$$\frac{dP}{dt} = \frac{\Gamma - P}{\tau_t} - \frac{P}{\tau_t'} - \frac{P}{\tau_s}, \quad (1)$$

$$\frac{d\Gamma}{dt} = \frac{\Gamma_{tr} - \Gamma}{\tau_a} - \frac{\Gamma}{\tau_d} - \frac{P}{\tau_s}. \quad (2)$$

Here, P is the surface density of charged molecules (atoms), Γ is the total surface density of neutral and charged molecules, Γ_{tr} is the surface density of active adsorption centers (traps), τ_t (τ_t') is the time of direct (backward) tunneling of charge carriers for molecules or atoms, τ_a (τ_d) is the adsorption (desorption) time for a molecule or atom, and τ_s is the time taken for a charged molecule to overcome an activation barrier on the surface. The system of Eqs. (1) and (2) was solved in detail for different cases elsewhere [13, 17, 19].

1063-7842/05/5012-1535$26.00 © 2005 Pleiades Publishing, Inc.

Solutions to a similar system of kinetic equations for stationary etching (the rate of silicon etching by atomic fluorine is time-independent) are presented in [17].

Equations similar to (1) and (2) can be used for description of silicon anodizing in a hydrofluoric acid solution [19]. In this case, a stationary solution to the system, a relation between the band bending and applied voltage, and the activation type of the time constants preceding the reaction are used. The reaction should proceed at selected sites where the probability of interaction is maximal. Such conditions may be identified with the conditions for pore formation [19]. In this case, the dependence of the current density on the applied voltage obeys the Tafel law

$$j = e\tilde{k}_r \exp\left\{\frac{V}{kT}\right\},$$

where the rate constant of the chemical reaction is expressed as

$$k_r = k_r^0 \exp\left\{-\frac{E-V}{kT}\right\} = \tilde{k}_r \exp\left\{\frac{V}{kT}\right\},$$

barrier E of the reaction being decreased by $V = eU$, where U is the applied potential.

To study a nonstationary (time-dependent) solution to the system stated by (1) and (2), we express Γ from (1) and substitute it into (2). It should also be taken into account that, because of the lateral interaction, the *I–V* characteristics have a portion with a negative differential conductivity [13]. It was shown [13] that, with regard to the nonlinearity of the lateral interaction, the system of Eqs. (1) and (2) can be reduced to a one-dimensional van der Pol equation in some averaged value of the charged molecule surface density. The phase portraits of the dynamic variables that are solutions to the one-dimensional van der Pol equation indicate the presence of a limiting cycle (oscillations of the variables) in the dynamic system under consideration.

Thus, as was demonstrated in [13, 17, 19], system (1)–(2) can be applied to a wide class of problems dealing with molecules (atoms) that can be in one of two, neutral or charged, states. However, the dynamics of some of the processes turns out to be more complicated than that predicted by system (1)–(2) [6–10]. Specifically, there is good reason to think that laterally propagating phase waves of different configurations may arise in such systems [15, 16, 20]. All these facts necessitate further generalization of the given theoretical approach [18].

The aim of this study is to reproduce the dynamics and characteristic properties of as many processes observed in [2–10, 12–16] as possible based on the theoretical principles described by Eqs. (1) and (2). The next objective is to extend the developed approach as much as basic pure mathematical principles allow, i.e., to go beyond the scope of the mathematical formalism that suffices only to generalize Eqs. (1) and (2) for the two-dimensional case with allowance for lateral interaction. Thus, the approach presented below is rather general and covers a large number of particular cases.

THREE-STATE TWO-DIMENSIONAL DISCRETE MODEL

The problem of reproducing the complex behavior of dynamic systems was solved by the method of cellular automata with allowance for molecule (atom)–solid electron exchange by tunneling. The surface of the solid was divided into square unit cells, which could be in one of three states: a white state (–1) without an adsorbed molecule or atom, a gray state (0) with an adsorbed neutral molecule or atom, and a black state (+1) with an adsorbed charged molecule or atom. An important point here is that characteristic times τ_a, τ_d, τ_t, τ_t', and τ_s of physical processes are finite. This is because all physical processes proceed not instantly but take some characteristic time for which a certain state of the system sets in. Each process features a characteristic time of its own. For instance, for free charge redistribution, this time is on the order of the Maxwellian time ($\tau_M \sim 10^{-12}$ s for Ge), etc. It is assumed that these times may be different for white (–1), gray (0), and black (+1) states of a unit cell.

Central to determining the system dynamics by means of the cellular automaton method is setting local rules for step transition of unit cells from one state to another. This means setting corresponding rules for discrete mapping. The lateral interaction is introduced by taking into account the states of the nearest neighbors. A simple mapping can be conventionally represented as consisting of two steps, each involving an initial (intermediate) mapping of a set into another, wider set and a final mapping of this wider set into an initial (but not identical!) one. It should be emphasized that such a mapping as a whole is not an identity mapping. This simplest ("basic") variant of mapping can be schematically represented as follows:

$$\begin{aligned}\text{(i)}\ \ \bar{X}(i,j,t+1) &= [\theta(\tau_{m_{i,j}(t_{on})} - t)X(i,j,t) \\ &+ \theta(t - \tau_{m_{i,j}(t_{on})})g(n_2(t), n_3(t))] \\ &\times [1 - \delta_{m_{i,j}(t), m_{i,j}(t+1)}\theta(t - (\tau_{m_{i,j}(t_{on})} + 1))],\end{aligned} \quad (3)$$

with $\bar{X}(i, j, t+1) = X(i, j\ t)$ if $t < \tau_{m_{i,j}(t_{on})}$. Next, if $t \geq \tau_{m_{i,j}(t_{on})}$, mapping follows: if $A_l' < \bar{X}(i, j, t+1) < A_l$ (where $l = l_{min}, \ldots, l_{max}$), then

$$X(i,j,t+1) = F(x) = \left\{\begin{array}{c} -1 \\ 0 \\ +1 \end{array}\right\}; \quad (4)$$

$$\text{(ii)}\ X(i,j,t+1) = [X(i,j,t) + g(n_2(t), n_3(t))] \times \delta_{m_{i,j}(t),\, m_{i,j}(t+1)}\theta(t - \tau_{m_{i,j}(t_{on}+1)}). \quad (5)$$

Next, mapping follows: if $A_l' < \bar{X}(i,j,t+1) < A_l$ (where $l = l_{min}$–l_{max}), then

$$X(i,j,t+1) = F(x) = \left\{ \begin{array}{c} -1 \\ 0 \\ +1 \end{array} \right\}; \quad (6)$$

(iii) the first step follows again and so on.

Here,

$$\theta(t) = \begin{cases} 0, & t < 0 \\ 1, & t \geq 0 \end{cases}$$

is the theta (switching) function or the Heaviside function; $g(n_2(t), n_3(t))$ is the weighting factor taking into account the state of the neighborhood of the starting cell; $\delta_{i,j}$ is the Kronecker delta; $m_{i,j}(t) = 1, 2, 3$ is the state of cell (i, j) at time instant t, where 1, 2, and 3 are assigned to white (–1), gray (0), and black (+1) states, respectively; $n_1(t)$, $n_2(t)$, and $n_3(t)$ are the numbers of white, gray, and black cells, respectively, constituting the neighborhood of a given cell (i, j) at time instant t, with $n_1(t) + n_2(t) + n_3(t) = N$ (in our case, $N = 8$; the Moor domain); t_{on} is the time the second term in formula (3) is "switched on,"

$$X(i,j,t) = \left\{ \begin{array}{c} -1 \\ 0 \\ +1 \end{array} \right\};$$

and $g(n_2(t), n_3(t))$ is the weighting factor taking into account the effect of differently colored nearest neighbors. Since $n_1(t) + n_2(t) + n_3(t) = N$, this relationship gives the number of white cells; therefore, $g(n_2(t), n_3(t))$ depends on only $n_2(t)$ and $n_3(t)$, while the number of white neighbors, $n_1(t)$, plays a "passive" role.

The idea of the "basic" mapping can be clarified in simple terms as follows. Let us label, in one way or another, all possible combinations of color states by the numbers of nearest neighbors in a particular state. For example, if the neighborhood of a cell consists of white neighbors only, this situation is assigned number 1 (which is also the "weight" of this state). If one cell in the neighborhood is gray and others white, this situation is assigned number (weight) 4. It should be noted that here we have degeneracy in gray cell permutations, since there are eight equivalent states with equal "weights." Moreover, numbers ("weights") 1, 4, 8, 12, … are chosen so that the mapping is unique; i.e., a state is mapped into a certain number that takes the value of –1, 0, or +1 after the first term in (3) is added (degeneracy is only in permutations). Then, the intermediate mapping will be into numbers 0, 1, 2, 3, 4, …; i.e., the state of starting cell (i, j) (which equals –1, 0, or +1) and the weight of the neighborhood (equal to 1, 4, 8, …) will be mapped into 0, 1, 2, 3, 4, …, according to (3). By numbering specific color combinations in the neighborhood (with permutation degeneracy alone), we will know into which number a specific cell (i, j) is mapped depending on the state of nearest cells. It should be emphasized once again that degeneracy remains only in permutations.

The first stage of the mapping, i.e., the application of formulas (3) and (4), is switched on according to certain rules. The first term in (3) works up to time instant $\tau_{m_{i,j}(t_{on})}$, with instant $\tau_{m_{i,j}(t_{on})}$ depending on the state of a cell (i, j) at time t_{on} of its appearance in a new state, so that (3) specifies the intermediate mapping. If after the second phase of the first stage of mapping (formula (4)), the initial state of the starting cell changes, the process starts from the beginning, i.e., from formula (3) but already at the next stage.

If, however, the initial state of the original cell persists after the second phase of the first stage, we pass to the second stage (formula (5)). The bracketed delta in (3) is switched on at time instant $(\tau_{m_{i,j}(t_{on})} + 1)$, and, if the state of the cell is retained, formula (3) goes to zero and we proceed using formula (5).

Formula (5) is valid as long as the initial state of the cell (i, j) is retained. However, at the second stage, the transition to another state may happen at any subsequent time instant, unlike at the first stage, when the initial state of the cell persisted all the time from its emergence to instant $\tau_{m_{i,j}(t_{on})}$. Figuratively, the situation can be expressed as follows. To pass into another state, the cell must first "mature" for time $\tau_{m_{i,j}(t_{on})}$ and only then change (or retain) its state at any time. The theta function in (5) is switched on at the time instant after t_{on}, i.e., when a subsequent cycle begins (time $t_{on} + 1$). The delta in (5) leaves only transitions with invariable states.

Consider now the second parts of the mappings given by (3) and (5), i.e., of formulas (4) and (6). These mappings establish relationships between the intermediate map and the map of this intermediate set into three main states of the cell. A numerical range (A_l', A_l) is specified such that a cell in the final state, when falling into it, is declared to be in a certain final color state. Physically, this is substantiated as follows. (Note that, in setting mapping rules, one may be guided by purely mathematical principles rather than physical considerations. However, here we are using mostly physically meaningful arguments.). If there is good reason to believe that a gray cell surrounded by three (and more) black cells will turn into the black state, a range (A_l', A_l) is taken such that these combinations with $n_3 \geq 3$ fall

into this range and all these combinations are then mapped into the (+1) (black) state and so on.

Now we pass to the most general statement of mapping. It is specified by the following rules.

$$\text{(i)}\ \ \bar{X}(i,j,t+1) = \Bigg[\theta(\tau_{m_{i,j}(t_{on})} - t)X(i,j,t)g_{m_{i,j}(t)} + \theta(t-\tau_{m_{i,j}(t_{on})}) \sum_{\substack{n_3(t)=n_3 \\ n_3(t)\geq n_3}}^{N} \sum_{\substack{n_2(t)=n_2 \\ n_2(t)\geq n_2}}^{N-n_3} C_N^{n_3(t)} C_{N-n_3(t)}^{n_2(t)} \times g(n_2(t), n_3(t))\Bigg] D[1-\delta_{m_{i,j}(t), m_{i,j}(t+1)} \times \theta(t-(\tau_{m_{i,j}(t_{on})}+1))]P_{m_{i,j}(t), m_{i,j(t+1)}}, \quad (7)$$

where

$$D = \left[3\sum_{n_3(t)=1}^{N}\sum_{n_2(t)=1}^{N-n_3} C_N^{n_3(t)} C_{N-n_3(t)}^{n_2(t)}\right]^{-1}$$

is the normalization factor taking into account all possible states of a cell (i, j) and of its neighborhood. Here, $\bar{X}(i, j, t+1) = X(i, j\ t)$ if $t < \tau_{m_{i,j}(t_{on})}$; $n_3(t) \geq n_3$ in the summation sign means that summation is over $n_3(t)$ that are greater than, or equal to, n_3; and $C_N^{n_3(t)}$ is the number of combinations of N things $n_3(t)$ at a time. Next is the mapping: if $A_l' < \bar{X}(i, j, t+1) < A_l$ (where $l = l_{\min}$–$l_{\max}$), then

$$X(i,j,t+1) = F(x) = \left\{\begin{array}{c} -1 \\ 0 \\ +1 \end{array}\right\}, \quad (8)$$

with probability $P_{m_{i,j}(t), m_{i,j(t+1)}}$.

$$\text{(ii)}\ \ \bar{X}(i,j,t+1) = \Bigg[X(i,j,t+1)g_{m_{i,j}(t)} + \sum_{\substack{n_3(t)=n_3 \\ n_3(t)\geq n_3}}^{N} \sum_{\substack{n_2(t)=n_2 \\ n_2(t)\geq n_2}}^{N-n_3} C_N^{n_3(t)} C_{N-n_3(t)}^{n_2(t)} g(n_2(t), n_3(t))\Bigg] \times D\delta_{m_{i,j}(t), m_{i,j}(t+1)}\theta(t-\tau_{m_{i,j}(t_{on})})P_{m_{i,j}(t), m_{i,j}(i+1)}, \quad (9)$$

where

$$P_{m_{i,j}(t), m_{i,j(t+1)}} = \begin{pmatrix} w_{11} & w_{12} & w_{13} \\ w_{21} & w_{22} & w_{23} \\ w_{31} & w_{32} & w_{33} \end{pmatrix} \quad (10)$$

is the probability matrix of transitions from a state $m_{i,j}(t)$ to a state $m_{i,j}(t+1)$; $m_{i,j}(t) = 1, 2, 3$; and $g_{m_{ij}(t)}$ and $g(n_2(t), n_3(t))$ are, respectively, the weighting factor of the corresponding initial state and the factor taking into account the state of the neighborhood of the initial cell.

The writing $n_3(t) \geq n_3$ in the summation sign means that all states with the number of black neighbors $n_3(t)$ that is larger than, or equal to, n_3 fall into one general set that is then mapped into one specific color state $m_{i,j}(t)$ (the same refers to the writing $n_2(t) \geq n_2$, where n_2 is the number of gray neighbors). Such summation can also be applied to other relationships between $n_3(t)$ and n_3, as well as between $n_2(t)$ and n_2, depending on conditions imposed on the transitions. For instance, if the transitions to other states are allowed (or "blocked") at $n_3(t) \leq n_3$ and $n_2(t) \leq n_2$, summation will be as follows:

$$\sum_{\substack{n_3(t)=0 \\ n_3(t)\leq n_3}}^{n_3} \sum_{\substack{n_2(t)=0 \\ n_2(t)\leq n_2}}^{n_2} C_N^{n_3(t)} C_{N-n_3(t)}^{n_2(t)} g(n_2(t), n_3(t)),$$

where the condition $n_1 + n_2 + n_3 = N$ must be met at any time.

Weighting factor $g_{m_{ij}(t)}$ multiplying the first term in (7) and (9) determines the "addition" of the initial state to the intermediate state. This can be understood from the following considerations. If the second term stands for mapping into the numbers 0, 1, 2, 3, or 4 according to the state of the neighborhood (as was explained in the statement of the basic mapping given by formulas (3) and (4)), the resulting series of maps (numbers) will be different with regard to the weighting factor multiplying the first term. If we leave the final rules specifying the second phase of mapping, $A_l' < x < A_l$ (see, e.g., formula (6)) the same, i.e., those without the weighting factors (that is, the ranges of mapping are not redefined), weight factor $g_{m_{i,j}(t)}$ adds somewhat different combinations of states into these ranges: cell (i, j) + its neighborhood.

In our opinion, the mapping given by (7)–(10) is the most general mapping that can represent the class of problems under study. By switching different components on or off in this general mapping, one can obtain particular cases, such as basic mapping (3)–(6).

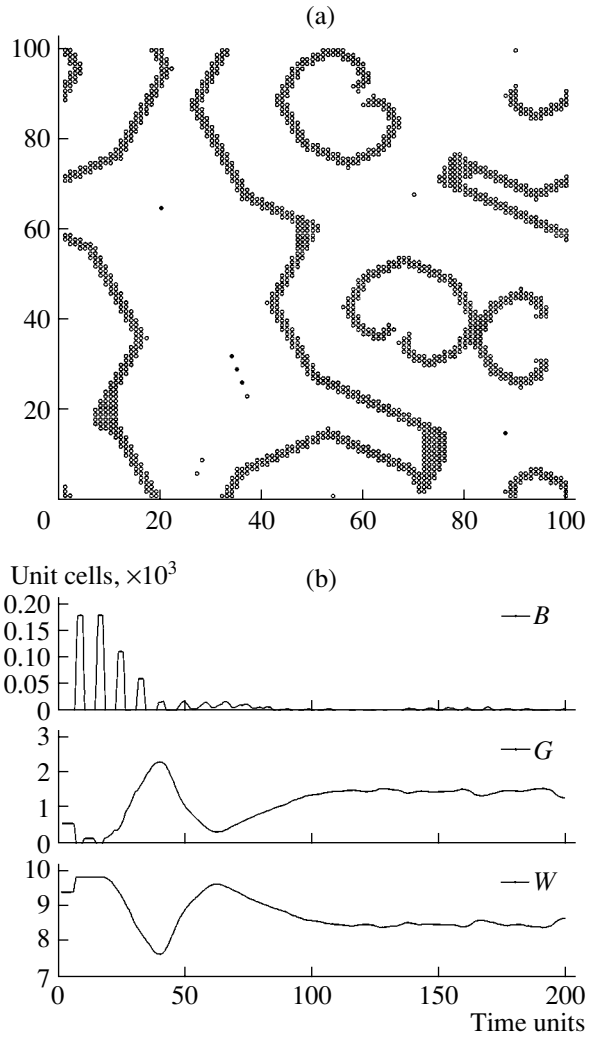

Fig. 1. (a) Helical waves (gray cells on the white background) and (b) the dependences of the number of black (*B*), gray (*G*), and white (*W*) cells on time (on the number of cycles).

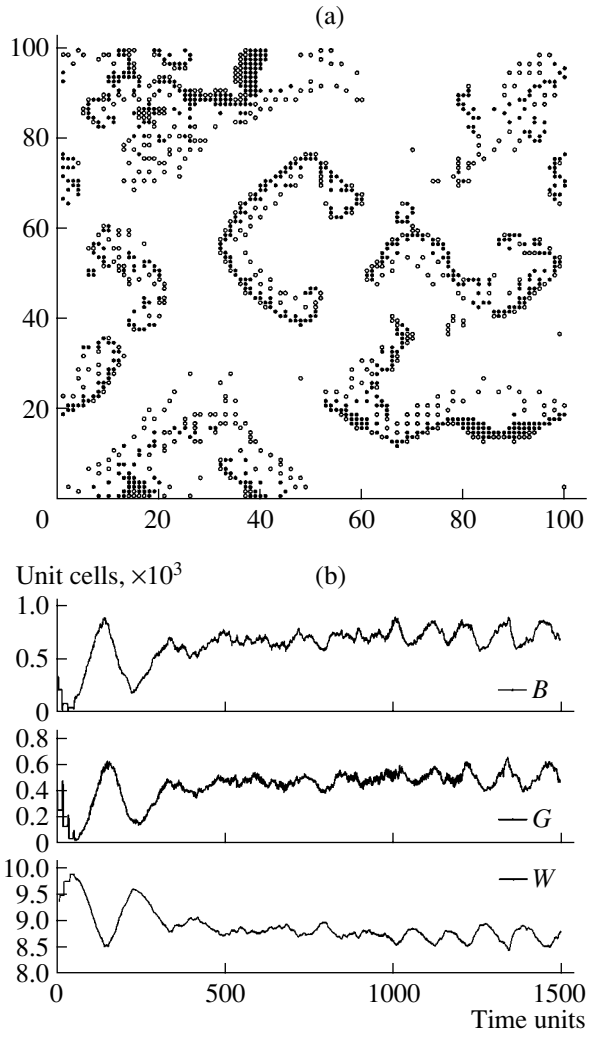

Fig. 2. (a) Helical waves, including those interacting with each other (gray and black cells on the white background), and (b) the dependences of the number of black (*B*), gray (*G*), and white (*W*) cells on time (on the number of cycles).

RESULTS AND DISCUSSION

Note that general mapping (7)–(10) yields such a vast diversity of dynamic (from strictly periodic to chaotic) structures of different configurations, color combinations, leading centers, and helical waves that today it seems infeasible to cover all possible results of mapping (7)–(10). We will concentrate on a number of regularities that have been found to date. Some features of our model were considered in [18]. In that work, we presented the characteristic structures arising under the conditions of leading center formation and the variation of the number of black cells with time (with the number of cycles). These structures reflect the strictly periodic and chaotic dynamics of the system and also its dynamics under the conditions of leading center formation at certain values of the system parameters.

Below, we show several patterns representing the dynamic structures resulting from mapping (7)–(10), as well as the dependence of the number of black (*B*), gray (*G*), and white (*W*) cells on time (on the number of cycles). Figures 1 and 2 demonstrate the "snapshots" of helical waves consisting of gray cells (on the background of white cells, Fig. 1) and black-and-gray-and-white cells (on the background of white cells, Fig. 2), along with the corresponding time (cycle) dependences of the number of cells in specific states. The helical waves consist of two portions with different chirality, and their composition may vary, as indicated by Figs. 1 and 2. It should be noted that spiral waves represent elementary self-sustaining structures in excitable media. The structure of spiral waves depends on the excitability of an active medium. The formation of leading centers is mainly related to external factors (to the initial number of active unit cells in our case).

Figure 3 presents the snapshots of octagonal leading centers and associated dynamic dependences. The structures with well-defined angles nucleate when

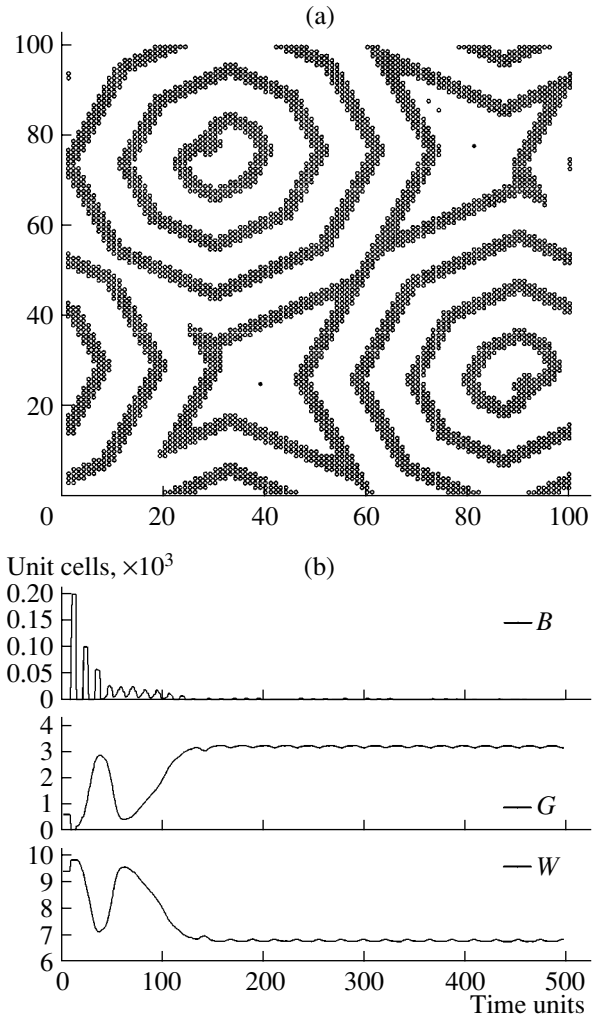

Fig. 3. (a) Octagonal leading centers (gray cells on the white background) and (b) the dependences of the number of black (*B*), gray (*G*), and white (*W*) cells on time (on the number of cycles).

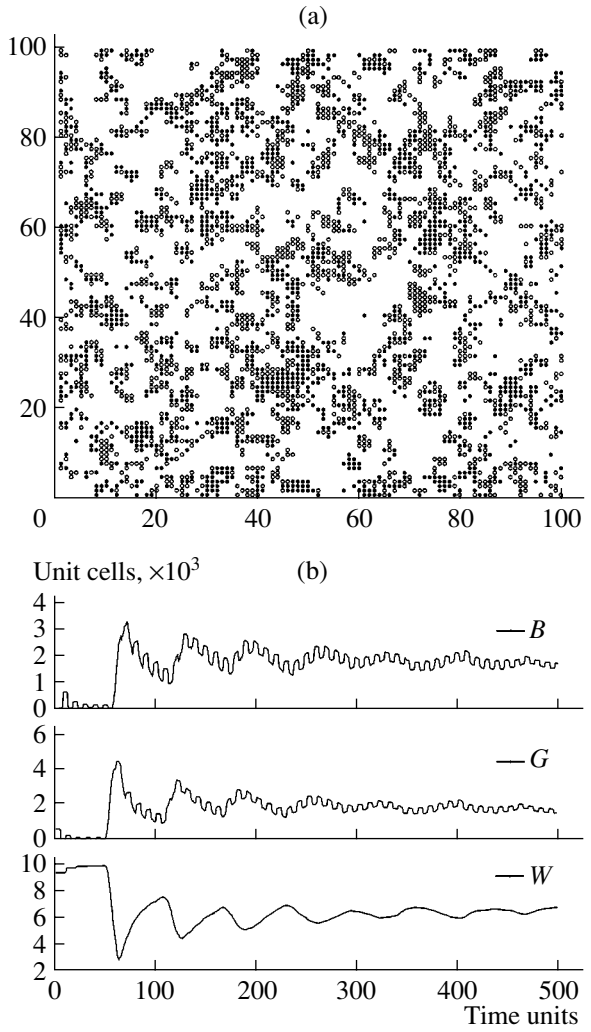

Fig. 4. (a) Chaotic dynamics (gray and black cells on the white background) and (b) the dependences of the number of black (*B*), gray (*G*), and white (*W*) cells on time (on the number of cycles).

probability factor $P_{m_{i,j}(t),\, m_{i,j}(t+1)}$ is blocked (switched off). When it is switched on, rounded structures may well form. That is, the stochastic factor may impart rounded shapes, along with others, to the forming structures.

Figures 4 and 5 demonstrate the snapshots of the systems under different chaotic conditions and the dynamic dependences of the number of different points on time (on the number of cycles). In this case, the dynamic behavior takes a variety of forms.

The behavior of a three-state adsorption system, which is described by local rules (7)–(10), is much richer than that of averaged macroscopic characteristics described by the van der Pol equation [13]. This fact is largely explained by the effective dimensionality of the system. It is known that the generalization of the one-dimensional van der Pol equation to the three-dimensional space [21] involves a stochastic (strange) attractor as a solution. These generalized equations describe a generator with inertial nonlinearity (Anishchenko–Astakhov generator) [21].

Significantly, the one-dimensional two-state adsorption problem for probabilistic cellular automata does not offer such a variety of solutions [22]. Moreover, oscillating solutions and solutions with pacemakers are totally absent. The one-dimensional three-state problem for classical cellular automata results in three types of solution: turbulent solutions, periodic solutions, and solutions of propagating soliton type [23]. As was noted in [24], nobody may today answer the question of how to find local rules following which a set of individual elements will reproduce a desired dynamics.

Under oscillatory conditions of pore formation, Buchin and Prokaznikov [20] observed different localized porous structures, which can be viewed as being related to the effect of pacemakers of spherical or right-

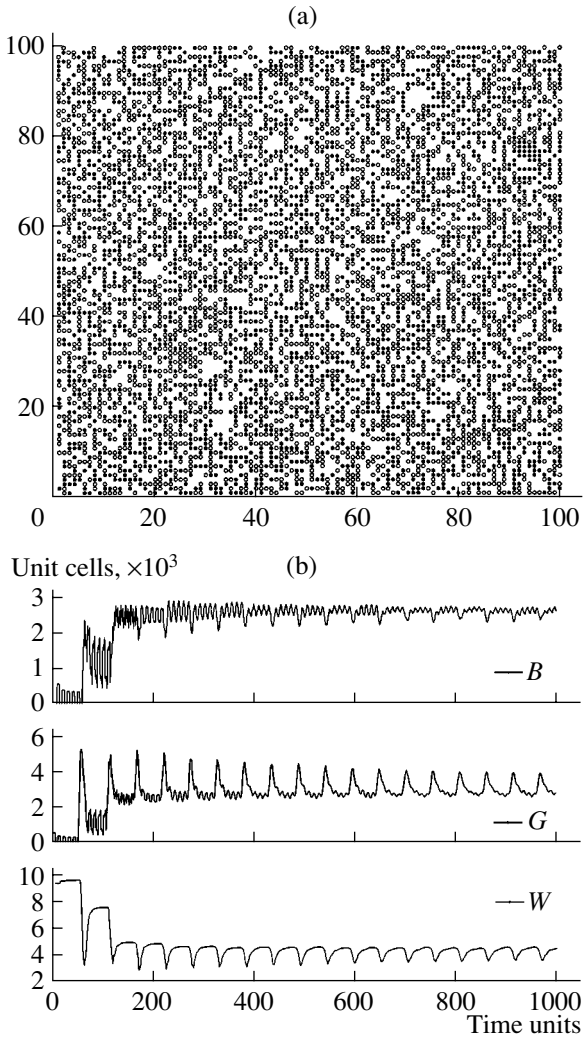

Fig. 5. (a) Chaotic dynamics (gray and black cells on the white background) and (b) the dependences of the number of black (*B*), gray (*G*), and white (*W*) cells on time (on the number of cycles).

angle configuration. The phase wave fronts in these two types of leading center run away both concentrically and at right angles. As was shown in [18], our model describes leading centers similar to those observed in [20].

A most interesting inference that can be drawn from this study is that, when passing from chaos to global synchronization, the system synchronizes first in the presence of leading centers. This means that locally oscillating centers with certain oscillation frequencies arise. The most convenient parameter characterizing different dynamic regimes in the system under study is the dynamic (Kolmogorov–Sinay) entropy, which is related to Lyapunov exponents [25]. Its value is maximal for chaotic oscillations and equal to that for regular oscillations. In the presence of leading centers, this entropy takes an intermediate value.

Thus, we developed a two-dimensional model of a non-Hamiltonian system exhibiting all properties characteristic of active media with self-organization. The results of this study can be used for predicting and interpreting the operation of various sensors (see, e.g., [12, 13]).

It should be emphasized that the subject of this investigation is the dynamic properties of adsorption systems with variable states of its basic building blocks (atoms or molecules), whereas the traditional approach handles mainly averaged macroscopic characteristics of the system (see, e.g., [1, 26, 27]).

The model can be extended to cells with a number of states of more than three. Such an extension may take into account the participation of molecules (atoms) in various chemical reactions on the solid surface. Similarly, a greater number of factors attendant to processes on the solid surface may be allowed for. Finally, the model might be helpful in sociological studies (see, e.g., [28] and Refs. therein).

ACKNOWLEDGMENTS

The authors are grateful to Profs. H. Föll and J.C. Claussen (University of Kiel, Germany) for highlighting this problem.

APPENDIX

An algorithm based on mapping (7)–(10) was implemented in the MatLab software environment [29], which is the most suitable for vector and matrix computations.

The algorithm relies on an adsorption system model according to which atoms adsorbed on the solid surface may be in two, neutral and charged, states. The latter is due to tunnel exchange of electrons between an atom and the solid. The algorithm considers unit cells on the surface that may (i) be free of an adsorbed atom (molecule), (ii) contain an adsorbed neutral atom, and (iii) contain a charged adsorbed atom. The charge state of the unit cell may vary depending on the state of the nearest neighbors. In this way, the lateral interaction between adsorbed atoms is taken into account. This model, being two-dimensional, is related to the solid surface, which is considered ideal: surface defects and surface inhomogeneities are ignored. The boundary of the working area is assumed to be cyclically closed in both dimensions.

The computer model considered in this work is based on the theory of probabilistic cellular automata. The whole field of events on the solid surface is divided into square unit cells, which may be empty (white), occupied by a neutral molecule (gray), or occupied by a charged molecule (black). Two 100×100 sparse

square matrices are used to store locational data for black and gray cells. The lateral interaction is taken into account in such a way that the probability of a cell turning into one or another state depends on the number of nearest neighbors being in a certain state.

The dynamics of color-to-color cell transitions is calculated by means of matrix operations, which considerably accelerates the execution of the algorithm [29]:

% initialization of matrices for location data storage,

% gray and black points,

m = 100; % dimension of matrices,

% initialization of matrices *X* and *Y* of gray and black points, respectively, on white background,

X = *sparse*(*m*, *m*); *Y* = *sparse*(*m*, *m*);

% 100 × 100 matrix of uniformly distributed random numbers [0…1],

R = *rand*(*m*);

% matrix of cell lifetimes,

T = *zeros*(*m*, *m*);

% number of gray, *N*1, and black, *N*2, neighbors,

*N*1 = *neighbors*(*X*); *N*2 = *neighbors*(*Y*);

% corresponding transition probabilities *tau_i*, where *i* = 1, …, 7;

% white ⟶ (gray|white);

% gray ⟶ (white|gray|black);

% black ⟶ (white|gray|black);

% lifetimes of corresponding points *ttl_w*; *ttl_g*; *ttl_b*;

% local transition rules

% white ⟶ (gray|white)

*dX*1 =~ *X*& ~ *Y*&*T* >= *ttl_w*&(((*N*1 >= 1|*N*2 >= 2)&

R <= *tau*_1)|(*N*1 == 0&…, *N*2 == 0&R <= *tau*_7));

% gray ⟶ (black|white|gray),

*dY*1 = *X*&*T*> =*ttl_g*&*R*< = *tau*_2&

(*N*1 > = 3|*N*2 > = 2);

% gray ⟶ black,

*dW*1 = ~*dY*1&*X*&*T*> = *ttl_g*&*R* < = *tau*_3;

% gray ⟶ white,

% black ⟶ (gray|white|black),

*dX*2 = *Y*&*T* >= *ttl_b*&*R* <= *tau*_4&

(*N*1 >= 3|*N*2 >= 2);

% black ⟶ gray,

*dW*2 =~ *dX*2&*Y* & *T* >= *ttl_b*&*r* <= *tau*_5;

% black ⟶ white,

% reset of TTL for newly modified cells,

T =~ ((*dX*1|*dY*1|*dW*1|*dX*2|*dW*2)&*T*). **T*;

X = *X* + *dX*1 – *dY*1 – *dW*2 + *dX*2; % modification of gray matrix,

Y = *Y* + *dY*1 – *dX*2 – *dW*2; % modification of black matrix,

T = *T* + 1; % increase of TTL by 1.

Implementation of this algorithm generates a large number of dynamic conditions, which can nevertheless be categorized into four basic groups [30].

REFERENCES

1. A. W. Adamson, *The Physical Chemistry of Surfaces*, 4th ed. (Wiley, New York, 1982; Mir, Moscow, 1979).
2. F. Ozanam, J.-N. Chazalviel, A. Radi, *et al.*, Phys. Chem. **95**, 98 (1991).
3. J. Carstensen, R. Prange, G. S. Poprikov, and H. Föll, Appl. Phys. A **67**, 459 (1998).
4. R. L. Smith and S. D. Collins, J. Appl. Phys. **71**, R1 (1992).
5. E. Yu. Buchin and A. V. Prokaznikov, Pis'ma Zh. Tekh. Fiz. **23** (5), 1 (1997) [Tech. Phys. Lett. **23**, 244 (1997)].
6. D. Dini, S. Catarin, and F. Decker, in *Proceedings of the International Conference "Porous Semiconductors: Science and Technology," Mallorca, 1998*, p. 13.
7. V. Parhutik, Y. Chu, Z. Nagy, and P. A. Montano, in *Proceedings of the International Conference "Porous Semiconductors: Science and Technology," Mallorca, 1998*, pp. 16–17.
8. V. Parhutik and E. Matveeva, in *Proceedings of the International Conference "Porous Semiconductors: Science and Technology," Madrid, 2000*, pp. 66–68.
9. V. Parhutik, E. Matveeva, I. Tkachenko, *et al.*, in *Proceedings of the International Conference "Porous Semiconductors: Science and Technology," Madrid, 2000*, pp. 297–298.
10. B. M. Kostishko and Yu. S. Nagornov, Zh. Tekh. Fiz. **71** (7), 60 (2001) [Tech. Phys. **46**, 847 (2001)].
11. Yu. E. Babanov, A. V. Prokaznikov, N. A. Rud, and V. B. Svetovoy, Phys. Status Solidi A **162**, R7 (1997).
12. A. N. Laptev, A. V. Prokaznikov, and N. A. Rud, Pis'ma Zh. Tekh. Fiz. **26** (23), 47 (2000) [Tech. Phys. Lett. **26**, 1049 (2000)].
13. A. N. Laptev, A. V. Prokaznikov, and N. A. Rud, Mikrosist. Tekh., No. 6, 31 (2002).
14. D. I. Bilenko, O. Y. Belobrovaya, E. A. Zharkova, *et al.*, Semiconductors **36**, 466 (2002).
15. D. P. Bernatskiĭ and V. G. Pavlov, Pis'ma Zh. Tekh. Fiz. **26**, 22 (2000) [Tech. Phys. Lett. **26**, 233 (2000)].
16. D. P. Bernatskiĭ and V. G. Pavlov, Fiz. Tverd. Tela (St. Petersburg) **46**, 1494 (2004) [Phys. Solid State **46**, 1538 (2004)].
17. Yu. E. Babanov, A. V. Prokaznikov, and V. B. Svetovoy, Vacuum **41**, 902 (1990).
18. S. A. Kapliĭ, A. V. Prokaznikov, and N. A. Rud, Pis'ma Zh. Tekh. Fiz. **30** (14), 46 (2004) [Tech. Phys. Lett. **30**, 595 (2004)].
19. Yu. A. Babanov, A. V. Prokaznikov, and V. B. Svetovoĭ, in *All-Russia Conference with the Participation of Foreign Scientists "Mikroelektronika-94," Zvenigorod, 1994*, Chap. 2, pp. 593–594.
20. E. Yu. Buchin and A. V. Prokaznikov, Phys. Low-Dimens. Semicond. Struct. **7–8**, 69 (2003).

21. V. S. Anishchenko, *Complex Oscillations in Simple Systems* (Nauka, Moscow, 1990) [in Russian].
22. H. Fuks, nlin.CG/0302015 (2003).
23. Y. Oono and M. Kohmoto, Phys. Rev. Lett. **55**, 2927 (1985).
24. V. K. Vanag, Usp. Fiz. Nauk **169**, 481 (1999) [Phys. Usp. **42**, 413 (1999)].
25. G. Benettin, L. Galgani, and J.-M. Strelcyn, Phys. Rev. A **14**, 2338 (1976).
26. I. O. Protod'yakonov and S. V. Siparov, *Mechanics of Adsorption in Gas–Solid Systems* (Nauka, Leningrad, 1985) [in Russian].
27. I. Vosilyus and L. Pranyavichyus, *Ion-Beam-Activated Processes on Solid Surfaces* (Mokslas, Vil'nyus, 1987) [in Russian].
28. A. Traulsen and J. C. Claussen, cond-mat/0404694 (2004).
29. S. A. Kapliĭ, A. V. Prokaznikov, and N. A. Rud, in *Proceedings of the 2nd All-Russia Scientific Conference on the Design of Engineering and Scientific Applications in the MatLab Environment, Moscow, 2004*, pp. 559–564.
30. S. Wolfram, Rev. Mod. Phys. **55**, 601 (1983).

Translated by M. Lebedev

Technical Physics, Vol. 50, No. 12, 2005, pp. 1544–1550. Translated from Zhurnal Tekhnicheskoĭ Fiziki, Vol. 75, No. 12, 2005, pp. 10–15.

THEORETICAL AND MATHEMATICAL PHYSICS

Nonstationary Motion of Electrons in a Double Plasma Layer Subjected to the Self-Consistent Electric Field of the Space Charge

V. A. Fedorov

Mintz Radio Engineering Institute, Moscow, 125083 Russia
e-mail: f_v99@mail.ru

Received December 15, 2004

Abstract—Nonstationary 1D equations describing the motion of electrons in a double plasma layer subjected to the self-consistent electric field of the space charge are investigated with allowance for friction force. Analytical solutions to a set of nonlinear hydrodynamic equations for plasma electrons are derived. The variation of the electric field strength, as well as of the electron velocity and concentration, in space and time is found. Electron plasma motions of different types of symmetry are characterized in terms of dynamic parameters. © *2005 Pleiades Publishing, Inc.*

(1) Charged particle flow dynamics is a subject of great interest in such areas of science and technology as radio physics; generation, injection, and transport of electron and/or ion beams in a plasma or vacuum; etc. [1, 2]. Most frequently, relevant studies are carried out as applied to the double plasma layer, which is the basic structural component of the plasma and is dealt with both in laboratory conditions (plasma-filled devices, plasma probes, etc.) and in outer space (e.g., auroras and experiments with charged particle injection in the ionosphere) [3, 4]. As a rule, the double plasma layer consists of two space-separated unlike electrical layers with different particle concentrations. Accordingly, the plasma becomes charged, i.e., charged particle flows in it have an uncompensated volume charge. Furthermore, the double plasma layer is usually studied either in the steady state (the boundary conditions are set, and the charged particle current is a desired parameter) [5] or in equilibrium (the electric field potential is set, and the subject under study is the behavior of the system, e.g., conditions of its stability) [6].

In this work, we study the 1D motion of electrons in the double plasma layer where electrons and ions are initially ($t = 0$) completely separated in space and have a mutual boundary and their net electrical charge equals zero. The ions are assumed to remain quiescent for $t \geq 0$. A solution to the problem will be sought for the time interval $0 \leq t \leq t_r$, where t_r is the time instant the electron velocity becomes zero at any point of the space or the electron front reaches the boundary of the layer. The first restriction follows from the fact that, at $t > t_r$, a counter flow of electrons may arise and, hence, the particle trajectories will cross each other, which makes the hydrodynamic approach invalid. The second restriction implies that the electrons can move only within the double plasma layer. Those reaching the boundary and leaving the layer at $t > t_r$ should be omitted from consideration, since they cease to contribute to the electric field strength in the layer. Because of these restrictions, the problem cannot be solved analytically.

Consider a double plasma layer of volume $V = V_e + V_i$, where V_e and V_i are the respective volumes occupied by electrons and ions at $t = 0$. These volumes are bounded coordinates $0 \leq R < \Delta$ and $\Delta \leq R \leq R_c$. Here, 0, R_c, and Δ are the distances from the origin to the left-hand boundary of the layer, right-hand boundary of the layer, and boundary between V_e and V_i, respectively. The electrons can move within the interval $0 \leq R \leq R_c$, and the ions are at rest within $\Delta \leq R \leq R_c$. Let electron charge Q_e in volume V_e and ion charge Q_i in volume V_i be such that

$$Q_e + Q_i = 0. \tag{1}$$

Charges Q_e and Q_i are assumed to be continuous functions in V_e and V_i,

$$Q_e = \int_{V_e} en_e dV_e, \quad Q_i = \int_{V_i} |e| n_i dV_i; \tag{2}$$

where e is the electron charge and n_e and n_i are the concentrations of electrons and ions, respectively, in the plasma.

Since the motion is one-dimensional, we can represent (1), in view of (2), as

$$\int_0^\Delta en_e(R, 0)R^k dR - \int_\Delta^{R_c} en_i(R, 0)R^k dR = 0, \tag{3}$$

where $k = 0$, 1, or 2 for plane, cylindrical, and spherical symmetry, respectively.

(2) To study the electron dynamics with regard to the above approximations and restrictions, we will use a set of equations for one-liquid cold plasma hydrodynamics with allowance for a friction force proportional to the motion velocity [7]. With thermal effects ignored, this set in the 1D representation appears as

$$\frac{\partial V_e}{\partial t} + V_e\frac{\partial V_e}{\partial R} + \nu_e V_e = \frac{e}{m_e}E, \tag{4}$$

$$\frac{1}{R^k}\frac{\partial}{\partial R}(R^k E) = 4\pi e(n_e - n_i), \tag{5}$$

$$\frac{\partial E}{\partial t} = -4\pi e n_e V_e. \tag{6}$$

Here, $E(R, t) = E_e(R, t) + E_i(R, 0)$ is the total electric field of electrons and ions, $V_e(R, t)$ is the electron velocity, R is the distance to a point in space, m_e is the electron mass, and ν_e = const is the electron–neutral collision rate.

To close set (4)–(6), we set initial and boundary conditions [8]. As the former ($t = 0$), we take

$$V_{e,i}(R_*, 0) = 0, \quad n_{e,i}(R_*, 0) = n^0_{e,i} f_{e,i}(R_*, 0), \tag{7}$$

$$E(R_*, 0) = \frac{4\pi}{R_*^k}\int_0^{R_*}[en^0_e f_e(R_*, 0) - \chi en^0_i f_i(R_*, 0)]R_*^k dR_*, \tag{8}$$

where $0 \le R_* \le R_c$; $n^0_e = n^0_i$ = const are the undisturbed concentrations of electrons and ions, respectively, in the plasma; and $f_{e,i}(R, 0) \ge 1$ are functions specifying $n_{e,i}(R, 0)$. Parameter $\chi = 0$ or 1 for $0 \le R < \Delta$ and $\Delta \le R \le R_c$, respectively.

The boundary conditions at the outer (stationary) boundaries of V_e and V_i are given by

$$V_e(0, t) = 0, \quad n_e(0, t) = n^0_e f_e(0, 0),$$
$$V_i(R_c, t) = 0, \quad n_i(R_c, t) = n^0_i f_i(R_c, 0), \tag{9}$$

$$E(0, t) = 0, \quad E(R_c, t) = 0. \tag{10}$$

The boundary conditions for electrons at the mobile boundary of V_e and the position of this boundary are found by solving set (4)–(6).

Integrating (5) over V between 0 and R, where R is the coordinate of the final position of the mobile boundary of volume V_e (at $t = 0$, this boundary has coordinate R_*), and applying the Gaussian theorem, we get

$$E(R, t) = \frac{m_e}{e}\frac{\omega_0^2}{P(k)n^0_e}[\Psi_e(R, t) - \chi\Psi_i(R, 0)]\frac{1}{R^k}. \tag{11}$$

Here, $\omega_0^2 = 4\pi e^2 n^0_e/m_e$ and $P(k) = 1$, 2π, or 4π for plane, cylindrical, and spherical symmetry, respectively. Functions $\Psi_e(R, t) = P(k)\int_0^R n_e(R, t)R^k dR$ and $\Psi_i(R, t) = \chi P(k)\int_\Delta^R n_i(R, 0)R^k dR$ are the functions of the Lagrangean material variable [9] that define, in the given case, the number of electrons and ions, as well as their charges $q_e = e\Psi_e$ and $q_i = |e|\Psi_i$, in volumes $V_e(0, R)$ and $V_i(\Delta, R)$.

Let us assume that the trajectories of moving volume elements do not cross each other; then, the number of electrons in volume V_e specified by coordinates $[0, R_*(0)]$ and $[0, R(t)]$ (where $R_*(0)$ and $R(t)$ are the initial and final positions of the mobile boundary) is time-independent. Therefore, we can write [9]

$$\int_0^R n_e(R, t)R^k dR = \int_0^{R_*} n_e(R_*, 0)R_*^k dR_*. \tag{12}$$

Thus, in view of (12), expression (11) can be recast as

$$E(R_*, R) = \frac{m_e}{e}\left[C(R_*) - \chi\omega_0^2\int_\Delta^R f_i(R_*, 0)R_*^k dR_*\right]\frac{1}{R^k}, \tag{13}$$

where $C(R_*) = \omega_0^2\int_0^{R_*} f_e(R_*, 0)R_*^k dR_*$.

Substituting (13) into (4) yields

$$\frac{\partial V_e}{\partial t} + V_e\frac{\partial V_e}{\partial R} + \nu_e V_e = \left[C(R_*) - \chi\omega_0^2\int_\Delta^R f_i(R_*, 0)R_*^k dR_*\right]\frac{1}{R^k}. \tag{14}$$

Passing to the substantial derivative in (14), we find that

$$\frac{d^2R}{dt^2} + \nu_e\frac{dR}{dt} = \left[C(R_*) - \chi\omega_0^2\int_\Delta^R f_i(R_*, 0)R_*^k dR_*\right]\frac{1}{R^k}. \tag{15}$$

Writing (5) in the Lagrangean variables, we obtain an equation for $n_e(R_*, t)$,

$$n_e(R_*, t) = \chi n_i(R_*, 0) + \frac{1}{4\pi e}\left(k\frac{E}{R} + \frac{\partial E}{\partial R} + \frac{\partial E}{\partial R_*}\frac{1}{\partial R/\partial R_*}\right). \tag{16}$$

(3) Let $k = 0$ and $n_i(R_*, 0) = n_i^0$, i.e., $f_i(R_*, 0) = 1$. Then, the electron motion is of plane symmetry and proceeds in the presence of neutrals at $R < \Delta$ and in the presence of neutrals and homogeneous background of plasma ions at $\Delta \le R \le R_c$.

(i) For $R < \Delta$, the solutions to set (4)–(6) have the form (in view of (13)–(16))

$$E(R_*) = \frac{m_e}{e}C(R_*), \tag{17}$$

$$R(R_*, t) = R_* + \frac{C(R_*)}{\nu_e^2}[\nu_e t - 1 + \exp(-\nu_e t)], \tag{18}$$

$$V_e(R_*, t) = \frac{C(R_*)}{\nu_e}[1 - \exp(-\nu_e t)], \tag{19}$$

$$n_e(R_*, t) = \frac{n_e^0 f_e(R_*, 0)}{1 + \dfrac{\omega_0^2}{\nu_e^2}\{\nu_e t - [1 - \exp(-\nu_e t)]\} f_e(R_*, 0)}. \tag{20}$$

The constants of integration entering into expressions (17)–(20) can be found with regard to the initial conditions.

From (17)–(20), it follows that $E(R_*) = \text{const}|_R$ by virtue of plane symmetry and the initial conditions and $E(R_*) = \text{const}|_t$ owing to the fact that $\partial q_e/\partial t = 0$, where q_e is the electron charge in the volume corresponding to $0 \le R \le R_*$ (see (12)). In this case, $E(R_*)$ is the electric field strength at a charged infinitely large plane. Let the condition $\nu_e t \gg 1$ be met for the particles moving in the interval $0 < R < \Delta$; then, $R(R_*, t) \approx R_* + [C(R_*)/\nu_e]t$, $V_e(R_*, t) \longrightarrow C(R_*)/\nu_e = \text{const}|_t$, and $n_e(R_*, t) \approx n_e^0 \nu_e/\omega_0^2 t$. The time of motion of these particles can be estimated from expression (18) where we put $R(R_*, t) \le \Delta$. Eventually, we have

$$t(R_*, \Delta) \le \frac{\nu_e R_*}{C(R_*)}\left(\frac{\Delta}{R_*} - 1\right). \tag{21}$$

Putting $f_e(R_*, 0) = \mu = \text{const}$ (the uniform distribution of $n_e(R_*, 0)$), we obtain from (21)

$$t(R_*, \Delta) \le \frac{\nu_e}{\mu\omega_0^2}\left(\frac{\Delta}{R_*} - 1\right). \tag{22}$$

For $\nu_e \longrightarrow 0$, expressions (17)–(20) become solutions to set (4)–(6), which describes the motion of electrons in a vacuum [10].

(ii) For $\Delta \le R \le R_c$ and $\nu_e < 2\omega_0$ (low drag), we arrive, in view of (13)–(16), at the solutions to set (4)–(6) in the form

$$E(R_*, t) = -\frac{m_e}{e}\omega_0^2 \exp\left(-\nu_e\frac{t}{2}\right)(G_1 \sin\Omega t + G_2 \cos\Omega t), \tag{23}$$

$$R(R_*, t) = \Delta + \frac{C(R_*)}{\omega_0^2} + \exp\left(-\nu_e\frac{t}{2}\right)(G_1 \sin\Omega t + G_2 \cos\Omega t), \tag{24}$$

$$V_e(R_*, t) = \exp\left(-\nu_e\frac{t}{2}\right)(G_3 \sin\Omega t + G_4 \cos\Omega t), \tag{25}$$

$$n_e(R_*, t) = \frac{n_e^0 f_e(R_*, 0)}{f_e(R_*, 0) + \exp\left(-\nu_e\dfrac{t}{2}\right)(G_1' \sin\Omega t + G_2' \cos\Omega t)}. \tag{26}$$

Here, $\Omega = (4\pi e^2 n_i^0/m_e - \nu_e^2/4)^{1/2} = (\omega_0^2 - \nu_e^2/4)^{1/2}$ and functions G_1–G_4 are functions of R_*. The prime in (26) means differentiation with respect to R_*. From (23)–(26), it follows that, if $\nu_e t \gg 1$, electron oscillations decay; namely, $E(R_*, t) \longrightarrow 0$, $R(R_*, t) \longrightarrow \Delta + C(R_*)/\omega_0^2$, $V_e(R_*, t) \longrightarrow 0$, and $n_e(R_*, t) \longrightarrow n_e^0$. In other words, the particles tend toward the state of rest. Also, they must stay within the plasma layer; i.e., the condition $R(R_*, t) \longrightarrow \Delta + C(R_*)/\omega_0^2 \le R_c$ must be fulfilled. Assuming that $f_e(R_*, 0) = \mu$, we have $R(R_*, t) \longrightarrow \Delta + \mu R_* \le R_c$. Then, $\mu \le (R_c - \Delta)/R_*$. Now, putting $R_* = \Delta$ (the initial coordinate of the electron flow front), we can find the maximal value of $n_e(R_*, 0) = n_e^0 \mu = n_e^0 (R_c/\Delta - 1)$, at which the particles at the front still remain within R_c; that is, $R(R_*, t) \le R_c$. Note that the need to determine constants G_1–G_4 is related to the use of expressions (17)–(20), which specify "initial conditions" for solutions (23)–(26) at point $R(R_*, t) = \Delta$. To find G_1–G_4 in explicit form for the motion in the domain $\Delta \le R \le R_c$, it is necessary that each particle with coordinate R_* from the domain $0 < R < \Delta$ be assigned specific $t(R_*, \Delta)$ and $V_e(R_*, \Delta)$. In the general case, however, this task cannot be accomplished, since the equations to be solved are nonlinear. Therefore, constants G_1–G_4 in (23)–(26) remained undetermined.

(iii) If $\Delta \le R \le R_c$ and $\nu_e > 2\omega_0$ (high drag), the solutions to set (2)–(4) in view of (13)–(16) are given by

$$E(R_*, t) = -\frac{m_e}{e}\omega_0^2 \exp\left(-\nu_e \frac{t}{2}\right) \times [G_5 \exp(\xi t) + G_6 \exp(-\xi t)], \tag{27}$$

$$R(R_*, t) = \Delta + \frac{C(R_*)}{\omega_0^2} + \exp\left(-\nu_e \frac{t}{2}\right)[G_5 \exp(\xi t) + G_6 \exp(-\xi t)], \tag{28}$$

$$V_e(R_*, t) = \xi \exp\left(-\nu_e \frac{t}{2}\right)[G_7 \exp(\xi t) - G_8 \exp(-\xi t)], \tag{29}$$

$$n_e(R_*, t) = \frac{n_e^0 f_e(R_*, 0)}{f_e(R_*, 0) + \exp\left(-\nu_e \frac{t}{2}\right)[G_5' \exp(\xi t) + G_6' \exp(-\xi t)]}, \tag{30}$$

where $\xi = (\nu_e^2/4 - \omega_0^2)^{1/2}$.

Expressions (27)–(30) describe the aperiodic motion of the particles, which tend toward the state of rest without oscillations. If $\nu_e t \gg 1$, $\nu_e^2/\omega_0^2 \gg 1$, and $R(R_*, t) \le R_c$, we have from (27)–(30)

$$E(R_*, t) \approx -(m_e/e)\omega_0^2 G_5 \exp[-\nu_e t/(\nu_e^2/\omega_0^2)],$$

$$R(R_*, t) \approx \Delta + C(R_*)/\omega_0^2 + G_5 \exp[-\nu_e t/(\nu_e^2/\omega_0^2)],$$

$$V_e(R_*) \approx \xi G_7 \exp[-\nu_e t/(\nu_e^2/\omega_0^2)],$$

$$n_e(R_*) \approx n_e^0 f_e(R_*, 0)/\{f_e(R_*, 0) + G_5' \exp[-\nu_e t/(\nu_e^2/\omega_0^2)]\}.$$

Constants G_5–G_8 in solutions (27)–(30) cannot be generally expressed in explicit form.

Let us study the motion of the particles at the front of the electron flow. Substituting the expressions

$$C(\Delta) = \omega_0^2 f_e(\Delta, 0)\Delta,$$

$$G_5 = -(1 + \nu_e/2\xi) f_e(\Delta, 0)\Delta/2,$$

$$G_6 = -(1 - \nu_e/2\xi) f_e(\Delta, 0)\Delta/2,$$

$$G_7 = (1 - \nu_e/2\xi)G_5, \quad G_8 = (1 + \nu_e/2\xi)G_6,$$

$$G_5' = -(1 + \nu_e/2\xi) f_e(\Delta, 0)/2,$$

$$G_6' = -(1 - \nu_e/2\xi) f_e(\Delta, 0)/2,$$

which are found for $R_* = \Delta$ and $V_e(\Delta, 0) = 0$, into formulas (27)–(30), we obtain

$$E(\Delta, t) = \frac{f_e(\Delta, 0)}{2}\frac{\Delta m_e}{e}\omega_0^2 \exp\left(-\nu_e \frac{t}{2}\right) \times \left[\left(1 + \frac{\nu_e}{2\xi}\right)\exp(\xi t) + \left(1 - \frac{\nu_e}{2\xi}\right)\exp(-\xi t)\right], \tag{31}$$

$$R(\Delta, t) = \Delta + f_e(\Delta, 0)\Delta\left\{1 - \frac{1}{2}\exp\left(-\nu_e \frac{t}{2}\right) \times \left[\left(1 + \frac{\nu_e}{2\xi}\right)\exp(\xi t) + \left(1 - \frac{\nu_e}{2\xi}\right)\exp(-\xi t)\right]\right\}, \tag{32}$$

$$V_e(\Delta, t) = -\frac{f_e(\Delta, 0)\Delta}{2}\left(1 - \frac{\nu_e^2}{4\xi^2}\right)\xi \exp\left(-\nu_e \frac{t}{2}\right) \times [\exp(\xi t) - \exp(-\xi t)], \tag{33}$$

$$n_e(\Delta, t) = \frac{n_e^0}{1 - \frac{1}{2}\exp\left(-\nu_e \frac{t}{2}\right)\left[\left(1 + \frac{\nu_e}{2\xi}\right)\exp(\xi t) + \left(1 - \frac{\nu_e}{2\xi}\right)\exp(-\xi t)\right]}. \tag{34}$$

For $\nu_e t \gg 1$ and $\nu_e^2/\omega_0^2 \gg 1$, we get from (31)–(34)

$$E(\Delta, t) \approx (m_e/e)\omega_0^2 f_e(\Delta, 0)\Delta \exp[-\nu_e t/(\nu_e^2/\omega_0^2)],$$

$$R(\Delta, t) \approx \Delta + f_e(\Delta, 0)\Delta\{1 - \exp[-\nu_e t/(\nu_e^2/\omega_0^2)]\},$$

$$V_e(\Delta, t) \approx [\omega_e^2 f_e(\Delta, 0)\Delta/\nu_e] \exp[-\nu_e t/(\nu_e^2/\omega_0^2)],$$

$$n_e(\Delta, t) \approx n_e^0/\{1 - \exp[-\nu_e t/(\nu_e^2/\omega_0^2)]\}.$$

Putting $R(\Delta, t) = R_c$ in (32), we can find the time instant the electron flow front reaches right-hand boundary R_c (i.e., time t_r) (see Sect. (1)),

$$t(\Delta, R_c) \approx -\frac{\nu_e}{\omega_0^2}\ln\left[\frac{1}{f_e(\Delta, 0)}\left(\frac{R_c}{\Delta} - 1\right)\right] \equiv t_r. \tag{35}$$

Let we have $(R_c/\Delta - 1)/f_e(\Delta, 0) \approx 1$ in (35); then, $t_r \longrightarrow \infty$. This means that the electrons in this case cannot reach boundary R_c. As follows from (33), if $t \geq 0$, then $V_e(\Delta, t) \geq 0$; that is, the sign of the particle velocity at the flow front remains the same. The velocity reaches a maximum when

$$t(V_{e\,max}(\Delta)) = \frac{1}{2\xi}\ln\left(\frac{1+2\frac{\xi}{\nu_e}}{1-2\frac{\xi}{\nu_e}}\right). \quad (36)$$

If $\nu_e^2/\omega_0^2 \gg 1$, we find from (36) that $t(V_{e\,max}(\Delta)) \approx (2/\nu_e)\ln(\nu_e/\omega_0)$. For this value of $t(V_{e\,max}(\Delta))$, we get from (33)

$$V_{e\,max}(\Delta) \approx f_e(\Delta, 0)\Delta\frac{\omega_0^2}{\nu_e}. \quad (37)$$

For $f_e(R_*, 0) = \mu$, expressions (35) and (37) yield $t(\Delta, R_c) \approx -(\nu_e/\omega_0^2)\ln[1 - (R_c - \Delta)/\mu\Delta]$ and $V_{e\,max}(\Delta) \approx \mu\Delta\omega_0^2/\nu_e$.

(4) Equation (14) can be reduced to the Abelian equation of the second kind [11],

$$V_e\frac{\partial V_e}{\partial R} + \nu_e V_e = \left[C(R_*) - \chi\omega_0^2\int_\Delta^R f_i(R_*, 0)R_*^k dR_*\right]\frac{1}{R^k}. \quad (38)$$

For $\nu_e = 0$, the solution to Eq. (38) may be written as

$$V_e(R_*, R) = \sqrt{2\int_{R_*}^R\left[C(R_*) - \chi\omega_0^2\int_\Delta^R f_i(R_*, 0)R_*^k dR_*\right]\frac{dR}{R^k}}. \quad (39)$$

Taking into account that $V_e = dR/dt$, where R is the time-dependent coordinate of a fixed particle in the medium, we have from (39)

$$t(R_*, R) = \pm\int_{R_*}^R \frac{dR}{\sqrt{2\int_{R_*}^R\left[C(R_*) - \chi\omega_0^2\int_\Delta^R f_i(R_*)R_*^{\hat{e}}dR_*\right]\frac{dR}{R^{\hat{e}}}}}. \quad (40)$$

Writing Eq. (5) in terms of the Lagrangean variables and using expressions (13) and (40), we find $n_e(R_*, R)$,

$$n_e(R_*, R) = \chi n_i^0 + \frac{1}{4\pi e}\left(k\frac{E}{R} + \frac{\partial E}{\partial R} - \frac{\partial E}{\partial R_*}\frac{\partial t/\partial R}{\partial t/\partial R_*}\right). \quad (41)$$

Let, e.g., $k = 2$ (the cases $k = 0$ and 1 can be considered in a similar manner) and $n_i(R_*, 0) = n_i^0$ (i.e., $f_i(R_*, 0) = 1$). Then, the spherically symmetric motion of electrons proceeds in a vacuum at $R < \Delta$ or in the presence of the homogeneous plasma ion background at $\Delta \leq R \leq R_c$.

(i) $R < \Delta$, the solutions to set (4)–(6) have the form, in view of (13) and (39)–(41),

$$E(R_*, R) = \frac{m_e}{e}\frac{C(R_*)}{R^2}, \quad (42)$$

$$V_e(R_*, R) = \sqrt{\frac{2C(R_*)}{R_*}\left(1 - \frac{R_*}{R}\right)}, \quad (43)$$

$$t(R_*, R) = \sqrt{\frac{R_*^3}{2C(R_*)}}\left(\frac{R}{R_*}\sqrt{1 - \frac{R_*}{R}} - \mathrm{Arctanh}\sqrt{1 - \frac{R_*}{R}}\right), \quad (44)$$

$$n_e(R_*, R) = n_e^0\frac{R_*^3}{R^3} \times \frac{f_e(R_*, 0)}{1 - \frac{3}{2}\left[1 - \frac{\omega_0^2 f_e(R_*, 0)R_*^3}{3C(R_*)}\right]\left(1 - \frac{R_*}{R}\sqrt{\frac{R}{R - R_*}}\mathrm{Arctanh}\sqrt{1 - \frac{R_*}{R}}\right)}. \quad (45)$$

Expression (42) implies that $E(R_*, R) \sim 1/R^2$ because of the spherical symmetry of the electron flow. Since $V_e(R_*, R) > 0$ in (43), the electrons move without crossing the trajectories. At $R_*/R \ll 1$, we find from (43) and (44) that $V_e(R_*) \approx \sqrt{2C(R_*)/R_*} = \mathrm{const}|_R$ and $t(R_*, R) \approx (R/R_*)\sqrt{R_*^3/2C(R_*)}$; that is, the motion velocity does not vary with distance, while the time grows with distance linearly. For $f_e(R_*, 0) = \mu$, we have $V_e(R_*) \sim R_*$. Hence, it follows that the particles do not outdistance each other if $n_e(R_*, R)$ is uniformly distrib-

uted. Putting $R = \Delta$ in (43), we obtain the velocity at which a particle with initial coordinate R_* falls into the plasma layer (or into the segment $R_c - \Delta$),

$$V_e(R_*, \Delta) = \sqrt{\frac{2C(R_*)}{R_*}\left(1 - \frac{R_*}{\Delta}\right)}. \quad (46)$$

Expression (46) is "the initial condition" in determining $V_e(R_*, R)$ for the particles that start moving in the presence of the ions. It follows from (45) that, when the electrons move in a vacuum, their concentration drops by the law $n_e(R_*, R) \sim 1/R^3$.

(ii) For $\Delta \le R \le R_c$, the solutions to set (2)–(4) can be written, in view of (13), (39), and (40), as

$$E(R_*, R) = \frac{m_e}{e}\frac{\omega_0^2}{3}\left\{\left[1 + \frac{3C(R_*)}{\omega_0^2\Delta^3}\right]\frac{\Delta^3}{R^2} - R\right\}, \quad (47)$$

$$V_e(R_*, R) = \omega_0 R_* \times \sqrt{\frac{2}{3}\left[\frac{3C(R_*)}{\omega_0^2 R_*^3} + \frac{\Delta^3}{R_*^3}\right]\left(1 - \frac{R_*}{R}\right) + \frac{1}{3}\left(1 - \frac{R^2}{R_*^2}\right)}, \quad (48)$$

$$t(R_*, R) = \pm\frac{1}{\omega_0 R_*} \times \int_{R_*}^{R} \frac{dR}{\sqrt{\frac{2}{3}\left[\frac{3C(R_*)}{\omega_0^2 R_*^3} + \frac{\Delta^3}{R_*^3}\right]\left(1 - \frac{R_*}{R}\right) + \frac{1}{3}\left(1 - \frac{R^2}{R_*^2}\right)}}. \quad (49)$$

The integral in expression (49) can be reduced to the elliptic integral of the third kind [12], which is nonrepresentable in elementary functions for $k = 2$ (unlike the cases $k = 0$ and 1). To find an analytical expression for $t(R_*, R)$, we consider this integral for $R_*/R \approx 1$ and $R_*/R \ll 1$. In the former case, we have $R/R_* \approx 1$ and $R_*/\Delta \approx 1$. Then, it follows from (49) that

$$t(R_*, R) \approx \frac{1}{\omega_0}\sqrt{\frac{\omega_0^2 R_*^3}{2C(R_*)}\left(\frac{R}{R_*} - 1\right)}. \quad (50)$$

If $R_*/R \ll 1$, then $R/R_* \gg 1$ and, from (49),

$$t(R_*, R) \approx \frac{\sqrt{3}}{\omega_0}\arcsin\left\{\frac{\frac{R}{R_*}}{\sqrt{2\left[\frac{3C(R_*)}{\omega_0^2 R_*^3} + \frac{\Delta^3}{R_*^3}\right]}}\right\}, \quad (51)$$

where it is taken into account that $\sqrt{2[3C(R_*)/\omega_0^2 R_*^3 + \Delta^3/R_*^3]} \gg 1$.

Putting $R_* = \Delta$ and $R = R_*$ in (51), we arrive at the time it takes for the electron front to reach boundary R_c (cf. (35)),

$$t(\Delta, R_c) \approx \frac{\sqrt{3}}{\omega_0}\arcsin\left\{\frac{\frac{R_c}{\Delta}}{\sqrt{2[f_e(\Delta, 0) + 1]}}\right\} \equiv t_r. \quad (52)$$

Subsequently, the electrons at the front leave the layer (recall that the motion outside the layer is omitted from consideration). It should be noted that $t_r \equiv \pi\sqrt{3}/2\omega_0$ if $f_e(R_*, 0) = 1$ and $R_c/\Delta = 2$.

To determine $n_e(R_*, R)$, we first put $R_*/R \approx 1$; then, $t(R_*, R)$ is given by formula (50). Substituting (47) and (50) into (41) yields

$$n_e(R_*, R) \approx n_e^0 f_e(R_*, 0). \quad (53)$$

Such a result is explained by the fact that the condition $R_*/R \approx 1$ is valid when the coordinate of the particle is close to Δ; that is, $R_*/\Delta \approx 1$. The associated time for these particles is $t(R_*, R) \approx 0$ (see (50)). Actually, the above approximations apply to particles at the electron flow front that has coordinate $R_* = \Delta$ and starts to move within the interval $R_c - \Delta$. Therefore, $n_e(R_*, R)$ is the initial distribution. If $R_*/R \ll 1$, $t(R_*, R)$ is given by formula (51). Substituting (47) and (51) into (41) yields

$$n_e(R_*, R) = n_e^0\frac{R_*^3}{R^3}\frac{2}{3}\left[\frac{3C(R_*)}{\omega_0^2 R_*^3} + \frac{\Delta^3}{R_*^3} - 1\right]. \quad (54)$$

Now we pass to the electron dynamics in the double plasma layer for a given initial electron distribution. By way of example, we put $f_e(R_*, 0) = \mu$ in formulas (42)–(45), (47), (48), (50), (51), (53), and (54).

For $R < \Delta$, the solutions to set (4)–(6), in view of (42)–(45), have the form

$$E(R_*, R) = \mu\frac{m_e}{e}\frac{\omega_0^2}{3}\frac{R_*^3}{R^2}, \quad (55)$$

$$V_e(R_*, R) = \omega_0 R_*\sqrt{\frac{2}{3}\mu\left(1 - \frac{R_*}{R}\right)}, \quad (56)$$

$$t(R_*, R) = \frac{1}{\omega_0}\sqrt{\frac{3}{2\mu}}\left(\frac{R}{R_*}\sqrt{1 - \frac{R_*}{R}} - \operatorname{Arctanh}\sqrt{1 - \frac{R_*}{R}}\right), \quad (57)$$

$$n_e(R_*, R) = \mu n_e^0 \frac{R_*^3}{R^3}. \quad (58)$$

Note that formulas (55)–(58) were also obtained in [10].

For $\Delta \le R \le R_c$, the solutions to set (2)–(4), in view of (47), (48), (50), (51), (53), and (54), can be represented as follows:

$$E(R_*, R) = \frac{m_e}{e}\frac{\omega_0^2}{3}\left[\left(1 + \mu\frac{R_*^3}{\Delta^3}\right)\frac{\Delta^3}{R^2} - R\right], \quad (59)$$

$$V_e(R_*, R) = \omega_0 R_* \sqrt{\frac{2}{3}\left(\mu + \frac{\Delta^3}{R_*^2}\right)\left(1 - \frac{R_*}{R}\right) + \frac{1}{3}\left(1 - \frac{R^2}{R_*^2}\right)}, \quad (60)$$

$$t(R_*, R) \approx \frac{1}{\omega_0}\sqrt{\frac{6}{\mu}\left(\frac{R}{R_*} - 1\right)}, \quad R_*/R \approx 1, \quad (61)$$

$$n_e(R_*, R) \approx \mu n_e^0, \quad R_*/R \approx 1, \quad (62)$$

$$t(R_*/R) \approx \frac{\sqrt{3}}{\omega_0}\arcsin\left[\frac{\frac{R}{R_*}}{\sqrt{2\left(\mu + \frac{\Delta^3}{R_*^3}\right)}}\right], \quad R_*/R \ll 1, \quad (63)$$

$$n_e(R_*, R) \approx n_e^0 \frac{R_*^3}{R^3}\frac{2}{3}\left(\mu + \frac{\Delta^3}{R_*^3}\right), \quad R_*/R \ll 1. \quad (64)$$

(5) To conclude, let us discuss the conditions under which the simplifications adopted in this work are valid.

(i) The hydrodynamic approach as applied to a cold plasma implies that the thermal velocity is disregarded. This simplification is valid if the directional velocity of plasma electrons that is gained in the electric field far exceeds their thermal velocities; that is,

$$\left|\frac{V_e(R_*, t), V_e(R_*, R)}{V_{e,\,th}}\right| \gg 1, \quad (65)$$

where $V_{e,\,th}$ is the thermal velocity of plasma electrons.

Let $k = 0$. In this case, the validity condition for inequality (65) can be found from formulas (19) and (37) for $V_e(R_*, t)$ provided that the constants of integration in them are known. For example, substituting formula (37) into (64), we arrive at a condition (a relationship between parameters n_e^0, ν_e, and $V_{e,\,th}$ of the medium and geometrical factor Δ) under which this inequality works. From (65), we have

$$\frac{\omega_0^2}{\nu_e}\frac{\Delta}{V_{e,\,th}} \gg 1. \quad (66)$$

A similar estimate can be obtained for $k = 2$.

(ii) The statement of the problem ignores the ion motion; that is, it is assumed that the ions are of an indefinitely large weight ($m_i \longrightarrow \infty$). Such an assumption implies that the processes in the system are fast and is valid if

$$t \ll T_i \approx \frac{1}{\omega_{0i}}, \quad (67)$$

where $\omega_{0i}^2 = 4\pi e^2 n_i^0 / m_i$.

(iii) The solution method assumes that the volume element trajectories specified by the solutions do not cross each other. Otherwise, shock waves, discontinuities of the density of the medium, etc., may appear. The condition that the trajectories of electron volumes do not intersect is met if $\partial R/\partial R_* > 0$ or $n_e(R_*)/(\partial R/\partial R_*) > 0$. For $n_e(R_*) = n_e^0$, the condition $|(dV_e(R_*, 0)/d(R_*))/\omega_0| < 1$ is sufficient for the trajectories not to intersect. In other words, the distribution of initial velocity $V_e(R_*, 0)$ over R_* must be fairly uniform [10].

REFERENCES

1. A. A. Rukhadze, L. S. Bogdankevich, S. E. Rosinskiĭ, *et al.*, *Physics of High-Current Relativistic Electron Beams* (Atomizdat, Moscow, 1980) [in Russian].
2. B. Grandal, *Artificial Particle Beams in Space Plasma Studies* (Plenum, New York, 1982; Mir, Moscow, 1985).
3. S. Eliezer and H. Hora, Phys. Rep. **172**, 339 (1989).
4. L. P. Block, in *Physics of Hot Plasma in the Magnetosphere*, Ed. by B. Hultqvist and L. Stenflo (Plenum, New York, 1975), pp. 229–250.
5. I. Langmuir, Phys. Rev. **33**, 954 (1929).
6. I. B. Bernstein, J. M. Green, and M. D. Kruskal, Phys. Rev. **108**, 546 (1957).
7. V. L. Ginzburg and A. A. Rukhadze, *Waves in Magnetoactive Plasma* (Nauka, Moscow, 1975); Handbuch der Physik **49**, 395 (1972).
8. L. I. Sedov, *A Course in Continuum Mechanics* (Wolters-Noordhoff, Groningen, 1972; Nauka, Moscow, 1983), Vol. 1.
9. K. P. Stanyukovich, *Unsteady Motions of Continuous Media* (Nauka, Moscow, 1971) [in Russian].
10. V. A. Fedorov, Radiotekh. Élektron. (Moscow) **47**, 103 (2002).
11. E. von Kamke, *Differentialgleichungen. Losungsmethoden und Losungen* (Akademie, Leipzig, 1951; Nauka, Moscow, 1976).
12. I. S. Gradshtein and I. M. Ryzhik, *Table of Integrals, Series, and Products* (Nauka, Moscow, 1971; Academic, New York, 1980).

Translated by V. Isaakyan

Technical Physics, Vol. 50, No. 12, 2005, pp. 1551–1560. Translated from Zhurnal Tekhnicheskoĭ Fiziki, Vol. 75, No. 12, 2005, pp. 16–25.

GASES AND LIQUIDS

Efficiency of Arc Production of Fullerenes Versus Discharge Chamber Geometry. I: The Axisymmetric Case

N. I. Alekseyev and G. A. Dyuzhev

Ioffe Physicotechnical Institute, Russian Academy of Sciences, Politekhnicheskaya ul. 26, St. Petersburg, 194021 Russia

e-mail: aleks@mail.ioffe.ru

Received February 2, 2005

Abstract—The gas dynamics in a discharge chamber for arc production of fullerenes in the inert gas atmosphere is analyzed for the first time. A turbulent fanlike jet due to the carbon flow from the discharge gap is shown to be a crucial factor in the gasdynamic pattern formation. The dependence of the fraction of fullerenes extracted from the chamber on the total amount of the product is constructed, with the gas flow rate, as well as the radius and length of the chamber, being adjustable parameters. Tangential twisting of the gas, a way of improving the fullerene extraction efficiency, is considered. *© 2005 Pleiades Publishing, Inc.*

INTRODUCTION

The complex process of fullerene formation in an arc [1–3] and the relation of the product extraction efficiency to the discharge chamber geometry account for the fact that a consistent theoretical model that makes it possible to optimize the arc is still lacking. However, the potential of the arc method of fullerene production is far from being exhausted and it is believed that a major part of this material will be produced worldwide precisely with this method. Considerable evidence for the beneficial role of the plasma at different stages of fullerene molecule assembly counts in favor of this statement [4–6].

In this work, which elaborates upon study [7], we construct a simple model that allows one to calculate the gas flow pattern in a cylindrical discharge chamber the axis of which coincides with the axis of the electrodes. Such a geometry is common to most arc-discharge chambers for fullerene production. Based on this calculation, one can estimate the flow distribution in a chamber of any geometry with given dimensions. Emphasis is on the gas flow along the electrodes, in which case fullerene soot can be accumulated in a special collector rather than being scraped out of the chamber walls [8].

Initial information on the gasdynamic pattern in the chamber that was extracted from analysis of fullerene production in an infinite chamber without the gas flow [7] can be summarized as follows.

(1) Near the source, the concentration of carbon (in the form of the atomic gas and ions) is high; that is, the plasma is heavily ionized. The carbon pressure forces most of a buffer gas (helium) out of the discharge zone.

(2) A gas-plasma jet forms near the source. Its initial velocity can be estimated as

$$\mathbf{V}_0 = \frac{DP}{P - n_C T}\left(\frac{\nabla n_C}{n_C} + \frac{\nabla T}{T}\right), \qquad (1)$$

where T and n_C are the temperature and concentration of carbon atoms in the arc [7].

Calculated by (1), the flow (jet) velocity agrees well with experimental data [9]. It sharply grows with current (hence, carbon concentration). Under optimal production conditions, it equals 20–60 m/s depending on the arc-discharge mode.

(3) The jet is inclined, rather than perpendicular, to the arc axis (z axis) at angle $\theta_0 = 60°$–$70°$ if the electrode axis is taken to be directed from the anode to cathode (Fig. 1). A jet making an angle with the arc axis is generated by a conical nozzle [10], while a fanlike (or radial-slot) jet is incident on the arc axis almost normally, $\theta_0 \approx 90°$.

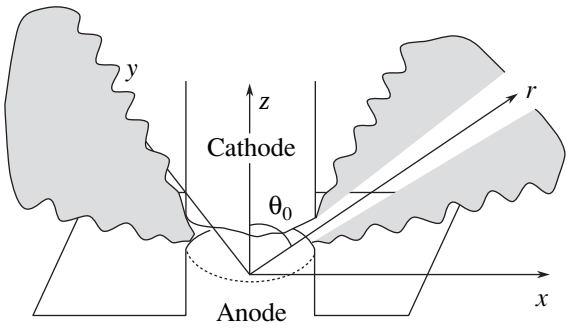

Fig. 1. Discharge gap geometry.

1063-7842/05/5012-1551$26.00 © 2005 Pleiades Publishing, Inc.

(4) The jet is turbulent: the Reynolds number calculated with regard to the characteristic size of the discharge gap far exceeds unity.

(5) The jet is binary. Initially, it has largely one component (carbon); as the buffer gas is pumped to the jet, it becomes a helium jet with a small carbon additive. However, the results obtained for an incompressible fluid are applicable just in the case at hand (a jet of a heavy gas strikes a light gas when the temperatures of the source of the jet and of its environment differ by almost one order of magnitude), since the jet density changes insignificantly [7].

Therefore, with an accuracy sufficient for our purposes, we can apply the results following from the theory of a free turbulent jet of incompressible liquid [11, 12] and represent jet half-width δ, longitudinal (radial) velocity u_m of the jet at its axis, transverse velocity V_m of the gas incoming to the jet at the boundary $\delta(x)$, and flow rate G of the gas pumped into the jet versus distance x from the jet axis in the form

$$\delta = 2.4ax, \tag{2}$$

$$u_m = n/ax, \tag{3}$$

$$V_m = n/x, \tag{4}$$

$$G = 4\pi x 1.2\sqrt{ar_0b_0}. \tag{5}$$

Parameter $a \approx 0.1$ entering into (2)–(5) is the phenomenological parameter of the turbulence theory [11], $n = 1.2\sqrt{ar_0b_0}\,u_0$, $2r_0$ is the diameter of the graphite electrodes, and $2b_0$ is the electrode gap width. Formulas (2)–(5) refer to the main portion of the jet; however, neglect of the initial portion changes final results insignificantly. Importantly, formula (5) gives a fairly accurate result for the initial portion as well.

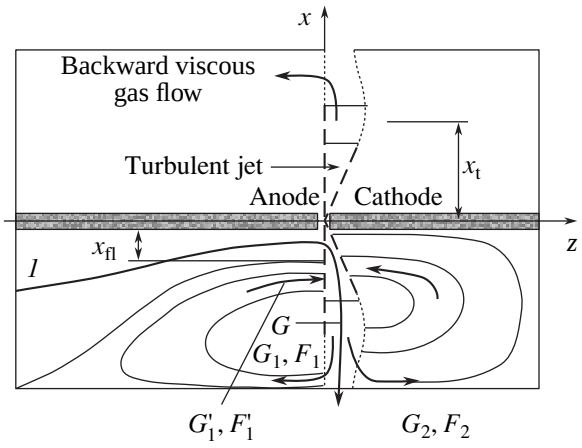

Fig. 2. 2D gas flow pattern in a cylindrical chamber for the case when the jet decays at the wall. The gas is delivered through the entire cross section of the anodic flange and leaves the chamber through the slotted ring. The dashed line shows the boundary of the turbulent jet; the dotted line, its virtual extension to the outlet.

(6) Fullerenes form at distance $x_1 = 3$–4 cm from the discharge axis [13]. This distance is at least several times shorter than typical dimensions of the chamber used in the experiments [1–3, 8]. Therefore, one can consider the chamber geometry as not influencing primary fullerene production. Subsequently, the amount of primary fullerenes reduces because of the UV radiation from the arc [14], association of fullerenes and fullerene-like clusters [9, 15], and other effects related to the gas dynamics in the chamber.

The assumption that the chamber geometry does not influence the jet parameters (at least within the fullerene formation zone) is substantiated by relevant experiments [11].

Thus, the production of fullerenes in large amounts and their extraction from the chamber are essentially different processes, which should be considered separately. The former is controlled by the current, gas pressure, and electrode sizes; the latter, by the buffer gas dynamics in a specific chamber and impurity (fullerene) flow in the buffer gas.

The results related to the first problem are presented at length in [7]. Important additional information concerning the effect of a plasma on fullerene assembling can be found elsewhere [4–6].

COMPUTATIONAL MODEL

Gas flow pattern in the chamber. A feature of a gas jet is that it diverges (its cross-sectional area increases) with distance from the source and the jet sucks the gas from the environment (which is the chamber volume in our case).

The initial gas flow pattern can easily be inferred from the following considerations and estimates. For initial (at $x = r_0$) jet velocity $V_0 = 40$ m/s and typical parameters of the electrode gap, the flow rate of the gas sucked by the jet from the chamber is roughly $G = 130$ ^{3}/h for the chamber radius $R = 10$ cm. Below, it is assumed, according to the experimental findings [8], that gas flow rate G_g at the inlet and outlet of the chamber (pumping-through) is at least three to four times lower than this value. This means that the direct gas flow is responsible for only a part of the cross-sectional area of the jet (the domain $x < x_{fl}$ in Fig. 2). Over the rest of the cross-sectional area of the chamber, the jet sucks the gas from the backward flow along the chamber walls.

A general scheme of solution will first be based on the 2D geometry, which corresponds to the radially symmetric gas flow pattern in the chamber. Such a pattern is observed when the gas enters and leaves the chamber either along the electrodes or through radially running slots in the walls (such a gas outlet is shown by thick line *1* in Fig. 2). According to the experimental conditions, its was assumed that the gas flows from the anode to the cathode. Accordingly, the entrance flange and the half of the chamber upstream of the flow will be

called "anodic" (the left half in Fig. 2); that adjacent to the cathode (the right half) will be called "cathodic." These terms will also apply to those jet parts adjacent to the anodic and cathodic parts of the chamber.

The variations of the radial velocity along the jet axis and of the transverse velocity at the jet boundary (as well as along an extension of this boundary to the wall if the turbulence of the jet fades out; the dotted line in Fig. 2) are qualitatively shown in Fig. 3. On the side walls of the chamber, the radial velocity of the jet depends on the gas pump velocity if the jet is directed to the inlet (curve *1*) or vanishes (if pumping-through is absent or the gas leaves the chamber, for example, along the axis of the cathodic flange (curve *1*')). The velocity transverse to the jet boundary (or to the extension of this boundary) is bound to change sign when approaching the wall (curve *2*). Such a situation, namely, a turbulent reflection-free jet outgoing from the chamber and the reflection of the turbulent jet from the walls or from the edge of the outlet (or fadeout of turbulence before the jet reaches the wall), occurs under any flow conditions near the hole.

In the case of turbulent reflection (Fig. 4), the jet propagating near the walls is bound to decay at a distance from the point of reflection. The position of the stagnation zone (point *D* in Fig. 4) depends on the chamber length and gas balance condition: the total amount of the gas absorbed by the jet (minus the gas pumped through the chamber) must be restored to the chamber, the flow velocity in the restore region having to meet the viscous flow condition (Re < 1). This condition specifies a minimal length (more exactly, half-length) L of the chamber in the direction of jet reflection from the wall. When the gas is not pumped, the inequality

$$\frac{L}{R-\delta} > \frac{n}{(\eta/\rho)\gamma}, \tag{6}$$

must be fulfilled, where η and ρ are, respectively, the dynamic viscosity and density of the gas.

At a working pressure of 300 Torr in the chamber and temperature 1000 K, (inequality (6)) is fulfilled if the chamber is unrealistically long, $L \geq 5R$. With pumping taken into account, condition (6) changes insignificantly and so actually is not fulfilled. Therefore, two situations should be considered: (i) the jet ceases to be turbulent before reaching the walls and gas absorption by the jet changes to gas escape from the jet along the walls (Fig. 2) and (ii) when escaping from the chamber, the gas is turbulent, the qualitative picture of turbulent zones near the outlet having to be the same as in the case of the "internal" jet flow from an annular source of radius R and width h up to velocity sense (Fig. 5).

In case (i), radius x_t of turbulence fadeout determined from the same considerations as for turbulent

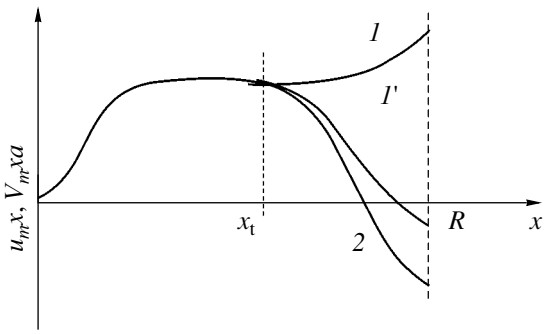

Fig. 3. Variation of the radial velocity of the jet along its axis and of the transverse velocity of the jet at its boundary.

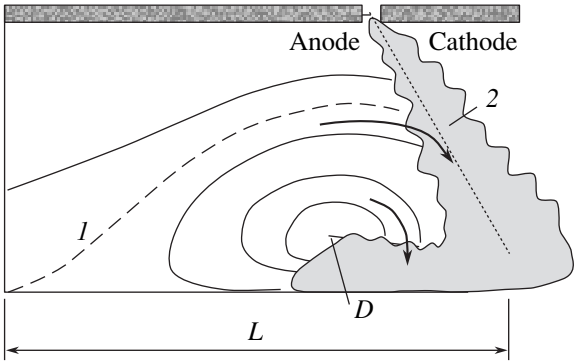

Fig. 4. Turbulent reflection of the jet from the walls (radially symmetric case): (*1*) the boundary of the flow part of the chamber (the wavy line is the boundary of the jet) and (*2*) the jet axis.

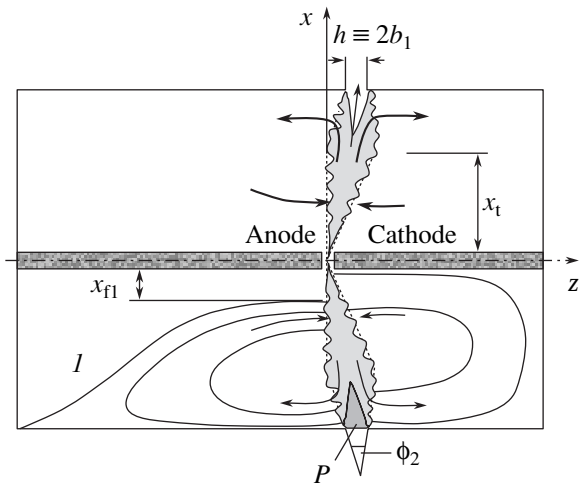

Fig. 5. Turbulent jet structure between the gap and ring outlet for turbulent outflow from the chamber. The boundaries of the jet are shown by the wavy lines. *P* is the potential core of the outgoing jet.

reflection can be easily found from the estimator

$$x_t = \left(\frac{\eta}{\rho} + \frac{G_g}{2\pi R}\right)\left(n + \frac{\eta}{\rho}\right)^{-1} \tag{7}$$

provided that the condition for viscous jet flow from the outlet,

$$\frac{\rho R}{\eta}\frac{G_g}{2\pi Rh} < 1 \quad (8)$$

is simultaneously fulfilled.

In (7), as in (6), the gas velocity along the wall, which specifies the backward flow rate into the chamber, is assumed to equal η/ρ, which corresponds to the condition Re = 1.

Conditions (7) and (8) are fulfilled for only a low pump rate and a very short jet,

$$\frac{x_t}{R} \le \frac{\eta}{\rho}\left(\frac{h}{R}+1\right)\left(n+\frac{\eta}{\rho}\right)^{-1}, \quad (9)$$

the length of which exceeds its potential core only slightly. Therefore, case (ii) (Fig. 5) seems to be more realistic. Thus, the gas flow from the discharge gap to the outlet combines two turbulent jets passing into each other. For brevity, the jet portion between the discharge gap and point x_t will hereafter be called the gap jet and that between point x_t and the outlet, the outlet jet. Point x_t in Fig. 5 has the same meaning as in Fig. 2: the point where the transverse velocity at the jet boundary changes sign.

For the outlet jet, the dependences of parameters u_m, V_m, G, and δ on distance $R - x$ to the wall are well known from the theory of plane turbulent jet. They are similar to relationships (2)–(5) for the gap jet and are given in Appendix 1. The gas balance in the jet results in the following equation for point x_t, where the transverse velocity changes sign (see Appendix 2):

$$x_t^2 + x_t x_{fl}\left(0.36\frac{x_{fl}a}{b_1} - 1\right) = 0.36\left(\frac{x_{fl}}{R}\right)^2\frac{aR}{b_1} - \frac{1}{4}\left(\frac{x_{fl}}{R}\right)^2. \quad (10)$$

An essential point in deriving (10) is that the values of x_t for the anodic (open) and cathodic ("plugged") parts of the chamber are different. Since a jet where regions symmetric about its axis act in such a way that one absorbs the gas and the other forces the gas out of the jet can hardly be conceived, x_t was assumed to be equal to the half-sum of the values calculated for the cathodic and anodic halves of the jet.

Clearly, the above speculations are true only for $x_{fl} < x_t$. In this case, the flow pattern in that part of the jet adjacent to the anodic half of the chamber is identical to the flow pattern in the cathodic half (there exists the backward flow along the walls). It is natural to think that high-rate pumping, $x_{fl} \longrightarrow x_t$, will cause arc breaking.

Analysis of the flow pattern in the entire volume of the chamber is complicated by the presence of areas with turbulent and viscous flows and by the finite dimensions of the chamber. In addition, initial escape angle θ_0 of the jet relative to the chamber axis may generally depend on the position of the ring slot through which the jet leaves the chamber.

Significantly, a full solution (i.e., a solution to a set of equations for the entire volume of the chamber with regard to boundary conditions at the inlet and outlet of the chamber and at its walls) is not only difficult to obtain but also is not necessarily true. The fact is that averaged turbulence equations involve many time correlation functions, which may vary with the geometry of the chamber.

Therefore, we used the available analytical solutions for a free turbulent jet in the boundary layer approximation [11, 12]. At the natural boundaries of the jet, these solutions were joint with viscous solutions for the rest of the chamber.

The position of the slot for gas axial withdrawal was taken to be such that the natural axis of the jet (the axis in the absence of pumping) was directed to the slot. Based on experimental data, we also assumed for convenience that the boundary between the jet and the anodic part of the chamber (on the left in Figs. 2 and 5) makes a right angle with the chamber axis.

The gas flow outside the jet and its extension to the wall was assumed to be viscous. Then, a set of 2D Navier–Stokes continuity equations reduces to a fourth-order equation for stream function Ψ specified by the conditions

$$V_y \equiv V = (1/x)(\partial\Psi/\partial x), \quad V_x \equiv u = -(1/x)(\partial\Psi/\partial z), \quad (11)$$

and has the form of the curl transfer equation,

$$(V\nabla)\cdot \mathrm{curl}\mathbf{V} - (\mathrm{curl}\mathbf{V}\cdot\nabla)V = \nu\Delta\mathrm{curl}\mathbf{V}, \quad (12)$$

where $\nu = \eta/\rho$ is the kinematic viscosity of the gas and Δ is the Laplacian.

In the absence of gas twisting and jet viscous attenuation, the simple potential approximation [10]

$$\Delta\Psi = 0 \quad (13)$$

provides a reasonable accuracy.

At the walls, stream function Ψ can be set equal to zero; at the inlet, it is defined by the boundary conditions at the inlet. If the gas enters the chamber uniformly over the cross section of the entrance flange, function $\Psi(x)$ at the inlet depends only on pump rate G_g. At the boundaries of the turbulent jet with the cathodic and anodic parts of the chamber, the stream function outside the neighborhood of point x_t (Fig. 5) is easy to calculate from the first condition in (11) by formulas (4) and (23) (see Appendix 1); in the neighborhood of point x_t, it is found by linearly joining (4) and (23) and integrating over coordinate x.

For the cylindrical chamber, a desired solution is constructed by analytically expanding into the Fourier–Bessel series. Analysis of the anodic part of the cham-

ber is a trivial task in this case, since the boundaries of this part have a simple cylindrical form (Fig. 5). For the cathodic part, the situation is more complicated, since this boundary makes an angle of $2 \times 2.4a \approx \pi/6$ with the jet (such is the angle of divergence of a fanlike jet from the discharge gap calculated by formula (2) and supported experimentally [11, 12]). For the outward jet, the angle of divergence (angle φ_2 in Fig. 5) is related to the angle of divergence of another, plane, jet [11, 12]. However, in our case, angle φ_2 is uncertain: the point where the gap jet passes into the outlet jet may lie just at the beginning of the outlet jet. Therefore, the boundary conditions were set on the axial plane of symmetry for simplicity (the x axis in Fig. 5) and were taken such that derivative $d\varphi/dl$ of the potential along the real boundary that is obtained from the solution coincides with the true derivative at least at the beginning of the gap jet (at point x_t near the outlet of the chamber).

Fullerene extraction from the discharge chamber. The efficiency of fullerene production by the arc method in a flow-type chamber is most natural to estimate by fullerene percentage α' in the soot flux leaving the chamber and by relative fullerene yield Γ. The latter parameter can be defined as the ratio of the fullerene flux from the chamber, F, to the amount of arising fullerenes, F_0 (Fig. 2),

$$\Gamma \equiv \frac{F}{F_0} = \frac{F_0 - F_1 + F' - F_2 + F_2'}{F_0}. \qquad (14)$$

Fullerene fluxes F_1 and F_2 coming from the jet along the wall to the anodic and cathodic parts of the chamber, as well as fluxes F_1' and F_2' returning to the jet from the chamber (Fig. 2), must be found from a solution to the problem of heavy impurity (fullerene) diffusion in a gas flow. This solution must also include fullerene losses due to UV irradiation and deposition on the walls. Obviously, such a problem can be posed only in a greatly simplified form. This is because fullerenes near the cold walls of the chamber associate into clusters, the kinetic properties of which differ radically from those of fullerenes, and systematic data for fullerene decomposition under UV radiation are virtually lacking.

When solving the problem of impurity (fullerene) diffusion in a known gas velocity field,

$$\mathrm{Div}(n_C \mathbf{V}(x, y) - D\nabla n_C) = -n_C/\tau \qquad (15)$$

we used the diffusion coefficient for soot clusters of characteristic mean size $\langle r_s \rangle = 3 \times 10^{-3}$ cm [15]. The boundary conditions to problem (15) and characteristic time τ of fullerene irradiation by UV light are considered in Appendix 3.

Percentage α' is obtained in a natural way during the solution of problem (15), which considers fullerenes incorporated into soot particles, and a problem similar to (15) that describes fullerene-free soot particles (the right of (15) is zero in the latter case).

ANALYSIS OF TWO-DIMENSIONAL GAS FLOW AND FULLERENE YIELD

To compare the results of calculation with the performance of the real 3D chamber where the gas goes out through a circular hole of radius $R_{out} \approx 2.5$ cm on the side wall [8], width $2b_1$ of the ring slotted outlet was taken to be 0.5 cm starting from the equivalence condition for surface areas: $2b_1 \times 2\pi R = \pi R_{out}^2$.

As a parameter controlling the relative fullerene yield, we took gas flow rate G_g (Fig. 6). It is seen that yield Γ grows with increasing flow rate. On the right, the curves terminate at $x_{fl} \longrightarrow x_t$. Thus, for a chamber of the given geometry, a maximal flow rate at which the arc still persists is optimal for the fullerene yield.

For the given radius of the chamber, the G_g dependence of fullerene percentage α' is very weak, in full accordance with the experiment.

For a given G_g, Γ is virtually independent of the dimensions of the chamber (Fig. 7). The left extremity of curve *3* in Fig. 7 corresponds to $x_{fl} \longrightarrow x_t$. When the chamber dimensions are scaled up, Γ increases with G_g (Fig. 8).

Qualitatively, the results of calculation can be interpreted as follows. The value of Γ can be found not only by solving the diffusion equation but also from the approximate relationship

$$\Gamma = \left(\frac{1}{\varepsilon_1}\left(\frac{1}{1-g} + \frac{G_2}{G_1}\right) - 1 - \frac{\varepsilon_2}{\varepsilon_1}\frac{G_2}{G_1}\right) \times \left(\frac{1}{\varepsilon_1}\left(\frac{1}{1-g} + \frac{G_2}{G_1}\right) - P_1 - P_2\frac{\varepsilon_2}{\varepsilon_1}\frac{G_2}{G_1}\right)^{-1}, \qquad (16)$$

where $P_1 = F_1'/F_1$ and $P_2 = F_2'/F_2$ are the integral "survival" probabilities of the fullerenes when they are once passed through the areas of closed gas flow in the

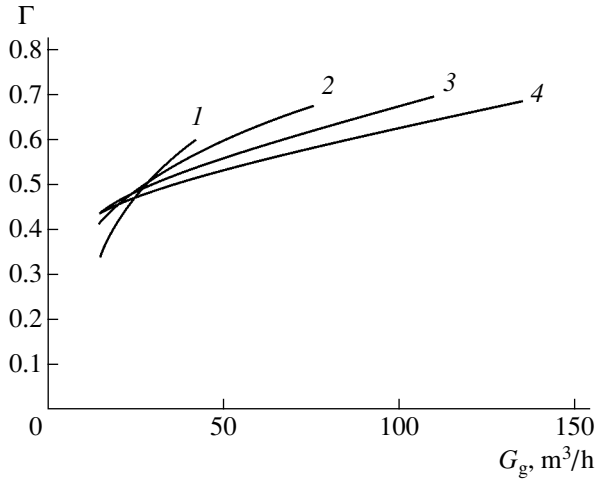

Fig. 6. Relative fullerene yield vs. flow rate G_g. The radius of the chamber is (*1*) 10, (*2*) 15, (*3*) 20, and (*4*) 25 cm.

anodic and cathodic parts of the chamber, respectively; G_1/G_2 is the ratio of the gas flows reflected into the anodic and cathodic parts of the chamber (Fig. 2);

$$g \equiv \frac{G_g}{G_1 + G_g}$$

is the contribution of the flowing gas to the anodic part of the jet; and quantities

$$\varepsilon_1 = \frac{F_1/F}{G_1/G}, \quad \varepsilon_2 = \frac{F_2/F}{G_2/G}$$

characterize the behavior of the fullerene impurity in the gas flow near the walls at the time instant this flow ($G = G_1 + G_g$) splits into the backward flow along the walls and the outward flow.

Relationship (16) follows from the balance conditions for the gas and fullerenes and from the definitions of parameters ε_1, ε_2, and g. In the absence of the cathodic half of the chamber and under the assumption $\varepsilon = 1$, this relationship takes the very simple form

$$\Gamma = \frac{g}{1 - P(1-g)},$$

which is the sum of an infinite geometrical progression each term of which is the survival probability of the fullerenes passed once more through the closed viscous gas flow.

For the geometry used in this work (the chamber with the plugged cathodic part) and under the assumption $\varepsilon_1 = \varepsilon_2 = 1$, it follows from (16) that

$$\Gamma = g\left(1 - P_1(1-g) + \frac{G_2}{G_1}(1-P_2)(1-g)\right)^{-1}. \quad (17)$$

If the jet leaves the gap at a right angle, it is natural to assume that $G_1 + G_g \approx G_2$ and (17) simplifies even more,

$$\Gamma = g(2 - P_2 - P_1(1-g))^{-1}, \quad (18)$$

where $g \approx x_{fl}/x_t$ and x_t is found from (10).

Probabilities P_1 and P_2 can be estimated from the time of irradiation and the rate of fullerene and soot particle deposition on the walls,

$$P = 1 - (L/\tau V)\chi(1 - L/\tau V) - (L/\tau_{diff} V)\chi(1 - L/\tau_{diff} V),$$

where τ_{dif} is the characteristic time of particle diffusion across streamlines of the gas and $\chi(q) = 1$ (for $q > 0$) or 0 (for $q < 0$).

Even (17) and (18) allow one to qualitatively "see" the results obtained above. From (10), it follows that, for the chamber considered, the dependence $g(G_g)$ obeys a near-square-root law when the flow rate is high. However, as G_g increases, the closed-flow area in the anodic part of the chamber shrinks and, consequently, the irradiation dose of the fullerenes declines; therefore, probability P_1 of fullerene survival in (18) grows and the dependence $\Gamma(G_g)$ in Fig. 6 is a supra-square-root function.

If the dimensions of the chamber grow with the flow rate remaining constant (Fig. 7), the fullerene irradiation zone moves away from the arc. However, this effect is compensated for by an expansion of the closed-flow area and an increase in the amount of fullerenes drawn in this area. To raise the fullerene yield, it is necessary to raise the flow rate.

Figure 9 shows the maximal fullerene yield (i.e., the yield at a flow rate above which the arc breaks) versus chamber radius R. In a chamber with $R = 30$ cm, the yield basically may exceed the yield at $R = 10$ cm by 20–30%; to this end, however, the flow rate should be raised fourfold(!). Clearly, the fabrication of a gas blower with such a high capacity, to say nothing of the fabrication of such a large chamber, greatly increases the cost of the installation.

From the engineering standpoint, a small-radius chamber with a near-threshold flow rate seems to be optimal.

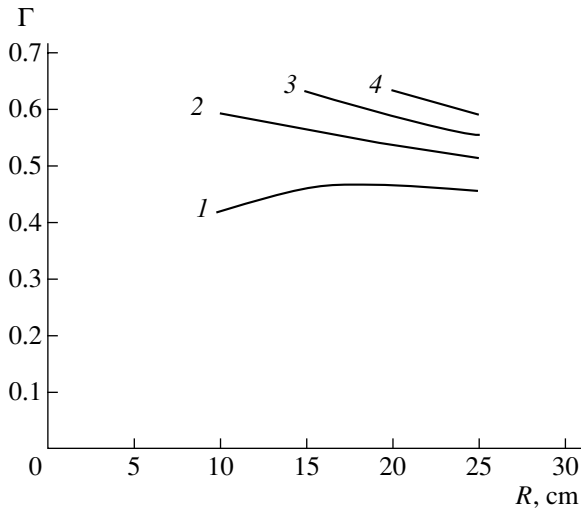

Fig. 7. Relative fullerene yield vs. the chamber radius at flow rate G_g of (*1*) 20, (*2*) 40, (*3*) 60, and (*4*) 80 m^3/h.

WAYS OF IMPROVING THE FULLERENE YIELD IN THE CONTEXT OF TWO-DIMENSIONAL PROBLEM DEFINITION

The 2D definition of the problem is the simplest; therefore, quantitative analysis of other 2D versions that could increase the fullerene yield, first of all a chamber with tangential gas inlet and outlet, is of interest. The situation can be provided in such a chamber when a heavy component (fullerenes) is not only entrained by the main gas flow but is also continuously extracted from the chamber by centrifugal separation of the components.

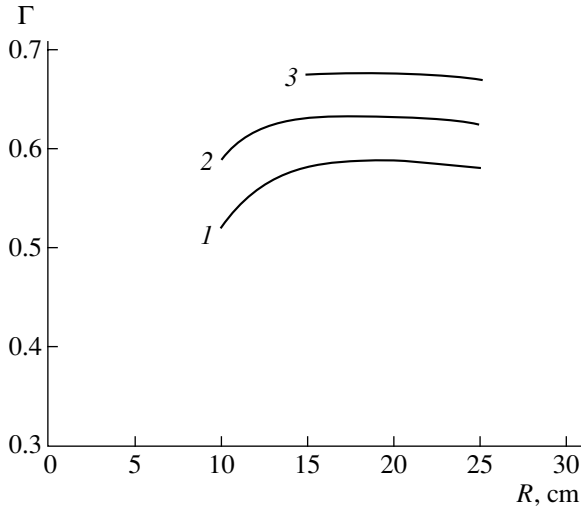

Fig. 8. Relative fullerene yield vs. the chamber radius for ratio G_g (m^3/h)/R (cm) = (*1*) 3, (*2*) 4, and (*3*) 5.

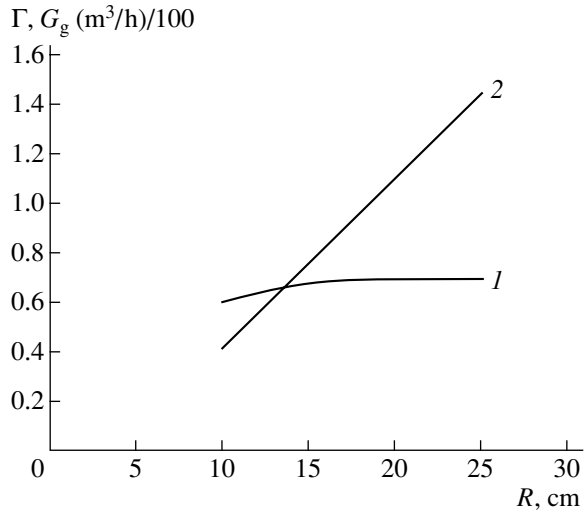

Fig. 9. (*1*) Maximal fullerene yield achievable at a given radius of the chamber and (*2*) its associated flow rate.

Even before performing related calculations, it is evident that the gas streamline patterns are the same for twisted and untwisted gas flows (Figs. 2 and 5). However, a turbulent fanlike jet turns into a twisted fanlike jet. Twisting is accomplished twofold: by tangential outlet of the gas from the chamber (and, correspondingly, by turbulent transfer of vortices upstream) or by viscous transfer of vortices from the entrance cross section of the chamber through its flow-through part. Obviously, the first effect is much stronger. If it is assumed, for definiteness, that the gas leaves the chamber through a set of outlets with sizes h and $l \ll R$ (Fig. 10), the angular momentum persisting upstream [10],

$$M \approx \rho \frac{G_g^2 R}{\pi h \sqrt{2lR}}, \qquad (19)$$

grows in proportion to the flow rate squared.

The centrifugal mechanism may act in either of the two following ways. (i) It may displace the boundary between the stream and closed-flow areas toward the wall. In this case, the closed-flow area will shrink and the capture of arising fullerenes into the chamber will decrease. (ii) This mechanism may stimulate the escape of the fullerenes from the outlet of the chamber by turning part of the gas flowing along the walls.

The amount of the former effect can be estimated from an equation for the gas flow across the jet using a cylindrical coordinate system appropriate for a fanlike jet [10],

$$u\frac{\partial w}{\partial x} + V\frac{\partial w}{\partial z} + \frac{uw}{x} = -\frac{\partial P}{\partial z} + \nu\frac{\partial^2 V}{\partial z^2} \qquad (20)$$

(in the turbulent case, shear viscosity ν changes to turbulent viscosity ν_t determined by one or another empirical method). In the boundary layer approximation, it follows from (20) that P = const.

Thus, unlike the similar equation for an axisymmetric jet,

$$-w^2/y = -\partial P/\partial y + \nu(\partial^2 V/\partial y^2) \qquad (21)$$

in the spherical coordinate system [11], (the y coordinate is shown in Fig. 1), velocity V in (20) is insensitive to rotation. Accordingly, the pressure at the center of the jet does not drop (more exactly, it turns out to be a small quantity of lower order than in the axisymmetric case). Neither does the relatively slowly decreasing correction (on the order of $1/x^2$) to the transverse velocity arise. As for the correction on the order of $1/x^3$, it is localized at the center of the jet and its effect at the boundary is not perceived (see Appendix 4). Thus, at the boundary, rotation does not affect the gas velocity across the jet.

The amount of the latter effect, centrifugal separation of a heavy component near the escape zone, can be estimated from an equation of impurity diffusion relative to the gas flow, $D\Delta n_C = \mathrm{Div}(n_C\mathbf{V})$ (Eq. 15 with the zero right-hand side).

If the angular dependence is absent, the form of this equation is the same for the twisted and untwisted cases, since the angular velocity is not involved. Hence, the transfer of a heavy component in the jet is also insensitive to twisting.

Thus, tangential twisting of the gas flow offers no advantages from the standpoint of fullerene production. Another possible modification of the chamber configuration, double-sided gas delivery to the chamber (through both the anodic and cathodic sides), as well as the 3D geometry of the chamber, will be considered in part II of this work. The need for considering the 3D geometry is related to the fact that gas outlet through a

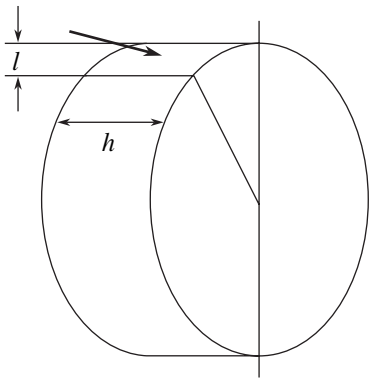

Fig. 10. Gas outflow from a set of outlets with sizes h and $l \ll R$.

hole in the side wall is the simplest way of gas outlet in engineering terms. However, it can be shown based on the above results that the fullerene yield may decrease in this case. The only question is how much this decrease is.

CONCLUSIONS

(1) A turbulent fanlike jet arising when the carbon flow leaves the discharge gap plays a key role in the gasdynamic pattern in the chamber.

(2) At a moderate rate of gas pumping from the anode to the cathode, a characteristic flow pattern with the backward flow along the walls forms in the anodic (flow) part of the chamber.

(3) In a wide range of flow rates, relative fullerene yield Γ grows with flow rate G_g. However, at a certain (threshold) value of G_g (specific for a specific chamber), the arc breaks.

(4) The threshold value of the flow rate sharply increases with the chamber radius; however, the fullerene yield grows much more slowly in this case. Therefore, a small-radius chamber with near-threshold pumping seems optimal from the engineering standpoint.

(5) The transition to a chamber with symmetric tangential twisting of the gas at the inlet and outlet of the chamber raises the fullerene yield insignificantly. The gasdynamic pattern in the chamber does not change radically: the gas flow merely twists as a whole.

APPENDIX 1

Jet parameters versus distance to the chamber walls. The formulas for the axisymmetric effusion of a jet form a fanlike source are well known [10]. However, by virtue of the condition $h \ll R$ and also of the fact that the area under consideration does not exceed half the chamber radius (as follows from subsequent calculations), one can apply the known results for the main part of a plane jet with initial velocity V' and initial width $2b_1 = h$ [11, 12],

$$u_m = V'1.2\sqrt{b_1/ay}, \tag{22}$$

$$V_m = V'0.6a\sqrt{b_1/ay}, \tag{23}$$

where y is the distance to the source of the jet.

The flow rate per unit length of the slot is given by

$$G' = 2.4V'\sqrt{ab_1y}. \tag{24}$$

APPENDIX 2

Position of the point where the transverse velocity at the jet boundary changes sign. As applied to our problem, the gas flow entering the chamber from the jet forming at the outlet is given by

$$2.4V'\sqrt{ab_1(R-x_t)}2\pi R$$

for total length $2\pi R$ of the slot.

Then, the gas balance in the anodic part of the chamber (with regard to the stream part of the jet with radius x_{fl} and the closed-flow part (with width $R - x_t$) of the chamber near the wall) has the form

$$2\pi n(x_t - x_{fl}) = \frac{1}{2}2.4V'2\pi R\sqrt{ab_1(R-x_t)},$$

where V' is the gas velocity at the slotted ring outlet of the chamber and x_{fl} is found from the law of conservation of the gas flow in the chamber,

$$2\pi n x_{fl} = G_g = 2\pi R2b_1V'.$$

In this case, x_t calculated in the anodic (flow) part of the chamber must be found from the quadratic equation

$$x_t - x_{fl} = 0.6x_{fl}\sqrt{a(R-x_t)/b_1}.$$

It is easy to see that, for the cathodic part of the chamber,

$$x_t = 0.6x_{fl}\sqrt{a(R-x_t)/b_1}.$$

Taking the half-sum of these values, one readily arrives at (10).

Significantly, in the course of solution, we used formulas (5) and (24) for the rate of pumping into the jet, which can be applied in the initial portion of the jet. If we used relationships of type (2) for the geometrical shape of the jet, which are valid only for its main portion, the position of point x_t would be defined once and for all (i.e., at any flow rate) by the geometric relationship $2.4ax_t = 2.4a(R - x_t)$ and the relevant information would be lost.

APPENDIX 3

Boundary conditions for the impurity diffusion equation at the jet boundary and the rate of fullerene lost under irradiation.

(1) Clearly, the problem of fullerene diffusion from the area of their birth, $x \approx x_1$, should be posed for the entire chamber in the domain $x_1 < x < R$. However, the question arises of how to define the fullerene turbulent diffusion coefficient within the jet. Taking into account the linearity of the problem and the natural boundary condition at the wall, $n_C = 0$ ("black wall" condition), one may try to set $n_C(x)$ at the jet boundary in the model form

$$n_C = n_C(x_1)\frac{x_1}{x}\left(\frac{R-x}{R-x_1}\right)^{\Pi}, \quad \Pi > 1.$$

Fluxes F_1, F_2, F_1', and F_2' appearing in (14) are determined as derivatives $D\partial n/dx$ at the outer boundaries of the jet.

(2) The available results for fullerene losses due to UV radiation are contradictory. Experiments [3] on keeping the fullerene soot under daylight (illuminance up to 1 cd/cm^2) and in the dark did not show any significant effect of radiation, unlike those performed in [14]. In any case, the upper limit of undangerous illumination can be estimated as follows. It is known that the fullerene yield in a chamber with pumping is no higher than 10–12% under optimal conditions. If it is assumed that UV irradiation "kills" fullerenes, such a high percentage of the fullerenes lost at the walls is possible only if at least one monolayer of the fullerene soot deposits on the walls for characteristic time τ of irradiation. Then, we have

$$\tau = \frac{2\pi RH}{dm/dt}\rho_s\langle r_s\rangle,$$

where H is the characteristic thickness of the soot layer on the walls, dm/dt is the amount of the soot per unit time deposited within this layer, and ρ_s is the soot density.

The dependence of the fullerene lost time on the distance to the discharge gap is estimated from the condition of conservation of radiation flux within a cone specified by the gap geometry,

$$1/\tau = (r_{UV}^2/r^2)(1/\tau_{UV}),$$

where the ratio of reference values, r_{UV}^2/τ_{UV}, depends only on the arc discharge conditions.

APPENDIX 4

Twist-related correction to the transverse velocity of a fanlike jet. As follows from (20), the transverse pressure difference between the axis of the jet and its boundary does not depend on twisting and should be set equal to zero (as in the absence of twisting). Then, the equation of motion and the continuity equation are the same as those considered in [10],

$$u\frac{\partial u}{\partial x} + V\frac{\partial u}{\partial z} - \frac{w^2}{x} = \nu\frac{\partial^2 u}{\partial z^2}, \tag{25}$$

$$u\frac{\partial w}{\partial x} + V\frac{\partial w}{\partial z} + \frac{uw}{x} = \nu\frac{\partial^2 w}{\partial z^2}, \tag{26}$$

where velocities u and V are related to stream function Ψ by (11).

A solution is sought in the form [10]

$$\Psi = Ax + \frac{a_1}{x}\ldots, \quad w = \frac{b_2}{x^2} + \frac{b_4}{x^4}\ldots.$$

In the zeroth approximation, coefficient A obtained in [10] is

$$A = \alpha\tanh\frac{\alpha\Lambda}{2\nu},$$

where $\Lambda = y/x$, and

$$b_2 = C/\cosh^2\frac{\alpha\Lambda}{2\nu}.$$

The next approximation, which is easily found from (26), follows from the equation

$$a_1A'' - a_1''A - 4a_1'A' - b_2^2 = \nu a_1^{(3)}. \tag{27}$$

Since we are interested in only the velocity at the boundary, where $\alpha\Lambda/2\nu \gg 1$, correction a_1 can be sought in the form of the expansion

$$a_1 = p + m\exp\left(-\frac{\alpha\Lambda}{2\nu}\right) + n\exp\left(-\frac{\alpha\Lambda}{2\nu}\right), \tag{28}$$

which is similar to the asymptotics of A. Substituting (28) into (27) yields

$$a_1 = p\left(1 - \exp\left(-\frac{\alpha\Lambda}{2\nu}\right)\right) + \frac{4C^2\nu^2}{\alpha^3}\exp\left(-\frac{\alpha\Lambda}{\nu}\right). \tag{29}$$

The first term in expansion (29) is unrelated to twisting. The second one is proportional to the angular momentum of jet motion; however, it is localized at the axis of the jet and has no effect at its boundary.

REFERENCES

1. W. Kratschmar, L. D. Lalb, K. Fostiroupolos, and D. R. Huffman, Nature **347**, 354 (1990).
2. D. V. Afanas'ev, A. A. I. O. Blinov, and A. A. Bogdanov, Zh. Tekh. Fiz. **64** (10), 76 (1994) [Tech. Phys. **39**, 1017 (1994)].
3. D. V. Afanas'ev, A. A. Bogdanov, G. A. Dyuzhev, and A. A. Kruglikov, Zh. Tekh. Fiz. **67** (2), 125 (1997) [Tech. Phys. **42**, 234 (1997)].

4. G. Churilov, A. Fedorov, V. Taranko, *et al.*, Carbon **41**, 173 (2003).
5. G. Churilov, P. Novikov, V. Taranko, *et al.*, Carbon **40**, 891 (2002).
6. D. V. Afanas'ev, G. A. Dyuzhev, and V. I. Karataev, Pis'ma Zh. Tekh. Fiz. **25** (5), 35 (1999) [Tech. Phys. Lett. **25**, 182 (1999)].
7. N. I. Alekseyev and G. A. Dyuzhev, Zh. Tekh. Fiz. **75** (11), 32 (2005) [Tech. Phys. **50**, 1423 (2005)].
8. G. A. Dyuzhev, I. V. Basargin, B. M. Filippov, *et al.*, Int. Appl. Publ. PCT WO02/096800; PCT/RU02/00083.
9. N. I. Alekseyev, F. Chibante, and G. A. Dyuzhev, Zh. Tekh. Fiz. **71** (6), 122 (2001) [Tech. Phys. **46**, 761 (2001)].
10. L. G. Loitsyanskii, Trudy Leningr. Politekh. Inst., No. 5, 5 (1953).
11. G. N. Abramovich, *Theory of Turbulent Jets* (Nauka, Moscow, 1984) [in Russian].
12. A. S. Ginevskii, *Theory of Turbulent Jets and Wakes* (Mashinostroenie, Moscow, 1969) [in Russian].
13. G. A. Dyuzhev and V. I. Karataev, Fiz. Tverd. Tela (St. Petersburg) **36**, 2795 (1994) Phys. Solid State **36**, 1528 (1994)].
14. R. Tailor, J. P. Parsons, A. G. Avent, *et al.*, Nature **351**, 271 (1991).
15. O. P. Gorelik, G. A. Dyuzhev, D. V. Novikov, *et al.*, Zh. Tekh. Fiz. **70** (11), 118 (2000) [Tech. Phys. **45**, 1489 (2000)].

Translated by V. Isaakyan

Technical Physics, Vol. 50, No. 12, 2005, pp. 1561–1567. Translated from Zhurnal Tekhnicheskoĭ Fiziki, Vol. 75, No. 12, 2005, pp. 26–32.

GASES AND LIQUIDS

Efficiency of Arc Production of Fullerenes Versus Discharge Chamber Geometry. II: Double-Sided Gas Delivery and 3D Geometry

N. I. Alekseyev and G. A. Dyuzhev

Ioffe Physicotechnical Institute, Russian Academy of Sciences, Politekhnicheskaya ul. 26, St. Petersburg, 194021 Russia

e-mail: aleks@mail.ioffe.ru

Received February 2, 2005

Abstract—Based on the model suggested in part I of this work and analysis of a chamber for arc production of fullerenes, two ways of gas delivery to the chamber, one-sided pumping of the gas (from the side of the anode) and double-sided pumping (from both the cathodic and anodic flanges), are considered. In the latter case, the efficiency of fullerene extraction from the discharge chamber rises substantially. The axisymmetric 2D case considered earlier is extended for the 3D geometry of the chamber, where gas outlet is accomplished through the side wall of the chamber. © *2005 Pleiades Publishing, Inc.*

INTRODUCTION

This paper elaborates upon investigation [1, 2] into the process of fullerene production in an arc-discharge chamber pumped through by a buffer gas (helium). The analysis made in [2] and qualitative considerations show that, in an "asymmetric" flow-type chamber, where the gas is delivered through its anodic part and the cathodic part is "plugged" [2, Fig. 5], a closed gas flow arises, which entrains a large amount of fullerenes and eventually reduces the total fullerene yield. An increase in the gas flow rate makes the gas flow pattern in the chamber even more asymmetric; the jet breaks when the flow rate exceeds a critical (threshold) value; and the arc, which is intimately related to the jet, becomes unstable.

The simplest way of improving the fullerene yield in the cylindrical chamber is to deliver the gas through both (anodic and cathodic) flanges and to discharge it through an axisymmetric slot the position of which corresponds to the jet direction (Fig. 1). It will be shown that the influence of vortices can be considerably depressed in this case by appropriately selecting the flow rate.

It is clear, however, that the implementation of such a "truly" 2D geometry is difficult. It seems that analysis of fullerene production in an axisymmetric chamber with double-sided gas delivery and a subsequent extension of the results to the 3D problem, where gas outlet is accomplished through a circular hole in the wall, would be of great value for fullerene production optimization.

CALCULATION OF THE FULLERENE YIELD IN THE CASE OF DOUBLE-SIDED GAS DELIVERY

As in [2], our goal is to solve a set of equations for the gas flow in the chamber (Fig. 1). Following [2], the area of turbulence is separated out from the volume of the chamber and is subjected to approximate analysis using the results known from the theory of free turbulent jet [3, 4] with the aim of determining conditions at the boundaries between the jet and the anodic and cathodic parts of the chamber. However, the boundaries of the flow region with the anodic and cathodic parts of the chamber ($x_{fl}^{(a)}$ and $x_{fl}^{(c)}$, respectively, in Fig. 1) differ from those adopted in [2]. The positions of points

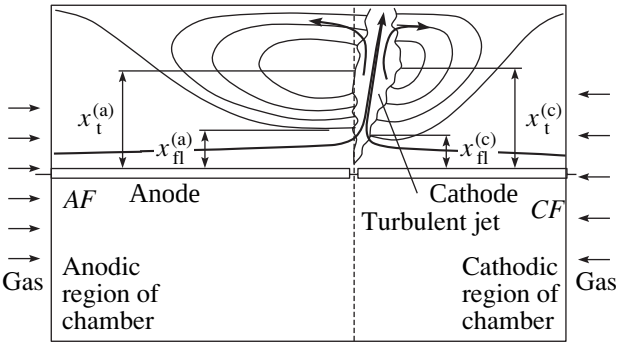

Fig. 1. Schematic of a discharge chamber with the symmetry axis along the electrodes and the streamline pattern for the case of double-sided gas delivery and gas outflow through a radial–annular slot. *AF* and *CF* are the anodic and cathodic flanges, respectively.

1063-7842/05/5012-1561$26.00 © 2005 Pleiades Publishing, Inc.

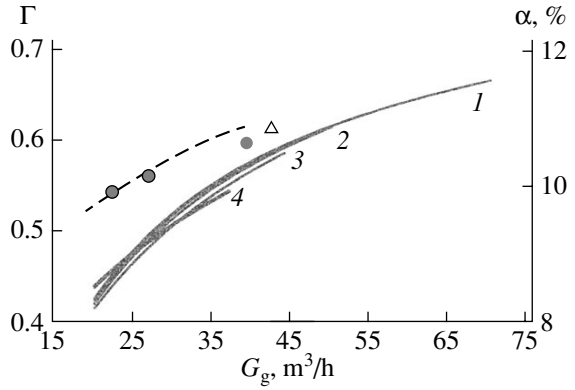

Fig. 2. Relative fullerene yield Γ (the left vertical axis) vs. gas flow rate G_g for chamber radius R = 10 cm. Gas delivery asymmetry parameter θ_a = (*1*) 0.5, (*2*) 0.6, (*3*) 0.7, and (*4*) 1.0 (one-sided delivery from the anodic side). The dashed line refers to the fullerene percentage in the soot (the right vertical axis) vs. G_g. Symbols (●) are data points.

$x_t^{(a)}$ and $x_t^{(c)}$, where the gap jet transforms into the outgoing jet [2] are also different in the general case (Fig. 1). When calculating the positions of $x_t^{(a)}$ and $x_t^{(c)}$, one may either find them independently or assume them to be the same and use some averaged value in subsequent calculations, as was done in [2] (for details, see below).

As in [2], the calculated values of characteristic points $x_{fl,t}^{(a,c)}$ specify the conditions for the stream function at the boundaries of the jet with the anodic and cathodic parts of the chamber (the wavy lines in Fig. 1).

The procedures of calculating the gas velocity field under boundary conditions specified at the walls, as well as at the anodic and cathodic flanges (surfaces *AF* and *CF* in Fig. 1), and the carbon impurity concentration are virtually the same as those used in [2].

In [2], the efficiency of the chamber in terms of the fullerene yield was estimated with parameter Γ, which is defined as the ratio of the fullerene flux from the chamber to the amount of arising fullerenes. The factors that decrease Γ are the UV irradiation of the fullerenes by the arc and the deposition of the fullerenes on the walls.

Figure 2 plots Γ against flow rate G_g at different values of θ_a, the fraction of the incoming flux that passes through the anodic part of the chamber ($\theta_a + \theta_c = 1$). The value of θ_a was assumed to be minimal, $\theta_a = 1/2$, when the gas flows pumped through the anodic and cathodic parts of the chamber coincide. For ease of contrasting with the previous results, the computational technique in the case of one-sided pumping ($\theta_a = 1$) was slightly modified compared with that used in [2]; namely, parameters $x_t^{(a)}$ and $x_t^{(c)}$ were calculated independently.

As in [2], there appears a "crisis" of solution at a certain value of flow rate G_g; i.e., the solution becomes physically meaningless. However, unlike the situation in [2], where the crisis means that the condition $x_{fl} < x_t$ is no longer valid, here the crisis lies in the fact that distance $x_t^{(c)}$ becomes equal to chamber radius R and the free turbulent gas flow just cannot leave the chamber in the absence of a pressure gradient along the jet axis. Physically, this formal result means the same as before: the need for providing a considerable pressure gradient along the jet and the need to take into account this gradient in the solution. This will cause a substantial change in the arc discharge conditions and instability of the discharge.

The crisis values of the flow rate calculated by the two techniques mentioned above differ by 15–20% and vary in a basically similar manner. Therefore, we will speak of the limiting value of the flow rate at which $x_t^{(a)}$ and $x_t^{(c)}$ still differ (are calculated separately) and the condition $x_t^{(a)} < R$ holds. The boundary $x_t^{(a)} = R$ is to an extent conventional. One could equally well assume that the maximum flow rate corresponds to $x_t^{(a)} = (x_t^{(c)} + R)/2$, in which case point $x_t^{(a)}$ with the zero transverse (to the jet) velocity is close to the middle of the closed-flow area. However, speculations at such a definition do not change at all and associated estimates change insignificantly.

Figure 3 shows the relative fullerene yield versus the flow rate at different θ_a. Double-sided pumping is seen to noticeably raise threshold flow rate $G_g^{(th)}$ and relative fullerene yield $\Gamma^{(th)}$ achievable at $G_g^{(th)}$.

Moreover, at a total flow rate far from the threshold value, the fullerene yield grows with flow rate until gas delivery becomes more symmetric: at $G_g \geq 25$ m^3/h, curve *1* (the flux ratio is 1 : 1, $\theta_a = 1/2$) runs above curve *4* (one-sided gas delivery from the side of the anodic part of the chamber). Such a result could not be predicted in advance, since, as gas delivery becomes more and more symmetric, the boundary of the cathodic closed-flow area moves away from the radiation source, while the anodic area of closed flow approaches the source. Consequently, the fullerenes entrained by the two flows experience different actions.

Figure 3 and 4 show the dependences of $G_g^{(th)}$ and $\Gamma^{(th)}$ on θ_a for different chamber radii R. Interestingly, when pumping is symmetric, $\Gamma^{(th)}$ varies with R only slightly (the left-hand ends of curves *1–3* in Fig. 4). If one-sided pumping prevails ($\theta_a \longrightarrow 1$), conversely, a small chamber (R = 10 cm, curve *1*), which is more

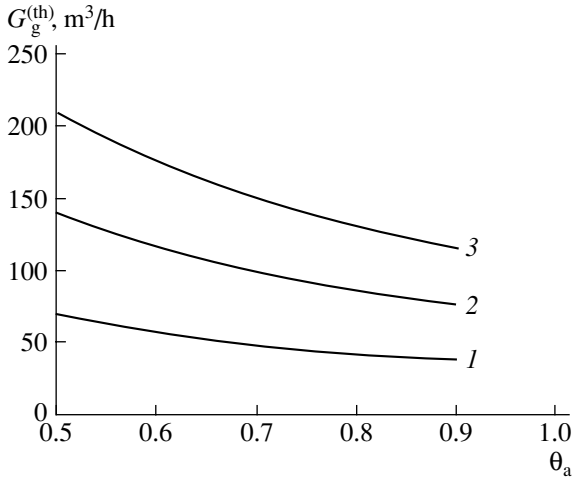

Fig. 3. Gas flow rate threshold value $G_g^{(th)}$ vs. θ_a for chamber radius R = (*1*) 10, (*2*) 20, and (*3*) 30 cm.

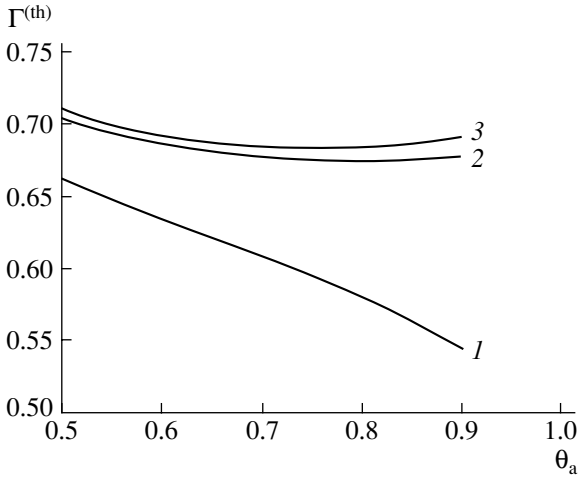

Fig. 4. Relative fullerene yield $\Gamma^{(th)}$ achievable at threshold flow rate $G_g^{(th)}$ vs. θ_a for R = (*1*) 10, (*2*) 20, and (*3*) 30 cm.

appropriate from the engineering standpoint, cannot provide a high fullerene extraction efficiency and so a large chamber should be designed.

BOUNDARY CONDITIONS AND STREAMLINES FOR THE ASYMMETRIC AXIAL GAS FLOW IN THE 3D CHAMBER

As was indicated in [2], the need to consider the 3D problem is related to the fact that gas outlet through a hole in the side wall is much simpler from the engineering standpoint [3].

We will consider first a chamber with one-sided gas inlet uniform over the cross section of the anodic flange (as in [2]) and gas outlet through a hole in the side wall of the chamber. It is assumed that the center of the hole is roughly aligned with the direction of the arc-produced gas jet.

The streamline pattern in the axial section of the anodic part that passes through the center of the outlet is shown at the left of Fig. 5. Clearly, this section is the only one that involves all streamlines originating in it and is crossed by no other streamlines at none of the points. It is natural to assume that the same pattern will be observed in the cathodic part of the chamber. However, one could imagine quite a different streamline pattern in the cathodic part with a "bottom to top" gas flow toward the outlet (Fig. 6). The feasibility of such a pattern can be evaluated by contrasting Fig. 6 with the formally identical case of 2D geometry. In such a 2D representation, the problem becomes two-dimensional and one may take advantage of the idea of the stream function. Then, if gas delivery through the inlet flange is symmetric, the stream function has equal values over half-plane *2* and band *1* (to the left of the outlet in Fig. 6). In going through the outgoing jet to band *3* (Fig. 6), the stream function changes. However, for the flow pattern in the cathodic part of the chamber shown in Fig. 6, such a situation is unrealizable, since intake of the gas from the lower part of the chamber entails "short circuiting."

Therefore, the gas flow pattern in the cathodic part must be identical to that in the anodic part (Fig. 5) with

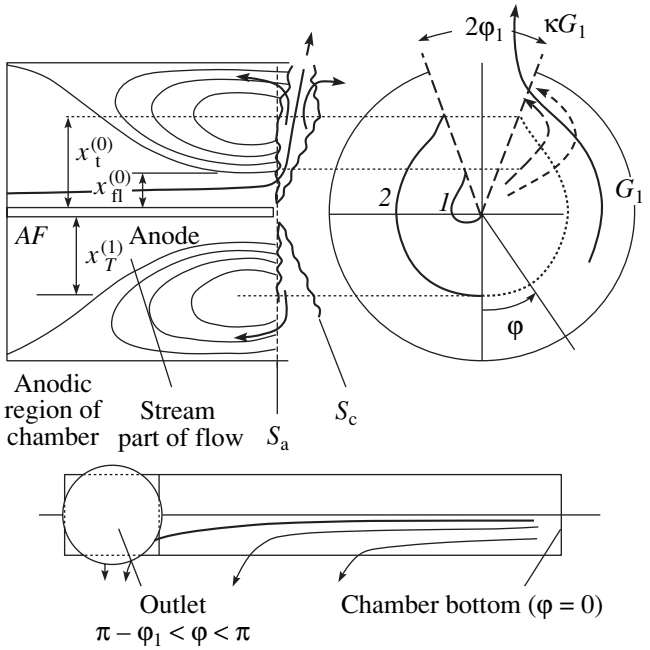

Fig. 5. (a) Characteristic regions of the flow in the anodic part of the chamber in the axial plane passing through the outlet section: surfaces S_a and S_c are the boundaries of the jet with the anodic and cathodic parts of the chamber; (b) (*1*) streamlines at the jet boundary and (*2*) φ-dependent boundary of the viscous decay region; and (c) plane projection of the part of the chamber surface that is imaginary cut by the gap jet and streamlines along the chamber surface.

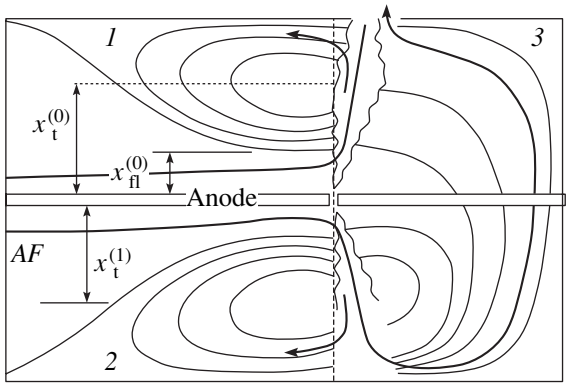

Fig. 6. Imaginary picture of streamlines when the gas passes through the cathodic ("plugged") part of the chamber.

the only exception that the stream part of the flow in the cathodic part is absent. Thus, the streamline pattern differs from the axisymmetric case only quantitatively.

For convenience, let the gas leave the discharge gap toward the outlet of radius R_{out} within solid angle (the exit cone angle) $2\varphi_1 = 2R_{out}/R$ (Fig. 5).

In the gas flow model shown in Fig. 5, the gas flow through the jet to the outlet is accomplished as follows. A fraction of the gas enters the exit cone immediately from the anodic part of the chamber. The rest of the gas is sucked into the jet; scatters along the radius to the center; and then falls into the exit cone together with the circular flow, entirely remaining within the jet (and its geometric extension to the walls; dashed arrow *4* at the right of Fig. 5).

In the upper part of the chamber, the streamline pattern is akin to the axisymmetric case: turbulent outflow from the chamber, the structure of the jet incoming to the outlet being identical to the structure of the outgoing plane jet up to velocity sense. In the lower part of the chamber and in all axial cross sections not passing through the outlet, the jet decays before it reaches the walls. Accordingly, the flow becomes viscous and spreads over the walls with a velocity specified by the condition Re = 1.

Each section not passing through the outlet covers the flow region and the region where the flow along the walls is closed (stagnation zone). Therefore, as in the axisymmetric case, here two characteristic points are separated out: point x_{fl} (the radial boundary of the flow region) and point x_t, where the velocity longitudinal along the walls and transverse to the jet changes sign. The positions of points x_{fl} and x_t considerably depend on angle φ (see the right-hand part of Fig. 5). If the flow pattern inside the jet is known, boundary conditions for gas flow analysis in the chamber should be set at the jet boundaries and their geometric extension to the walls (surfaces S_a and S_c in Fig. 5).

The internal friction of the jet should be calculated as follows. The integral conditions for curves $x_{fl}(\varphi)$ and $x_t(\varphi)$ can be obtained by analogy with a set of equations for gas balance under one-sided gas delivery (pumping) in the 2D case [2]. These equations are

$$2\pi n x_{fl} = G_g = 2\pi R 2 b_1 u_{out}, \quad (1)$$

which describes the balance for the flowing gas (the gas flow into the stream part of the jet, $x \le x_{fl}$, equals the flow leaving the outlet), and

$$2\pi n(x_t - x_{fl}) = 1.2 u_{out} 2\pi R\sqrt{a b_1 (R - x_t)}, \quad (2)$$

which describes the balance of the gas circulating in the chamber. In (1) and (2), $2b_1$ is the width of the outlet ring slot and u_{out} is the gas velocity inside this slot.

In the 3D case, the balance equation for the flowing gas (an analogue of (1)) has the form

$$2n\int_0^\pi d\varphi x_{fl}(\varphi) = 4d^2 u_{out}, \quad (3)$$

where d is the half-side of an imaginary square outlet whose cross-sectional area equals that of a circular hole of radius R_{out} ($\pi R_{out}^2 = 4d^2$).

When calculating the balance of the circulating gas, one should take into account circular flow G_1 entering the exit cone. A fraction of this current (κG_1, $\kappa < 1$) subsequently falls into the outlet of the chamber, while the remainder turns back to the chamber (Fig. 5).

The circulating gas has the following components. The inflow to the jet from the stagnation zone is given by

$$2n\int_0^\pi d\varphi(x_t(\varphi) - x_{fl}(\varphi)). \quad (4)$$

The backward flow from the jet to the chamber is the sum of backward current $G_{back}^{(1)}$, which completely forms in the exit cone (i.e., in the range $\varphi = (\pi - \varphi_1)$–$\pi$ on the right of Fig. 5); the part of the circular current that falls into the exit sector but returns to the chamber (the lower part of Fig. 5); and backward current $G_{back}^{(2)}$, which completely forms in the range $\varphi = 0$–$(\pi - \varphi_1)$ (Fig. 5).

Flow $G_{back}^{(1)}$ is specified by a model of gas flow in the outlet. Here, it is viewed as a portion of a jet outgoing from an infinite plane slot with an appropriate flow rate streamwise [4, 5]. Then, flow $G_{back}^{(1)}$ can be related to the flow $2\pi R^{1/2}\sqrt{ad(R - x_t)}\tilde{u}_{out}$, which would enter a plane jet of half-width d effusing from a slot of length $2\pi R$ at flow velocity

$$\tilde{u}_{out} = \frac{G_g - \kappa G_1}{4d^2}$$

(i.e., the gas inflow to the exit cone due to the circular flows is excluded). Thus,

$$G_{\text{back}}^{(1)} = 2\pi R\frac{\varphi_1}{\pi}1.2\sqrt{ad(R-x_t)}\frac{G_g-\kappa G_1}{4d^2}. \quad (5)$$

Flow $G_{\text{back}}^{(2)}$ can be calculated under the assumption that axial radial velocity u_m varies from $u_m^{\text{turb}} = n/ax$ [2, 4] at $x < x_t(\varphi)$ (the part of the jet that is considered to be free) to zero at $x = R$ and that incoming gas velocity V_m transverse to the jet varies from $V_m^{\text{turb}} = n/x$ [2] at $x < x_t(\varphi)$ to $V_{\text{Re}} = \eta/\rho$, which sets in when Re = 1 [2]. For gas circular velocity in the jet, V_φ, we can put

$$u_m = u_m^{\text{turb}}(1-\zeta(x, x_t)), \quad (6)$$

$$\begin{aligned} V_m - V_{\text{Re}} &= (V_m^{\text{turb}} - V_{\text{Re}})(1-\zeta(x, x_t)) \\ &= V_{\text{Re}}\zeta + V_m^{\text{turb}}(1-\zeta), \end{aligned} \quad (7)$$

where function ζ varies from 0 at $x = x_t$ to 1 at $x = R$, and use the jet-thickness-averaged continuity equation. Eventually, we easily find that

$$\frac{\partial V_\varphi}{\partial\varphi} = A_1 u_m^{\text{turb}} x\frac{\partial\zeta}{\partial x} - \frac{x}{\delta(x)}V_{\text{Re}}\zeta, \quad (8)$$

$$G_{\text{back}}^{(2)} = 2n\int_0^{\pi-\varphi_1} d\varphi\int_{x_t(\varphi)}^{R} dx(n(1-\zeta(x)) + V_{\text{Re}}x\zeta). \quad (9)$$

The integral $A_1 = \int_0^1 d\Lambda f_u(\Lambda)$ in (8) depends on the form of the radial (transverse) velocity curve in the jet [1].

In the final form, the analogue of balance (2) appears as

$$2n\int_0^{\pi} d\varphi(x_t - x_{\text{fl}}) = G_{\text{back}}^{(1)} + G_{\text{back}}^{(2)} + (1-\kappa)G_1, \quad (10)$$

where

$$G_{\text{back}}^{(1)} = 2\pi R\frac{\varphi_1}{\pi}1.2\sqrt{ad(R-x_t)}\frac{G_g-\kappa G_1}{4d^2}, \quad (11)$$

$$G_{\text{back}}^{(2)} = 2n\int_0^{\pi-\varphi_1} d\varphi\int_{x_t(\varphi)}^{T} dx(n(1-\zeta(x)) + V_{\text{Re}}x\zeta), \quad (12)$$

$$G_1 = 2\int_{x_t^{(0)}}^{R} dx\left(\delta(x_t^{(0)}) + \frac{d-\delta(x_t^0)}{R-x_t}(x-x_t)\right)V_\varphi^{(1)}(x). \quad (13)$$

In (13),

$$V_\varphi^{(1)}(x) = \int_0^{\pi-\varphi_1} d\varphi\left(A_1 u_m^{\text{turb}} x\frac{\partial\zeta}{\partial x} - \frac{x}{\delta(x)}V_{\text{Re}}\zeta\right) \quad (14)$$

is the angular velocity of the gas entering the exit cone together with the circular flow.

Parameter κ can be found under the assumption that the flow entering the exit cone comes largely from the domain $x > x_t(\varphi)$ (such an assumption is totally equivalent to the idea that the jet does not "sense" the outlet until it reaches the point $x = x_t(\varphi)$ and, accordingly, the circular current does not distort the streamlines in the jet). Then, calculated at the end of the exit cone, the flow through the chamber is given by $2n\varphi_1 + \kappa G_1$. Hence,

$$2n\varphi_1 + \kappa G_1 = G_g. \quad (15)$$

In relationships (10)–(15), parameters $x_t^{(0)} = x_t(\varphi = \pi)$ and $x_{\text{fl}}^{(0)} = x_{\text{fl}}(\varphi = \pi)$ (the right-hand side of Fig. 5) can be considered unknown and calculated by preassigning some analytical dependences $x_{\text{fl}}(\varphi)$ and $x_t(\varphi)$ within the interval between $\varphi = \pi$ and $\varphi = 0$.

The jet pattern at $\varphi = 0$ must be the same as in the absence of pumping ($x_{\text{fl}}^{(1)} = 0$). In the absence of pumping, the value of $x_t^{(1)}$ was calculated as in the 2D axisymmetric statement ([2]) (see Appendix 1 in part I) and so was considered known in the 3D problem.

From the calculated values of $x_c^{(1)}$ and $x_t^{(1)}$; constructed curves $x_t(\varphi)$ and $x_c(\varphi)$; and dependences (6), (7), and (14), one can set conditions for velocity fields u, V, and V_φ at the boundary of the jet. However, unlike in the 2D problem, here most of the anodic and cathodic parts of the chamber are occupied by the viscous circular flow adjacent to the area where the jet viscously decays. Therefore, the velocity field in the chamber should be calculated based on the classical equation of motion of the curl for a viscous incompressible liquid [6],

$$(V\nabla)\cdot\text{curl}\mathbf{V} - (\text{curl}\mathbf{V}\cdot\nabla)V = \nu\Delta\text{curl}\mathbf{V}. \quad (16)$$

Equation (16), being a third-order equation, requires, along with the obvious condition $u = 0$, an additional boundary condition at the walls. Therefore, bearing in mind that the boundary conditions and the problem as a whole are of approximate character, we did not solve Eq. (16). Instead, we approximated velocities u, V, and V_φ from the plane $z = -L$ to the plane $z = 0$ (for the anodic part of the chamber) and from the body of revolution $z = 2\delta x$ to the plane $z = 0$ (for the

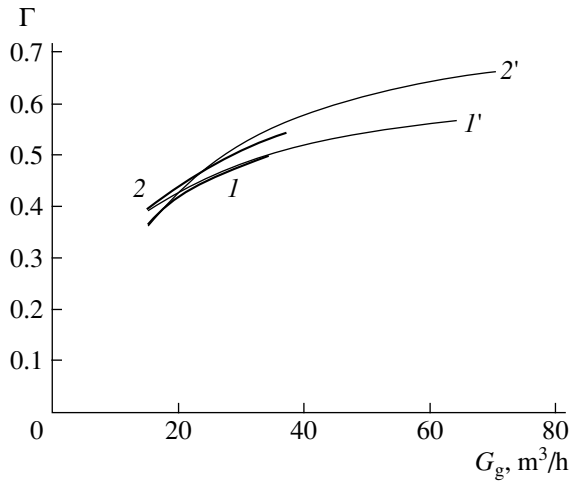

Fig. 7. Relative fullerene yield Γ vs. G_g under (*1*, *1*') one-sided gas delivery and (*2*, *2*') totally symmetric double-sided gas delivery for the (*1*, *2*) 3D and (*1*', *2*') 2D cases.

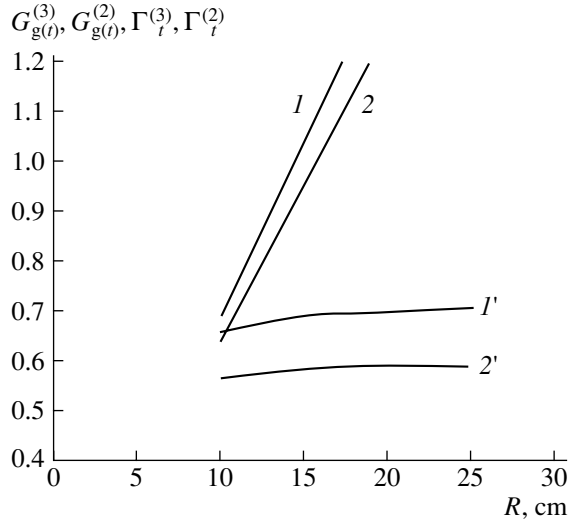

Fig. 8. (*1*, *2*) Threshold gas flow rate $G_g^{(th)}$ and (*1*', *2*') relative fullerene yield $\Gamma^{(th)}$ achievable at $G_g^{(th)}$ vs. chamber radius R for the (*1*, *1*') 2D and (*2*, *2*') 3D cases.

cathodic part of the chamber) by relationships of type

$$V(x, z, \varphi) = V_{AF}(x, \varphi) + (V_{S_a}(x, \varphi) - V_{AF}(x, \varphi))((z + L)/L)^{\Pi},$$

where $V_{S_a}(x, \varphi) = V(x, z = 0, \varphi)$ is the velocity field at the boundary of the jet (S_a in Fig. 5) with the anodic part of the chamber and $V_{AF}(x, \varphi) = V(x, z = -L, \varphi)$ is the velocity field at the anodic flange.

Exponent Π was varied. For the curves given below, it was taken to be Π = 2. It is essential, however, that the variation of exponent Π changes the final result much less significantly than the transition to the axisymmetric 2D geometry.

ANALYSIS OF THE THREE-DIMENSIONAL PROBLEM

Fullerene yield Γ versus the gas flow rate dependence was taken for chambers of different radii (curves *1* and *2* in Fig. 7). For comparison, Fig. 7 also plots the same dependences for an axisymmetric chamber (curves *1*' and *2*'). When constructing curves *1*' and *2*', we took slot width $2b_1$ such that the cross-sectional area of the outlet in the 3D problem, πR_{out}^2, was equal to $2\pi R 2b_1$.

It follows from Fig. 7 that, compared with the axisymmetric case, Γ reaches a maximum at a lower flow rate and is smaller in magnitude by roughly 20%. This drop depends on parameter $2b_1$ only slightly.

The qualitative inference that an increase in the chamber radius is an effective means for improving the yield provided that the flow rate increases simultaneously (which leads to the need for a higher capacity blower) also remains valid.

The dependences of threshold flow rate $G_g^{(th)}$ and relative fullerene yield achievable at $G_g = G_g^{(th)}$, $\Gamma^{(th)}$, on the chamber radius are shown in Fig. 8 (curves *2* and *2*'). The same dependences for the 2D axisymmetric case are also given for comparison.

The dependence of $\Gamma^{(th)}$ on parameter θ_a at a fixed chamber radius also resembles this curve for the axisymmetric case (Fig. 9). This means that a loss in the efficiency of the 3D chamber compared with the 2D axisymmetric one does not grow, if not compensated, when one-sided gas delivery is replaced by double-sided delivery.

Of great interest is the dependence of the relative fullerene yield on the chamber length that is calculated for the simpler, 2D case. As the length increases (all other parameters being the same), Γ slightly grows. However, this growth is very sensitive to a specified coordinate dependence of the fullerene irradiation intensity. If it is assumed that the intensity is uniform (direction-independent), this effect is much weaker or even changes sign. This is because, as the chamber elongates, so does the wall area of fullerene deposition. The same is true for fullerene-free soot particles. At the same time, if the radiation is isotropic, the fullerene irradiation conditions vary insignificantly. As a result, Γ decreases with increasing chamber length. If, however, the radiation intensity has a distinct peak in the cross section of the chamber that passes through the gap, some of the fullerenes in a longer chamber fall outside the irradiation zone and the survivability of fullerenes twisted in the vortex flow rises, albeit insignificantly. In general, the length of the chamber has a weak effect on the efficiency of fullerene extraction from the chamber.

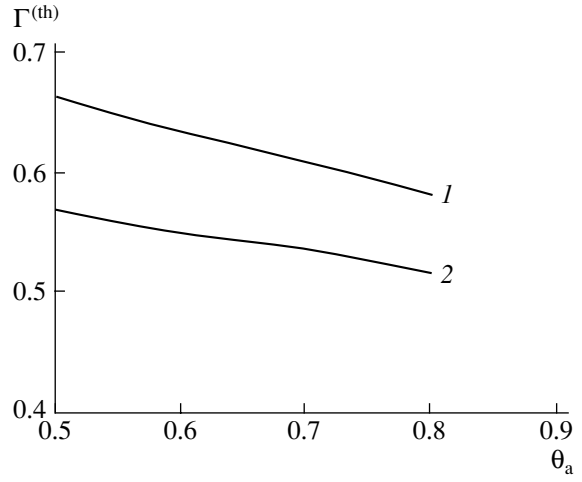

Fig. 9. Relative fullerene yield $\Gamma^{(th)}$ vs. parameter θ_a in the (*1*) 2D and (*2*) 3D cases. The chamber radius is $R = 10$ cm.

COMPARISON WITH EXPERIMENTAL DATA

The dependence of the fullerene yield (in percentage) on the gas flow rate, $\alpha(G_g)$, in the case of the 3D geometry is the only characteristic that makes qualitative comparison with experiment possible. Both the experiment carried out with the setup described in [3] and the calculation indicate that the curve $\alpha(G_g)$ slightly increases (Fig. 2). Therefore, as G_g rises, the efficiency of the setup is not directly associated with the absolute amount of fullerenes produced; rather, it is related to an increase in the absolute amount of the soot (and, hence, fullerenes) extracted from the arc.

It should be noted that the comparison in this case can be made only on the qualitative basis, since the absolute value of α is hard to calculate directly: the calculated (dashed) curve in Fig. 2 is drawn so as to fit experimental data (circles) at the initial point with $G_g = 16$ m^3/h.

The triangle in Fig. 2 corresponds to the onset of arc instability under one-sided gas delivery and roughly corresponds to the threshold value of flow rate.

Unfortunately, we have not managed to find any other publications that can be employed to make an independent comparison of our calculations with experiment. For example, in works [7, 8], which are similar to ours in design of experiment, the gas is delivered through a large inlet hole in the cathode, so that the gas velocity at the exit from the gap is a function of the flow rate.

CONCLUSIONS

The basic results of this work are as follows.

(1) Double-sided gas delivery (from both the anodic and cathodic sides) raises the efficiency of fullerene extraction from the chamber. The higher the total gas flow rate, the stronger this effect.

(2) In addition, double-sided delivery makes it possible to raise the flow rate threshold level at which the arc still persists and, accordingly, to greatly improve the fullerene yield.

(3) The advantages of double-sided gas delivery are highlighted at a small radius of the chamber, $R \le 10$ cm. In a larger chamber, these advantages are not so pronounced.

(4) In a 3D chamber with fullerene extraction through a hole in the side wall, the fullerene yield drops by 15–20% compared with a 2D axisymmetric chamber. The drop is slightly dependent on the width of an annular slot equiareal to a real circular hole.

REFERENCES

1. N. I. Alekseyev and G. A. Dyuzhev, Zh. Tekh. Fiz. **75** (11), 32 (2005) [Tech. Phys. **50**, 1423 (2005)].
2. N. I. Alekseyev and G. A. Dyuzhev, Zh. Tekh. Fiz. **75** (12), 16 (2005) [Tech. Phys. **50**, 1551 (2005)].
3. G. A. Dyuzhev, I. V. Basargin, B. M. Filippov, *et al.*, Int. Appl. Publ. PCT WO02/096800; PCT/RU02/00083.
4. G. N. Abramovich, *Theory of Turbulent Jets* (Nauka, Moscow, 1984) [in Russian].
5. A. S. Ginevskii, *Theory of Turbulent Jets and Wakes* (Mashinostroenie, Moscow, 1969) [in Russian].
6. L. G. Loitsyanskii, *Mechanics of Liquids and Gases* (GITTL, Moscow, 1957; Pergamon, New York, 1966).
7. R. Dubrovsky and V. Bezmelnitsyn, Rev. Adv. Mater. Sci. **5**, 420 (2003).
8. B. Todorovic-Marcovic, Z. Marcovic, and T. Marcovic, J. Serb. Chem. Soc. **67**, 543 (2003).

Translated by V. Isaakyan

Technical Physics, Vol. 50, No. 12, 2005, pp. 1568–1582. Translated from Zhurnal Tekhnicheskoĭ Fiziki, Vol. 75, No. 12, 2005, pp. 33–46.

GASES AND LIQUIDS

Analytical Study of Nonlinear Vibrations of a Charged Viscous Liquid Drop

A. N. Zharov, A. I. Grigor'ev, and S. O. Shiryaeva

Demidov Yaroslavl State University, ul. Sovetskaya 14, Yaroslavl, 150000 Russia

e-mail: grig@uniyar.ac.ru

Received March 29, 2005

Abstract—The generatrix of a nonlinearly vibrating charged drop of a viscous incompressible conducting liquid is found by directly expanding the equilibrium spherical shape of the drop in the amplitude of initial multimode deformation up to second-order terms. A fact previously unknown in the theory of nonlinear interaction is discovered: the energy of an initially excited vibration mode of a low-viscosity liquid drop is gradually (within several vibrations periods) transferred to the mode excited by only nonlinear interaction. Irrespectively of the form of the initial deformation, an unstable viscous drop bearing a charge slightly exceeding the critical Rayleigh value takes the shape of a prolate spheroid because of viscous damping of all the modes (except for the fundamental one) for a characteristic time depending on the damping rates of the initially excited modes and the further evolution of the drop is governed by the fundamental mode. In a high-viscosity drop, the rate of rise of the unstable fundamental mode amplitude does not increase continuously with time, contrary to the predictions of nonlinear analysis in terms of the ideal liquid model: it first decreases to a value slightly differing from zero (which depends on the extent of supercriticality of the charge and viscosity of the liquid), remains small for a while (the unstable mode amplitude remains virtually time-independent), and then starts growing.

(1) Investigation into the nonlinear vibration of the charged drop was begun about two decades ago, and today more than 50 publications concerning this issue are available. However, all the analytical studies have been carried out in the approximation of an ideal liquid [1–4], the nonlinear vibrations of viscous drops being studied only by numerical methods (see, for example, [5, 6]). Accordingly, both the epistemological and prognostic value of such works are limited (regardless of the degree of correctness and methods employed). The reason for such a situation is obvious: analytical calculations of nonlinear vibrations of a viscous liquid drop and resulting expressions are extremely awkward. Nevertheless, the analysis of the time evolution of a viscous liquid drop deformed at the zero time that was performed in an approximation linear in initial deformation amplitude [4] suggest that the nonlinear vibrations of a charged viscous liquid drop are quite computable by asymptotic approaches, at which the present paper is aimed.

(2) Let a spherical drop of an incompressible viscous perfectly conducting liquid of radius r_0, density ρ, kinematic viscosity ν, and surface tension σ bear electric charge Q. The velocity field of the liquid flow in the drop is denoted by $\mathbf{U}(r, \vartheta, t)$; the pressure field, by $p(r, \vartheta, t)$; and the electric field potentials near the drop and on its surface, by $\phi(r, \vartheta, t)$ and $\phi_s(t)$, respectively. In spherical coordinate system (r, ϑ, ϕ), the equation for the surface of the drop executing axisymmetric vibrations at any time instant t can be written in the form

$$F(r, \vartheta, t) \equiv r - r_0 - \xi(\vartheta, t) = 0. \quad (1)$$

The initial deformation of the drop is represented as a superposition of modes,

$$t = 0: \xi(\vartheta) = \varepsilon \sum_{m \in \Omega} h_m P_m(\mu);$$
$$\sum_{m \in \Omega} h_m = 1; \quad \mu \equiv \cos\vartheta; \quad (2)$$

where ε is a small parameter characterizing the initial perturbation amplitude; $P_m(\mu)$ is the mth-order Legendre polynomial; and Ω is the set of indices of the modes that, when superposed, specify the initial deformation of the equilibrium (spherical) shape of the drop.

Mathematically, the problem of nonlinear axisymmetric capillary vibrations of such a drop the shape of which at the zero time is described by (1) and (2) is stated as

$$\partial_t \mathbf{U} + (\mathbf{U} \cdot \nabla)\mathbf{U} = -\frac{1}{\rho}\mathrm{grad}\, p + \nu\Delta\mathbf{U}; \quad \mathrm{div}\mathbf{U} = 0;$$
$$\Delta\phi = 0;$$
$$t = 0: \mathbf{U} = 0; \quad r \longrightarrow 0: \mathbf{U} < \infty;$$
$$r \longrightarrow +\infty: \nabla\phi \longrightarrow 0; \quad r = r_0 + \xi(\vartheta, t): \phi = \phi_s(t);$$

$$r = r_0 + \xi(\vartheta, t)\colon \partial_t F + (\mathbf{U}\cdot\nabla)F = 0;$$
$$\boldsymbol{\tau}\cdot(\mathbf{n}\cdot\nabla)\mathbf{U} + \mathbf{n}\cdot(\boldsymbol{\tau}\cdot\nabla)\mathbf{U} = 0;$$
$$-p + 2\rho\nu\mathbf{n}\cdot(\mathbf{n}\cdot\nabla)\mathbf{U} - \frac{1}{8\pi}(\nabla\phi)^2 + \sigma\mathrm{div}\mathbf{n} = 0; \quad (3)$$
$$\int_S \mathbf{n}\cdot\nabla\phi dS = -4\pi Q;$$
$$S = \{r, \vartheta, \varphi | r = r_0 + \xi;\ 0 \le \vartheta \le \pi;\ 0 \le \varphi \le 2\pi\};$$
$$\int_V r^2 \sin\vartheta dr d\vartheta d\varphi = \frac{4\pi}{3} r_0^3;$$
$$V = \{r, \vartheta, \varphi | 0 \le r \le r_0 + \xi;\ 0 \le \vartheta \le \pi;\ 0 \le \varphi \le 2\pi\};$$
$$\int_V \mathbf{r} r^2 \sin\vartheta dr d\vartheta d\varphi = 0,$$

where ∂_t means partial time differentiation, $\boldsymbol{\tau}$ and $\mathbf{n}$ are the unit vectors of the tangent and external normal to the free surface defined by expression (1), and Δ is the Laplacian.

(3) The above set of equations is nonlinear, and its solution will be sought by direct expansion in small parameter ε. For this purpose, all the desired values are represented in the form of asymptotic expansions in ε,

$$\xi(\vartheta, t) = \varepsilon\xi^{(1)}(\vartheta, t) + \varepsilon^2\xi^{(2)}(\vartheta, t) + O(\varepsilon^3);$$
$$\mathbf{U}(r, \vartheta, t) = \varepsilon U_r^{(1)}(r, \vartheta, t)\mathbf{e}_r + \varepsilon^2 U_r^{(2)}(r, \vartheta, t)\mathbf{e}_r + \varepsilon U_\vartheta^{(1)}(r, \vartheta, t)\mathbf{e}_\vartheta + \varepsilon^2 U_\vartheta^{(2)}(r, \vartheta, t)\mathbf{e}_\vartheta + O(\varepsilon^3);$$
$$p(r, \vartheta, t) = p^{(0)}(r, \vartheta, t) + \varepsilon p^{(1)}(r, \vartheta, t) + \varepsilon^2 p^{(2)}(r, \vartheta, t) + O(\varepsilon^3); \quad (4)$$
$$\phi(r, \vartheta, t) = \phi^{(0)}(r, t) + \varepsilon\phi^{(1)}(r, \vartheta, t) + \varepsilon^2\phi^{(2)}(r, \vartheta, t) + O(\varepsilon^3);$$
$$\phi_s(t) = \phi_s^{(0)}(t) + \varepsilon\phi_s^{(1)}(t) + \varepsilon^2\phi_s^{(2)}(t) + O(\varepsilon^3),$$

where $\mathbf{e}_r$ and $\mathbf{e}_\vartheta$ are the unit vectors of the spherical coordinate system.

Substituting these expansions into the above set of equations and equating the coefficients multiplying equal powers of small parameter ε on the left and on the right to each other, we split the initial nonlinear problem into a set of interrelated linear inhomogeneous subproblems.

(i) In the zeroth order of smallness, the subproblem is stated as

$$\Delta\phi^{(0)} = 0; \quad r \longrightarrow +\infty\colon \nabla\phi^{(0)} \longrightarrow 0;$$
$$r = r_0\colon \phi^{(0)} = \phi_s^{(0)}(t);$$
$$-p^{(0)} - p_Q^{(0)} + p_\sigma^{(0)} = 0; \quad \int_{-1}^{1} r_0^2 \partial_r\phi^{(0)} d(\cos\vartheta) = -2Q.$$

The solution to this subproblem has the form

$$\phi^{(0)} = \frac{Q}{r}; \quad \phi_s^{(0)} = \frac{Q}{r_0}; \quad p^{(0)} + \frac{Q^2}{8\pi r_0^4} = \frac{2\sigma}{r_0}. \quad (5)$$

(ii) Collecting the terms involving the small parameter in the first power and taking into account the vector identity

$$\Delta\mathbf{U} = \mathrm{grad}(\mathrm{div}\mathbf{U}) - \mathrm{curl}(\mathrm{curl}\mathbf{U}), \quad (6)$$

we come to the first-order subproblem,

$$\partial_t U_r^{(1)} = -\frac{1}{\rho}\partial_r p^{(1)} + \nu\left(\frac{1}{r^2}\partial_{\vartheta\vartheta} U_r^{(1)} + \frac{\cot(\vartheta)}{r^2}\partial_\vartheta U_r^{(1)} - \frac{1}{r}\partial_{r\vartheta} U_\vartheta^{(1)} - \frac{\cot(\vartheta)}{r}\partial_r U_\vartheta^{(1)} - \frac{1}{r^2}\partial_\vartheta U_\vartheta^{(1)} - \frac{\cos(\vartheta)}{r^2} U_\vartheta^{(1)}\right);$$
$$\partial_t U_\vartheta^{(1)} = -\frac{1}{\rho}\frac{1}{r}\partial_\vartheta p^{(1)} + \nu\left(\partial_{rr} U_\vartheta^{(1)} + \frac{2}{r}\partial_r U_\vartheta^{(1)} - \frac{1}{r}\partial_{r\vartheta} U_r^{(1)}\right);$$
$$\partial_r U_r^{(1)} + \frac{2}{r} U_r^{(1)} + \frac{1}{r}\partial_\vartheta U_\vartheta^{(1)} + \frac{\cot(\vartheta)}{r} U_\vartheta^{(1)} = 0;$$
$$t = 0\colon \mathbf{U}^{(1)} = 0; \quad \xi^{(1)} = \varepsilon\sum_{m\in\Omega} h_m P_m(\mu);$$
$$r \longrightarrow 0\colon \mathbf{U}^{(1)} < \infty; \quad (7)$$
$$\Delta\phi^{(1)} = 0; \quad r \longrightarrow +\infty\colon \nabla\phi^{(1)} \longrightarrow 0;$$
$$r = r_0\colon \phi^{(1)} + \xi^{(1)}\partial_r\phi^{(0)} = \phi_s^{(1)}(t);$$
$$\int_{-1}^{1} (r_0\partial_r\phi^{(1)} + \xi^{(1)}(r_0\partial_{rr}\phi^{(0)} + 2\partial_r\phi^{(0)}))d(\mu) = 0;$$
$$\int_{-1}^{1} \xi^{(1)} d(\mu) = 0; \quad \int_{-1}^{1} \xi^{(1)} P_1(\mu) d(\mu) = 0;$$
$$\partial_t\xi^{(1)} = U_r^{(1)}; \quad \partial_r U_\vartheta^{(1)} + \frac{1}{r}\partial_\vartheta U_r^{(1)} - \frac{1}{r} U_\vartheta^{(1)} = 0;$$
$$-p^{(1)} + 2\rho\nu\partial_r U_r^{(1)} - \frac{1}{4\pi}\partial_r\phi^{(0)}(\partial_r\phi^{(1)} + \xi^{(1)}\partial_{rr}\phi^{(0)}) - \frac{\sigma}{r_0^2}(2 + \Delta_\Omega)\xi^{(1)} = 0.$$

Here, Δ_Ω is the angular part of the Laplacian in the spherical coordinates.

With regard to (5), the solution to set (7) can be presented in the form [4]

$$\xi^{(1)}(\vartheta, t) = \sum_{n \in \Omega} \xi_n^{(1)}(t) P_n(\mu);$$

$$U_r^{(1)}(r, \vartheta, t) = \sum_{n \in \Omega} U_{rn}^{(1)}(r, t) P_n(\mu);$$

$$U_\vartheta^{(1)}(r, \vartheta, t) = \sum_{n \in \Omega} U_{\theta n}^{(1)}(r, t) \partial_\vartheta P_n(\mu); \qquad (8)$$

$$p^{(1)}(r, \vartheta, t) = \sum_{n \in \Omega} p_n^{(1)}(r, t) P_n(\mu);$$

$$\phi^{(1)}(r, \vartheta, t) = \sum_{n \in \Omega} \phi_n^{(1)}(r, t) P_n(\mu);$$

where

$$\xi_n^{(1)}(t) = \sum_{j=1}^{+\infty} a_{\xi n}(S_n^{(j)}) \exp(S_n^{(j)} t);$$

$$\phi_n^{(1)}(r, t) = \frac{Q}{r_0^2}\left(\frac{r_0}{r}\right)^{n+1} \xi_n^{(1)}(t);$$

$$U_{rn}^{(1)}(r, t) = \sum_{j=1}^{+\infty}\left(a_n(S_n^{(j)})\left(\frac{r}{r_0}\right)^{n-1} + b_n(S_n^{(j)})\frac{1}{r}\frac{j_n(\chi_n^{(j)} r)}{j_n(\chi_n^{(j)} r_0)}\right)\exp(S_n^{(j)} t);$$

$$U_{\vartheta n}^{(1)}(r, t) = \sum_{j=1}^{+\infty}\left(a_n(S_n^{(j)})\left(\frac{r}{r_0}\right)^{n-1} + b_n(S_n^{(j)})\left(\frac{1}{r}\frac{j_n(\chi_n^{(j)} r)}{j_n(\chi_n^{(j)} r_0)} + \frac{\chi_n^{(j)}}{n+1}\frac{j_{n+1}(\chi_n^{(j)} r)}{j_n(\chi_n^{(j)} r_0)}\right)\right)\frac{\exp(S_n^{(j)} t)}{n};$$

$$a_{\xi n}(S_n^{(j)}) = \left(S_n^{(j)} + 2(n-1)(2n+1)\frac{\nu}{r_0^2} + 2(n-1)^2(n+1)\frac{\nu}{\eta_n(1, \chi_n^{(j)}) r_0^2}\right)\frac{h_n}{\partial_{s_n^{(j)}} D_n(S_n^{(j)})};$$

$$a_n(S_n^{(j)}) = \left((2(n^2-1) + (r_0\chi_n^{(j)})^2)\frac{1}{2\chi_n^{(j)} r_0}\frac{j_n(\chi_n^{(j)} r_0)}{j_{n+1}(\chi_n^{(j)} r_0)} - 1\right) \times \frac{h_n}{\eta_n(1, \chi_n^{(j)})}\frac{\omega_n^2}{\partial_{s_n^{(j)}} D_n(S_n^{(j)})};$$

$$b_n(S_n^{(j)}) = 2(n^2-1) \times \left(1 - \frac{2}{\chi_n^{(j)} r_0}\frac{j_{n+1}(\chi_n^{(j)} r_0)}{j_n(\chi_n^{(j)} r_0)}\right)^{-1} \frac{h_n \omega_n^2 \nu}{r_0 S_n^{(j)} \partial_{s_n^{(j)}} D_n(S_n^{(j)})};$$

$$\chi_n^{(j)} = \sqrt{\frac{S_n^{(j)}}{\nu}};$$

$$\partial_{s_n^{(j)}} D_n(S_n^{(j)}) = 2S_n^{(j)} + 2(n-1)(2n+1)\frac{\nu}{r_0^2} + (n-1)^2(n+1)\frac{\nu}{r_0^2}\left(2 + \frac{(2n+1)\chi_n^{(j)} r_0}{2}\frac{j_n(\chi_n^{(j)} r_0)}{j_{n+1}(\chi_n^{(j)} r_0)} + \frac{(\chi_n^{(j)} r_0)^2}{2}\left(1 - \left(\frac{j_n(\chi_n^{(j)} r_0)}{j_{n+1}(\chi_n^{(j)} r_0)}\right)^2\right)\right)\frac{1}{\eta_n(1, \chi_n^{(j)})};$$

$$D_n(S_n^{(j)}) = (S_n^{(j)})^2 + 2(n-1)(2n+1)\frac{S_n^{(j)}}{r_0^2} + 2(n-1)^2(n+1)\frac{S_n^{(j)}\nu}{\eta_n(1, \chi_n^{(j)}) r_0^2} + \omega_n^2;$$

$$\omega_n^2 \equiv \frac{\sigma}{\rho r_0^3} n(n-1)(n+2-W); \quad W = \frac{Q^2}{4\pi\sigma r_0^3};$$

$$\eta_n(\tau, \chi_n^{(j)}) = \tau - \frac{r_0\chi_n^{(j)}}{2}\frac{j_n(\chi_n^{(j)} r_0)}{j_{n+1}(\chi_n^{(j)} r_0)}.$$

Here, $S_n^{(j)}$ is the root of dispersion relation $D_n(S_n^{(j)}) = 0$ and $j_n(\chi_n^{(j)} r_0)$ is the nth-order modified spherical Bessel function of the first kind.

(iii) In the second order of smallness, the problem is stated as

$$\partial_t U_r^{(2)} + U_r^{(1)}\partial_r U_r^{(1)} + \frac{1}{r}U_\vartheta^{(1)}\partial_\vartheta U_r^{(1)} - \frac{1}{r}(U_\vartheta^{(1)})^2 = -\frac{1}{\rho}\partial_r p^{(2)} + \nu\left(\frac{1}{r^2}\partial_{\vartheta\vartheta} U_r^{(2)} + \frac{\cot(\vartheta)}{r^2}\partial_\vartheta U_r^{(2)} - \frac{1}{r}\partial_{r\vartheta} U_\vartheta^{(2)} - \frac{\cot(\vartheta)}{r}\partial_r U_\vartheta^{(2)} - \frac{1}{r^2}\partial_\vartheta U_\vartheta^{(2)} - \frac{\cot(\vartheta)}{r^2}U_\vartheta^{(2)}\right);$$

$$\partial_t U_\vartheta^{(2)} + U_r^{(1)}\partial_r U_\vartheta^{(1)} + \frac{1}{r}U_\vartheta^{(1)}\partial_\vartheta U_\vartheta^{(1)} + \frac{1}{r}U_r^{(1)}U_\vartheta^{(1)} = -\frac{1}{\rho}\frac{1}{r}\partial_\vartheta p^{(2)} + \nu\left(\partial_{rr} U_\vartheta^{(2)} + \frac{2}{r}\partial_r U_\vartheta^{(2)} - \frac{1}{r}\partial_{r\vartheta} U_r^{(2)}\right);$$

$$\partial_r U_r^{(2)} + \frac{2}{r}U_r^{(2)} + \frac{1}{r}\partial_\vartheta U_\vartheta^{(2)} + \frac{\cot(\vartheta)}{r}U_\vartheta^{(2)} = 0.$$

$$t = 0: \mathbf{U}^{(2)} = 0;$$

$$\xi^{(2)} = -\frac{1}{r_0}\sum_{m\in\Omega}\frac{h_m^2}{2m+1}P_0(\mu)$$

$$-\frac{9}{r_0}\sum_{m\in\Omega}\frac{(m+1)h_m h_{m+1}}{(2m+1)(2m+3)}P_1(\mu);$$

$$r \longrightarrow 0: \mathbf{U}^{(2)} < \infty;$$

$$\Delta\phi^{(2)} = 0; \quad r \longrightarrow +\infty: \nabla\phi^{(2)} \longrightarrow 0;$$

$$r = r_0: \phi^{(2)} + \xi^{(2)}\partial_r\phi^{(0)} + \frac{1}{2}(\xi^{(1)})^2\partial_{rr}\phi^{(0)}$$

$$+\xi^{(1)}\partial_r\phi^{(1)} = \phi_s^{(2)}(t);$$

$$\int_{-1}^{1}[r_0^2\partial_r\phi^{(2)} + r_0\xi^{(1)}(r_0\partial_{rr}\phi^{(1)} + 2\partial_r\phi^{(1)}) \tag{9}$$

$$+ r_0\xi^{(2)}(r_0\partial_{rr}\phi^{(0)} + 2\partial_r\phi^{(0)}) + (\xi^{(1)})^2\left(\frac{1}{2}r_0^2\partial_{rrr}\phi^{(0)}\right.$$

$$\left. + 2r_0\partial_{rr}\phi^{(0)} + \partial_r\phi^{(0)}\right) - \partial_\vartheta\xi^{(1)}\partial_\vartheta\phi^{(1)}\Big]d(\mu) = 0;$$

$$\int_{-1}^{1}(r_0\xi^{(2)} + (\xi^{(1)})^2)d(\mu) = 0;$$

$$\int_{-1}^{1}(2r_0\xi^{(2)} + 3(\xi^{(1)})^2)P_1(\mu)d(\mu) = 0;$$

$$-\partial_t\xi^{(2)} + U_r^{(2)} + \partial_r U_r^{(1)}\xi^{(1)} - \frac{1}{r_0}U_\vartheta^{(1)}\partial_\vartheta\xi^{(1)} = 0;$$

$$\frac{1}{r_0}\partial_\vartheta U_r^{(2)} + \partial_r U_\vartheta^{(2)} - \frac{1}{r_0}U_\vartheta^{(2)} + \left(\frac{1}{r_0}\partial_{r\vartheta}U_r^{(1)}\right.$$

$$\left. - \frac{1}{r_0^2}\partial_\vartheta U_r^{(1)} + \partial_{rr}U_\vartheta^{(1)} - \frac{1}{r_0}\partial_r U_\vartheta^{(1)} + \frac{1}{r_0^2}U_\vartheta^{(1)}\right)\xi^{(1)}$$

$$-2\left(\frac{1}{r_0^2}\partial_\vartheta U_\vartheta^{(1)} + \frac{1}{r_0^2}U_r^{(1)} - \frac{1}{r_0}\partial_r U_r^{(1)}\right)\partial_\vartheta\xi^{(1)} = 0;$$

$$-p^{(2)} - \frac{\sigma}{r_0^2}(2+\Delta_\Omega)\xi^{(2)} + \frac{2\sigma}{r_0^3}\xi^{(1)}(1+\Delta_\Omega)\xi^{(1)}$$

$$-\frac{1}{8\pi}\Big[2\xi^{(2)}\partial_{rr}\phi^{(0)}\partial_r\phi^{(0)} + (\xi^{(1)})^2\Big((\partial_{rr}\phi^{(0)})^2$$

$$+\partial_{rrr}\phi^{(0)}\partial_r\phi^{(0)}\Big) + \frac{1}{r_0^2}(\partial_\vartheta\phi^{(1)})^2 + (\partial_r\phi^{(1)})^2$$

$$+2\partial_r\phi^{(2)}\partial_r\phi^{(0)} + 2\xi^{(1)}(\partial_{rr}\phi^{(0)}\partial_r\phi^{(1)} + \partial_{rr}\phi^{(1)}\partial_r\phi^{(0)})\Big]$$

$$+2\rho\nu\partial_r U_r^{(2)} - (\partial_r p^{(1)} - 2\rho\nu\partial_{rr}U_r^{(1)})\xi^{(1)}$$

$$-2\rho\nu\left(\frac{1}{r_0^2}\partial_\vartheta U_r^{(1)} + \frac{1}{r_0}\partial_r U_\vartheta^{(1)} - \frac{1}{r_0^2}U_\vartheta^{(1)}\right)\partial_\vartheta\xi^{(1)} = 0.$$

Substituting solutions (5) and (8) of the zeroth- and first-order subproblems into set (9) yields a set of second-order partial linear inhomogeneous differential equations for $U_r^{(2)}$, $U_\vartheta^{(2)}$, $p^{(2)}$, $\xi^{(2)}$, and $\phi^{(2)}$.

To solve this set, we apply the time Laplace transformation

$$f(S) = \int_0^{+\infty} f(t)\exp(-St)dt = \Im[f(t)];$$

$$f = \{U_r^{(2)}; U_\vartheta^{(2)}; p^{(2)}; \xi^{(2)}; \phi^{(2)}\}.$$

The second-order Laplace transforms are now expanded into series in Legendre polynomials (this is possible, since the problem is axisymmetric) and in their first derivatives with respect to the polar angle [4, 7],

$$U_r^{(2)}(r,\vartheta,S) = \sum_{n=0}^{+\infty}U_{rn}^{(2)}(r,S)P_n(\mu);$$

$$U_\vartheta^{(2)}(r,\vartheta,S) = \sum_{n=1}^{+\infty}U_{\vartheta n}^{(2)}(r,S)\partial_\vartheta P_n(\mu);$$

$$\xi^{(2)}(\vartheta,S) = \sum_{n=0}^{+\infty}\xi_n^{(2)}(S)P_n(\mu); \tag{10}$$

$$\phi^{(2)}(r,\vartheta,S) = \sum_{n=1}^{+\infty}\phi_n^{(2)}(r,S)P_n(\mu);$$

$$p^{(2)}(r,\vartheta,S) = \sum_{n=0}^{+\infty}p_n^{(2)}(r,S)P_n(\mu).$$

Let us take into account that the first-order projections of the liquid velocity field onto the unit vectors of the spherical coordinate system are related by the continuity equation,

$$U_{\vartheta n}^{(1)}(r,t) = \frac{r}{n(n+1)}\left(\partial_r U_{rn}^{(1)}(r,t) + \frac{2}{r}U_{rn}^{(1)}(r,t)\right).$$

Then, set (9) takes the form

$$SU_{rn}^{(2)}(r,S) - \sum_{k,m\in\Omega}\frac{\alpha_{kmn}}{k(k+1)m(m+1)}r\Im$$

$$\times[\partial_r U_{rk}^{(2)}(r,t)\partial_r U_{rm}^{(1)}(r,t)]$$

$$+\sum_{k,m\in\Omega}\left(K_{kmn} + \frac{(k^2+k-4)\alpha_{kmn}}{k(k+1)m(m+1)}\right)$$

$$\times \Im[U_{rk}^{(1)}(r,t)\partial_r U_{rm}^{(1)}(r,t)] \quad (11)$$

$$+\sum_{k,m\in\Omega}\frac{2(m-1)(m+2)\alpha_{kmn}}{k(k+1)m(m+1)}\frac{1}{r}\Im[U_{rk}^{(1)}(r,t)U_{rm}^{(1)}(r,t)]$$

$$= -\frac{1}{\rho}\partial_r p_n^{(2)}(r,S)+n(n+1)\frac{\nu}{r}\Big(\partial_r U_{\vartheta n}^{(2)}(r,S)$$

$$+\frac{1}{r}U_{\vartheta n}^{(2)}(r,S)-\frac{1}{r}U_{rn}^{(2)}(r,S)\Big);\quad n\geq 0;$$

$$SU_{\vartheta n}^{(2)}(r,S)+\sum_{k,m\in\Omega}\frac{\Gamma_{kmn}}{m(m+1)}r\Im[U_{rk}^{(1)}(r,t)\partial_{rr}U_{rm}^{(1)}(r,t)]$$

$$+\sum_{k,m\in\Omega}\frac{\alpha_{kmn}}{2k(k+1)m(m+1)}r\Im[\partial_r U_{rk}^{(1)}(r,t)\partial_r U_{rm}^{(1)}(r,t)]$$

$$+\sum_{k,m\in\Omega}\frac{2}{m(m+1)}\Big(2\Gamma_{kmn}+\frac{\alpha_{kmn}}{k(k+1)}\Big)$$

$$\times\Im[U_{rk}^{(1)}(r,t)\partial_r U_{rm}^{(1)}(r,t)]$$

$$+\sum_{k,m\in\Omega}\frac{2}{m(m+1)}\Big(\Gamma_{kmn}+\frac{\alpha_{kmn}}{k(k+1)}\Big)\frac{1}{r}\Im \quad (12)$$

$$\times[U_{rk}^{(1)}(r,t)U_{rm}^{(1)}(r,t)] = -\frac{1}{\rho}\frac{1}{r}p_n^{(2)}(r,S)$$

$$+\nu\Big(\partial_{rr}U_{\vartheta n}^{(2)}(r,S)+\frac{2}{r}\partial_r U_{\vartheta n}^{(2)}(r,S)-\frac{1}{r}\partial_r U_{rn}^{(2)}(r,S)\Big);$$

$$n\geq 1;$$

$$\partial_r U_{rn}^{(2)}(r,S)+\frac{2}{r}U_{rn}^{(2)}(r,S)-\frac{n(n+1)}{r}U_{\vartheta n}^{(2)}(r,S)=0; \quad (13)$$

$$n\geq 0;$$

$$r\longrightarrow 0:\ U_{rn}^{(2)}<\infty;\quad U_{\vartheta n}^{(2)}<\infty; \quad (14)$$

$$\partial_{rr}\phi_n^{(2)}(r,S)+\frac{2}{r}\partial_r\phi_n^{(2)}(r,S)-n(n+1)\phi_n^{(2)}(r,S)=0; \quad (15)$$

$$n\geq 0;$$

$$r\longrightarrow +\infty:\ \partial_r\phi_n^{(2)}(r,S)\longrightarrow 0;\quad \phi_n^{(2)}(r,S)\longrightarrow 0; \quad (16)$$

$$r=r_0:\ \phi_n^{(2)}(r,S)-\frac{Q}{r_0^2}\xi_n^{(2)}(S)$$

$$-\frac{Q}{r_{0}^3}\sum_{k,m\in\Omega}mK_{kmn}\Im[\xi_k^{(1)}(t)\xi_m^{(1)}(t)]=\phi_s^{(2)}(S)\delta_{n0}; \quad (17)$$

$$n\geq 0;$$

$$\int_{-1}^{+1}\sum_{n=0}^{+\infty}\Big[r_0^2\partial_r\phi_n^{(2)}(r,S)$$

$$+\frac{Q}{r_{0}^2}\sum_{k,m\in\Omega}m(m+1)K_{kmn}\Im[\xi_k^{(1)}(t)\xi_m^{(1)}(t)] \quad (18)$$

$$-\frac{Q}{r_{0}^2}\sum_{k,m\in\Omega}\alpha_{kmn}\Im[\xi_k^{(1)}(t)\xi_m^{(1)}(t)]\Big]P_n(\mu)d(\mu)=0;$$

$$\int_{-1}^{+1}\sum_{n=0}^{+\infty}\Big(r_0\xi_n^{(2)}(S)$$

$$+\sum_{k,m\in\Omega}K_{kmn}\Im[\xi_k^{(1)}(t)\xi_m^{(1)}(t)]\Big)P_n(\mu)d(\mu)=0; \quad (19)$$

$$\int_{-1}^{+1}\sum_{n=0}^{+\infty}\Big(2r_0\xi_n^{(2)}(S)$$

$$+3\sum_{k,m\in\Omega}K_{kmn}\Im[\xi_k^{(1)}(t)\xi_m^{(1)}(t)]\Big)P_n(\mu)P_1(\mu)d(\mu)=0; \quad (20)$$

$$-S\xi_n^{(2)}(S)-\frac{1}{r_0}\sum_{m\in\Omega}\frac{h_m^2}{2m+1}\delta_{n0}-\frac{9}{r_0}$$

$$\times\sum_{m\in\Omega}\frac{(m+1)h_m h_{m+1}}{(2m+1)(2m+3)}\delta_{n1}+U_{rn}^{(2)}(r,S)$$

$$+\sum_{k,m\in\Omega}\Big(K_{kmn}-\frac{\alpha_{kmn}}{m(m+1)}\Big)\Im[\xi_k^{(1)}(t)\partial_r U_{rm}^{(1)}(r,t)] \quad (21)$$

$$-\sum_{k,m\in\Omega}\frac{2\alpha_{kmn}}{m(m+1)}\frac{1}{r_0}\Im[\xi_k^{(1)}(t)U_{rm}^{(1)}(t)]=0;$$

$$n\geq 0;$$

$$\frac{1}{r_0}U_{rn}^{(2)}(r,S)+\partial_r U_{\vartheta n}^{(2)}(r,S)-\frac{1}{r_0}U_{\vartheta n}^{(2)}(r,S)$$

$$+\sum_{k,m\in\Omega}\frac{\Gamma_{kmn}}{m(m+1)}r_0\Im[\xi_k^{(1)}(t)\partial_{rrr}U_{rm}^{(1)}(r,t)]$$

$$+\sum_{k,m\in\Omega}\frac{3\Gamma_{kmn}}{m(m+1)}\Im[\xi_k^{(1)}(t)\partial_{rr}U_{rm}^{(1)}(r,t)]$$

$$+\sum_{k,m\in\Omega}\Big(\Gamma_{kmn}+2\Gamma_{mkn}-\frac{2\Gamma_{kmn}}{m(m+1)}-\frac{2\Lambda_{kmn}}{m(m+1)}\Big) \quad (22)$$

$$\times\frac{1}{r_0}\Im[\xi_k^{(1)}(t)\partial_r U_{rm}^{(1)}(r,t)]$$

$$+\sum_{k,m\in\Omega}\left(\frac{2\Gamma_{kmn}}{m(m+1)}-\Gamma_{kmn}-2\Gamma_{mkn}-\frac{4\Lambda_{kmn}}{m(m+1)}\right)$$

$$\times\frac{1}{r_0^2}\Im[\xi_k^{(1)}(t)U_{rm}^{(1)}(r,t)]=0;\quad n\geq 1;$$

$$-p_n^{(2)}(r,S)+\frac{\sigma}{r_0^2}(n-1)(n+2)\xi_n^{(2)}(S)$$

$$-\frac{2\sigma}{r_0^3}\sum_{k,m\in\Omega}K_{kmn}(k(k+1)-1)\Im[\xi_k^{(1)}(t)\xi_m^{(1)}(t)]$$

$$+\frac{1}{8\pi}\left[\frac{2Q}{r_0^2}\partial_r\phi_n^{(2)}(r,S)+\frac{4Q^2}{r_0^5}\xi_n^{(2)}(S)\right.$$

$$-\frac{Q^2}{r_0^6}\sum_{k,m\in\Omega}\alpha_{kmn}\Im[\xi_k^{(1)}(t)\xi_m^{(1)}(t)]$$

$$-\frac{Q^2}{r_0^6}\sum_{k,m\in\Omega}(10+(k+1)(m+1)-2(m+1)(m+4))$$

$$\left.\times K_{kmn}\Im[\xi_k^{(1)}(t)\xi_m^{(1)}(t)]\right]+2\rho\nu\partial_r U_{rn}^{(2)}(r,S)$$

$$+2\rho\nu\sum_{k,m\in\Omega}\left(K_{kmn}-\frac{\alpha_{kmn}}{m(m+1)}\right)\Im[\xi_k^{(1)}(t)\partial_{rr}U_{rm}^{(1)}(r,t)] \quad (23)$$

$$-\sum_{k,m\in\Omega}K_{kmn}\Im[\xi_k^{(1)}(t)\partial_r p_m^{(1)}(r,t)]$$

$$-2\rho\nu\frac{1}{r_0}\sum_{k,m\in\Omega}\frac{2\alpha_{kmn}}{m(m+1)}\Im[\xi_k^{(1)}(t)\partial_r U_{rm}^{(1)}(r,t)]$$

$$+2\rho\nu\frac{1}{r_0^2}\sum_{k,m\in\Omega}\left(\frac{2\alpha_{kmn}}{m(m+1)}-\alpha_{kmn}\right)$$

$$\times\Im[\xi_k^{(1)}(t)U_{rm}^{(1)}(r,t)]=0;\quad n\geq 0.$$

Here, coefficients K_{kmn}, α_{kmn}, Γ_{kmn}, Λ_{kmn} are defined by relationships

$$\alpha_{kmn}=-C_{k0m0}^{n0}C_{k(-1)m1}^{n0}\sqrt{k(k+1)m(m+1)};$$

$$K_{kmn}=(C_{k0m0}^{n0})^2;\quad \Gamma_{kmn}=\frac{(2n+1)}{n(n+1)}\frac{\alpha_{nmk}}{(2k+1)};$$

$$\Gamma_{kmn}+\Gamma_{mkn}=K_{kmn};$$

$$\Lambda_{kmn}=\frac{2n+1}{n(n+1)}\left(-\frac{m^2}{2m+1}\alpha_{nkm}+\sum_{j=1}^{[m/2]}\alpha_{n,k,m-2j}\right);$$

$$\Lambda_{kmn}+\Lambda_{mkn}=\alpha_{kmn};$$

where C_{k0m0}^{n0} and $C_{k(-1)m1}^{n0}$ are the Clebsch–Gordan coefficients.

(iv) Equations (19) and (20) entering into set (11)–(23) will be solved first to find coefficients $\xi_0^{(2)}(t)$ and $\xi_1^{(2)}(t)$,

$$\xi_0^{(2)}(t)=-\frac{1}{r_0}\sum_{m\in\Omega}\frac{1}{2m+1}(\xi_m^{(1)}(t))^2;$$

$$\xi_1^{(2)}(t)=-\frac{9}{r_0}\sum_{m\in\Omega}\frac{(m+1)}{(2m+1)(2m+3)}\xi_m^{(1)}(t)\xi_{m+1}^{(1)}(t). \quad (24)$$

Now we find the potential of the surface of the drop and the electrostatic field potential of near the drop from set (15)–(18),

$$\phi_s^{(2)}(t)=\frac{Q}{r_0^3}\sum_{m\in\Omega}\frac{m-1}{2m+1}(\xi_m^{(1)}(t))^2; \quad (25)$$

$$\phi_n^{(2)}(r,S)=0;\quad n=0;$$

$$\phi_n^{(2)}(r,S)=\frac{Q}{r_0^2}\left(\xi_n^{(2)}(S)\right.$$

$$\left.+\frac{1}{r_0}\sum_{k,m\in\Omega}mK_{kmn}\Im[\xi_k^{(1)}(t)\xi_m^{(1)}(t)]\right)\left(\frac{r_0}{r}\right)^{n+1}; \quad (26)$$

$$n\geq 1.$$

Expressing velocity projection $U_{\vartheta n}^{(2)}(r,S)$ from continuity equation (13),

$$U_{\vartheta n}^{(2)}(r,S)=\frac{1}{n(n+1)}(r\partial_r U_{rn}^{(2)}(r,S)+2U_{rn}^{(2)}(r,S)); \quad (27)$$

and substituting it into (12) yields

$$p_n^{(2)}(r,S)=-\frac{\rho S}{n(n+1)}(r^2\partial_r U_{rn}^{(2)}(r,S)+2rU_{rn}^{(2)}(r,S))$$

$$+\frac{\rho\nu}{n(n+1)}(r^2\partial_{rrr}U_{rn}^{(2)}(r,S)+6r\partial_{rr}U_{rn}^{(2)}(r,S)$$

$$+6\partial_r U_{rn}^{(2)}(r,S))-\rho\nu\partial_r U_{rn}^{(2)}(r,S)$$

$$-\sum_{k,m\in\Omega}\frac{\rho\Gamma_{kmn}}{m(m+1)}r^2\Im[\xi_{rk}^{(1)}(r,t)\partial_{rr}U_{rm}^{(1)}(r,t)]$$

$$
\begin{aligned}
&- \sum_{k,m\in\Omega} \frac{\rho\alpha_{kmn}}{2k(k+1)m(m+1)} r^2 \\
&\times \Im[\partial_r U^{(1)}_{rk}(r,t)\partial_r U^{(1)}_{rm}(r,t)] \\
&- \sum_{k,m\in\Omega} \frac{2\rho}{m(m+1)}\left(2\Gamma_{kmn} + \frac{\alpha_{kmn}}{k(k+1)}\right) r \\
&\times \Im[U^{(1)}_{rk}(r,t)\partial_r U^{(1)}_{rm}(r,t)] \\
&- \sum_{k,m\in\Omega} \frac{2\rho}{m(m+1)}\left(\Gamma_{kmn} + \frac{\alpha_{kmn}}{k(k+1)}\right) \\
&\times \Im[U^{(1)}_{rk}(r,t)U^{(1)}_{rm}(r,t)].
\end{aligned} \tag{28}
$$

Finally, substituting the expressions for $U^{(2)}_{\vartheta n}(r, S)$ and $p^{(2)}_n(r, S)$ into Eq. (11), we arrive at a fourth-order ordinary inhomogeneous differential equation for function $U^{(2)}_{rn}(r, S)$,

$$
\begin{aligned}
&\left(\partial_{rr} + \frac{4}{r}\partial_r - \frac{(n-1)(n+2)}{r^2}\right) \\
&\times\left(\partial_{rr} + \frac{4}{r}\partial_r - \frac{(n-1)(n+2)}{r^2} - \frac{S}{\nu}\right) U^{(2)}_{rn}(r,S) \\
&= \frac{n(n+1)}{\nu}\sum_{k,m\in\Omega} f_{kmn}(r,S);
\end{aligned}
$$

$$
\begin{aligned}
f_{kmn}(r,S) &= \frac{\Gamma_{kmn}}{m(m+1)}\Im[U^{(1)}_{rk}(r,t)\partial_{rrr}U^{(1)}_{rm}(r,t)] \\
&+ \frac{1}{m(m+1)}\left(\Gamma_{kmn} + \frac{\alpha_{kmn}}{k(k+1)}\right)\Im[\partial_r U^{(1)}_{rk}(r,t)\partial_{rr}U^{(1)}_{rm}(r,t)] \\
&+ \frac{2}{m(m+1)}\left(3\Gamma_{kmn} + \frac{\alpha_{kmn}}{k(k+1)}\right)\frac{1}{r}\Im[U^{(1)}_{rk}(r,t)\partial_{rrr}U^{(1)}_{rm}(r,t)] \\
&+ \frac{4}{m(m+1)}\left(\Gamma_{kmn} + \frac{\alpha_{kmn}}{k(k+1)}\right)\frac{1}{r}\Im[\partial_r U^{(1)}_{rk}(r,t)\partial_r U^{(1)}_{rm}(r,t)] \\
&+ \left(\frac{6\Gamma_{kmn}}{m(m+1)} + \frac{2\Gamma_{mkn}}{k(k+1)} - K_{kmn} - \frac{(k^2+k-10)\alpha_{kmn}}{k(k+1)m(m+1)}\right) \\
&\times \frac{1}{r^2}\Im[U^{(1)}_{rk}(r,t)\partial_r U^{(1)}_{rm}(r,t)] - \frac{2\alpha_{kmn}}{k(k+1)}\frac{(m-1)(m+2)}{m(m+1)} \\
&\times \frac{1}{r^3}\Im[U^{(1)}_{rk}(r,t)U^{(1)}_{rm}(r,t)].
\end{aligned} \tag{29}
$$

Homogeneous equation (29) has four linearly independent solutions [8],

$$
\begin{aligned}
&U^{(2)}_{rn}(r,S) = r^{n-1}, \quad U^{(2)}_{rn}(r,S) = \frac{1}{r^{n+2}}; \\
&U^{(2)}_{rn}(r,S) = \frac{1}{r} j_n\left(\frac{\sqrt{S}}{\sqrt{\nu}}r\right); \quad U^{(2)}_{rn}(r,S) = \frac{1}{r} y_n\left(\frac{\sqrt{S}}{\sqrt{\nu}}r\right),
\end{aligned} \tag{30}
$$

where $j_n(z)$ and $y_n(z)$ are the modified spherical Bessel functions of the first and second kind.

The Wronskian of set (30) is compactly written as

$$
W\left(r^{n-1}, \frac{1}{r^{n+2}}, \frac{1}{r} j_n\left(\frac{\sqrt{S}}{\sqrt{\nu}}r\right), \frac{1}{r} y_n\left(\frac{\sqrt{S}}{\sqrt{\nu}}r\right)\right) = (-1)^n \frac{(2n+1)}{r^8}\frac{S^{3/2}}{\nu^{3/2}},
$$

and the partial solution to Eq. (29) can be written in the form

$$
\begin{aligned}
U^{(2)(*)}_{rn}(r,S) &= -\frac{1}{(2n+1)}\frac{\nu}{S} r^{n-1}\int_0^r \frac{f(\tau)}{\tau^{n-2}} d\tau \\
&+ \frac{1}{(2n+1)}\frac{\nu}{S}\frac{1}{r^{n+2}}\int_0^r \tau^{n+3} f(\tau) d\tau \\
&+ (-1)^n \frac{\sqrt{\nu}}{\sqrt{S}}\frac{1}{r} j_n\left(\frac{\sqrt{S}}{\sqrt{\nu}}r\right)\int_0^r \tau^3 y_n\left(\frac{\sqrt{S}}{\sqrt{\nu}}\tau\right) f(\tau) d\tau \\
&- (-1)^n \frac{\sqrt{\nu}}{\sqrt{S}}\frac{1}{r} y_n\left(\frac{\sqrt{S}}{\sqrt{\nu}}r\right)\int_0^r \tau^3 j_n\left(\frac{\sqrt{S}}{\sqrt{\nu}}\tau\right) f(\tau) d\tau.
\end{aligned}
$$

Thus, the solution to Eq. (29) with regard to boundedness condition (14) has the form

$$
\begin{aligned}
U^{(2)}_{rn}(r,S) &= A_n(S) r^{n-1} \\
&+ B_n(S)\frac{1}{r} j_n\left(\frac{\sqrt{S}}{\sqrt{n}}r\right) + U^{(2)(*)}_{rn}(r,S),
\end{aligned} \tag{31}
$$

where $A_n(S)$ and $B_n(S)$ are arbitrary constants.

Substituting (31) into (27) and (28) and employing the recurrence relation [8]

$$
\partial_\chi j_n(\chi) = j_{n+1}(\chi) + \frac{n}{\chi} j_n(\chi); \quad \chi \equiv \frac{\sqrt{S}}{\sqrt{\nu}}r, \tag{32}
$$

we find functions $U^{(2)}_{\vartheta n}(r, S)$ and $p^{(2)}_n(r, S)$,

$$
\begin{aligned}
U^{(2)}_{\vartheta n}(r,S) &= \frac{A_n(S)}{n} r^{n-1} \\
&+ \frac{B_n(S)}{n(n+1)}\frac{1}{r}\left((n+1) j_n\left(\frac{\sqrt{S}}{\sqrt{\nu}}r\right) + \frac{\sqrt{S}}{\sqrt{\nu}} r j_{n+1}\left(\frac{\sqrt{S}}{\sqrt{\nu}}r\right)\right) \\
&+ \frac{1}{n(n+1)}(r\partial_r U^{(2)(*)}_{rn}(r,S) + 2U^{(2)(*)}_{rn}(r,S));
\end{aligned} \tag{33}
$$

$$
\begin{aligned}
p^{(2)}_n(r,S) &= -A_n(S)\frac{S\rho}{n} r^n \\
&- \frac{\rho S}{n(n+1)}(r^2\partial_r U^{(2)(*)}_{rn}(r,S) + 2r U^{(2)(*)}_{rn}(r,S))
\end{aligned}
$$

$$+\frac{\rho\nu}{n(n+1)}(r^2\partial_{rrr}U_{rn}^{(2)(*)}(r,S)+6r\partial_{rr}U_{rn}^{(2)(*)}(r,S)$$
$$+6\partial_r U_{rn}^{(2)(*)}(r,S))-\rho\nu\partial_r U_{rn}^{(2)(*)}(r,S)$$
$$-\sum_{k,m\in\Omega}\frac{\rho\Gamma_{kmn}}{m(m+1)}r^2\Im[U_{rk}^{(1)}(r,t)\partial_{rr}U_{rm}^{(1)}(r,t)] \quad (34)$$
$$-\sum_{k,m\in\Omega}\frac{\rho\alpha_{kmn}}{2k(k+1)m(m+1)}r^2\Im[\partial_r U_{rk}^{(1)}(r,t)\partial_r U_{rm}^{(1)}(r,t)]$$
$$-\sum_{k,m\in\Omega}\frac{2\rho}{m(m+1)}\left(2\Gamma_{kmn}+\frac{\alpha_{kmn}}{k(k+1)}\right)$$
$$\times r\Im[U_{rk}^{(1)}(r,t)\partial_r U_{rm}^{(1)}(r,t)]-\sum_{k,m\in\Omega}\frac{2\rho}{m(m+1)}$$
$$\times\left(\Gamma_{kmn}+\frac{\alpha_{kmn}}{k(k+1)}\right)\Im[U_{rk}^{(1)}(r,t)U_{rm}^{(1)}(r,t)].$$

(v) Substituting expressions (31)–(33) into boundary conditions (21)–(23) and taking into account (26), (32), and recurrent relation [6]

$$\partial_\chi j_n(\chi) = j_{n-1}(\chi)-\frac{n+1}{\chi}j_n(\chi),$$

we recast boundary conditions (21)–(23) in the form

$$A_n(S)r_0^n+B_n(S)j_n\left(\frac{\sqrt{S}}{\sqrt{\nu}}r_0\right)-Sr_0\xi_n^{(2)}(S)$$
$$=\sum_{m\in\Omega}\frac{h_m}{2m+1}\left(h_m\delta_{n0}+\frac{9(m+1)}{2m+3}h_{m+1}\delta_{n1}\right)$$
$$-r_0U_{rn}^{(2)(*)}(r_0,S)-\sum_{k,m\in\Omega}\left(K_{kmn}-\frac{\alpha_{kmn}}{m(m+1)}\right) \quad (35)$$
$$\times r_0\Im[\xi_k^{(1)}(t)\partial_r U_{rm}^{(1)}(r_0,t)]+\sum_{k,m\in\Omega}\frac{2\alpha_{kmn}}{m(m+1)}$$
$$\times\Im[\xi_k^{(1)}(t)U_{rm}^{(1)}(r_0,t)];\quad n\ge 0;$$
$$2\frac{n-1}{n}A_n(S)r_0^n+\frac{B_n(S)}{n(n+1)}\left(\left(2(n^2-1)+\frac{S}{\nu}r_0^2\right)\right.$$
$$\left.\times j_n\left(\frac{\sqrt{S}}{\sqrt{\nu}}r_0\right)-2\frac{\sqrt{S}}{\sqrt{\nu}}r_0j_{n+1}\left(\frac{\sqrt{S}}{\sqrt{\nu}}r_0\right)\right)$$
$$=-\frac{r_0}{n(n+1)}(r_0^2\partial_{rr}U_{rn}^{(2)(*)}(r_0,S)+2r_0\partial_r U_{rn}^{(2)(*)}(r_0,S)$$
$$+(n-1)(n+2)U_{rn}^{(2)(*)}(r_0,S))-\sum_{k,m\in\Omega}\frac{\Gamma_{kmn}}{m(m+1)} \quad (36)$$
$$\times r_0^2\Im[\xi_k^{(1)}(t)(r_0\partial_{rrr}U_{rm}^{(1)}(r_0,t)+3\partial_{rr}U_{rm}^{(1)}(r_0,t))]$$
$$-\sum_{k,m\in\Omega}\left(\Gamma_{kmn}+2\Gamma_{mkn}-\frac{2\Gamma_{kmn}}{m(m+1)}-\frac{2\Lambda_{kmn}}{m(m+1)}\right)$$
$$\times r_0\Im[\xi_k^{(1)}(t)\partial_r U_{rm}^{(1)}(r_0,t)]-\sum_{k,m\in\Omega}\left(\frac{2\Gamma_{kmn}}{m(m+1)}\right.$$
$$\left.-\Gamma_{kmn}-2\Gamma_{mkn}-\frac{4\Lambda_{kmn}}{m(m+1)}\right)\Im[\xi_k^{(1)}(t)U_{rm}^{(1)}(r_0,t)];$$
$$n\ge 1;$$
$$A_n(S)r_0^n\left(\frac{S}{n}+\frac{2\nu}{r_0^2}(n-1)\right)+\frac{2\nu}{r_0^2}B_n(S)\left((n-1)j_n\right.$$
$$\left.\times\left(\frac{\sqrt{S}}{\sqrt{\nu}}r_0\right)+r_0\frac{\sqrt{S}}{\sqrt{\nu}}j_{n+1}\left(\frac{\sqrt{S}}{\sqrt{\nu}}r_0\right)\right)+\frac{r_0\omega_n^2}{n}\xi_n^{(2)}(S)$$
$$=-\frac{Sr_0}{n(n+1)}(r_0\partial_r U_{rn}^{(2)(*)}(r_0,S)$$
$$+2U_{rn}^{(2)(*)}(r_0,S))+\frac{\nu}{n(n+1)}(r_0^2\partial_{rrr}U_{rn}^{(2)(*)}(r_0,S)$$
$$+6r_0\partial_{rr}U_{rn}^{(2)(*)}(r_0,S)-3(n-1)(n+2)\partial_r U_{rn}^{(2)(*)}(r_0,S))$$
$$-\sum_{k,m\in\Omega}\frac{r_0^2}{m(m+1)}\Im\left[\Gamma_{kmn}U_{rk}^{(1)}(r_0,t)\partial_{rr}U_{rm}^{(1)}(r_0,t)\right.$$
$$\left.+\frac{\alpha_{kmn}}{2k(k+1)}\partial_r U_{rk}^{(1)}(r_0,t)\partial_r U_{rm}^{(1)}(r_0,t)\right]$$
$$-\sum_{k,m\in\Omega}\frac{2}{m(m+1)}\left\{\left(2\Gamma_{kmn}+\frac{\alpha_{kmn}}{k(k+1)}\right)r_0\right. \quad (37)$$
$$\times\Im[U_{rk}^{(1)}(r_0,t)\partial_r U_{rm}^{(1)}(r_0,t)]+\left(\Gamma_{kmn}+\frac{\alpha_{kmn}}{k(k+1)}\right)$$
$$\left.\times\Im[U_{rk}^{(1)}(r_0,t)U_{rm}^{(1)}(r_0,t)]\right\}+\frac{\sigma}{\rho r_0^3}$$
$$\times\sum_{k,m\in\Omega}\left\{2K_{kmn}(k(k+1)-1)+\frac{W}{2}((m(2n-2m-7)\right.$$
$$\left.+k(m+1)+3)K_{kmn}+\alpha_{kmn})\right\}\Im[\xi_k^{(1)}(t)\xi_m^{(1)}(t)]-2\nu$$

$$\times \sum_{k,\,m\in\Omega} \Im\Big[\xi_k^{(1)}(t)\Big(\Big(K_{kmn}-\frac{\alpha_{kmn}}{m(m+1)}\Big)\partial_{rr}U_{rm}^{(1)}(r_0,t) - \frac{1}{r_0}\frac{2\alpha_{kmn}}{m(m+1)}\partial_r U_{rm}^{(1)}(r_0,t)\Big)\Big] - \sum_{k,\,m\in\Omega}\Im\Big[\xi_k^{(1)}(t) \times\Big(\frac{2\nu}{r_0^2}\Big(\frac{2\alpha_{kmn}}{m(m+1)}-\alpha_{kmn}\Big)U_{rm}^{(1)}(r_0,t) - \frac{1}{\rho}K_{kmn}\partial_r p_m^{(1)}(r_0,t)\Big)\Big];\quad n\ge 1.$$

The set of Eqs. (35)–(37) is a set of linear inhomogeneous algebraic equations for $A_n(S)$, $B_n(S)$, and $\xi_n^{(2)}(S)$. Substituting the solution to first-order subproblem (8) into this set, we find, upon tedious calculations, the expression for coefficient $\xi_n^{(2)}(S)$ in the form

$$\xi_n^{(2)}(S) = \sum_{k,\,m\in\Omega}\sum_{l,\,g=1}^{+\infty}\frac{\zeta_{kmn}^{lg}(S,S_k^{(l)},S_m^{(g)})}{(S-S_k^{(l)}-S_m^{(g)})D_n(S)};\quad n\ge 2; \tag{38}$$

where

$$\zeta_{kmn}^{lg}(S,S_k^{(l)},S_m^{(g)}) = \int_0^{r_0}\Big\{\Big((\chi r_0)^2+(n-1)(3n+1) + (n^2-1)\frac{\eta_n(2n-1,\chi)}{\eta_n(1,\chi)}\Big)\frac{2n(n+1)}{(2n+1)r_0\chi^2}\Big(\frac{r_0}{r}\Big)^{n-2} - \Big((\chi r_0)^2+2(n+1)(n(n-3)-1)+\frac{2(n+1)}{\eta_n(1,\chi)} \times\Big(n(2n^2+n-1)+1-n(n+2)\frac{r_0\chi}{2}\frac{j_n(\chi r_0)}{j_{n+1}(\chi r_0)}\Big)\Big) \times\frac{n}{(2n+1)r_0\chi^2}\Big(\frac{r}{r_0}\Big)^{n+3} - n(n+1)\frac{j_n(\chi r_0)}{\eta_n(1,\chi)} \times\Big(2(\chi r_0)^2+4n(n-1)(n+2)-\chi r_0((\chi r_0)^2 + 2(n-1)(2n+1))\frac{j_n(\chi r_0)}{j_{n+1}(\chi r_0)}\Big)\frac{(-1)^n}{\chi r_0^3}r^3 y_n(\chi r) + \frac{n(n+1)}{\eta_n(1,\chi)}(((n+1)(\chi r_0)^2+4n(n-1)(n+2) - \chi r_0((\chi r_0)^2+2(n-1)(2n+1))\frac{j_n(\chi r_0)}{j_{n+1}(\chi r_0)}\Big)y_n(\chi r_0) - (n-1)(\chi r_0)^2\frac{j_n(\chi r_0)}{j_{n+1}(\chi r_0)}y_{n+1}(\chi r_0)\Big)\frac{(-1)^n}{\chi r_0^3}r^3 j_n(\chi r)\Big\}$$

$$\times f_{kmn}^{lg}(r,S_k^{(l)},S_m^{(g)})dr + \Big(\frac{\eta_n(n,\chi)}{\eta_n(1,\chi)}2n(n+1) \times\Big(\frac{\Lambda_{kmn}+(m-2)\Gamma_{kmn}}{m}-(m-2)K_{kmn}\Big) - \frac{(D_n(S)-\omega_n^2)r_0^2}{\nu^2\chi^2}\Big(\frac{\alpha_{kmn}}{m}-(m-1)K_{kmn}\Big)\Big)\frac{\nu}{r_0^4} \times a_{\xi k}(S_k^{(l)})(a_m(S_m^{(g)})r_0+b_m(S_m^{(g)})) + \Big(\frac{4(m-1)\alpha_{kmn}}{m} - ((\chi_m^{(g)}r_0)^2+2(m-2)(m-1))K_{kmn}\Big)\frac{n\nu}{r_0^3}a_{\xi k}(S_k^{(l)}) \times a_m(S_m^{(g)}) + \Big(((\chi_m^{(g)}r_0)^2+2(m^2-1))\frac{2\alpha_{kmn}}{m(m+1)} - 2((\chi_m^{(g)}r_0)^2+(m-2)(m-1))K_{kmn} - \frac{\eta_n(n,\chi)}{\eta_n(1,\chi)} \times\frac{(n+1)(m-2)}{m(m+1)}(\chi_m^{(g)}r_0)^2\Gamma_{kmn}\Big)\frac{n\nu}{r_0^4}a_{\xi k}(S_k^{(l)})b_m(S_m^{(g)}) + \frac{n\sigma}{2r_0^4\rho}((4(k^2+k-1)+(3+k(m+1) + m(2n-2m-7))W)K_{kmn}+W\alpha_{kmn})a_{\xi k}(S_k^{(l)}) \times a_{\xi m}(S_m^{(g)}) + \Big(\frac{\eta_n(n,\chi)}{\eta_n(1,\chi)}\Big(2\Big(\frac{\Lambda_{kmn}}{m(m+1)}-K_{kmn}\Big) - ((\chi_m^{(g)}r_0)^2+4)\frac{\Gamma_{kmn}}{m(m+1)}\Big)n(n+1) - \frac{(D_n(S)-\omega_n^2)r_0^2}{\nu^2\chi^2}\Big(\frac{\alpha_{kmn}}{m(m+1)}-K_{kmn}\Big) + 4n\Big(2K_{kmn}-\frac{\alpha_{kmn}}{m(m+1)}\Big)\Big)a_{\xi k}(S_k^{(l)})b_m(S_m^{(g)})\frac{\nu\chi_m^{(g)}}{r_0^3} \times\frac{j_{m+1}(\chi_m^{(g)}r_0)}{j_m(\chi_m^{(g)}r_0)} - \Big(K_{kmn}+\frac{\alpha_{kmn}}{km}\Big)\frac{n}{2r_0}a_k(S_k^{(l)})a_m(S_m^{(g)}) - \Big(K_{kmn}+\frac{\Gamma_{kmn}}{m(m+1)}(\chi_m^{(g)}r_0)^2+\frac{\alpha_{kmn}}{km}\Big)\frac{n}{r_0^2}a_k(S_k^{(l)}) \times b_m(S_m^{(g)}) - \Big(\frac{1}{2}\Big(K_{kmn}+\frac{\alpha_{kmn}}{km}\Big)+\frac{\Gamma_{kmn}}{m(m+1)}(\chi_m^{(g)}r_0)^2\Big) \times\frac{n}{r_0^3}b_k(S_k^{(l)})b_m(S_m^{(g)}) - \frac{n}{r_0^2}\frac{\alpha_{kmn}\chi_m^{(g)}}{km(k+1)}b_m(S_m^{(g)})\Big(r_0a_k(S_k^{(l)})$$

$$+ b_k(S_k^{(l)})\left(1 + \frac{r_0\chi_k^{(l)}}{2(k+1)}\frac{j_{k+1}(\chi_k^{(l)}r_0)}{j_k(\chi_k^{(l)}r_0)}\right)\frac{j_{m+1}(\chi_m^{(g)}r_0)}{j_m(\chi_m^{(g)}r_0)},$$

$$f_{kmn}^{lg}(r, S_k^{(l)}, S_m^{(g)}) = \frac{\Gamma_{kmn}}{m(m+1)}(\chi_m^{(g)})^3 a_k(S_k^{(l)})b_m(S_m^{(g)})$$

$$\times\frac{r^{k-2}}{r_0^{k-1}}\frac{j_{m+1}(\chi_m^{(g)}r)}{j_m(\chi_m^{(g)}r_0)} + \frac{(m+k)k\Gamma_{kmn} + \alpha_{kmn}}{km(m+1)}(\chi_m^{(g)})^2$$

$$\times b_m(S_m^{(g)})\left(a_k(S_k^{(l)})\frac{r^{k-3}}{r_0^{k-1}} + b_k(S_k^{(l)})\frac{1}{r^3}\frac{j_k(\chi_k^{(l)}r)}{j_k(\chi_k^{(l)}r_0)}\right)$$

$$\times\frac{j_m(\chi_m^{(g)}r)}{j_m(\chi_m^{(g)}r_0)} + \left(\frac{\Gamma_{kmn}(\chi_m^{(g)})^2}{m(m+1)} + \frac{m(m+1)\Gamma_{mkn} + \alpha_{kmn}}{k(k+1)m(m+1)}\right.$$

$$\left.\times(\chi_k^{(l)})^2\right)\chi_m^{(g)}b_k(S_k^{(l)})b_m(S_m^{(g)})\frac{1}{r^2}\frac{j_k(\chi_k^{(l)}r)}{j_k(\chi_k^{(l)}r_0)}\frac{j_{m+1}(\chi_m^{(g)}r)}{j_m(\chi_m^{(g)}r_0)}.$$

It is seen that expression (28) has singular point $S = 0$ and an infinite countable set of singular points that are defined from the conditions $D_n(S) = 0$ and $S - S_k^{(l)} - S_m^{(g)} = 0$ and are simple poles. In addition, expression (38) tends to zero at $S \longrightarrow \infty$. This allows one to apply the Jordan lemma to the inverse Laplace transformation for the left half-plane and the residue theorem. Eventually, the inversion formula takes the form

$$f(t) = \frac{1}{2\pi i}\int_{\gamma - i\infty}^{\gamma + i\infty} F(S)\exp(St)dS = \sum_{j=1}^{+\infty}\operatorname{res}(F(S_n^{(j)})\exp(S_n^{(j)}t)), \quad (39)$$

where summation is over the roots of the equations $D_n(S) = 0$ and $S - S_k^{(l)} - S_m^{(g)} = 0$.

Employing formula (39) to calculate coefficient $\xi_n^{(2)}(S)$ gives

$$\xi_n^{(2)}(t) = \sum_{k,m\in\Omega}\sum_{l,g,j=1}^{+\infty}\frac{\zeta_{kmn}^{lg}(S_n^{(j)}, S_k^{(l)}, S_m^{(g)})}{(S_n^{(l)} - S_k^{(l)} - S_m^{(g)})\partial_{S_n^{(j)}}D_n(S_n^{(j)})}$$

$$\times\exp(S_n^{(j)}t) + \sum_{k,m\in\Omega}\sum_{l,g=1}^{+\infty}\frac{\zeta_{kmn}^{lg}(S_k^{(l)} + S_m^{(g)}, S_k^{(l)}, S_m^{(g)})}{D_n(S_k^{(l)} + S_m^{(g)})} \quad (40)$$

$$\times\exp((S_k^{(l)} + S_m^{(g)})t); \quad n \geq 2,$$

where $S_n^{(j)}$ is a root of dispersion relation $D_n(S_n^{(j)}) = 0$.

Substitution of expressions (40) and (24) into (10) yields coefficient $\xi^{(2)}(\vartheta, t)$ in explicit form. Next, substituting the expression for $\xi^{(2)}(\vartheta, t)$ thus found, as well as the expression for coefficient $\xi^{(1)}(\vartheta, t)$ (which is defined by expression (8)), into (4), we readily find the explicit form of function $\xi(\vartheta, t)$ and, thereby, of the generatrix of a nonlinearly vibrating axisymmetric drop of a viscous incompressible conducting liquid as a function of time and polar angle,

$$r(\vartheta, t) = r_0 + \varepsilon\sum_{n\in\Omega}\sum_{j=1}^{+\infty}a_{\xi n}(S_n^{(j)})\exp(S_n^{(j)}t)P_n(\mu)$$

$$-\frac{\varepsilon^2}{r_0}\sum_{m\in\Omega}\sum_{l,g=1}^{+\infty}\frac{a_{\xi m}(S_m^{(l)})a_{\xi m}(S_m^{(g)})}{2m+1}\exp((S_m^{(l)} + S_m^{(g)})t)$$

$$\times P_0(\mu) - \frac{9\varepsilon^2}{r_0}\sum_{m\in\Omega}\sum_{l,g=1}^{+\infty}\frac{(m+1)a_{\xi m}(S_m^{(l)})a_{\xi m+1}(S_{m+1}^{(g)})}{(2m+1)(2m+3)} \quad (41)$$

$$\times\exp((S_m^{(l)} + S_{m+1}^{(g)})t)P_1(\mu) + \varepsilon^2\sum_{n=2}^{+\infty}\sum_{k,m\in\Omega}$$

$$\times\left\{\sum_{l,g,j=1}^{+\infty}\frac{\zeta_{kmn}^{lg}(S_n^{(j)}, S_k^{(l)}, S_m^{(g)})}{(S_n^{(j)} - S_k^{(l)} - S_m^{(g)})\partial_{S_n^{(j)}}D_n(S_n^{(j)})}\exp(S_n^{(j)}t)\right.$$

$$\left.+\sum_{l,g=1}^{+\infty}\frac{\zeta_{kmn}^{lg}(S_k^{(l)} + S_m^{(g)}, S_k^{(l)}, S_m^{(g)})}{D_n(S_k^{(l)} + S_m^{(g)})}\exp((S_k^{(l)} + S_m^{(g)})t)\right\}P_n(\mu).$$

Passing to the ideal-liquid limit in expression (41) (using the asymptotic representation of the modified spherical functions at large values of the argument at $\nu \longrightarrow 0$), we easily arrive at the expression for the generatrix of a nonlinearly vibrating charged drop of an ideal liquid that was found in [9].

(4) Consider the case of a high-viscosity liquid, when $(\nu\rho^{1/2}/(r_0\sigma)^{1/2}) \geq 1$ (this inequality is met, e.g., for a water drop with a characteristic linear size of less than 0.1 μm [10]). In this case, one may leave only the first several terms in the asymptotic representation of the modified spherical Bessel functions of the first and second kind at small values of the argument [8],

$$j_n(\chi) = \frac{\chi^n}{(2n+1)!!}\left(1 + \frac{\chi^2/2}{1!(2n+3)}\right.$$

$$\left.+\frac{(\chi^2/2)^2}{2!(2n+3)(2n+5)} + \ldots\right); \quad \chi \longrightarrow 0;$$

$$y_n(\chi) = \frac{(2n-1)!!}{(-1)^n\chi^{n+1}}\left(1 + \frac{\chi^2/2}{1!(1-2n)}\right. \quad (42)$$

$$\left.+\frac{(\chi^2/2)^2}{2!(1-2n)(3-2n)} + \ldots\right); \quad \chi \longrightarrow 0.$$

Eventually, we obtain

$$a_{\xi n}(S_n^{(j)}) \cong h_n - \frac{3(2n(2n(n+2)+3)+3)}{2(n-1)(2n+1)(2n+5)(2n(n+2)+3)}\frac{r_0^2 h_n S_n^{(j)}}{\nu};$$

$$a_{\xi n}(S_n^{(j)}) \cong -\frac{(n+1)(2n+3)}{(2n(n+2)+3)}\frac{h_n\omega_n^2}{S_n^{(j)}} + \frac{(4n+3)(2n(n+2)(4n^2+6n+5)+9)}{2(n-1)(2n+1)(2n+5)(2n(n+2)+3)^2}\frac{r_0^2 h_n\omega_n^2}{\nu};$$

$$b_n(S_n^{(j)}) \cong \frac{(n+1)(2n+3)}{(2n(n+2)+3)}\frac{r_0 h_n\omega_n^2}{S_n^{(j)}} - \frac{(n+1)(2n(4n(n(3n+11)+14)+35)+21)}{(n-1)(2n+1)(2n+5)(2n(n+2)+3)^2}\frac{r_0^3 h_n\omega_n^2}{\nu}; \quad (43)$$

$$D_n(S_n^{(j)}) \cong \frac{3(2n(2n(n+2)+3)+3)}{(2n+1)^2(2n+5)} \times\left((S_n^{(j)})^2 + 2S_n^{(j)}\frac{\tau_n\nu}{r_0^2} + \tau_n^2\beta_n\omega_n^2\right);$$

$$\tau_n = \frac{(2n+1)(2n+5)(n-1)(2n^2+4n+3)}{3(4n^3+8n^2+6n+3)};$$

$$\beta_n = \frac{3(4n^3+8n^2+6n+3)}{(2n+5)(n-1)^2(2n^2+4n+3)^2}.$$

Now, dispersion relation $D_n(S_n^{(j)}) = 0$ has only two roots [4],

$$S_n^{(1)} = -\tau_n\frac{\nu}{r_0^2} + \tau_n\frac{\nu}{r_0^2}\sqrt{1-\beta_n\frac{r_0^4\omega_n^2}{\nu^2}};$$
$$S_n^{(2)} = -\tau_n\frac{\nu}{r_0^2} - \tau_n\frac{\nu}{r_0^2}\sqrt{1-\beta_n\frac{r_0^4\omega_n^2}{\nu^2}}. \quad (44)$$

If the liquid viscosity is so large that inequality $\nu^2 \gg \beta_n r_0^4\omega_n^2$ holds, then the roots of (44) can be written in the form [4]

$$S_n^{(1)} \cong -\tau_n\beta_n\frac{r_0^2\omega_n^2}{2\nu}; \quad S_n^{(2)} \cong -2\tau_n\frac{\nu}{r_0^2}. \quad (45)$$

It is not difficult to check that $|S_n^{(1)}| \ll |S_n^{(2)}|$; therefore, in expression (40), the terms involving the second root $S_n^{(2)}$ rapidly decay with time. The time evolution of an initially deformed drop is governed by the terms involving the first root $S_n^{(1)}$. Then, with regard to the above expansions for coefficients $a_{\xi n}(S_n^{(j)})$, $a_n(S_n^{(j)})$, and $b_n(S_n^{(j)})$, one readily obtains from (40)

$$\xi_n^{(2)}(t) = \sum_{k,m\in\Omega}\left\{\exp\left(-(\tau_k\beta_k\omega_k^2 + \tau_m\beta_m\omega_m^2)\frac{r_0^2}{2\nu}t\right) - \exp\left(-\tau_n\beta_n\omega_n^2\frac{r_0^2}{2\nu}t\right)\right\}\frac{2n+1}{(n-1)(2n(n+2)+3)} \times\frac{h_k h_m}{\tau_n\beta_n\omega_n^2 - \tau_k\beta_k\omega_k^2 - \tau_m\beta_m\omega_m^2} \times\left\{\frac{n\sigma}{\rho r_0^4}K_{kmn}\left(2(k(k+1)-1) + (3+k(m+1) - m(7+2m-2n))\frac{W}{2}\right) + \frac{W}{2}\frac{n\sigma}{\rho r_0^4}\alpha_{kmn} - \left(K_{kmn} + \frac{\alpha_{kmn}}{km}\right)\frac{n\omega_k^2}{2r_0}\frac{(2k+1)(m-1)(m+1)(2m+3)}{(k-1)(2k(k+2)+3)(2m+1)} - \frac{1}{2kmr_0}\left(km(6(2k+1)(m-1) + (20m - k(k(2k+3)(2m+1) - 2(16m+5)) + 7)n + 2(7m + k(6(m+3) - k(2k+3)(2m+1)) + 11)n^2 - 4(2k+1)(m-1)n^3\right)K_{kmn} + \left(3(2m+1)n(2n+1) - 2k^3(2m+1)n(2n+1) + 2k(2n(m+2+2(m-1)n - 3n^2) + 9) - 3k^2(n(2n(2m+4n+5)+2m-3) - 12)\right)\alpha_{kmn} + 6k(2k+1)n \times\frac{(n+1)(m(m(2m-1)-4)\Gamma_{kmn} + 3\Lambda_{kmn})\omega_m^2}{((2k+1)(m-1)(2m(m+2)+3)(2n+1))}\right\}; \quad n \geq 2. \quad (46)$$

In the adopted approximation, expressions (24) with regard to (8) can be written in the form

$$\xi_0^{(2)}(t) = -\frac{1}{r_0}\sum_{m\in\Omega}\frac{h_m}{2m+1}\exp\left(-\tau_m\beta_m\frac{r_0^2\omega_m^2}{\nu}t\right);$$

$$\xi_1^{(2)}(t) = -\frac{9}{r_0}\sum_{m\in\Omega}\frac{(m+1)h_m h_{m+1}}{(2m+1)(2m+3)}\exp\left(-\tau_m\beta_m\frac{r_0^2\omega_m^2}{2\nu}t\right)$$

Minimal number of the roots of the dispersion relation that should be taken into account to provide a satisfactory convergence of the series expressing nonlinear correction $\xi_n^{(2)}(t)$ to the profile of the drop at $k = m = 2$ and different dimensionless viscosity ν, Rayleigh parameter W, and number n of a nonlinearly excited mode.

ν	$n = 2$				$n = 4$			
	$W = 0$	$W = 2$	$W = 3$	$W = 3.5$	$W = 0$	$W = 2$	$W = 3$	$W = 3.5$
0.02	16	12	9	6	48	28	22	18
0.03	10	8	7	5	30	18	12	10
0.05	8	6	5	4	16	10	8	6
0.07	6	5	4	3	12	8	6	4
0.1	4	4	3	3	10	6	4	4
0.2	3	3	3	3	6	4	3	3
0.5	3	3	3	2	4	3	2	2
1.5	2	2	2	2	3	2	2	2
2.0	2	1	1	1	3	2	1	1

$$\times \exp\left(-\tau_{m+1}\beta_{m+1}\frac{r_0^2\omega_{m+1}^2}{2\nu}t\right).$$

Interestingly, the accuracy of asymptotic expression (46) depends on parameter W: as W approaches the critical Rayleigh value, the accuracy of (46) rises. This is because (46) is valid only if $\nu^2 \gg \beta_n r_0^4 \omega_n^2$ (see (44)), and when W approaches a critical value, ω_n^2 decreases rapidly. It then becomes appropriate to use relation (46) in studying mechanisms making the drop unstable against its self-charge when W differs little from a critical value. This is especially true if one takes into account that relation (46), like expressions (40) and (41), is also valid at supercritical values of the self-charge ($W > 4$).

(5) Numerical simulations with the use of (40) in the dimensionless variables such that $\rho = \sigma = r_0 = 1$ demonstrate the different convergence of the sums over the roots of the dispersion relation at various values of liquid viscosity ν, Rayleigh parameter W, and number n of the mode excited in the second order of smallness. In particular, at a low liquid viscosity, the roots of dispersion relation $D_n(S) = 0$ are closely spaced; therefore, summation should be over a large set of the roots (see the table). If the liquid viscosity is high, one may take two or even one root of the dispersion relation (see Sect. 4). It also follows from the table that an increase in Rayleigh parameter W improves the convergence of series (40).

Comparison of coefficients $\xi_n^{(2)}(t)$ for a low-viscosity liquid, when the dimensionless viscosity is low, $(\nu\rho^{1/2}/(r_0\sigma)^{1/2}) \le 0.01$ (such a condition is met, e.g., for a water drop with $r_0 \ge 100$ μm), and for an ideal liquid [9] shows that, in the former case, coefficient $\xi_n^{(2)}(t)$ may be noticeably higher (Fig. 1). This means that nonlinear mode interaction is enhanced in a low-viscosity liquid. It seems that, in a low-viscosity liquid, energy transfer from a mode governing the initial deformation to that nonlinearly interacting with the former proceeds not instantly (at the zero time) but takes some finite time, unlike in an ideal liquid. The amplitudes of nonlinearly exciting modes first grow (within several vibration periods) and only then exponentially decay because of viscous energy dissipation (Fig. 1a). In low-viscosity liquids, the damping of vibrations occurs in an oscillatory manner (Figs. 1a and 1b); in high-viscosity liquids, this process is aperiodic (Fig. 2). "Long-term" (over several vibration periods) energy transfer from an initially exited mode to a mode nonlinearly interacting with the former is typical of only low-viscosity liquids: even in moderate-viscosity liquids (Fig. 1b) and *a fortiori* in high-viscosity ones (Fig. 2), energy transfer occurs instantly, as in an ideal liquid.

The characteristic spindle-shaped form of the envelope of the oscillating curve in Fig. 1a is explained by the following factors: (i) the energy is transferred from the mode governing the initial deformation to that nonlinearly excited in the second order of smallness; (ii) the amplitude of the initial deformation exponentially decreases with time because of viscous dissipation, and, consequently, the energy transferred to the mode excited by nonlinear interaction alone also decreases; and (iii) the amplitude of the mode nonlinearly excited in the second order of smallness decays too. The sum of the first- and second-order amplitudes will exponentially decrease with time, as is seen in Fig. 3. Yet, the fact that the nonlinearly excited modes gradually build up allows one to imagine real physical mechanisms underlying nonlinear interactions between modes of a vibrating drop with a nonzero viscosity.

For a viscous drop with $W < 4$, when the fundamental mode and, hence, the drop are stable against the self-charge, expressions (40), (41), and (46) specify a law of recovery of the drop equilibrium shape (Fig. 4a). From

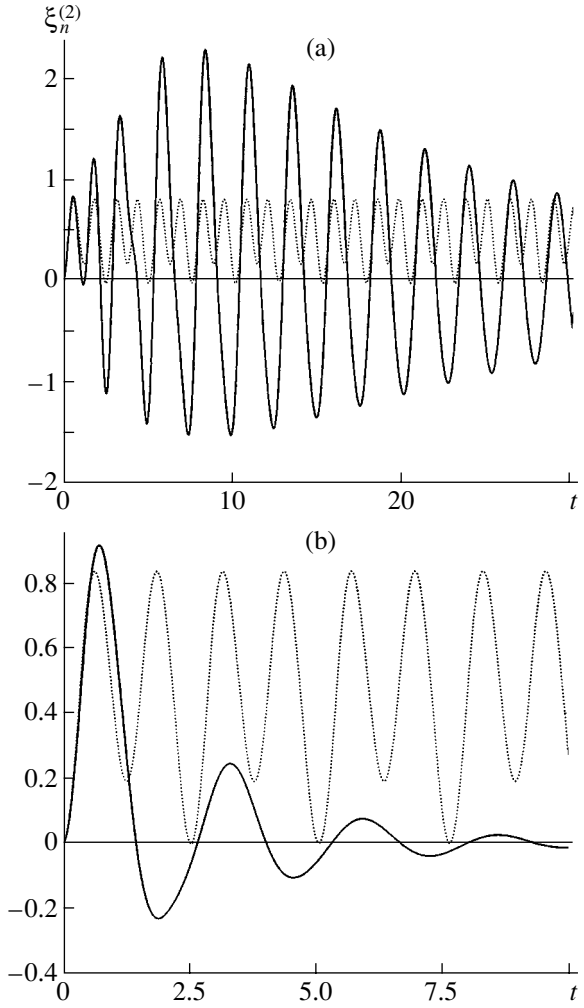

Fig. 1. Dimensionless coefficient $\xi_n^{(2)}$ for the fundamental mode vs. dimensionless time t for the single-mode initial deformation at $k = m = 2$, $n = 2$, $W = 1$, and ν = (a) 0.01 and (b) 0.1. The solid lines are plotted using expression (40); dotted lines, using the expression valid for an ideal liquid.

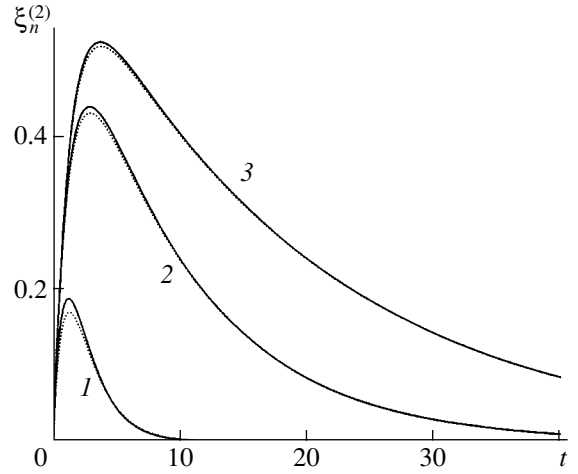

Fig. 2. Dimensionless coefficient $\xi_n^{(2)}$ vs. dimensionless time t for $k = m = 2$, $n = 4$, $h_2 = 1$, $\nu = 1$, and W: (*1*) 3, (*2*) 3.8, and (*3*) 3.9. The solid lines are plotted using expression (40); dotted lines, using asymptotic expression (46).

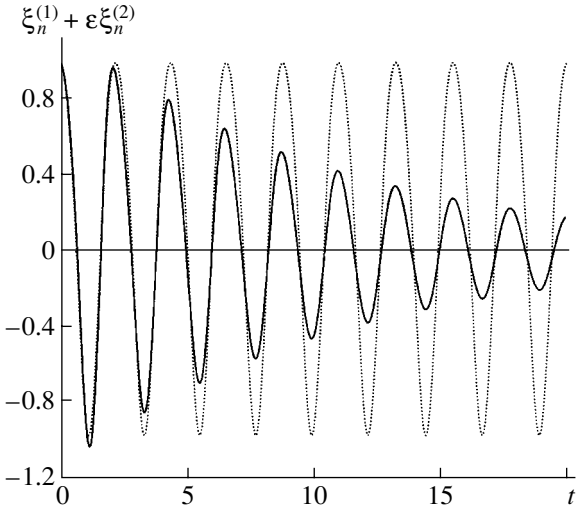

Fig. 3. Linear superposition $\xi_n^{(1)} + \varepsilon\xi_n^{(2)}$ of the first- and second-order solutions for the dimensionless amplitude of the fundamental mode vs. dimensionless time t at $k = m = 2$, $n = 2$, $W = 1$, $\nu = 0.02$, and $\varepsilon = 0.3$. The curves mean the same as in Fig. 1.

(40), (41), and (46), it follows that the amplitudes of modes specifying the initial deformation, as well as the amplitudes of nonlinearly excited modes, exponentially decrease with time, the indices of the exponentials growing with increasing mode number.

At $4 < W < 5$, when the fundamental mode ($n = 2$) loses stability and higher modes do not, the time evolution of the shape becomes more complicated. The indices involving the fundamental mode frequency squared change sign (because, at $4 < W < 5$, so does squared frequency ω_2^2), and the corresponding term starts exponentially increasing with time, whereas the rest of the components in expressions (40), (41), and (46) continue decreasing (Fig. 4b). After a lapse of time, the initial deformation disappears and the shape of the drop is specified by the fundamental mode growing with time; that is, the drop evolves toward a prolate spheroid. Such a process (extension of a charged drop of a conducting liquid as a result of fundamental mode amplitude buildup) can be terminated for two reasons. One is field emission of charges when the self-charge field at the vertices of the drop, which grows with radius of curvature at the vertices, becomes sufficiently high (as was described earlier [10]). The other reason is disintegration of the drop into two parts comparable in size [11]. The fundamental mode becomes unstable irrespective of whether it enters into the spectrum of modes specifying the initial deformation, because this mode is

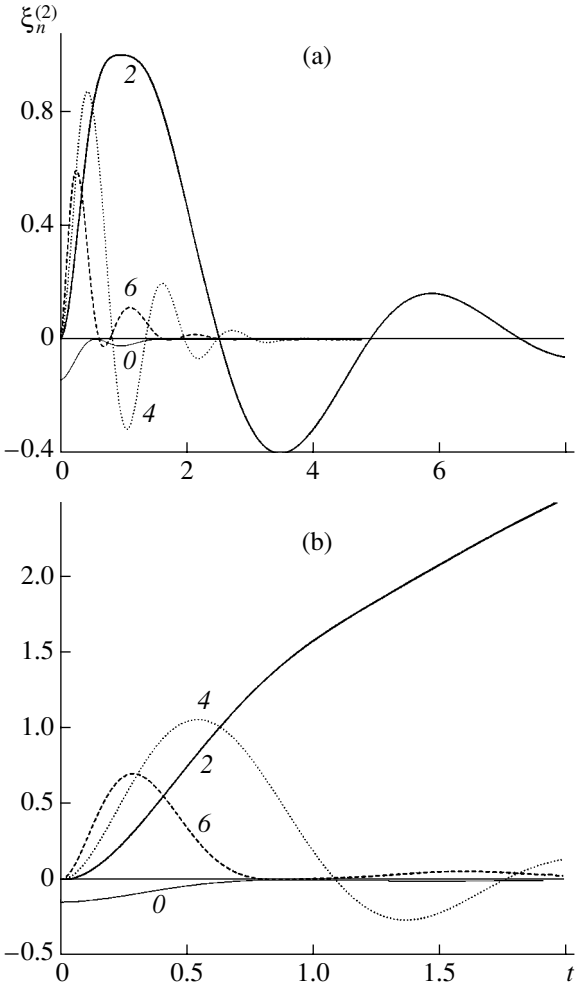

Fig. 4. Dimensionless coefficient $\xi_n^{(2)}$ on dimensionless time t at $k = m = 3$, $h_3 = 1$, $\nu = 0.1$, and various n. The figures by the curves coincide with numbers n of excited modes. W = (a) 3 and (b) 4.01.

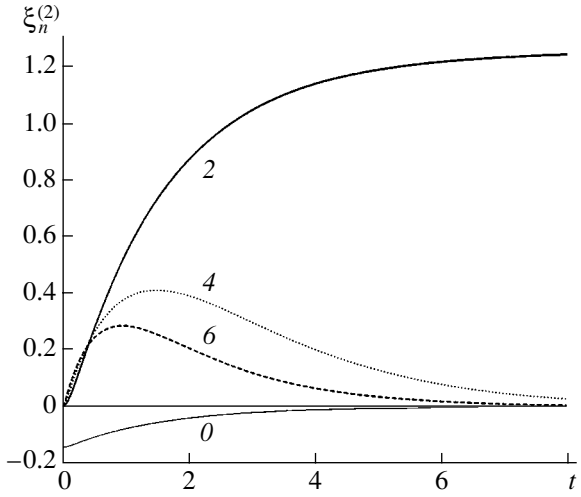

Fig. 5. The same dependences as in Fig. 4b for $\nu = 1$.

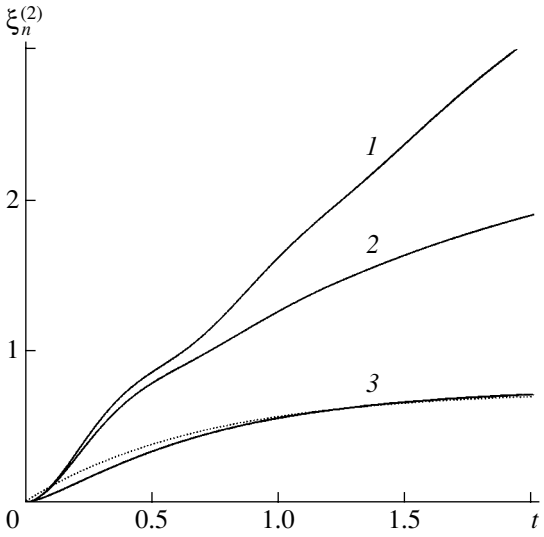

Fig. 6. Dimensionless coefficient $\xi_n^{(2)}$ for the fundamental mode vs. dimensionless time t at $k = m = 4$, $n = 2$, $W = 4.01$, and viscosity ν = (*1*) 0.05, (*2*) 0.1, and (*3*) 1. The solid lines are plotted using expression (40); dotted line, using expression (46) for $\nu = 1$.

excited in the second order of smallness at any form of the initial deformation through nonlinear interaction [3, 12, 13].

In a high-viscosity liquid drop, when the dimensionless viscosity is large ($\nu\rho^{1/2}/(r_0\sigma)^{1/2}) \geq 1$), the damping of nonlinearly excited modes that are stable against the self-charge is an aperiodic process (Figs. 2 and 5). Then, if the fundamental mode of a high-viscosity drop is unstable and the rest of the excited modes are stable against the charge of the drop (Fig. 5), the amplitude of the fundamental mode will grow with time and the drop will extend, taking the shape of a spheroid. However, unlike a drop of an ideal liquid, a high-viscosity drop will extend rather slowly and the rate of its deformation will decrease, rather than increase, with increasing eccentricity [14] (see Fig. 5 and 6). In this case, as follows from detailed analysis, the rate of growth of the unstable fundamental mode, which initially depends on supercriticality ΔW of the Rayleigh parameter for the fundamental mode, first decreases for some ΔW-dependent time to a very small value, remains constant for the time inversely proportional to ΔW, and then starts rising following a near-exponential law with the rate of rise inversely proportional to the liquid viscosity. At a small supercriticality of the Rayleigh parameter ($\Delta W \sim 0.001$), the evolution curve for the unstable fundamental mode exhibits a plateau (Figs. 5 and 6), where the fundamental mode amplitude varies insignificantly. Physically, this means that an unstable high-viscosity drop with ΔW and ν mentioned above rapidly (for a time interval close to oscillation period T_2 of the fundamental mode

of an uncharged drop) acquires a spheroidal deformation $\sim\varepsilon$, remains so for a time interval $\approx 10T_2$, and only then continues to elongate with an increasing rate. Recall that the time dependence of the spheroidal deformation amplitude for an unstable drop of an ideal liquid is supraexponential [14]. With low viscosity taken into account [15], the unstable drop evolution pattern changes only quantitatively.

If parameter W lies in the range $5 < W < 6$, the third mode ($n = 3$) also becomes unstable. However, whether the instability of the third mode will contribute to spheroidal deformation depends on whether this mode is in the spectrum of modes specifying the initial deformation or in the spectrum of modes excited by nonlinear interaction. According to (46), if the third mode is absent in both spectra, it will not influence the drop's shape (provided that thermal vibrations of a vanishingly small amplitude, which are always present in the drop due to the thermal motion of molecules, are disregarded).

CONCLUSIONS

Nonlinear vibrations of viscous drops can be studied analytically using classical asymptotic methods. In the limit of large viscosity, the resulting analytical expressions are fairly compact. The time evolution of nonlinearly excited modes shows that, in a low-viscosity liquid, the energy transfer from a mode specifying the initial deformation to a nonlinearly excited mode occurs not instantly but takes several vibration periods, unlike in an ideal or high-viscosity liquid. Such a mechanism of energy transfer to a nonlinearly excited mode provides it with more energy and was unknown previously. When a high-viscosity drop bearing a charge slightly exceeding the critical value for the fundamental mode becomes unstable ($(\nu\rho^{1/2}/(r_0\sigma)^{1/2}) \geq 1$), the growth of the spheroidal deformation amplitude differs appreciably from that predicted earlier for an ideal or low-viscosity liquid.

ACKNOWLEDGMENTS

This work was supported by a grant of the President of the Russian Federation (grant no. MK-2946-2004-1) and the Russian Foundation for Basic Research (grant no. 03-01-00760).

REFERENCES

1. J. A. Tsamopolous and R. A. Brown, J. Fluid Mech. **147**, 373 (1984).
2. Z. C. Feng, J. Fluid Mech. **333**, 1 (1997).
3. A. N. Zharov, S. O. Shiryaeva, and A. I. Grigor'ev, Zh. Tekh. Fiz. **73** (12), 9 (2003) [Tech. Phys. **48**, 1511 (2003)].
4. A. N. Zharov and A. I. Grigor'ev, Zh. Tekh. Fiz. **75** (1), 22 (2005) [Tech. Phys. **50**, 19 (2005)].
5. O. A. Basaran, J. Fluid Mech. **241**, 169 (1992).
6. E. Becker, W. J. Hiller, and T. A. Kowalewski, J. Fluid Mech. **258**, 191 (1994).
7. S. Chandrasekhar, Proc. London Math. Soc. **3**, 141 (1959).
8. M. Abramovitz and I. A. Stegun, *Handbook of Mathematical Functions* (Dover, New York, 1971; Nauka, Moscow, 1979).
9. S. O. Shiryaeva, Izv. Ross. Akad. Nauk, Mekh. Zhidk. Gaza, No. 3, 173 (2001).
10. A. I. Grigor'ev, Zh. Tekh. Fiz. **71** (10), 1 (2001) [Tech. Phys. **46**, 1205 (2001)].
11. D. F. Belonozhko, S. O. Shiryaeva, and A. I. Grigor'ev, Pis'ma Zh. Tekh. Fiz. **26** (19), 16 (2000) [Tech. Phys. Lett. **26**, 940 (2000)].
12. S. O. Shiryaeva, Zh. Tekh. Fiz. **71** (2), 27 (2001) [Tech. Phys. **46**, 158 (2001)].
13. V. A. Koromyslov, A. I. Grigor'ev, and S. O. Shiryaeva, Zh. Tekh. Fiz. **74** (9), 23 (2004) [Tech. Phys. **49**, 1126 (2004)].
14. S. O. Shiryaeva and A. I. Grigor'ev, Zh. Tekh. Fiz. **65** (9), 39 (1995) [Tech. Phys. **40**, 889 (1995)]
15. S. O. Shiryaeva, Pis'ma Zh. Tekh. Fiz. **26** (4), 5 (2000) [Tech. Phys. Lett. **26**, 137 (2000)].

Translated by N. Mende

Technical Physics, Vol. 50, No. 12, 2005, pp. 1583–1591. Translated from Zhurnal Tekhnicheskoĭ Fiziki, Vol. 75, No. 12, 2005, pp. 47–55.

GASES AND LIQUIDS

Nonlinear Secondary Raman Resonances of Oscillations of the Fundamental Mode of a Charged Drop Moving in an Environment

A. I. Grigor'ev

Demidov State University, Sovetskaya ul. 14, Yaroslavl, 150000 Russia
e-mail: grig@uniyar.ac.ru

Received March 29, 2005

Abstract—Second-order calculations show that, when a gas flows about a charged drop, the fundamental mode of the multimode initial deformation of its equilibrium shape builds up through nonlinear secondary Raman resonant interaction with higher modes if this mode is present in the mode spectrum specifying the initial deformation. This circumstance accounts for large-amplitude spheroidal oscillations of drops in natural liquid-drop systems and provides an insight into corona initiation in the vicinity of drops in thunderstorm clouds and into lightning initiation. © *2005 Pleiades Publishing, Inc.*

(1) Charged drops moving in an environment are the object of much investigation, since they are frequently encountered in various fields of technology (see, e.g., the reviews [1–3] and Refs. cited therein). For example, cumuli causing thunderstorms consist of numerous charged water drops, which are suspended in air owing to ascending flows counterbalancing the weight of the drops. Studying the electrohydrodynamic stability of their charged surface is also expected to shed light on the physical mechanism of lightning initiation [4, 5]. According to the present-day concepts, streak lightning arises from a corona discharge initiated by an intracloud electric field near a coarse drop or water-covered hail freely falling in a thunderstorm cloud (see, e.g., [6, 7], where critical conditions for corona initiation near the top of a drop nonlinearly vibrating in a cloud are analyzed). However, the maximal self-charge of drops and maximal electric fields measured in thunderstorm clouds [8] are much lower than those causing instability of the surface of the drops against the self-charge or induced charges [9, 10]. The measured values of these parameters may initiate a corona discharge near the top of the drop only if the spheroidal vibration amplitude is very high [6–8].

To date, not much has been known about the physical mechanism of lightning initiation near a drop in clouds (in spite of much effort made in this field). It seems that, when studying the instability of the drop moving in an environment against its self-charge, researchers overlook some important factor. This may be interaction of the drop with a flowing medium. For real velocities of drops, the flow around the drop can be simulated by an incompressible liquid. The real liquid model assumes that the velocity field at the interface experiences a tangential discontinuity, which results in the vibrational instability of the interface (Kelvin–Helmholtz instability for the planar interface between immiscible incompressible liquids [11, 12]). Kelvin–Helmholtz instability radically changes the physics of interface instability; specifically, it loosens the critical conditions for instability of the drop against the self-charge [9, 10]. In this work, we study the nonlinear resonance redistribution of the initial deformation energy among the modes of a nonlinearly vibrating drop placed in a laminar flow and analyze critical conditions for interface instability in such a system.

The nonlinear vibrations of a charged drop in a flowing environment were studied previously [13]. However, the resulting expressions, being very awkward, were analyzed only numerically and the point of resonant energy exchange between the modes has not been touched upon. Degenerate nonlinear resonances in the system studied were considered in [14], where it was found that such resonances transfer the energy only from lower to higher modes. Reverse energy transfer is typical of multimode Raman resonances [15, 16]. However, for a charged drop placed in an ideal insulating incompressible medium, the lowest mode that could be excited in three-mode secondary Raman resonances is the third mode [17, 18]. The resonant buildup of the fundamental mode, which is of particular importance in elaborating a mechanism of lightning initiation [4–6], was found only in nonlinear four-mode Raman resonances [16]. However, the fundamental mode discovered only as a third-order effect in terms of initial deformation amplitude [16] turned out to be very weak and so could not explain real observations [19, 20], where the spheroidal vibration amplitude of drops falling in the atmosphere exceeded half the drop's radius.

(2) Let an ideal incompressible insulating medium of density ρ_2 and permittivity ε_* occupying an infinitely

1063-7842/05/5012-1583$26.00

large volume flow with constant velocity $\mathbf{U}_0$ about an immobile drop of an ideal incompressible perfectly conducting liquid of density ρ_1. The radius of the drop is R; the surface tension coefficient at the interface, σ; and the total charge of the drop, Q. We assume that, at the zero time $t = 0$, the equilibrium (spherical) shape of the drop experiences virtual axisymmetric deformation of finite amplitude that is, however, much smaller than the radius of the drop. At the zero time, the flow velocity field in the drop is taken to be identically zero. We are interested in nonlinear oscillations of the drop at $t > 0$.

To simplify the mathematics, we introduce dimensionless variables such that $R = \sigma = \rho_1 = 1$. Then, in the spherical coordinate system with the origin at the center of mass of the drop, the equation for the interface disturbed by the axisymmetric capillary wave motion has the form $r = 1 + \xi(\theta, t)$, $|\xi| \ll 1$. The liquid flow in the drop and environment is assumed to be potential; that is, the flow velocity fields in the drop and environment are given by $\mathbf{V} = \nabla\psi(\mathbf{r}, t)$ and $\mathbf{U} = \nabla\varphi(\mathbf{r}, t)$, respectively.

Mathematically, the problem of nonlinear oscillations of the interface in this system is described by the Laplace equations for velocity potentials $\psi(\mathbf{r}, t)$ and $\varphi(\mathbf{r}, t)$ and for electrostatic potential $\Phi(\mathbf{r}, t)$ [6, 7, 13–16],

$$\Delta\Phi(\mathbf{r}, t) = 0; \quad \Delta\psi(\mathbf{r}, t) = 0; \quad \Delta\varphi(\mathbf{r}, t) = 0,$$

subject to the boundary conditions

$$r \longrightarrow 0: \psi(\mathbf{r}, t) \longrightarrow 0;$$

$$r \longrightarrow \infty: \Phi(\mathbf{r}, t) \longrightarrow 0: \nabla\varphi(\mathbf{r}, t) \longrightarrow \mathbf{U}_0;$$

$$r = 1 + \xi: \frac{\partial\xi}{\partial t} = \frac{\partial\psi}{\partial r} - \frac{1}{r^2}\frac{\partial\psi}{\partial\theta}\frac{\partial\xi}{\partial\theta};$$

$$\frac{\partial\psi}{\partial r} - \frac{1}{r^2}\frac{\partial\psi}{\partial\theta}\frac{\partial\xi}{\partial\theta} = \frac{\partial\varphi}{\partial r} - \frac{1}{r^2}\frac{\partial\varphi}{\partial\theta}\frac{\partial\xi}{\partial\theta};$$

$$-\frac{\partial\psi}{\partial t} - \frac{1}{2}(\nabla\psi)^2 + P_{\text{in}} + P_E - P_\sigma = -\rho\frac{\partial\varphi}{\partial t} - \frac{\rho}{2}(\nabla\varphi)^2 + P_{\text{ex}}; \quad (1)$$

$$P_E = \frac{\varepsilon_*(\nabla\Phi)^2}{8\pi}; \quad P_\sigma = \text{div}\mathbf{n}; \quad \Phi(\mathbf{r}, t) = \Phi_s(t).$$

$$-\frac{\varepsilon_*}{4\pi}\oint_S(\mathbf{n}\cdot\nabla\Phi)dS = 0; \quad S = \begin{cases} r = 1 + \xi(\theta, t) \\ 0 \le \theta \le \pi \\ 0 \le \vartheta \le 2\pi; \end{cases}$$

$$\int_{V_1} r^2 dr\sin\theta d\theta d\vartheta = \frac{4}{3}\pi; \quad V_1 = \begin{cases} 0 \le r \le 1 + \xi(\theta, t) \\ 0 \le \theta \le \pi \\ 0 \le \vartheta \le 2\pi; \end{cases}$$

$$t = 0: \xi(\theta, t) = \xi_0 P_0(\mu) + \varepsilon\sum_{i\in\Xi} h_i P_i(\mu);$$

$$\sum_{i\in\Xi} h_i = 1; \quad \frac{\partial\xi(\theta, t)}{\partial t} = 0;$$

$$\xi_0 \approx -\varepsilon^2\sum_{i\in\Xi}\frac{h_i^2}{(2i+1)} + O(\varepsilon^3).$$

Here, ε is the initial deformation amplitude (the small parameter of the problem); $P_i(\mu)$ is the ith-order Legendre polynomial ($m \equiv \cos(\theta)$); P_{in} and P_{ex} are the internal and external pressures (inside and outside the drop), respectively; P_E is the pressure of the self-charge of the drop on the interface; P_σ is the Laplace pressure; $\mathbf{n}$ is the unit positive normal to the surface of the drop; $\Phi_s(t)$ is the electrostatic potential that is assumed to be constant over the surface; $\rho \equiv \rho_2/\rho_1$; h_i are the coefficients that specify the partial contribution of an ith vibration mode to the total disturbance; Ξ is the set of the numbers of initially excited vibration modes specifying the initial deformation of the drop; and ξ_0 is the constant that is found from the condition that the volume of the drop remains constant at the zero time. The hydrodynamic velocities are assumed to be much lower than the speed of an electromagnetic signal in a vacuum, because of which the Maxwell equations for the electric field near a nonlinearly vibrating drop are reduced to the electrostatics equations.

Along with the initial and boundary conditions, we should include the stationary condition for the center of mass. If the characteristic linear dimensions of the surrounding medium are sufficiently large, this condition is fulfilled automatically, as follows from [21], and the amplitude of the translational (first) mode, as well as the amplitudes of higher modes, should be calculated based on boundary hydrodynamic conditions at the interface.

(3) The problem thus stated will be solved in the second-order approximation in small parameter ε using the asymptotic method of many scales. According to this method, desired functions $\psi(\mathbf{r}, t)$, $\varphi(\mathbf{r}, t)$, and $\Phi(\mathbf{r}, t)$, as well as envelope $\xi(\theta, t)$ of the shape of the drop, are considered to be dependent not on standard time t but on many time scales $T_m = \varepsilon^m t$, which reflect the presence of fast and slow processes in the vibrating system. Analytical expressions for $\xi(\theta, t)$, $\psi(\mathbf{r}, t)$, $\varphi(\mathbf{r}, t)$, and $\Phi(\mathbf{r}, t)$ will be sought as asymptotic expansions in Legendre polynomials,

$$\xi(\theta, t) = \sum_{m=1}^{\infty}\varepsilon^m\xi^{(m)}(\theta, T_0, T_1, \ldots);$$

$$\psi(\mathbf{r}, t) = \sum_{m=1}^{\infty} \varepsilon^m \psi^{(m)}(r, \theta, T_0, T_1, \ldots);$$
$$\varphi(\mathbf{r}, t) = \sum_{m=0}^{\infty} \varepsilon^m \varphi^{(m)}(r, \theta, T_0, T_1, \ldots); \quad (2)$$
$$\Phi(\mathbf{r}, t) = \sum_{m=0}^{\infty} \varepsilon^m \Phi^{(m)}(r, \theta, T_0, T_1, \ldots);$$

where

$$\xi^{(m)}(\theta, T_0, T_1, \ldots) = \sum_{n=0}^{\infty} M_n^{(m)}(T_0, T_1, \ldots) P_n(\mu);$$
$$\psi^{(m)}(r, \theta, T_0, T_1, \ldots) = \sum_{n=0}^{\infty} E_n^{(m)}(T_0, T_1, \ldots) r^n P_n(\mu);$$
$$\varphi^{(m)}(r, \theta, T_0, T_1, \ldots) = \sum_{n=0}^{\infty} G_n^{(m)}(T_0, T_1, \ldots) r^{-n-1} P_n(\mu); \quad (3)$$
$$\Phi^{(m)}(r, \theta, T_0, T_1, \ldots) = \sum_{n=0}^{\infty} F_n^{(m)}(T_0, T_1, \ldots) r^{-n-1} P_n(\mu).$$

With regard to many time scales, the time derivatives will be calculated by the rule

$$\frac{\partial}{\partial t} = \frac{\partial}{\partial T_0} + \varepsilon \frac{\partial}{\partial T_1} + O(\varepsilon^2). \quad (4)$$

Substituting expansions (2)–(4) into statement (1) and equating the terms of the same order of smallness to each other in each of the equations, we easily arrive at a set of zeroth-, first-, and second-order subproblems for unknown coefficients $M_n^{(m)}(T_0, T_1, \ldots)$, $E_n^{(m)}(T_0, T_1, \ldots)$, $G_n^{(m)}(T_0, T_1, \ldots)$, and $F_n^{(m)}(T_0, T_1, \ldots)$ appearing in (2) and (3).

Below, we will restrict our calculation to coefficients $M_n^{(m)}(T_0, T_1)$, which specify the shape of the nonlinearly vibrating drop as a function of time. The other coefficients in expansions (2) and (3) are easily, while awkwardly, expressed through $M_n^{(m)}(T_0, T_1)$ [13].

(4) In the first order of smallness in ε, unknown coefficients $M_n^{(1)}(T_0, T_1)$ are found from the infinite set of coupled differential equations

$$M_0^{(1)}(T_0, T_1, \ldots) \equiv 0; \quad M_1^{(1)}(T_0, T_1, \ldots) \equiv 0;$$
$$n \geq 2: A_n M_{n-2}^{(1)}(T_0, T_1, \ldots)$$
$$+ B_n \frac{\partial M_{n-1}^{(1)}(T_0, T_1, \ldots)}{\partial T_0} + \frac{\partial^2 M_n^{(1)}(T_0, T_1, \ldots)}{\partial T_0^2}$$
$$+ \omega_n^{(2)} M_n^{(1)}(T_0, T_1, \ldots) + C_n \frac{\partial M_{n+1}^{(1)}(T_0, T_1, \ldots)}{\partial T_0}$$
$$+ D_n M_{n+2}^{(1)}(T_0, T_1, \ldots) = 0;$$
$$A_n = \frac{9}{4} \mathrm{We} \chi(n) \frac{n^2(n-1)(n-2)}{(2n-3)(2n-1)};$$
$$B_n = \frac{3}{2} \sqrt{\rho \mathrm{We}} n \chi(n); \quad (5)$$
$$C_n = \frac{3}{2} \sqrt{\rho \mathrm{We}} \chi(n) \frac{n(2n+1)}{2n+3};$$
$$D_n = \frac{9}{4} \mathrm{We} \chi(n) \frac{n^2(n+1)(n+2)}{(2n+3)(2n+5)};$$
$$\omega_n^2 = \chi(n) \left(n(n-1)(n+2-W) \right.$$
$$\left. - \mathrm{We} \frac{9n^2((2n+1)(n^2-1)+3)}{2(2n-1)(2n+1)(2n+3)} \right);$$
$$W = \frac{Q^2}{4\pi\varepsilon_*}; \quad \chi(n) = \left(1 + \rho \frac{n}{n+1}\right)^{-1};$$
$$\mathrm{We} \equiv \rho U_0^2; \quad \Phi_s^{(1)} \equiv 0.$$

It is easy to see that, putting $U_0 = 0$, we split set (5) into uncoupled second-order differential equations with constant coefficients that describe the harmonic oscillations of the modes (as was done earlier in [17, 18] for the vibration of a charged drop of an incompressible liquid that is at rest in an incompressible insulating medium). Thus, the motion of the surrounding medium causes mode interaction linear in small parameter ε. According to (5), an nth mode interacts with the four nearest, $(n-2)$th, $(n-1)$th, $(n+1)$th, and $(n+2)$th, modes. Earlier, first-order interaction between the modes was found for the planar interface between immiscible ideal incompressible liquids, one of which executes translational motion along the interface [11, 12], i.e., in the situation when the interface is prone to Kelvin–Helmholtz instability. It was shown [10] that, when an ideal liquid flows around the drop, its surface starts vibrating, which is typical of this type of instability.

One more linear effect showing up when an ideal liquid flows around the drop is noteworthy: according to [9], the drop flattens along the flow, taking the shape of a spheroid with an eccentricity depending on the flow velocity and charge of the drop. In this case, the drop is expected to vibrate about the spherical (equilibrium) shape. However, the sphericity of the drop at reasonable velocities (i.e., as long as the encircling flow remains laminar) is, as a rule, small. For example, when air with density $\rho_2 \approx 0.001$ g/cm^3 flows around a drop of radius $R = 100$ μm with velocity $U_0 \leq 100$ cm/s, sphe-

roidal deformation amplitude $M_2^{(1)} = (3\mathrm{We}/16)$ is negligible and can be ignored in second-order calculations.

(5) Second-order corrections (i.e., coefficients $M_n^{(2)}$) are found from the set of coupled inhomogeneous harmonic differential equations

$$\begin{aligned} M_0^{(2)}(T_0) &= \sum_{n=2}^{\infty} \frac{1}{2n+1}(M_n^{(1)}(T_0))^2; \\ A_n M_{n-2}^{(2)}(T_0) &+ B_n \frac{\partial M_{n-1}^{(2)}(T_0)}{\partial T_0} \\ &+ \frac{\partial^2 M_n^{(2)}(T_0)}{\partial T_0^2} + \omega_n^2 M_n^{(2)}(T_0) \\ + C_n \frac{\partial M_{n+1}^{(2)}(T_0)}{\partial T_0} &+ D_n M_{n+2}^{(2)}(T_0) = \chi(n) f_n(T_0); \quad n \geq 1 \end{aligned} \tag{6}$$

with zero boundary conditions. Inhomogeneity functions $f_n(T_0)$ are determined through coefficients $M_n^{(1)}$, which are solutions to set (5), as follows:

$$\begin{aligned} f_n(T_0) &= \sum_{m \in \Xi} \sum_{l \in \Xi} \left\{ G_1 M_n^{(1)}(T_0) M_l^{(1)}(T_0) \right. \\ &+ G_2 \left(\frac{M_{m-1}^{(1)}(T_0) M_l^{(1)}(T_0)}{2m-1} - \frac{M_{m+1}^{(1)}(T_0) M_l^{(1)}(T_0)}{2m+3} \right) \\ &+ G_3 \left(\frac{m M_{m-1}^{(1)}(T_0)}{2m-1} - \frac{m M_{m+1}^{(1)}(T_0)}{2m+3} \right) \\ &\times \left(\frac{l M_{l-1}^{(1)}(T_0)}{2l-1} - \frac{l M_{l+1}^{(1)}(T_0)}{2l+3} \right) \\ &+ G_4 \left[\frac{m}{l+1} \left(\frac{M_{m+1}^{(1)}(T_0)}{2m+3} \frac{\partial M_l^{(1)}(T_0)}{\partial T_0} \right. \right. \\ &\left. - \frac{M_{m-1}^{(1)}(T_0)}{2m-1} \frac{\partial M_l^{(1)}(T_0)}{\partial T_0} \right) \\ &+ \left. \frac{l}{m+1} \left(\frac{\partial M_m^{(1)}(T_0)}{\partial T_0} \frac{M_{l+1}^{(1)}(T_0)}{2l+3} - \frac{\partial M_m^{(1)}(T_0)}{\partial T_0} \frac{M_{l-1}^{(1)}(T_0)}{2l-1} \right) \right] \\ &+ G_5 \frac{\partial^2 M_m^{(1)}(T_0)}{\partial T_0^2} M_l^{(1)}(T_0) + G_6 \frac{\partial M_m^{(1)}}{\partial T_0} \frac{\partial M_l^{(1)}}{\partial T_0} \\ &+ G_7 \frac{\partial M_m^{(1)}(T_0)}{\partial T_0} M_l^{(1)}(T_0) + G_8 M_m^{(1)}(T_0) \frac{\partial M_l^{(1)}(T_0)}{\partial T_0} \\ &+ \left. G_9 \left(\frac{\partial M_{m+1}^{(1)}(T_0)}{\partial T_0} \frac{M_l^{(1)}(T_0)}{2m+3} - \frac{\partial M_{m-1}^{(1)}(T_0)}{\partial T_0} \frac{M_l^{(1)}(T_0)}{2m-1} \right) \right\}, \end{aligned} \tag{7}$$

where

$$\begin{aligned} G_1 &\equiv \left\{ K_{m,l,n} \left(2n[l(l+1)-1] + W\frac{n}{2}[l(m+1) \right. \right. \\ &- m(2m-2n+7)+3] + \mathrm{We}\frac{n(9m^2+9m-7)}{(2m-1)(2m+3)} \Big) \\ &+ W\frac{n}{2}\alpha_{m,l,n} + \mathrm{We}\frac{9n(n-1)}{4(2n-1)(2m+1)} \\ &\times [m(m-1)^2 K_{m-1,l,n-1} - (m+1)^2(m+2)K_{m+1,l,n-1} \\ &- (m-1)\alpha_{m-1,l,n-1} + (m+1)\alpha_{m+1,l,n-1}] \\ &+ \mathrm{We}\frac{9n(n+1)}{(4(2n+3)(2m+1))}[(m+1)^2(m+2)K_{m+1,l,n+1} \\ &- m(m-1)^2 K_{m-1,l,n+1} - (m+1)\alpha_{m+1,l,n+1} \\ &+ (m-1)\alpha_{m-1,l,n+1}] - \mathrm{We}\frac{9n}{8(2m+1)} \\ &\times \left. \left[\frac{m(m-1)}{2m+1} K_{m-2,l,n} + \frac{(m+1)(m+2)}{2m+3} K_{m+2,l,n} \right] \right\}, \\ G_2 &\equiv \mathrm{We}\frac{9nm(m+1)}{4(2m+1)} \\ &\times [(m-1)(m+2)K_{m+1,l,n} - m(m+5)K_{m-1,l,n}], \\ G_3 &\equiv \mathrm{We}\frac{9}{8}n[(m+1)(l+1)K_{m,l,n} + \alpha_{m,l,n}], \\ G_4 &\equiv \frac{4}{3}\frac{G_3}{U}, \\ G_5 &\equiv \left[(m-n-1)K_{m,l,n} - \frac{\alpha_{m,l,n}}{m} \right. \\ &- \left. \frac{\rho n}{n+1} \left((m-n+1)K_{m,l,n} - \frac{\alpha_{m,l,n}}{m+1} \right) \right], \\ G_6 &\equiv \frac{K_{m,l,n}(2m-n-2)}{2} - \frac{(n+2l)\alpha_{m,l,n}}{2ml} \\ &+ \frac{\rho n}{2(n+1)} \left((n-2m-3)K_{m,l,n} + \frac{(n+2l+3)\alpha_{m,l,n}}{(m+1)(l+1)} \right), \\ G_7 &\equiv \frac{3}{2}\sqrt{\rho \mathrm{We}}n \left(\frac{m(4+5n+3m+mn+m^2)}{(n+1)(2m+1)} K_{m-1,l,n} \right. \\ &+ \frac{(m+2)(2+n+m-mn+m^2)}{(n+1)(2m+1)} K_{m+1,l,n} \\ &+ \left. \frac{(n-1)(m+2)}{2n-1} K_{m,l,n-1} - \frac{(n+1)(m+2)}{2n+3} K_{m,l,n+1} \right. \end{aligned} \tag{8}$$

$$+\frac{(m-1)\alpha_{m-1,l,n}}{(n+1)(2m+1)}-\frac{(n-1)\alpha_{m,l,n-1}}{(m+1)(2n-1)}$$
$$+\frac{(n+1)\alpha_{m,l,n+1}}{(m+1)(2n+3)}-\frac{(n+1)\alpha_{m+1,l,n}}{(n+1)(2m+1)}\Bigg),$$

$$G_8\equiv\sqrt{\rho\mathrm{We}}\frac{3n}{2(n+1)(2m+1)}$$
$$\times[(m+1)^2(m+2)K_{m+1,l,n}-m(m-1)^2K_{m-1,l,n}$$
$$-(m+1)\alpha_{m+1,l,n}+(m-1)\alpha_{m-1,l,n}],$$

$$G_9\equiv\sqrt{\rho\mathrm{We}}\frac{3}{2}nm(m+1)K_{m,l,n};$$

$$\alpha_{mln}\equiv-\sqrt{m(m+1)l(l+1)}C^{n0}_{m0l0}C^{0}_{m-1l1};$$

$$K_{mln}\equiv[C^{n0}_{m0l0}]^2;$$

and C^{n0}_{m0l0} and C^{n0}_{m-1l1} are the Clebsch–Gordan coefficients.

The presence of the Clebsch–Gordan coefficients makes the number of inhomogeneity functions $f_n(T_0)$ that are not identically zero finite. For example, if an mth mode is initially excited, the Clebsch–Gordan coefficients (and, hence, the inhomogeneity functions) with numbers from 0 to $2m+2$ will be other than zero.

(6) In our consideration, emphasis is on the nonlinear vibration of large water drops in thunderstorm clouds. Let, for definiteness, $R = 100$ μm; then, the free-fall velocity of such a drop in a cloud is $U_0 = 72$ cm/s and its associated Reynolds number is Re = 9.61 [22]. This means that the air flow around the drop is laminar; hence, the conditions that were set in stating the problem are fulfilled. The Weber number for this drop is very small, $\mathrm{We}\approx 0.7\times10^{-3}$. Dimensionless density ρ, which enters into expressions (7) and (8) defining the inhomogeneity functions, has the same order of magnitude. In sets (5) and (6), coefficients A_n, B_n, C_n, and D_n involve the Weber number and its combination with dimensionless density ρ in the form $\sqrt{\rho\mathrm{We}}$. Coefficients G_j entering into definition (7) of the inhomogeneity functions contain We, ρ, and $\sqrt{\rho\mathrm{We}}$ as factors. As is evident from the aforesaid, quantities We, ρ, and $\sqrt{\rho\mathrm{We}}$ are of the same order of magnitude (this follows from the fact that dimensionless velocity U_0 of the drop is on the order of unity for those values of physical quantities adopted in this paper); so, they will serve as parameters in asymptotic expansions of solutions to sets (5) and (6).

In our problem, dimensionless Rayleigh parameter W characterizing the stability of the drop against its self-charge may vary between 0 and 4. According to [8], self-charges of drops in thunderstorm clouds are small: for maximal values of the Rayleigh parameter, they are no higher than several tenths. Yet, parameter W in asymptotic calculations will be viewed as a quantity of zeroth-order of smallness.

(i) To be definite, we assume that the initial deformation of the drop is specified by a superposition of jth and kth modes with $j > k$, $|j > k| \geq 4$. Then, in the first-order approximation in We, ρ, and $\sqrt{\rho\mathrm{We}}$, solutions to set (5) with the boundary conditions

$$T_0 = 0\colon M_j^{(1)} = h_j;\quad M_k^{(1)} = h_k;\quad \frac{\partial M_j^{(1)}}{\partial T_0} = 0;$$
$$\frac{\partial M_k^{(1)}}{\partial T_0} = 0;\quad M_n^{(1)} = 0;\quad \frac{\partial M_n^{(1)}}{\partial T_0} = 0;$$
$$n\neq j;\quad n\neq k$$

have the form

$$M^{(1)}_{(g-2)} = \frac{D_{g-2}h_g}{\omega_{0g}^2-\omega_{g-2}^2}[\cos(\omega_{0g}T_0)-\cos(\omega_{g-2}T_0)];$$
$$M^{(1)}_{(g-1)} = \frac{C_{g-1}h_g\omega_{0g}}{\omega_{0g}^2-\omega_{g-1}^2}$$
$$\times\left[-\frac{\omega_{0g}}{\omega_{g-1}}\sin(\omega_{g-1}T_0)+\sin(\omega_{0g}T_0)\right];$$
$$M_g^{(1)} = h_g\cos(\omega_gT_0);$$
$$M^{(1)}_{(g+1)} = \frac{B_{g+1}h_g\omega_{0g}}{\omega_{g+1}^2-\omega_{0g}^2} \qquad (9)$$
$$\times\left[-\frac{\omega_{0g}}{\omega_{g+1}}\sin(\omega_{g+1}T_0)+\sin(\omega_{0g}T_0)\right];$$
$$M^{1}_{(g+2)} = \frac{A_{g+2}h_g}{\omega_{g+2}^2-\omega_{0g}^2}$$
$$\times[\cos(\omega_{g+2}T_0)-\cos(\omega_{0g}T_0)];\quad g = j,k.$$

Frequencies ω_n are found from the equation

$$\omega_n^2 = \chi(n)\Bigg(n(n-1)(n+2-W)$$
$$-\mathrm{We}\frac{9n^2((2n+1)(n^2-1)+3)}{2(2n-1)(2n+1)(2n+3)}\Bigg), \qquad (10)$$

which has the meaning of the dispersion relation of the problem that is written in the approximation linear in We, $\sqrt{\rho\mathrm{We}}$, and ρ without taking into account mode interaction. Such an approach is valid, since the influence of mode interaction on the dispersion relation for the tangential discontinuity at the interface shows up in the second-order approximation in We, $\sqrt{\rho\mathrm{We}}$, and ρ. Frequencies ω_n are found from Eq. (10) at We = 0.

Thus, at $|j-k| \geq 4$, four modes ($(g-1)$th, $(g-2)$th, $(g+1)$th, and $(g+2)$th) are excited near a gth mode ($g = j$ or k) entering into the mode spectrum that specifies the initial deformation. Such a situation is due to hydrodynamic interaction at the interface where the velocity field experiences a discontinuity. However, the amplitudes of these modes will have the first order of smallness in variables We, ρ, and $\sqrt{\rho We}$. If the condition $|j-k| \geq 4$ is not set, the form of solutions to set (5) will change insignificantly because of its linearity: the solutions will represent linear combinations of the functions appearing in (9).

(ii) Using solutions $M_n^{(1)}$, we will write expressions for inhomogeneity functions (7) appearing in set (6). Taking into account the order of smallness of the modes specifying the initial deformation and also of the modes excited via linear interaction due to the tangential discontinuity, one can easily see that the modes specifying the initial deformation of the equilibrium shape of the drop play a major role in nonlinear (quadratic in ε) interaction. Recall that the main goal of this study is to see whether the fundamental mode can be resonantly built up by absorbing the energy of higher modes involved in the initial deformation. Therefore, below, we will analyze the solutions to sets (6) and (7), ignoring mode interaction due to a tangential discontinuity of the velocity field at the interface. In this case, the infinite set of coupled inhomogeneous equations (6) and (7) will turn into a set of uncoupled inhomogeneous harmonic equations with zero initial conditions for all the modes and inhomogeneity function (7) written in the zeroth-order of smallness in We, ρ, and $\sqrt{\rho We}$ will simplify greatly. Actually, the resulting set of equations will describe the nonlinear vibrations of a charged immobile drop in a medium. A solution to this set was found earlier [17, 18]. The presence of the encircling flow will show up merely as a change in the vibration frequency, which can be found from dispersion relation (10). Eventually, in the quadratic (in small parameter ε) approximation, corrections to the envelope of the shape of a nonlinearly vibrating drop will have the form [17, 18]

$$M_n^{(2)}(T_0, T_1) = -\sum_{l,\, m \in \Xi} \frac{h_l h_m}{2}(\lambda_{lmn}^{(+)} + \lambda_{lmn}^{(-)})\cos(\omega_n T_0)$$

$$+ \sum_{l,\, m \in \Xi} \frac{h_l h_m}{2}(\lambda_{lmn}^{(+)}\cos((\omega_l + \omega_m)T_0)$$

$$+ \lambda_{lmn}^{(-)}\cos((\omega_l - \omega_m)T_0)),$$

$$\lambda_{mln}^{(\pm)} = (\gamma_{mln} \pm \omega_m\omega_l\eta_{mln})/(\omega_n^2 - (\omega_m \pm \omega_l)^2),$$

$$\gamma_{mln} = \chi_n K_{mln}(\omega_m^2(n - m + 1 - \rho n(n - m - 1)/(n + 1)) + 2n(l(l + 1) - 1) + (l(m + 1) - m(2m - 2n + 7) + 3)nW/2)$$

$$+ \chi_n\alpha_{mln}((1/m + n\rho/((n + 1)(m + 1)))\omega_m^2 + nW/2),$$

$$\eta_{mln} = (\chi_n K_{mln}(n/2 - m + 1 + \rho n(2m + 3 - n)/(2(n + 1))) + (\chi_n\alpha_{mln}((1 + n/(2l))/m - n\rho(n + 2l + 3)/(2(m + 1)(l + 1)(n + 1))).$$

(11)

(7) It is easy to check that, if the relationship $\omega_n^2 = (\omega_m \pm \omega_l)^2$ is valid, the denominators of some of the terms appearing in solutions (11) vanish and expressions (11) diverge; in other words, the second-order corrections become asymptotically invalid. In the theory of nonlinear oscillations, such a situation is treated as a resonance situation and should be analyzed separately using other mathematical means [16–18]. Physically, the resonance situation means that a wave with frequency ω_n vigorously exchanges energy with two waves with frequencies ω_m and ω_l (the case of secondary Raman resonance) or, at $m = l$, interacts twice with the wave of frequency $\omega_m = \omega_l$ (degenerate resonance) [16–18]. It was shown previously [14] that, when degenerate resonant mode interaction occurs in the system being considered, the energy is transferred only from lower to higher modes. In the case of secondary Raman resonance, the energy may be transferred in the reverse direction too: from lower to higher modes and vice versa [16–18]. The only factor that "spoils" the general consistent picture for a charged drop nonlinearly vibrating in a quiescent insulating medium (see [16–18]) is that the fundamental mode ($n = 2$) can be involved in resonance energy exchange between the modes in the second order of smallness in vibration amplitude. To put it otherwise, it is impossible for a immobile charged drop vibrating in an insulating medium to transfer energy from higher modes to the fundamental mode by means of secondary Raman resonance, since the condition $\omega_2^2 = (\omega_m \pm \omega_l)^2$ is fulfilled for none of m and l. If the drop moves relative to the medium, its vibration frequency is given by (11); that is, the dispersion relation involves the term proportional to Weber number We and so the fundamental mode can resonantly build up. Indeed, introducing the designation

$$\Delta\omega_n^2 \equiv (\omega_m \pm \omega_l)^2 - \omega_n^2, \tag{12}$$

where $\Delta\omega_n^2 = \Delta\omega_n^2(m, l, n, W, \mathrm{We})$, we construct for several values of n (specifically, for several lower modes to which the energy is transferred from higher modes) the dependences $\Delta\omega_n^2 = \Delta\omega_n^2(m, l)$ that are crossed by the plane $\Delta\omega_n^2 = 0$ at fixed values of Rayleigh and Weber parameters W and We (Fig. 1). In a similar way, we construct the dependences $\Delta\omega_n^2 =$

$\Delta\omega_n^2(W, \mathrm{We})$ for fixed pairs of mode numbers m and l specifying the initial deformation (Fig. 2). In Figs. 1 and 2, the condition for resonant energy exchange is strictly fulfilled along the lines of intersection of the surfaces. The dependences $\Delta\omega_n^2 = \Delta\omega_n^2(m, l)$ for the second, third, and fourth modes (Figs.1a–1c) indicate a considerable scope for energy transfer from higher to lower modes. It should be noted, however, that only a finite number of points in the lines of intersection in Fig. 1 corresponds to integer mode numbers m and l (when constructing Fig. 1, we assumed that discrete variables m and l vary continuously). The rest of the points in these lines indicate near-resonance situations. Remarkably, the nonlinear internal resonant mode interaction is slightly sensitive to small deviations of the physical parameters from the values corresponding to exact resonance positions [17, 18, 23]. This means that the resonant interaction will also take place in the neighborhood of the locus of points constituting the straight lines in Figs. 1 and 2 but its intensity (the fraction of the resonantly transferred energy and the time interval within which the transferred energy stays in a growing lower mode) will be somewhat lower [17, 23].

According to the calculations, the fundamental mode strictly resonantly interacts with the third mode alone if both modes are present in the spectrum of the modes specifying the initial deformation (this situation is illustrated in Fig. 2a). It follows from Fig. 2a that the exact values of the Rayleigh and Weber parameters meeting the resonance interaction amount to several fractions of unity, i.e., are somewhat larger than those obtained by the model calculation for a cloud drop of radius 100 μm. The discrepancy between the analytical calculations and the real situation in a thunderstorm cloud may be eliminated by (i) increasing the radius of the drop (then, the free-fall velocity of the drop will also increase and the Weber number will tend toward its value in Fig. 1a) or (ii) taking into account the weak dependence of the vibration frequency on the Rayleigh and Weber parameters when they are small and also the above-mentioned slight sensitivity of the resonant interaction to small deviations of the physical parameters from exact resonance values. These remedies can be applied in combination. In any case, the parameters of large drops in thunderstorm clouds ($W \sim 0.1$, $\mathrm{We} \le 0.5$) are such that they admit of energy transfer from the excited third vibration mode to the excited second mode. Certainly, a more detailed investigation is necessary to gain a better insight into the resonance energy transfer between these modes. Today, only the possibility of energy transfer between these modes can be viewed as a documented fact. The third mode energy can be replenished by resonant energy transfer from higher modes (Fig. 1b).

The calculations show that, unlike the second mode, the third mode may resonantly exchange energy with a large number of modes: from the fourth to the thirteenth

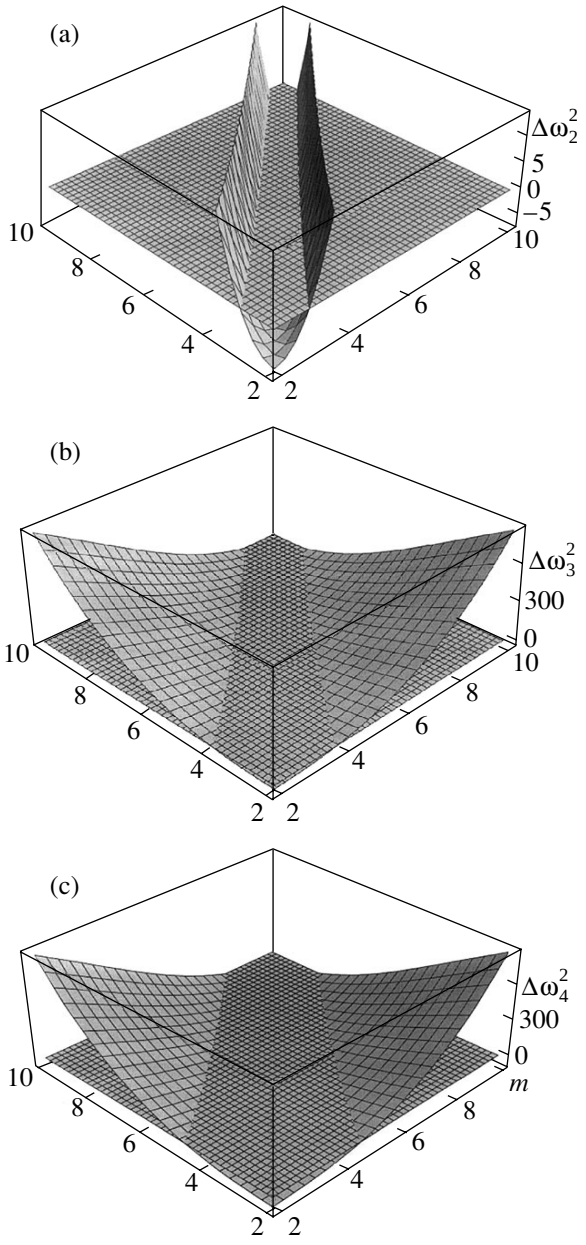

Fig. 1. Quadratic form $\Delta\omega_n^2$ (12) crossed by the plane $\Delta\omega_n^2 = 0$ vs. mode numbers m and l at $W = 0.1$, $\mathrm{We} = 0.001$, and n = (a) 2, (b) 3, and (c) 4.

mode. However, the resonant interaction with the twelfth and thirteenth modes corresponds to the least values of the Rayleigh and Weber parameters (Fig. 2b) (the necessary condition for analytical calculations to meet the reality is the smallness of the charge and velocity of the drop, which are characterized by the Rayleigh and Weber parameters). For the fourth mode, the spectrum of modes resonantly coupled with it is still wider (from the fifth to thirty-first mode); however, the optimal (in terms of the smallness of the Rayleigh and

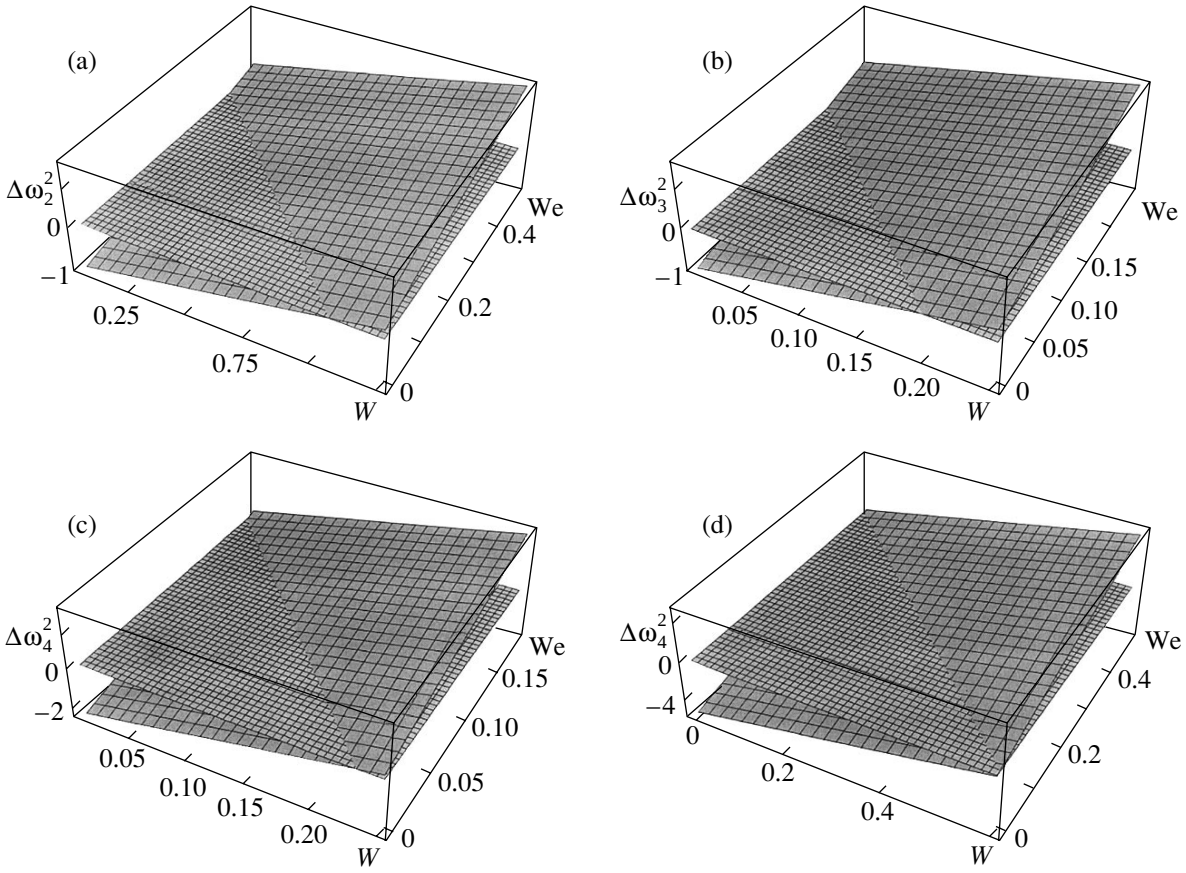

Fig. 2. Quadratic form $\Delta\omega_n^2$ (12) crossed by the plane $\Delta\omega_n^2 = 0$ vs. Rayleigh and Weber parameters. (a) $n = 2$, $m = 2$, $l = 3$; (b) $n = 3$, $m = 12$, $l = 13$; (c) $n = 4$, $m = 30$, $l = 31$; and (d) $n = 4$, $m = 6$, $l = 8$.

Weber parameters) interactions in this case are interactions with the thirteenth and thirty-first modes (see Fig. 2c).

Figures 2a–2c show the resonance interaction of an *n*th mode with two neighboring (*m*th and *l*th) higher modes ($|l - m| = 1$). As number *n* increases, the range of the *l*th and *m*th modes resonantly coupled with the *n*th mode widens, as illustrated by Fig. 2d for $n = 4$, $m = 6$, and $l = 8$. Eventually, the following situation may arise: the fundamental mode takes the energy from the third mode, the third mode absorbs the energy of the fourth to thirteenth modes, the fourth mode takes the energy from the fifth to thirty-first modes, etc. It can be conjectured that, in a nonlinearly vibrating charged drop moving in a medium, secondary Raman resonant interaction between vibration modes generates an energy flux from higher modes to the fundamental mode. The energy transfer from higher modes (which are regularly excited when a large drop moving in a cloud collides with finer and slower drops) builds up the amplitude of fundamental mode vibrations up to a value observed in full-scale experiments (which is comparable to the radius of the drop [19, 20]). Note, however, that the possibility exists of a reverse energy transfer (from lower to higher modes), which is supported by degenerate interaction between the modes. Physical mechanisms behind interaction between these oppositely directed fluxes in the vibrating system under consideration are as yet a mystery and call for special investigation.

The present study of internal nonlinear resonances in a charged drop placed in the laminar flow of an ideal incompressible insulating low-density medium ignores mode interaction at a tangential discontinuity of the velocity field at the interface, and inhomogeneity function (7) is written in the zeroth approximation in parameters We, ρ, and $\sqrt{\rho We}$. With these simplifying assumptions discarded, the solution to the problem will have extra terms of the first and second order of smallness in We, ρ, and $\sqrt{\rho We}$ but the resonance terms will persist. Taking into account mode interaction at the velocity field tangential discontinuity gives rise to second-order (in We, ρ, and $\sqrt{\rho We}$) corrections to the exact resonance positions. However, the basic inferences drawn in this work will remain valid.

CONCLUSIONS

The motion of a nonlinearly vibrating charged drop in a medium greatly expands the spectrum of realizable internal nonlinear resonances. A large charged drop in a cloud admits of resonant energy transfer from higher vibrating modes to the fundamental mode, which shows up even in the second order of smallness in deformation amplitude and builds up spheroidal vibrations of the drop, as is observed under natural conditions.

ACKNOWLEDGMENTS

This work was supported by the Russian Foundation for Basic Research, grant no. 03-01-00760.

REFERENCES

1. A. L. Gonor and V. Ya. Rivkind, Itogi Nauki Tekh., Ser.: Mekh. Zhidk. Gaza **17**, 98 (1982).
2. A. I. Grigor'ev and S. O. Shiryaeva, Izv. Ross. Akad. Nauk, Mekh. Zhidk. Gaza, No. 3, 3 (1994).
3. D. F. Belonozhko and A. I. Grigor'ev, Elektrokhim. Obrab. Met., No. 4, 17 (2000).
4. V. A. Dyachuk and V. M. Muchnik, Dokl. Akad. Nauk SSSR **248**, 60 (1979).
5. A. I. Grigor'ev and S. O. Shiryaeva, Phys. Scr. **54**, 660 (1996).
6. A. I. Grigor'ev, S. O. Shiryaeva, and M. V. Volkova, Zh. Tekh. Fiz. **73** (11), 31 (2003) [Tech. Phys. **48**, 1389 (2003)].
7. S. O. Shiryaeva, M. V. Volkova, and A. I. Grigor'ev, Zh. Tekh. Fiz. **75** (3), 36 (2005) [Tech. Phys. **50**, 321 (2005)].
8. I. P. Mazin, A. Kh. Khrgian, and I. M. Imyanitov, *Clouds and Cloud Atmosphere: A Handbook* (Gidrometeoizdat, Leningrad, 1989) [in Russian].
9. A. I. Grigor'ev, Zh. Tekh. Fiz. **72** (7), 41 (2002) [Tech. Phys. **47**, 834 (2002)].
10. V. A. Koromyslov and A. I. Grigor'ev, Zh. Tekh. Fiz. **72** (9), 21 (2002) [Tech. Phys. **47**, 1090 (2002)].
11. A. I. Grigor'ev, Zh. Tekh. Fiz. **70** (1), 24 (2000) [Tech. Phys. **45**, 22 (2000)].
12. A. I. Grigor'ev and A. S. Golovanov, Pis'ma Zh. Tekh. Fiz. **25** (20), 13 (1999) [Tech. Phys. Lett. **25**, 806 (1999)].
13. V. A. Koromyslov, A. I. Grigor'ev, and S. O. Shiryaeva, Zh. Tekh. Fiz. **74** (9), 23 (2004) [Tech. Phys. **49**, 1126 (2004)].
14. A. I. Grigor'ev, V. A. Koromyslov, S. O. Shiryaeva, and M. V. Volkova, Elektrokhim. Obrab. Met., No. 4, 25 (2004).
15. S. O. Shiryaeva, Zh. Tekh. Fiz. **73** (2), 19 (2003) [Tech. Phys. **48**, 152 (2003)].
16. S. O. Shiryaeva, A. N. Zharov, and A. I. Grigor'ev, Zh. Tekh. Fiz. **74** (1), 10 (2004) [Tech. Phys. **49**, 8 (2004)].
17. M. V. Rybakova, S. O. Shiryaeva, and A. I. Grigor'ev, Zh. Tekh. Fiz. **74** (1), 4 (2004) [Tech. Phys. **49**, 22 (2004)].
18. A. N. Zharov, A. I. Grigor'ev, and S. O. Shiryaeva, Zh. Tekh. Fiz. **74** (7), 19 (2004) [Tech. Phys. **49**, 824 (2004)].
19. K. V. Beard, Radio Sci. **19**, 67 (1984).
20. K. V. Beard, Rev. Geophys. **25**, 357 (1987).
21. S. O. Shiryaeva, A. I. Grigor'ev, V. A. Koromyslov, and A. N. Zharov, Zh. Tekh. Fiz. **73** (9), 60 (2003) [Tech. Phys. **48**, 1141 (2003)].
22. I. P. Mazin and S. M. Shmeter, *Clouds: Structure and Physics of Formation* (Gidrometeoizdat, Moscow, 1983) [in Russian].
23. S. O. Shiryaeva, D. F. Belonozhko, and A. I. Grigor'ev, Zh. Tekh. Fiz. **75** (2), 45 (2005) [Tech. Phys. **50**, 185 (2005)].

Translated by V. Isaakyan

Technical Physics, Vol. 50, No. 12, 2005, pp. 1592–1604. Translated from Zhurnal Tekhnicheskoĭ Fiziki, Vol. 75, No. 12, 2005, pp. 56–68.

GAS DISCHARGES, PLASMA

Investigation of the Glow and Contracted Discharge Plasmas in Nitrogen by Coherent Anti-Stokes Raman Spectroscopy, Optical Interferometry, and Numerical Simulation

V. A. Shakhatov* and O. A. Gordeev**

** Topchiev Institute of Petrohemical Synthesis, Russian Academy of Sciences, Leninskiĭ pr. 29, Moscow, 119991 Russia*

e-mail: shakhatov@ips.ac.ru

*** Moscow State Institute of Aviation, Volokolamskoe sh. 4, Moscow, 125993 Russia*

e-mail: perminov@mail.ru

Received March 16, 2005

Abstract—The translational temperature in the plasma of glow and contracted discharges is measured using the methods of coherent anti-Stokes Raman spectroscopy and optical interferometry. The current density in the discharge is determined by measuring the electron concentration with optical interferometry and emission spectroscopy. The distribution of nitrogen molecules over vibrational and rotational levels in the ground state, the electron energy distribution, and the time dependence of the gas temperature are numerically found based on a model including the homogeneous Boltzmann equation and balance equations for the concentrations of charged and excited particles and for the gas temperature. The dynamics of transition to the quasi-steady-state distribution of nitrogen molecules over vibrational levels is studied. © *2005 Pleiades Publishing, Inc.*

INTRODUCTION

Molecular nitrogen is used as a basic component in a variety of plasma-chemical processes and also as a small additive to various gases in studying the parameters of the gas discharge plasma. The glow discharge plasma in nitrogen is a heavily nonequilibrium weakly ionized gas. The factors responsible for nonequilibrium and affecting the kinetics of processes occurring in the plasma are the disturbance of equilibrium between the vibrational, rotational, and translational degrees of freedom of the molecules, as well as the deviation of the electron energy distribution function (EEDF) from the Maxwell distribution [1–3]. The retarded vibrational relaxation of nitrogen molecules in the discharge causes their high vibrational excitation, and the population of molecular vibrational levels is no longer described by the Boltzmann formula [4]. This greatly complicates experimental and theoretical investigation of the gas heating dynamics, as well as the EEDF and the molecule vibrational–rotational energy level distribution function (hereafter, molecule vibrational distribution function (MVDF)).

Numerical simulation of the process kinetics in the nonequilibrium gas discharge plasma requires experimental verification even if the processes are described in detail (*a fortiori* if they are briefly outlined). However, the published parameters entering into the relevant kinetic equations, such as the rate constants and the cross sections of elementary processes in a gas discharge, are frequently given with an insufficient accuracy, since they are difficult to calculate or measure. For example, the reported cross sections of electron-impact-induced vibrational level excitation in nitrogen molecules differ by a factor of 4 [5], and the scatter in the rate constants for vibrational–vibrational energy exchange (*VV* exchange) and vibrational–translational relaxation (*VT* relaxation) differ by one order of magnitude [6]. Therefore, it seems topical to develop efficient plasma diagnostics methods. However, development of diagnostics methods inevitably runs into the problem of gaining insight into elementary processes in the plasma and selecting a model substantiating the means of choice. A reasonable combination of experimental and theoretical studies would make it possible to experimentally verify numerical methods selected, gain lacking data for the rate constants and elementary process cross sections, optimize (with minimal costs) technologies using the plasma of a nonequilibrium gas discharge as an active medium, and comprehensively study its properties in a wide range of critical parameters.

An essential issue in studying the EEDF and MVDF in the nitrogen plasma is kinetic mechanisms behind the interplay between these functions [7–9]. An important parameter characterizing a discharge plasma is the translational temperature, which specifies the routes and rate constants of many plasma-chemical reactions.

The basic processes underlying the interplay between the EEDF and MVDF are electron collisions of the first and second kind with vibrationally excited

molecules in the ground state, $N_2(X^1\Sigma_g^+, v)$. In addition, when considering the MVDF formation, one should take into account the processes of *VV* exchange and *VT* relaxation. To include these processes, the EEDF was taken by probe methods [10, 11] and the MVDF was obtained by jointly solving the Boltzmann equation and the balance (master) equation [7–9]. The input data, such as the translational and vibrational temperatures, reduced electric field strength, and electron concentration, were measured by the methods of emission spectroscopy, optical interferometry, and coherent anti-Stokes Raman scattering (CARS). The emphasis in this work was on determining the low-energy part of the EEDF. However, reliable determination of the rate constants for high-threshold processes calls for investigation of the high-energy part of the EEDF.

The dynamics of nitrogen heating in the discharge has been the subject of extensive research [12–19]. In this field, a number of reasons makes comparison between measurements and calculations difficult. When nitrogen heats up, it is necessary to take into account not only the interrelation between EEDF and MVDF but also many other processes that may affect their formation in the discharge plasma. Such are electron collisions of the first and second kind with excited particles, relaxation, deactivation of excited molecules and recombination of atoms, thermal losses due to a gas translational temperature gradient, etc. Translational temperature T_{tr} was measured by optical interferometry and CARS. Of special importance in our experiments is a channel of *VV* energy exchange between nitrogen molecules. It should be noted here that the form of the analytical MVDF is sensitive to the rate constant of *VV* energy exchange between the molecules [15].

The glow discharge as an object of investigation was chosen for the following reasons. First, in the positive column plasma, equilibrium between the vibrational, rotational, and translational degrees of freedom of nitrogen molecules is noticeably disturbed. Second, the glow parameters, such as electrode potential, cathode drop, and current intensity, which are necessary for finding electron concentration N_e and reduced electric field strength E/N, can be reliably measured. Third, one can use EEDF measurements taken by the probe method.

EXPERIMENTAL

Figure 1 shows the experimental setup used in this work to study the gas heating dynamics, gas density and electron concentration distributions over the cross section of the discharge cell, rotational temperature, and MVDF in a nitrogen glow by the methods of emission spectroscopy, interferometry, and CARS.

A dc longitudinal glow discharge was initiated in a quartz cell at a pressure ranging from 3 to 30 Torr. The cell was cooled by water, and so wall temperature T_w could be kept at 300 K. A weak gas flow was pumped through the cell, the flowing gas being prepurified in nitrogen traps. Ring titanium electrodes were mounted flush with the inner surface of the discharge tube. The inner radius of the tube was $R = 1.8$ cm. Windows at the end faces of the cell were made of different materials depending on optical diagnostics means. For optical interferometry and emission spectroscopy, the windows were made of quartz, which is transparent for the near-UV and visible ranges (λ = 300–700 nm). When the translational temperature and the populations of nitrogen molecule vibrational levels were measured by CARS, ZhS-17 and SS-5 color filters served as the entrance and exit windows of the cell. The former eliminated the CARS signal due to the nonlinear interaction between the laser beams propagating in the atmosphere toward the cell. The latter filter separated out the CARS valid signal from the total radiation of the discharge and lasers.

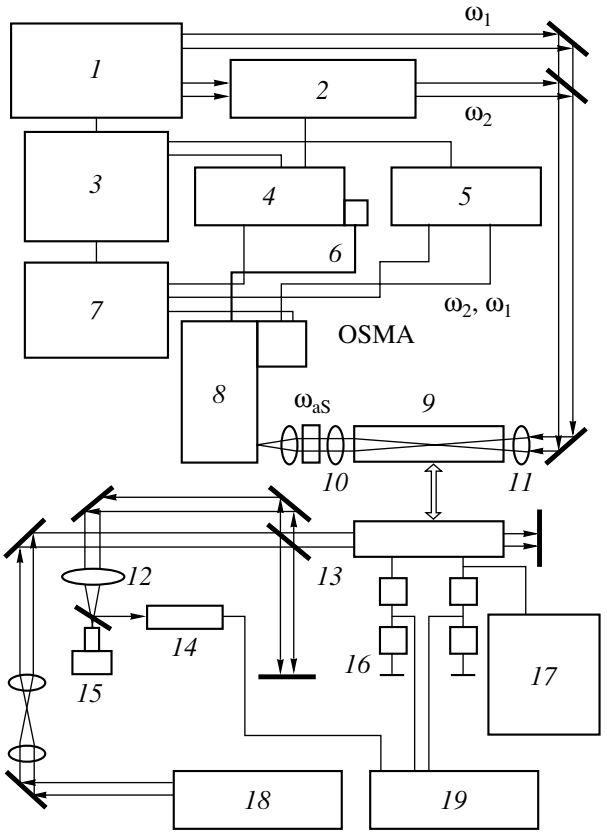

Fig. 1. Schematic of the experimental setup: (*1*) Nd^{3+} : YAG laser, (*2*) dye laser, (*3*, *17*) power suppliers, (*4*, *5*) controllers, (*6*, *14*) photoelectric multipliers, (*7*) PC, (*8*) monochromator, (*9*) discharge cell, (*10*) filter, (*11*) lens, (*12*) lens with focal length $f = 150$ cm, (*13*) wedge, (*15*) camera, (*16*) voltage dividers, (*18*) He–Ne laser, and (*19*) oscilloscope.

Translational temperature T_{tr} and the populations of nitrogen molecule vibrational levels were measured at two stages of the glow. At the first (transient) stage (t = 3–20 ms), T_{tr} was measured optically. It is at this stage of the discharge that its basic parameters (current inten-

sity, T_{tr}, and MVDF) are formed at a constant pressure. The glow discharge was initiated by stepwise increasing the voltage applied to the cell electrodes from a regulated high-voltage power supply. As soon as the discharge was initiated, a voltage drop and current intensity in the discharge gap were displayed and measured on the oscilloscope's screen using resistive voltage dividers.

In the time interval t = 20–25 ms, within which the low-frequency vibrations of the setup deteriorate the accuracy of interferometric measurements, T_{tr} and the MVDF were determined by narrow-band CARS. In addition, T_{tr} and gas density distributions N and N_e over the cross section of the cell were measured by optical interferometry and emission spectroscopy. At this stage, the discharge became quasi-stationary and its current remained at the level I_d = 20–50 mA.

From the measured values of p, T_{tr}, and electrode voltage, we found E/N. Electric field strength E in the positive column of the glow was determined with regard to the cathode drop [2], and molecular concentration N at the discharge axis was determined with allowance for a decrease in the gas density as a result of heating. The values of E/N varied from 40 to 80 Td. To take the time dependence of T_{tr} along the axis of the cell and the distribution of this temperature over the cell's cross section, we used a two-pass Michelson interferometer [20, 21].

As a source of monochromatic radiation in the interferometer, a single-mode 632.8-nm He–Ne laser with an output of 50 mW was applied. The laser beam was expanded to 4 cm in diameter with a telescope and then was wedge-split into two, object and reference, beams. The former was directed toward a mirror through the windows, reflected from the mirror, and then (upon being made coincident with the reference beam on the wedge) fell on a lens together with the reference beam reflected from the mirror. Such a double-pass optical scheme was used to improve the sensitivity of the setup at low pressures. Another lens with a focal length of 150 cm placed before the splitter matched the size of the interference pattern to that of the camera frame and to the slit of a photoelectric multiplier (PM). Photographing of the interference pattern provides information on the T_{tr} distribution along the radius of the gas-discharge tube. The maximal displacement of the fringes at the discharge axis was equal to 3.2–8.0 widths of the fringe. The fringe displacement was measured accurate to 0.2 of the fringe width. The axial displacement of the fringes was detected by the PM. The 0.3×4.5-mm^2 slit before the PM cathode was placed in such a way that its center was coincident with the center of the interference pattern. The fringes ran parallel to the slit. The signal from the PM was displayed on the screen of the oscilloscope. The time resolution of the PM was 5 μs. The typical waveforms of PM signals and typical interferograms were demonstrated earlier [22, 23]. The fringe displacement measurements were processed by the method described in [20, 21].

The variation of electron concentration N_e at the cell axis in time was calculated from the dependence of the current on the electron drift velocity and discharge cross section S_d ($S_d = \pi R_f^2$, where R_f is the effective radius of the current filament, which is found by the technique described in [14]). The drift velocity was found by solving the Boltzmann equation for the EEDF. As input data, the measured parameters of the glow discharge plasma were used.

It has been experimentally established [14] that, at p = 15–20 Torr in a contracted discharge, the distribution of the radiation intensity from the nitrogen second positive system over the cell's cross section correlates with the electron concentration distribution over the cross section. Therefore, the value of R_f was determined from the distribution of radiation intensity $I_\lambda(r)$ along cell radius r at wavelengths λ = 337, 354, 358, and 380 nm of the nitrogen second positive system. Intensity $I_\lambda(r)$ was measured with a photoelectric spectral instrument equipped with two 2×2-mm diaphragms. The spatial resolution along the cell radius was 2 mm. Effective radius R_f was determined from the relationship [14]

$$R_f^2 = 2\int_0^R \frac{I_\lambda(r)}{I_\lambda(0)} r\,dr. \quad (1)$$

In the stationary glow discharge, the rotational temperature and the populations of nitrogen molecule vibrational levels v = 0–4 in the ground state were measured with a Sopra (France) CARS spectrometer.

The second harmonic of a Nd^{3+} : YAG laser at the frequency corresponding to wavenumber ν_1 = 18797 cm^{-1} (the peak energy is 50 mJ, a pulse width of 25 ns, and a pulse repetition rate of 10 Hz)) and the radiation of a tunable dye laser (the peak energy 1 mJ at the frequency corresponding to wavenumber ν_2 = 16475 cm^{-1}) were focused along the positive column of the glow by a lens with a focal length of 50 cm. The populations of the levels at p = 3.5 Torr were measured with the collinear beams. Such a scheme provided a spatial resolution of 250 μm × 250 μm × 4 cm. When the vibrational temperature was measured at p = 11–20 Torr, the spatial resolution was raised by using sharp focusing of the beams in plane (Planar BOXCARS approach). Such an approach allowed us to improve the spatial resolution to $250 \times 250 \times 500$ μm. The valid signal at anti-Stokes frequency ω_{aS} was separated out from the total discharge and laser radiation by wide-band filters and a concave-grating monochromator. The CARS valid signal was recorded in the counting mode with an optical spectrum multichannel analyzer (OSMA).

To find the populations of the vibrational levels, we recorded the intensity distribution in the spectrum of

the Q branch of vibrational–rotational transitions from $v = 0 \longrightarrow v = 1$ (Q_{01}) to $v = 4 \longrightarrow v = 5$ (Q_{45}). The MVDF was determined from the CARS spectra by the method suggested in [22]. Rotational temperature T_{rot} was determined from the vibrational–rotational Raman spectrum of the Q branch of vibrational transition $v = 1 \longrightarrow v = 2$. From the experimentally found spectrum, the dependence of $\ln(N_J/g_J)$ on $J(J + 1)$ was constructed (N_J is the population of a rotational level with quantum number J, and g_J is the order of its degeneracy). When constructing this dependence, we took into account the degeneracy orders of rotational levels and spin degeneracy of the ground state. The rotational temperature was found from the slope of the straight line

$$\ln(N_J/g_J) = \text{const} + J(J+1)\frac{B_e}{kT_{rot}}, \qquad (2)$$

which was constructed by the rms method under the assumption that the populations of rotational levels obey the Boltzmann distribution. Here, B_e is the rotational constant of a nitrogen molecule and k is the Boltzmann constant. Under our experimental conditions, the translational and rotational temperatures coincide.

KINETIC MODEL

Figure 2 shows the scheme for finding the EEDF and MVDF, as well as for elucidating mechanisms underlying their interplay and gas heating. When finding the MVDF and low-energy part of the EEDF, we varied total (over the first eight vibrational levels) vibrational excitation cross section σ_Σ and rate constants of VV exchange in order to achieve the best agreement between the computational results and experimental data. Next, to improve the reliability of extracted quantitative information on the EEDF, MVDF, σ_Σ, and rate constants of VV exchange, the number of measured glow discharge plasma parameters used as input data was taken as large as possible.

The EEDF and its basic moments, drift velocity v_{dr} and characteristic temperature D/μ of electrons in the glow discharge plasma, were found by numerically solving the Boltzmann equation. The input data for determining the EEDF were measured values of E and T_{tr}. The value of E/N was found with regard to the cathode drop and a change in molecular concentration N due to gas heating. The cathode drops for various materials used as glow-sustaining electrodes are given in [2].

When comparing the calculated and measured [10, 11] EEDFs in the typical experimental range E/N = 40–80 Td (Table 1), we varied σ_Σ and vibrational temperature T_v of the first vibrational level ($T_v = \theta_v/\ln(N_1/N_0)$), where θ_v is the vibrational quantum of a nitrogen molecule).

The EEDF and MVDF were found by iterations from a solution to the Boltzmann equation and kinetic equations that describe the balance of vibrationally excited molecules and variation of the gas chemical composition. This set of equations also included an equation for T_{tr} variation in the isobaric approximation. The exited particle concentration obtained by calculation was used to refine the EEDF, which varies with the chemical composition of the gas and due to electron collisions of the second kind with excited particles. From the EEDF calculated, rate constants K_i, v_{dr}, electron energy losses η_{elas} due to electron–heavy particle elastic collisions, and electron energy losses η_{rot} due to molecule rotational excitation were found. The values

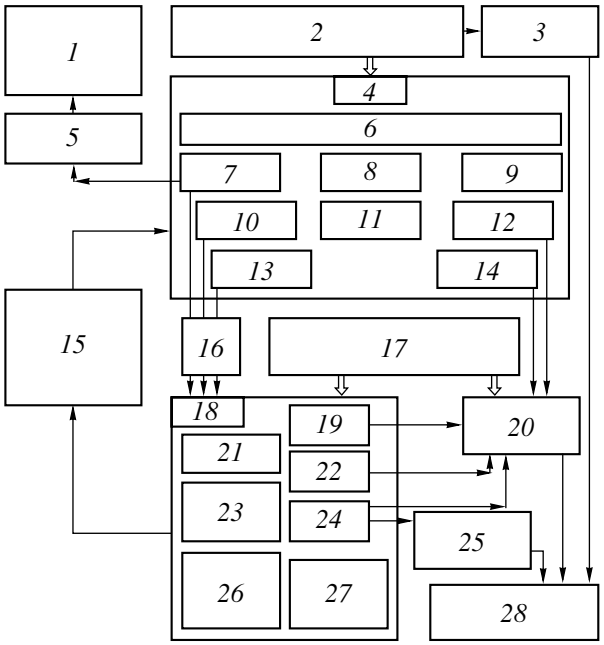

Fig. 2. Block diagram of calculating the discharge kinetics. (*1*) Comparison of calculated and experimental data for EEDF, v_{dr}, and D/μ; (*2*) input experimental data for EEDF, E/N, T_{tr}, and T_v; (*3*) variation of T_v and comparison with experiment; (*4*) EEDF; (*5*) refinement of cross section σ_Σ by comparing calculation and experiment; (*6*) heating of electrons by electric field E; (*7*, *21*) electron-impact-induced vibrational excitation of molecules; (*8*) electron-impact-induced ionization of molecules and atoms; (*9*) electron-impact-induced excitation of Rydberg states of molecules; (*10*, *23*) electron-impact-induced excitation of molecules and atoms; (*11*) electron–electron collisions; (*12*) electron–molecule and electron–atom elastic collisions; (*13*) electron-impact-induced dissociation of molecules; (*14*) electron-impact-induced rotational excitation of molecules; (*15*) iterations to determine EEDF, MVDF, v_{dr}, D/μ, T_{tr}, and T_v; (*16*) reaction rate constants K_i; (*17*) input experimental data for heat conduction equation and calculation of MVDF (N, R, N_e, γ_v, γ_{at}, and T_v); (*18*) MVDF; (*19*) VT molecule–molecule relaxation; (*20*) gas heating and heat removal toward the cell wall; (*22*) VT molecule–atom relaxation; (*24*) VV molecule–molecule energy exchange; (*25*) refinement of VV exchange rate constants by comparing calculation with experiment; (*26*) diffusion of excited molecules and atoms followed by heterogeneous relaxation at walls; (*27*) dissociation of molecules by electron impact and via vibrational excitation; and (*28*) comparison of calculated and experimental data for MVDF, T_v, and T_{tr}.

Table 1

T_{tr}, K		T_v, K		P, Torr	R, cm	t, ms	N_e, cm^{-3}	E/N, Td	Refs.
experiment	theory	experiment	theory						
530 ± 30^{CARS}	470 ($\gamma_v = 10^{-4}$)	5300 ± 350^{CARS}	4960 ($\gamma_v = 10^{-4}$)	2.0	1.0	11	2×10^{10}	80	[28]
	420 ($\gamma_v = 10^{-3}$)		4250 ($\gamma_v = 10^{-3}$)						
480 ± 40^{CARS}	512 ($\gamma_v = 10^{-4}$)	3790 ± 350^{CARS}	3700 ($\gamma_v = 10^{-4}$)	3.5	1.8	20	3.5×10^{9}	45	[22]
	470 ($\gamma_v = 10^{-3}$)		3475 ($\gamma_v = 10^{-3}$)						
530 ± 40^{CARS}	545 ($\gamma_v = 10^{-4}$)	4320 ± 350^{CARS}	4255 ($\gamma_v = 10^{-4}$)	7.0	1.8	15	1.2×10^{10}	60	
520 ± 50^{OI}	530 ($\gamma_v = 10^{-3}$)		4200 ($\gamma_v = 10^{-3}$)						
600 ± 40^{CARS}	610 ($\gamma_v = 10^{-4}$)	4270 ± 350^{CARS}	4240 ($\gamma_v = 10^{-4}$)	9.5	1.8	15	6×10^{9}	70	
570 ± 50^{OI}	605 ($\gamma_v = 10^{-3}$)		4240 ($\gamma_v = 10^{-3}$)						
395 ± 15^{CARS}	400 ($\gamma_v = 10^{-4}$)	2850 ± 100^{CARS}	2790 ($\gamma_v = 10^{-4}$)	12.0	0.7	30	$\propto 10^{9}$	<100	[27]
	360 ($\gamma_v = 10^{-3}$)		2615 ($\gamma_v = 10^{-3}$)						
1000 ± 100^{CARS}	1135 ($\gamma_v = 10^{-4}$)			15.0	1.8	30	2×10^{10}	70	
1140 ± 110^{OI}	1135 ($\gamma_v = 10^{-3}$)								
1200 ± 110^{CARS}	1230 ($\gamma_v = 10^{-4}$)			20.0	1.8	30	4×10^{10}	68	This work
1230 ± 120^{OI}	1230 ($\gamma_v = 10^{-3}$)								
1350 ± 130^{CARS}	1300 ($\gamma_v = 10^{-4}$)			30.0	1.8	30	5×10^{10}	67	
1300 ± 350^{OI}	1300 ($\gamma_v = 10^{-3}$)								
$1150–1200^{OI}$	1170 ($\gamma_v = 10^{-4}$)			20.0	1.0	30	3.9×10^{10}	59	[14]
	1170 ($\gamma_v = 10^{-3}$)								

of K_i, ν_{dr}, η_{elas}, and η_{rot} thus obtained were then used in calculating the variation of the gas composition in the plasma, N_e, and gas heating dynamics, respectively. Importantly, the rate constants of *VV* exchange and cross sections σ_Σ were refined at each iteration by comparing the calculated and experimental MVDF and T_{tr}, as well as the EEDF and its basic moments. Such a procedure was repeated until the rate constants and cross section started converging.

When determining N_e and T_{tr}, we took into consideration their nonuniform distribution over the cross section of the cell. In solving the master equation for the composition, allowance was made for particle diffusion toward the walls followed by heterogeneous (*VW*) relaxation in order to estimate the effect of these processes on the MVDF and gas heating.

KINETIC EQUATION FOR THE ELECTRON ENERGY DISTRIBUTION FUNCTION

The homogeneous Boltzmann equation was solved by the two-term approximation method, according to which the EEDF is expanded into a series in spherical harmonics (Legendre polynomials) up to the first two terms, which specify its isotropic part $f(\varepsilon)$ and current characteristics of electrons.

Isotropic part $f(\varepsilon)$ was obtained by solving the equation with regard to (i) electron–atom and electron–molecule elastic collisions; (ii) excitation of $A^3\Sigma_u^+$, $B^3\Pi_g$, $C^3\Pi_u$, $B'^3\Sigma_u^-$, $a'^1\Sigma_u^-$, $W^3\Delta_u$, $a^1\Pi_g$, $w^1\Delta_u$, and $a''^1\Sigma_g^+$ electron and Rydberg rotational and vibrational states, as well as electron-impact-excited (hereafter, impact-excited) states ^2P and ^2D; (iii) impact-induced dissociation of molecules in the ground state and also through electron levels with passage to repulsive terms; (iv) ionization of molecules in the ground state due to electron–molecule collisions; (v) impact-induced ionization of atoms from ground state ^4S; (vi) collisions of the second kind between vibrationally excited molecules that are in ground $X^1\Sigma_g^+$ state (only for the first ten levels) and in the impact-excited states listed above (except for state $a''^1\Sigma_g^+$) and electrons; and (vii) collisions of the second kind between electrons and atoms in impact-excited states ^2P and ^2D.

In the spatially homogeneous approximation, the equation for the isotropic part of the EEDF has the form [7–9]

$$\frac{E^2\varepsilon}{3\sum_l N_l\sigma_{ml}(\varepsilon)}\frac{df(\varepsilon)}{d\varepsilon} + \sum_l 2\frac{m}{M_l}N_l\varepsilon^2\sigma_{ml}(\varepsilon)$$

$$\times\left[f(\varepsilon)+\frac{T_{tr}}{e}\frac{df(\varepsilon)}{d\varepsilon}\right]+NB_e\varepsilon\sigma_{rot}(\varepsilon)$$

$$\times\left[f(\varepsilon)+\frac{T_{tr}}{e}\frac{df(\varepsilon)}{d\varepsilon}\right]=-\sum_l N_l\sum_{i,j}\int_{\varepsilon}^{\varepsilon+\varepsilon_{ij}}\sigma_{ij}(\varepsilon')\varepsilon' f(\varepsilon')d\varepsilon' \quad (3)$$

$$-\sum_{i,j}N_j\int_{\varepsilon}^{\varepsilon-\varepsilon_{ij}}q_{ij}(\varepsilon')\varepsilon' f(\varepsilon')d\varepsilon'.$$

Here, m and M_l are the masses of an electron and molecule ($l = 0$) or atom ($l = a$); N_l is the concentration of molecules or atoms in the ground state; ε is the electron energy; ε_{ij} is the change in the electron energy due to electron–molecule or electron–atom collisions; $\sigma_{ml}(\varepsilon)$ is the transport scattering cross section of an electron by a nitrogen molecule ($l = 0$) or atom ($l = a$); $\sigma_{rot}(\varepsilon)$ is the cross section of electron-impact-induced vibrational level excitation; $\sigma_{ij}(\varepsilon)$ are the cross sections of dissociation, ionization, vibrational level excitation, and electron level excitation for a molecule or atom in the case of direct reactions; q_{ij} are the cross sections of collisions of the second kind between electrons and molecules or atoms in impact-excited states, which is calculated from the principle of detailed balance; and N_j is the concentration of molecules and atoms, as well as vibrationally excited molecules in electron state $X^1\Sigma_g^+$ for vibrational levels $1 \le v \le 10$. The set of cross sections is the same as used in [7–9].

The first term in the left of Eq. (3) stands for an increase in the electron energy in field E; the second, for energy losses in electron–molecule and electron–atom elastic collisions; and the third, for energy losses due to electron-impact-induced excitation of nitrogen molecule vibrational levels. The right of this equation describes electron–heavy particle inelastic collisions, which change the energy state of the particles (the transition from state i to state j with energy change ε_{ij} or $-\varepsilon_{ij}$ for electron collisions of the second kind with excited heavy particles). The form of the equation implies that electron–electron collisions are disregarded.

The EEDF is normalized as follows:

$$\int_0^\infty\sqrt{\varepsilon}f(\varepsilon)d\varepsilon = 1. \quad (4)$$

The Boltzmann equation for the EEDF was solved by iterations [9]. The function calculated by the method given in [24] was used as a zeroth-order approximation.

The rate constants for excitation of nitrogen molecule electron states from unresolved higher vibrational levels of ground state $X^1\Sigma_g^+$ were calculated by relationships derived in [25]. Other rate constants for electron–heavy particle interaction were found by normalizing the cross sections of related reactions by the EEDF,

$$K_i = \sqrt{\frac{2e}{m}}\int_0^\infty\sigma_{ij}(\varepsilon)\varepsilon f(\varepsilon)d\varepsilon. \quad (5)$$

The values of v_{dr} and D/μ were determined from the relationships [26]

$$D/\mu = \int_0^\infty\frac{\varepsilon}{\sigma_m(\varepsilon)}f(\varepsilon)d\varepsilon\Big/\int_0^\infty\frac{\varepsilon}{\sigma_m(\varepsilon)}\frac{df(\varepsilon)}{d\varepsilon}d\varepsilon, \quad (6)$$

$$v_{dr} = 1/3\sqrt{\frac{2e}{m}}E/N\int_0^\infty\frac{\varepsilon}{\sigma_m(\varepsilon)}\left[-\frac{df(\varepsilon)}{d\varepsilon}\right]d\varepsilon. \quad (7)$$

MASTER EQUATIONS FOR GAS COMPONENTS AND GAS HEATING

The glow discharge positive column is characterized by a complex composition, many kinetic processes, and nonuniform distribution of parameters (molecular, atomic, and electron concentrations; gas temperature; etc.) over the column's cross section. When processing experimental data obtained in this work and in [14, 22, 27, 28], we took into consideration (i) nitrogen molecules in ground state $X^1\Sigma_g^+$ (47 vibrational levels, among which the level $v = 46$ was assumed to be a level of dissociation via vibrational excitation) and in impact-excited states $A^3\Sigma_u^+$, $B^3\Pi_g$, $C^3\Pi_u$, $B'^3\Sigma_u^-$, $a'^1\Sigma_u^-$, $W^3\Delta_u$, $a^1\Pi_g$, and $w^1\Delta_u$; (ii) nitrogen atoms in the ground, ^4S, and excited, ^2P and ^2D, states; and (iii) electrons e. The processes and rate constants that were included in describing the glow discharge plasma kinetics are listed in [7, 25].

Furthermore, the master equations for particles and gas temperature must include diffusion and transport phenomena, which greatly complicates the solution of the problems stated. A method was suggested [29, 30] that makes it possible to simplify the partial differential equations. With this method, the set of partial differential equations is reduced to a set of stiff ordinary differential equations for plasma parameters averaged over the cell's cross section. In experiments, however, the discharge parameters are usually measured at the axis of the cell. The approach used in this work allows one to derive a set of stiff ordinary differential equations for the parameters that describe the state of the plasma at the axis of the positive column with regard to heat removal and diffusion of vibrationally excited molecules and atoms from the positive column axis toward the walls with subsequent heterogeneous relaxation of the molecules and recombination of atoms. This approach is based on the assumptions that (i) during the establishment of the gas parameters, the radial profiles of the translational temperature and particle concentration are near-stationary; (ii) pressure p is constant along

the positive column; and (iii) the gas flow velocity, as well as the rates of dissociation and ionization, in the positive column are high.

It was also assumed that, in the diffusion- and/or recombination-controlled positive column, energy release $V_T(r)$ and atomic (molecular) concentration $V_{v,\,at}(r)$ vary along the cell radius by the law

$$V_{x,\,T}(r) = V_{x,\,T}(0)(1-(r/R)^z). \quad (8)$$

Here, z is an approximation parameter that is determined by comparing the calculated and measured radial temperature profiles $T_{tr}(r)$. Quantities $V_T(0)$ and $V_{v,\,at}(0)$ express, respectively, heat removal and diffusion of vibrationally excited molecules and atoms from the discharge axis with subsequent heterogeneous relaxation of the molecules and recombination of the atoms at the walls. Under the above assumptions, these quantities as functions of T_{tr} and particle concentration at the cell axis were found by solving the heat conduction and diffusion equations with appropriate boundary conditions [29, 30],

$$\frac{1}{r}\frac{\partial}{\partial r}\left(rD_x\frac{\partial N_x}{\partial r}\right) = -V_x(r), \quad (9)$$

$$\left.\frac{\partial N_x}{\partial r}\right|_{r=0} = 0, \quad \left.D_x\frac{\partial N_x}{\partial r}\right|_{r=R} = \left.\frac{\gamma_x\langle v_x\rangle}{4}N_x\right|_{r=R}, \quad (10)$$

$$\frac{1}{r}\frac{\partial}{\partial r}\left(r\chi\frac{\partial T_{tr}}{\partial r}\right) = -V_T(r), \quad (11)$$

$$\left.\frac{\partial T_{tr}}{\partial r}\right|_{r=0} = 0, \quad T_{tr}|_{r=R} = T_w, \quad \chi = \chi_0(T_{tr}/273)^a. \quad (12)$$

Here, $\langle v_x\rangle$ ($x = v$ or at) is the mean thermal velocity of molecules or atoms; γ_x is the probability of deactivation of the molecules or recombination of the atoms at the walls; N_x is the concentration of vibrationally excited molecules, $N_2(X^1\Sigma_g^+, v)$, or atoms, $N(^4S)$; D_x is the diffusion coefficient of the molecules or atoms; and $\chi_0 = 2.3\times10^{-4}$ W/(K cm) is the thermal conductivity [31]. For nitrogen molecules, $\alpha = 0.84$.

Regardless of vibrational level v, the diffusion coefficients were set equal to [31]

$$D_v = \frac{136.8}{p}(T_{tr}/273)^{1.5}, \quad D_{at} = \frac{220.4}{p}(T_{tr}/273)^{1.74}, \quad (13)$$

where p is expressed in Torr.

Under the experimental conditions considered, heterogeneous relaxation of the molecules proceeds largely through physical adsorption [1],

$$W + N_2(X^1\Sigma_g^+, v+1) \Rightarrow W + N_2(X^1\Sigma_g^+, v), \quad (14)$$

$$W + N(^4S) + N(^4S) \Rightarrow W + N_2(X^1\Sigma_g^+, v). \quad (15)$$

The value of γ_v was varied from 10^{-4} to 10^{-3} depending on the cell material (quartz, glass, or Pyrex), while γ_{at} was set equal to 10^{-4} [1, 4]. The temperature of the cell walls was taken to be $T_w = 300$ K. Calculations showed that wall (surface) deactivation of impact-excited molecules and atoms is a much weaker process than volume quenching of the excitation and, hence, may be ignored under our experimental conditions [14, 22, 27, 28].

The translational temperature profile taken by optical interferometry is given by

$$T_{tr}(r) = T_w\left[1+(1-(r/R)^2)\frac{(0.25-(r/R)^z/(z+2)^2)}{(0.25-1(z+2)^2)}\times((T_{tr}/T_w)^{\alpha+1}-1)\right]^{\frac{1}{1+\alpha}}. \quad (16)$$

For such a profile of $T_{tr}(r)$, thermal losses $V_T(0)$ at the axis are expressed (in terms of K/s) as

$$V_T(0) = \frac{4T_w\chi_0}{R^2(1+\alpha)}(T_{tr}/T_w)^\alpha\frac{[(T_{tr}/T_w)^{\alpha+1}-1]}{\left[1-\frac{4}{(z+2)^2}\right]}. \quad (17)$$

The variation of the concentration of molecules in the state with quantum number $v = 0$ or atoms due to diffusion from the discharge axis is given by

$$V_{0,\,at} = \frac{N_{1,\,at}}{\tau_\gamma+\tau_D}. \quad (18)$$

In the master equation, this term describes an increment of molecules in the state with $v = 0$ through VW deactivation of those in the state with $v = 1$. For atoms, this term describes a decline in the concentration because of wall recombination. The associated relationship for molecules with $v \geq 1$ has the form

$$V_v(0) = \frac{N_{v+1}-N_v}{\tau_\gamma+\tau_D}. \quad (19)$$

Characteristic times τ_D and τ_γ for diffusion and VW deactivation of molecules (recombination of atoms) at the wall depend on the translational temperature at the cell axis as follows:

$$\tau_D = \frac{R^2[0.25-1/(z+2)^2][(T_{tr}/T_w)^{1+\alpha}-(T_{tr}/T_w)^{\beta_{v,\,at}}]}{D_{v,\,at}[1-\beta_{v,\,at}/(1+\alpha)][(T_{tr}/T_w)^{1+\alpha}-1]},$$
$$\tau_\gamma = \frac{4R(0.5-1/(z+2))}{\langle v_{v,\,at}\rangle\gamma_{v,\,at}}. \quad (20)$$

Thus, in view of the earlier found expressions for $V_{v,\,at}(0)$ and $V_T(0)$, the simplified master equations for the excited particle concentration and translational temperature in the isobaric approximation have the form of

stiff ordinary differential expressions of type

$$\frac{dN_i}{dt} = \sum_f \sum_j k_{ji}^f N_j - \sum_f \sum_j k_{ij}^f N_i + \sum_f \sum_j k_{ji}^f N_i N_j$$

$$- \sum_f \sum_j k_{ij}^f N_i N_j + \sum_f \sum_j \sum_l k_{jil}^f N_j N_i N_l \qquad (21)$$

$$- \sum_f \sum_j \sum_l k_{ijl}^f N_i N_j N_l - \frac{N_i}{T_{tr}} \frac{dT_{tr}}{dt} + V_i(0),$$

$$3.5kN \frac{dT_{tr}}{dt} = \sum_j \Delta\varepsilon_{ij} \frac{dN_i}{dt} - V_T(0). \qquad (22)$$

The first two terms in Eqs. (21) and (22) describe one-particle processes responsible for an increase or decrease in the concentration of particles of sort i as a result of which a particle of sort j disappears or appears (such processes are, for example, radiation-induced processes). The third and fourth terms stand for two-particle processes, such as impact-induced excitation or de-excitation of molecules or atoms, *VT* molecule–molecule and molecule–atom relaxation, one-quantum *VV* exchange, molecular dissociation, and exchange reactions between molecules and atoms in the ground and impact-excited states. The fifth and sixth terms account for three-particle processes: recombination of nitrogen atoms in the ground and impact-excited states. Here, subscripts j and l denote the sort of interacting particles. The last two terms describe the thermal expansion of the elementary volume of the gas and diffusion of excited molecules and atoms toward the cell walls with subsequent *VW* heterogeneous relaxation. Superscript f indicates the type of reaction between the components, since the same pair of particles may be involved in reactions of several types.

When numerically simulating the MVDF, rate constant K_{10}^{01} of *VV* exchange was varied until the best agreement between the calculated and measured values of vibrational temperature T_v was achieved.

The basic factors that govern the translational temperature, i.e., are responsible for gas heating in a wall-bounded discharge, are (i) *VT* relaxation of excited molecules on molecules and resulting atoms, (ii) vibrational energy losses due to *VV* exchange between molecules, (iii) electron–molecule and electron–atom elastic collisions, (iv) excitation of molecular vibrational levels by an electron impact, and (v) thermal losses due to a translational temperature gradient. The model at hand also includes processes with the participation of molecules and atoms in excited states. These processes may noticeably affect the populations of vibrational levels responsible for the MVDF formation and, thereby, indirectly influence the gas heating dynamics. On the other hand, since the amount of energy directly converted to heat via collisions of molecules in ground state $X^1\Sigma_g^+$ and metastable states $A^3\Sigma_u^+$ and $B^3\Pi_g$ is not known exactly [6, 17], the direct contribution of these processes to gas heating was not carefully analyzed and so calls for further investigation. Note that gas heating due to ionization of molecules and atoms was not taken into consideration as well.

The set of equations was solved numerically by the method suggested in [32]. At the zero time, the MVDF corresponded to the Boltzmann distribution for T_{tr} = 300 K. The concentrations of atoms and molecules in the excited states were set equal to zero. In the course of integration of the equations for particle concentrations, the rate constants for vibrational excitation of the molecules were recalculated according to the variation of the vibrational temperature of the first excited level (300 K $\le T_v \le$ 6000 K) and translational temperature (300 K $\le T_{tr} \le$ 6000 K) with time.

RESULTS AND DISCUSSION

Electron energy distribution function. Figs. 3a–3c compare the calculated EEDF and the EEDF measured by the probe method [10, 11] for the quasi-stationary glow discharge. At E/N = 60–140 Td, the calculation and measurements are in good agreement when T_v = 3800–4000 K. It is these values of the vibrational temperature that were obtained by the CARS method under the conditions considered (Table 1).

In the quasi-stationary mode of the glow discharge plasma, near-resonance *VV* exchange, together with molecule–electron inelastic collisions, plays an essential role in redistribution of populations N_0 and N_1 over vibrational levels. Therefore, T_v depends on rate constant K_{10}^{01} of *VV* exchange. To provide simultaneous agreement between experimental and calculated data for the MVDF (lower states) and EEDF, σ_Σ was varied together with K_{10}^{01}. The former parameter ranged from 3.0 and 13.3 Å^2 (see [5 and Refs. cited therein]); the latter, from 9×10^{-15} to 1.5×10^{-13} cm^3/s [6, 33–36]. For the EEDF, the calculation and measurements are in best agreement when σ_Σ = 9–10.6 Å^2 and $K_{10}^{01} = 9 \times 10^{-15}$ cm^3/s, which almost coincides with the values recommended in [5, 6], respectively.

Thus, both the theory and experiment indicate the presence of an additional mechanism behind *VV* energy exchange between molecules in lower excited states, this mechanism indirectly influencing the form of the EEDF. For the nonequilibrium glow discharge plasma, a consistent description of the electronic component kinetics and vibrational kinetics is only possible if electron collisions of the first and second kind with vibrationally excited molecules and *VV* exchange in the states with quantum numbers v = 0 and 1 are taken into consideration concurrently.

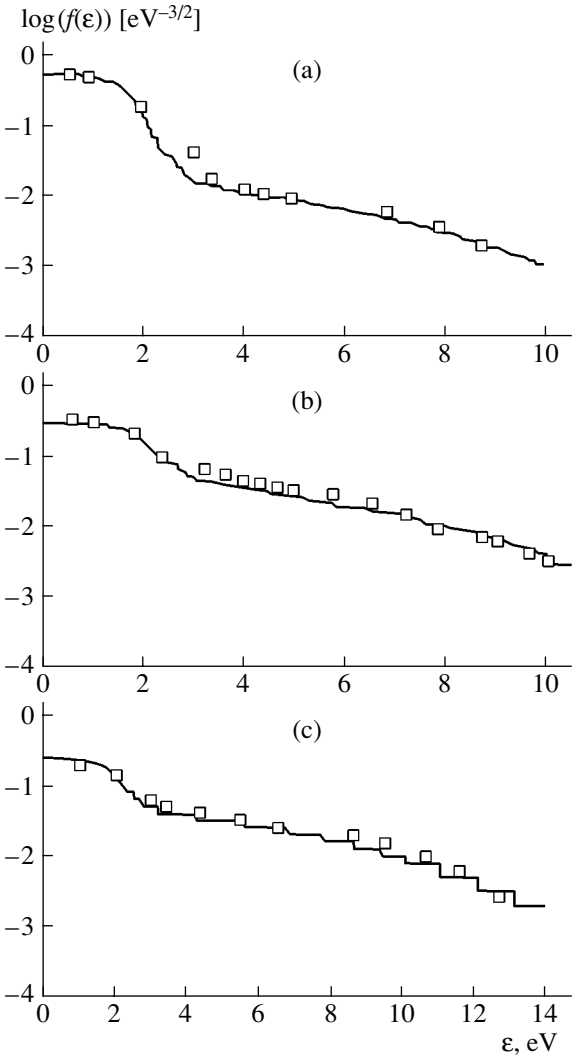

Fig. 3. EEDF in the glow discharge nitrogen plasma: (a) E/N = 60 Td, T_v = 3800 K; (b) E/N = 80 Td, T_v = 4000 K; and (c) E/N = 140 Td, T_v = 4000 K. Lines, calculation; squares, data points [10, 11].

As follows from calculations, the production of atoms affects the EEDF insignificantly when the degree of dissociation of molecules does not exceed 10^{-3}. *VT* molecule–atom relaxation also remains the MVDF for the first eight to ten vibrational levels and, hence, the EEDF is unaffected.

As E/N exceeds 70 Td, the electron energy is spent mostly on the excitation of electron degrees of freedom, as well as on dissociation and ionization of molecules. At E/N = 80 and 140 Td, variation of the vibrational temperature changes the EEDF only slightly. As follows from Figs. 3b and 3c, good agreement between the calculation and experiment is achieved when T_v is no higher than 4000 K.

The calculated values of drift velocity v_{dr} and characteristic temperature D/μ of electrons are consistent with reference data [26] in the range E/N = 10–85 Td.

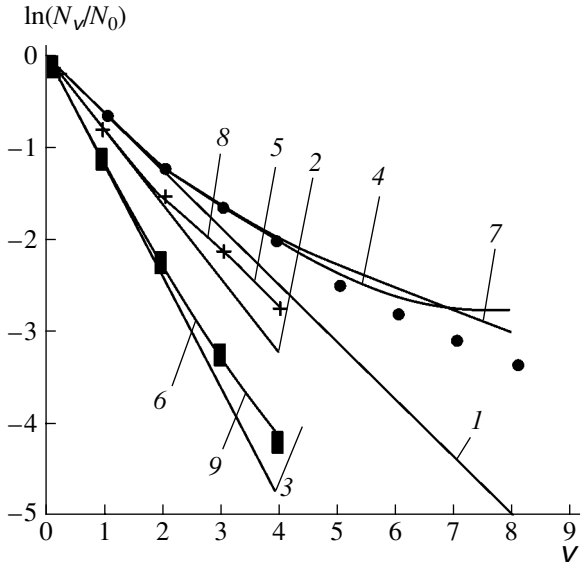

Fig. 4. MVDF in the glow discharge. Data points are taken from (■) [27], (+) [22], and (●) [28]. Computational results are shown by solid lines. Boltzmann distribution: T_v = (*1*) 5300, (*2*) 4320, and (*3*) 2850 K. Treanor distribution: (*4*) T_v = 5300 K, T_{tr} = 530 K; (*5*) T_v = 4320 K, T_{tr} = 530 K; and (*6*) T_v = 2850 K, T_{tr} = 395 K. (*7–9*) Calculation by the model adopted in this work. v is the vibrational quantum number.

Molecule vibrational distribution function and gas heating. Table 1 and Figs. 4 and 5 compare the computational results for the MVDF, T_{tr}, and T_v with the measurements performed in this work and in [4, 22, 27, 28]. Figure 5 shows the evolution of T_{tr} from its initial (at the time the discharge is initiated) to a steady-state value.

The experimental data listed in Table 1 were obtained in the positive column of the glow discharge plasma at the cell axis. Superscripts OI and CARS indicate that associated T_{tr} and T_v were measured by the methods of optical interferometry and CARS, respectively.

Temperatures T_{tr}^{CARS} and T_v^{CARS} were found from the populations of rotational and first two vibrational levels that were determined from the CARS spectra. The solid lines in Fig. 4 refer to the MVDFs calculated according to the kinetic model, as well as to the Boltzmann and Treanor distributions.

Residence time t of nitrogen molecules in the discharge zone listed in Table 1 coincides with the time of setting the quasi-stationary values of T_{tr} and T_v, which characterize the MVDF in the positive column. The quasi-stationary values of T_{tr} at pressures of 15 and 20 Torr are presented in Table 1 and in Figs. 5a and 5b. Figure 5 also shows the experimental time dependence of the current that was used in calculating T_{tr}. The calculation and measurements of T_{tr} and T_v indicate that

the quasi-stationary MVDFs for the first two vibrational levels and quasi-stationary T_{tr} are set within 15–20 ms.

The setting time for T_{tr} and T_v seems to depend on experimental conditions and is specified, directly or indirectly, by gas pressure p, wall temperature T_w, electron concentration N_e, reduced electric field E/N (which characterizes the discharge-sustaining power supply), probability γ_v of heterogeneous deactivation of the molecule vibrational energy, discharge tube radius R, positive column length L, and gas flow velocity (all the initial parameters are listed in Table 1). This list should be supplemented by other important parameters, namely, reaction rate constants K_i (which are related to the EEDF), T_{tr}, T_v, and elastic and inelastic cross sections.

The parenthetic figures by the values of T_{tr} and T_v in Table 1 are probabilities γ_v of vibrational energy heterogeneous deactivation based on which the temperatures were calculated. The evolution of the MVDF and the gas heating kinetics (Figs. 4 and 5, respectively) were constructed using *VV* exchange rate constant K_{01}^{10} taken from [6, 25, 33]. In addition, we slightly modified the approximated dependence of *VV* exchange rate constants on T_{tr} and v (that was suggested in [37]) to achieve a good quantitative fit to experimental data.

Figure 6 demonstrates the MVDF evolution calculated with the aim of analyzing gas heating. Within time interval $t = 10^{-7}$–2.0×10^{-3} s (solid lines *1*–*5*), the electron energy is spent mostly on the vibrational excitation of molecules in the states with $v = 1$–10 (*eV* processes). The populations of these levels obey the Boltzmann distribution with a vibrational temperature markedly differing from temperature T_v of the first vibrational level. The kink in the MVDF curve indicates that the initial stage of the MVDF evolution is due largely to the impact-induced excitation and de-excitation of molecular vibrational states. It should be noted that the results of calculating the MVDF evolution at the initial stage of gas heating in the glow discharge plasma qualitatively agree with those obtained in [25].

From time instant $t \geq 3 \times 10^{-3}$ s (line *6*), the redistribution of molecules over lower vibrational levels proceeds via competition of *eV* processes and near-resonance *VV* exchange. For lower levels (v = 1–5), the MVDF as a function of T_{tr} and T_v is approximated well by the Treanor distribution, which remains valid with time.

As follows from the calculations in terms of our model, for discharge tube radius R = 1.8 cm and pressures ranging from 3.5 to 9.0 Torr, the effect of *VW* deactivation and diffusion of molecules on the populations of vibrational levels v = 1–5 is insignificant compared with that of resonance *VV* exchange and *eV* processes. At $t \geq 3 \times 10^{-3}$ s, the form of the MVDF for lower vibrational levels turns out to be slightly sensitive to the way of their excitation. This is because the characteristic times of nitrogen molecule redistribution over lower levels as a result of resonance *VV* exchange become much shorter than those of *VW* deactivation and diffusion of the molecules, as well as the times of impact-induced excitation and deexcitation of impact-excited molecules [1]. The Treanor form of the MVDF (curves *4*–*6* in Fig. 6) and the weak dependence of the vibrational temperature on molecule deactivation probability γ_v when γ_v varies by one order of magnitude (Table 1), are direct evidence for the dominance of *VV* exchange processes.

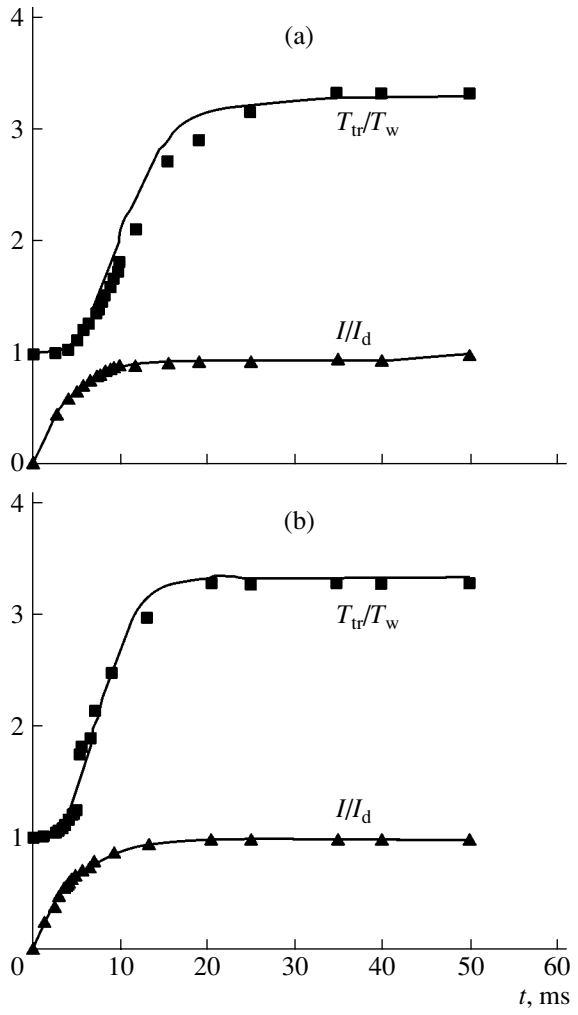

Fig. 5. Relative current I/I_d and relative gas temperature T_{tr}/T_w vs. time at the stage of discharge formation. Symbols, data points; solid lines, approximation of I/I_d and calculation of T_{tr}/T_w. (a) p = 20 Torr, I_d = 30 mA and (b) p = 15 Torr, I_d = 50 mA.

Table 2 lists rate constants K_{10}^{01} of *VV* exchange that were used in comparing the measured and calculated values of quasi-stationary T_v. As K_{10}^{01} grows, vibrational temperature T_v decreases noticeably. Contrasting the experimental and calculated values of the vibra-

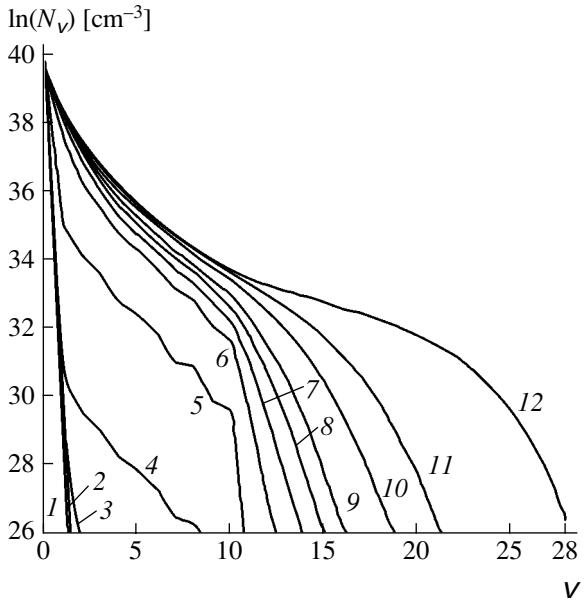

Fig. 6. MVDF at the stage of gas heating at p = 7 Torr. Time instants are (*1*) 10^{-7}, (*2*) 10^{-6}, (*3*) 10^{-4}, (*4*) 10^{-3}, (*5*) 2×10^{-3}, (*6*) 3×10^{-3}, (*7*) 4×10^{-3}, (*8*) 6×10^{-3}, (*9*) 7×10^{-3}, (*10*) 8×10^{-3}, (*11*) 15×10^{-3}, and (*12*) 15.5×10^{-3} s.

tional temperature, one can see that they are in quantitative agreement for *VV* exchange rate constant $K_{10}^{01} = 9 \times 10^{-15}$ cm^3/s, which is consistent with measurement and calculations performed elsewhere [6, 25, 33]. Note that the kinetic model in terms of which the EEDF is calculated in our work yields results similar to those obtained in [6], where the EEDF was assumed to be Maxwellian.

The results obtained in terms of the kinetic model are summarized in Table 1. It is seen that the calculated values of vibrational temperature T_v are one order of magnitude higher than the calculated values of T_{tr}. As the pressure grows from 3 to 10 Torr, the vibrational temperature varies between 3700 and 4400 K.

The values of the vibrational temperature obtained under experimental conditions [22] far exceed the values measured in [28]. This may be explained by the fact that the electron concentration in [28] is much higher than in the experiment [22]. The fact that, in [28], T_{tr} and T_v appreciably drop with increasing deactivation probability γ_v may be explained by a small radius of the discharge tube used in those experiments (as follows from Table 1). Furthermore, as follows from Fig. 4, the MVDF measured in [28] at $v > 6$ deviates markedly from the Treanor distribution. In this case, it becomes difficult to discriminate between effects due to *VV* exchange and impact-induced activation/deactivation of molecular vibrational levels and effects due to processes at the discharge cell walls. However, the calculations of T_{tr} and T_v performed for the experimental conditions [22] show that, as the pressure grows, the γ_v dependence of the temperatures becomes less pronounced.

At times far exceeding t = 3 ms (Fig. 6), molecules pass from lower to higher ($v \geq 10$) vibrational levels because of fast *VV* exchange, forming a plateau in the MVDF (curves *6–12*). As the plateau forms, T_{tr} at higher vibrational levels increases (see Fig. 5). The form of the MVDF is specified by competition between nonresonance *VV* energy exchange between molecules and *VT* processes. Specifically, the latter form the MVDF tail for $v \geq 15$, which is approximated well by the Boltzmann distribution with a temperature close to the translational temperature. Nonresonance *VV* exchange plays a significant role in increasing T_{tr}: it transfers a major part of the energy from vibrational to translational degrees of freedom because of molecule vibration anharmonicity.

In the time interval 4–10 ms (curves *7–10*), the calculated (using the *VV* exchange rate constants taken from [6, 25, 33] and the approximation suggested in [37]) and measured rates of rise of T_{tr} are nearly the same, ≈50 K/ms. The rate of rise of T_{tr} is related to nonresonance *VV* energy exchange between molecules in lower and higher ($10 < v < 15$) vibrational states. For T_{tr} = 300–500 K, the contribution of *VT* molecule–molecule and molecule–atom relaxation to heating is as low as less than several percent of the total energy deposition into translational and vibrational degrees of freedom.

Under our experimental conditions, atoms are produced mainly by direct impact-induced dissociation and also through electron levels with passage to repul-

Table 2

Experimental data		T_v calculated using published data for $K_{10}^{01} \times 10^{-14}$, cm^3/s (first row)				
		[6, 25, 33]	[13]	[34]	[35]	[36]
p, Torr	T_v, K	0.9	2.6	5.0	10	15
3.5	3790 ± 350	3764	3384	3266	3147	3093
7	4320 ± 360	4230	3642	3495	3356	3278
9.5	4270 ± 370	4183	3578	3451	3330	3266

sive terms. The effect of molecular dissociation through vibrational excitation and atomic losses due to volume recombination is minor. According to calculations, the fraction of dissociated molecules in the discharge positive column does not exceed 10^{-6}–10^{-4} by the time t = 10 ms. Thus, at such a low nitrogen molecule dissociation, the significance of channels for *VT* molecule–atom relaxation is low in terms of our model and, hence, *VT* relaxation has a negligible effect on the vibrational excitation and gas heating dynamics.

As follows from calculations, the processes involving nitrogen molecules and atoms in impact-excited states (see [25]) also contribute insignificantly to gas heating. For example, the occupation of impact-excited state $B^3\Pi_g$ of a nitrogen molecule through collisions of molecules in states $A^3\Sigma_u^+$ and $X^1\Sigma_g^+$ $(3 < v < 15)$ does not have a considerable effect on the gas heating dynamics. Neither do gas heating reactions involving atoms in metastable state ^2P and molecules in states $X^1\Sigma_g^+$ for $v > 8$, as well as reactions with the participation of molecules in state $A^3\Sigma_u^+$.

By the time t = 8–10 ms, thermal losses calculated for our experimental conditions do not exceed 20% of the heat release associated to nonresonance *VV* exchange.

For T_{tr} = 600–1000 K, the contributions of *VT* molecule–molecule relaxation and *VV* molecule–molecule exchange become comparable and are roughly compensated by thermal losses. As the pressure rises from 7 to 30 Torr, the values of T_{tr} both calculated for and measured at the quasi-stationary distribution of the glow discharge plasma parameters monotonically grow from 450 to 1300 K. At p > 10 Torr and at the same discharge current (50 mA) and E/N = 50–60 Td, the values of T_{tr} calculated and measured in this work and in [14] diverge only slightly in spite of a large difference in discharge cell radius. This is related to the fact that we are dealing with the contracted discharge. At p > 15 Torr, the glow is filamentary and is observed (localized) at the axis of the discharge cell. In this case, the thermal balance in the quasi-stationary positive column is controlled largely by relaxation processes taking place within a small area near the discharge axis, where the electron concentration is maximal. The wall cooling conditions influence the thermal balance to a small extent. For t > 20 ms, the values of T_{tr} measured in this work and in [14] and calculated using the vibrational–translational relaxation rate constants taken from [37] quantitatively coincide, as follows from Table 1.

It should be noted that the use of rate constants and cross sections other than those employed in the kinetic model may cause disagreement with our results. Particular emphasis should be on processes with a high excitation threshold, the correct description of which requires insight into the high-energy part of the EEDF.

ACKNOWLEDGMENTS

The authors are indebted to Yu.A. Levedev for encouragement and valuable discussion.

This work was supported by the Russian Foundation for Basic Research (grant nos.02-02-16021 and NWO 047.016.019) and the research program “Interaction of Plasma with Fast Gas Flows” at the Presidium of the Russian Academy of Sciences (program no. 20).

REFERENCES

1. D. I. Slovetskiĭ, *Mechanism of Chemical Reactions in Nonequilibrium Plasmas* (Nauka, Moscow, 1980) [in Russian].
2. Yu. P. Raizer, *Gas Discharge Physics* (Nauka, Moscow, 1992; Springer, Berlin, 1991).
3. Yu. B. Golubovskiĭ, A A. Kudryavtsev, I. A. Porokhova, *et al.*, in *Encyclopedia of Low-Temperature Plasma*, Ed. by V. E. Fortov (Nauka, Moscow, 2000), Vol. 2, pp. 18–43 [in Russian].
4. *Non-Equilibrium Vibrational Kinetics*, Ed. by M. Capitelli (Springer, Berlin, 1986; Mir, Moscow, 1989).
5. O. A. Gordeev and D. V. Khmara, Teplofiz. Vys. Temp. **32**, 133 (1994).
6. O. A. Gordeev and V. A. Shakhatov, Zh. Tekh. Fiz. **65** (7), 40 (1995) [Tech. Phys. **40**, 656 (1995)].
7. A. V. Bodronosov, K. A. Vereshchagin, O. A. Gordeev, *et al.*, Teplofiz. Vys. Temp. **34**, 666 (1996).
8. O. A. Gordeev, in *Encyclopedia of Low-Temperature Plasma*, Ed. by V. E. Fortov (Nauka, Moscow, 2000), Vol. 3, pp. 266–272 [in Russian].
9. O. A. Gordeev and D. V. Khmara, Mat. Model. **13** (9), 3 (2001).
10. Yu. A. Ivanov, Yu. A. Lebedev, and L. S. Polak, *Contact Diagnostic Methods in Nonequilibrium Plasma Chemistry* (Nauka, Moscow, 1981) [in Russian].
11. Yu. A. Ivanov, L. S. Polak, and D. I. Slovetskiĭ, Teplofiz. Vys. Temp. **9**, 1151 (1971).
12. A. D. Kosoruchkina, Zh. Tekh. Fiz. **45**, 1077 (1975) [Sov. Phys. Tech. Phys. **20**, 676 (1975)].
13. Yu. S. Akishev, A. V. Dem’yanov, and I. V. Kochetov, Teplofiz. Vys. Temp. **20**, 818 (1982).
14. Yu. B. Golubovskiĭ and V. M. Telezhko, Opt. Spektrosk. **54**, 60 (1983) [Opt. Spectrosc. **54**, 33 (1983)].
15. H. Brunet and J. Rocca-Serra, J. Appl. Phys. **57**, 1574 (1985).
16. J. P. Boeuf and E. E. Kunhardt, J. Appl. Phys. **60**, 915 (1986).
17. A. S. Zarin, A. A. Kuzovnikov, and V. M. Shibkov, *Microwave Discharge Freely Localized in Air* (Neft’ i Gaz, Moscow, 1996) [in Russian].
18. Yu. B. Golubovskii, V. A. Maiorov, J. Behnke, *et al.*, in *Proceedings of the 16th ESCAMPIG Conference and the 5th ICRP Conference (Joint European–Japanese Conference on Gas Discharges), Grenoble, 2002*, Vol. 1, pp. 233–234.
19. Yu. B. Golubovskii, R. V. Kozakov, V. A. Maiorov, *et al.*, in *Proceedings of the 16th ESCAMPIG Conference and 5th ICRP Conference (Joint European–Japanese Con-*

ference on Gas Discharges), Grenoble, 2002, Vol. 2, pp. 127–128.

20. *Plasma Diagnostic Techniques*, Ed. by R. H. Huddlestone and S. L. Leonard (Academic, New York, 1965; Mir, Moscow, 1967).
21. Yu. I. Ostrovskiĭ, M. M. Butusov, and G. V. Ostrovskaya, *Holographic Interferometry* (Nauka, Moscow, 1977) [in Russian].
22. A. V. Bodronosov, K. A. Vereshchagin, V. A. Gorshkov, *et al.*, Zh. Tekh. Fiz. **64** (1), 47 (1994) [Tech. Phys. **39**, 25 (1994)].
23. V. A. Shakhatov, O. De Pascale, and M. Capitelli, in *Proceedings of the 5th International Conference on Frontiers in Low Temperature Plasma Diagnostics, Villagio Cardigliano (Italy), 2003*, pp. 204–207.
24. G. Ya. Dynnikova, Prikl. Mekh. Tekh. Fiz., No. 5, 3 (1988).
25. K. A. Vereshchagin, V. V. Smirnov, and V. A. Shakhatov, Zh. Tekh. Fiz. **67** (5), 34 (1997) [Tech. Phys. **42**, 487 (1997)].
26. L. G. H. Huxley and R. W. Crompton, *The Diffusion and Drift of Electrons in Gases* (Wiley, New York, 1974; Mir, Moscow, 1977).
27. V. V. Smirnov and V. I. Fabelinskiĭ, Pis'ma Zh. Éksp. Teor. Fiz. **28**, 461 (1978) [JETP Lett. **28**, 427 (1978)].
28. B. Massabieaux, G. Gousset, M. Lefebvre, *et al.*, J. Phys. (France) **48**, 1939 (1987).
29. Yu. M. Gershenzon, V. B. Rozenshtein, and S. Ya. Umanskiĭ, *Chemistry of Plasma* (Atomizdat, Moscow, 1977), Vol. 4, pp. 61–67 [in Russian].
30. D. A. Frank-Kamenetskii, *Diffusion and Heat Transfer in Chemical Kinetics* (Nauka, Moscow, 1967; Plenum, New York, 1969).
31. *Handbook of Physical Quantities*, Ed. by I. S. Grigoriev and E. Z. Meilikhov (Énergoatomizdat, Moscow, 1991; CRC, Boca Raton, 1997).
32. L. S. Polak, M. Ya. Gol'denberg, and A. A. Levitskiĭ, *Computational Methods in Chemical Kinetics* (Nauka, Moscow, 1984) [in Russian].
33. G. D. Billing and E. R. Fisher, Chem. Phys. **43**, 395 (1979).
34. A. A. Devyatov, S. A. Dolenko, A. T. Rakhimov, *et al.*, Zh. Éksp. Teor. Fiz. **90**, 429 (1986) [Sov. Phys. JETP **63**, 246 (1986)].
35. S. I. Valyanskiĭ, K. A. Vereshchagin, A. Yu. Volkov, *et al.*, Kvantovaya Élektron. (Moscow) **11**, 1833 (1984).
36. S. I. Valyanskiĭ, K. A. Vereshchagin, A. Yu. Volkov, *et al.*, Preprint No. 109, IOFAN (Institute of General Physics, Russian Academy of Sciences, 1984).
37. Yu. N. Zhuk and K. S. Klopovskii, Chem. Phys. Lett. **153**, 181 (1988).

Translated by V. Isaakyan

Technical Physics, Vol. 50, No. 12, 2005, pp. 1605–1610. Translated from Zhurnal Tekhnicheskoĭ Fiziki, Vol. 75, No. 12, 2005, pp. 69–75.

SOLIDS

Unidirectional Anisotropy in Ferromagnetic–Ferrimagnetic Film Structures

G. I. Frolov[1], V. Yu. Yakovchuk[1], V. A. Seredkin[1], R. S. Iskhakov[1], S. V. Stolyar[1,2], and V. V. Polyakov[1]

[1]*Kirenskiĭ Institute of Physics, Siberian Division, Russian Academy of Sciences, Akademgorodok, Krasnoyarsk, 660036 Russia*

e-mail: sva@iph.krasn.ru

[2]*Krasnoyarsk State University, Krasnoyarsk, 660041 Russia*

Received April 5, 2005

Abstract—A mechanism of unidirectional anisotropy formation in an exchange-coupled ferromagnetic–ferrimagnetic film structure with orthogonal effective magnetizations in the layers is investigated. The reason for unidirectional anisotropy is the magnetic heterogeneity of the ferrimagnetic layer in the compensation range. Magnetization reversal in the magnetically soft layer of an (REE–transition metal)/NiFe film structure is discussed based on a model of uniform rotation of magnetization. It is found that unidirectional anisotropy sharply decreases the magnetic noise level in the magnetically soft layer. The field of application of these materials is outlined. © *2005 Pleiades Publishing, Inc.*

Exchange interaction between magnetically soft and magnetically hard layers imparts intriguing properties to related structures, which are of great fundamental and applied interest. One of these properties is unidirectional exchange anisotropy in the magnetically soft layer, which shifts hysteresis loop ΔH along the magnetic field axis. Although this effect was discovered 50 years ago [1], it has not been yet completely understood. Therefore, to gain a deeper insight into the nature of unidirectional anisotropy remains a topical problem. Hot interest in these materials as candidates, e.g., for magnetic memory devices [2], spintronics devices [3], and magnetic sensors [4] is giving an additional impetus to research in this field.

Unidirectional exchange anisotropy has been studied mostly in ferromagnetic–antiferromagnetic (FM/AFM) film structures [5]. However, a number of disadvantages limit the application of these materials [6]. These are a poor temperature stability of ΔH, an increased coercive force of the magnetically soft layer compared with that of a one-layer FM film, and the evolution of the hysteresis loop with the number of a magnetization reversal cycle.

At the beginning of the 1980s, unidirectional anisotropy was discovered [7] in a TbFe/NiFe ferromagnetic–ferrimagnetic (FoM/FiM) film structure. These structures attracted attention, since they, on the one hand, lack the disadvantages typical of their FM/AFM counterparts and, on the other hand, unidirectional anisotropy here appears in layers with orthogonal effective magnetizations. A large body of data concerning investigation and application of FoM/FiM structures has been gained in recent years [8–15]. In our opinion, it is an appropriate time to analyze the state of the art in this field. In this work, we consider the nature of unidirectional anisotropy, its effect on the magnetic performance of the FM layer, and applications of FoM/FiM strictures.

MECHANISMS OF UNIDIRECTIONAL ANISOTROPY FORMATION

The phenomenological description of the effect of unidirectional exchange anisotropy is straightforward. It is based on the assumption that the magnetic moments at the interface are collinear,

$$j\mathbf{M}_1 \cdot \mathbf{M}_2 = JM_1M_2\cos(\hat{M_1M_2}). \quad (1)$$

In [7], where the existence of unidirectional anisotropy in a Tb_xFe_{1-x}/NiFe exchange-coupled film structure with orthogonal effective magnetizations of the layers was reported for the first time, we applied some considerations to the origin of this effect. It was conjectured that an amorphous ferrimagnetic layer may have the in-plane magnetization component resulting, for example, from a chemical inhomogeneity across the amorphous alloy film. This inhomogeneity, in turn, produces a compensation plane, in which the magnetization reverses.

Further investigations into the chemical composition of REE–transition metal (REE–TM) amorphous alloy films obtained by thermal evaporation have shown, however, that a concentration gradient normal to the plane is absent in such films. Therefore, other mechanisms come to the fore. For example, the in-plane magnetization component in amorphous REE–

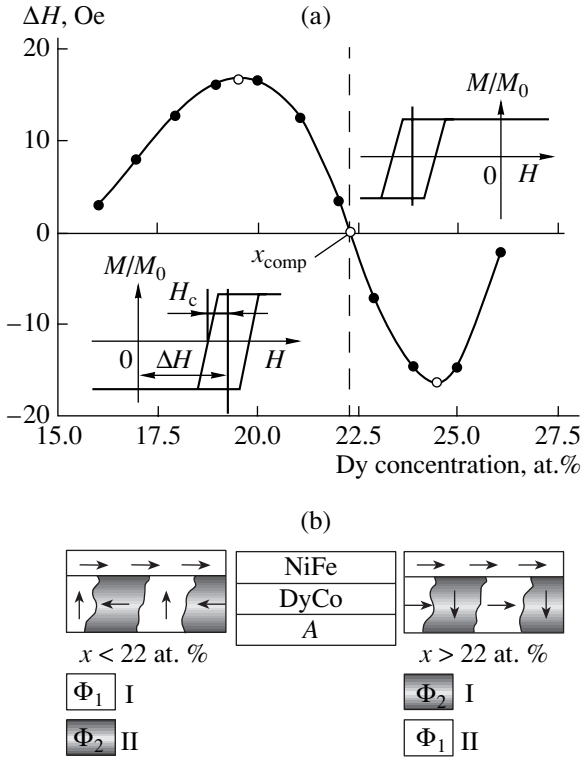

Fig. 1. (a) Hysteresis loop and concentration dependence of bias field $\Delta H(x)$ and (b) the orientation scheme for the magnetizations of 3*d* metals in exchange-coupled DyCo/NiFe film structures. *A*, substrate; I, matrix; and II, impurity.

TM films, which are characterized by perpendicular anisotropy, may be due to a local dispersion of the magnetic anisotropy axis. As a result, the general direction of the easy magnetic axis deviated from the normal to the film surface. If such a mechanism works and the composition of the REE–TM film is off-compensation, the amount of unidirectional anisotropy in exchange-coupled (REE–TM)/NiFe film structures is bound to grow, being minimal in those where the easy magnetic axis of the amorphous REE–TM layer lies in the plane of the film. However, our investigations [14], as well as those carried out by other authors [9, 11], show that the reverse is true. In (REE–TM)/NiFe structures, unidirectional anisotropy exists only in that concentration range of the amorphous alloy where perpendicular anisotropy in the REE–TM layer is observed.

The existence of unidirectional anisotropy in Tb_xFe_{1-x}/NiFe and Dy_xCo_{1-x}/NiFe film structures, which was first discovered in [7], indicates a specific magnetic microstructure of REE–TM layers. Namely, Dy_xCo_{1-x} and Tb_xFe_{1-x} alloys show nanoareas where the magnetization vector of the 3*d* metal sublattice has the in-plane component, and it is this component that takes part in exchange interaction with the FM layer of NiFe alloy.

To establish factors causing the in-plane component of the 3*d* metal sublattice in REE–TM alloy with layers that have near-compensation compositions and feature a high degree of integral perpendicular anisotropy is a challenge. This is because the amorphous ferrimagnetic REE–TM alloy has a low saturation magnetization ($M_s \longrightarrow 0$) and a high magnetic hardness (for example, the coercive field in the (REE–TM)/DyCo alloy may be as high as > 10 kOe). In light of this, we suggested that the physical properties of such magnetically hard materials be studied on NiFe/Dy_xCo_{1-x}/NiFe multilayer exchange-coupled film structures where the Dy_xCo_{1-x} layer is much thinner than NiFe, $d_{DyCo} \ll d_{NiFe}$. Exchange interaction between the Co sublattice of the ferrimagnetic alloy and the NiFe layer substantially modifies the magnetic performance of such a well-studied alloy as NiFe.

Based on the measurements of the dynamic and static magnetic characteristics of NiFe/Dy_xCo_{1-x}/NiFe composites, we developed a microheterogeneous model of the DyCo amorphous layer [15, 16]. The DyCo specific microstructure in the compensation range that follows from this model has allowed us to explain experimental data for FM resonance (FMR) and spin-wave resonance (SWR). To find specific features of DyCo, we (i) prepared NiFe/DyCo/NiFe three-layer structures with unidirectional exchange anisotropy and orthogonal effective magnetizations of the layers, (ii) studied the FMR and SWR spectra of these structures, and (iii) found that the spin system of the amorphous DyCo alloy in the concentration range of magnetic compensation can be represented in the form of two subsystems with the TM magnetization prevailing in one of them (nanophase Φ_1) and the REE magnetization in the other (nanophase Φ_2). This model embodies the basic structural feature of amorphous alloys: natural fluctuation (topological and composition) inhomogeneity. In the concentration ranges $x_i \pm \Delta x \ll x_{comp}$ (matrix Φ_1) and $x_i \pm \Delta x \gg x_{comp}$ (matrix Φ_2), the magnetic microstructures of amorphous ferrimagnets will differ substantially from the magnetic microstructure in the range $x_i - \Delta x < x_{comp} < x + \Delta x$. In this case, magnetic compensation point x_{comp} is defined by the condition $\langle M \rangle = pM_{eff}^{(\Phi_1)} + qM_{eff}^{(\Phi_2)} = 0$, where p and q are the volume fractions of nanophases Φ_1 and Φ_2 and $M_{eff}^{(\Phi_1)}$ and $M_{eff}^{(\Phi_2)}$ are the effective magnetizations of these phases at $x_i - \Delta x$ and $x_i + \Delta x$, respectively.

Figure 1 shows the experimental dependences of shift $\Delta H(x)$ of the hysteresis loop on the REE concentration in a planar DyCo/NiFe structure and the distributions of nanophases Φ_1 and Φ_2 in the DyCo layer. It is seen that the curve $\Delta H(x)$ for the Dy_xCo_{1-x}/NiFe structure is described by the asymmetric function $\Delta H(x - x_{comp})$ and has singular points: the coordinate of the zero (minimal value of ΔH) and extreme points. Also, it is seen that $\Delta H(x)$ in this planar structure reaches a maximum at $x \approx 19$ at.% for undercompensa-

tion compositions of DyCo and $x \approx 24$ at.% for overcompensation compositions.

The above results are readily explained in terms of the suggested model of amorphous DyCo alloy structure in the magnetic compensation range. Indeed, in the REE–TM concentration range $x \leq 16$ at.% ($x \geq 27$ at.%), the magnetic structure of amorphous DyCo is completely specified by magnetic nanophase Φ_1 (Φ_2). Hence, the magnetic moments of the Co and Dy sublattices are collinear with the perpendicular anisotropy axis in the DyCo layer and, as a consequence, the effective magnetizations of the DyCo and NiFe layers are mutually orthogonal (exchange coupling is absent). Such a situation takes place in the concentration range $x_i - \Delta x < x_{comp} < x + \Delta x$. Here, the magnetic structure of DyCo is formed by randomly mixed nanophases Φ_1 and Φ_2. If phase Φ_1 is a matrix, phase Φ_2 is an impurity and vice versa. The only exception is compensation point x_{comp}, where the volume fractions of the phases are roughly the same.

At any concentration x_i from the above range, the effective magnetization of matrix phase Φ_i in the DyCo layer is aligned with the perpendicular anisotropy field (M_{Co} and M_{Dy} are collinear with this field (as indicated by the polar Kerr effect). In this case, the magnetization of the Co sublattice, M_{Co}, in impurity nanophase Φ_j must have the in-plane component because of exchange interaction between the transition elements in the impurity and matrix and the effective magnetization of nanophase Φ_j has a chance to align with an external magnetic field. We believe that exchange interaction between magnetization M_{Co} of impurity phase Φ_j in the DyCo layer and the magnetization of the NiFe layer results in exchange unidirectional anisotropy in NiFe.

The form of the experimental dependence in Fig. 1 (asymmetry about x_{comp}) can also be treated in terms of our model. In this planar system, a Dy_xCo_{1-x} layer forms where the magnetization of the matrix phase is aligned with the perpendicular anisotropy axis, while the effective magnetization of the impurity phase lies in the plane of the payer. When a NiFe overlayer is grown, a permanent magnetic field is switched on to specify the easy direction and the effective magnetization of the impurity phase in the Dy_xCo_{1-x} layer is aligned with this field and, hence, with the unidirectional anisotropy axis in NiFe. In the range $x < x_{comp}$, the impurity phase meets the inequality $M_{Co} < M_{Dy}$, while at $x > x_{comp}$, the inverse inequality is valid. This means that, at $x < x_{comp}$, the magnetization vectors of the Co sublattice and NiFe layer are anticollinear, whereas, at $x > x_{comp}$, they are codirected (see Fig. 1b). That is why the sign of ΔH changes in going through concentration x_{comp} (Fig. 1a).

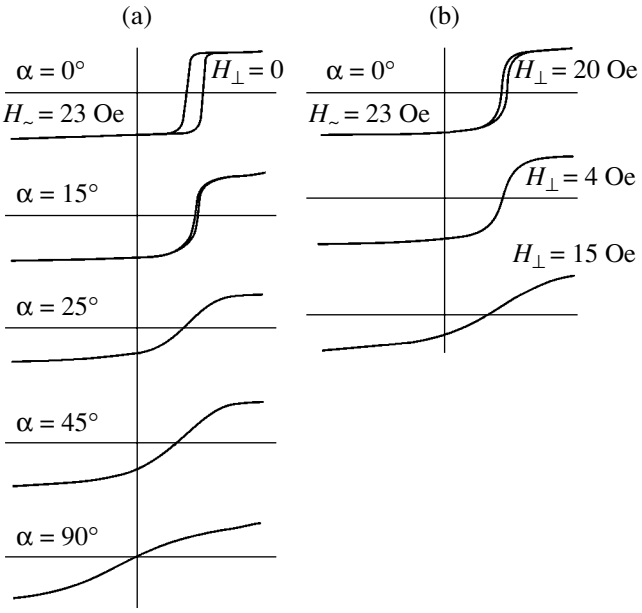

Fig. 2. (a) Angular dependence of ΔH and (b) dependence of the hysteresis loop on $H_\perp$ in the exchange-coupled DyCo/NiFe film structure.

QUASI-STATIC MAGNETIZATION REVERSAL IN FERROMAGNETIC–FERRIMAGNETIC FILM STRUCTURES

In exchange-coupled structures, the state of one layer may substantially affect the state of another. For example, direct exchange interaction between ferromagnetic layers (positive coupling) with different degrees of anisotropy may lead to the situation where both layers experiencing magnetization reversal will behave as a whole with a coercive force intermediate between the coercive forces of the layers [6]. In FM/AFM film structures, unidirectional anisotropy shifts the hysteresis loop, results in only one easy axis, stabilizes the domain structure of the ferromagnetic layer, etc. [17, 18].

In FoM/FiM structures, the magnetization reversal process somewhat differs from that in FM/AFM films. Figure 2a shows the angular dependence of the hysteresis loop for a DyCo/NiFe film (the layer thicknesses are, respectively, 70 and 210 nm; the easy axis coincides with the unidirectional anisotropy axis). In the easy axis direction ($\alpha = 0$), the hysteresis loop is the widest ($H_c = 2$ Oe) and is shifted along the field axis by $\Delta H = 10.5$ Oe. As angle α increases, the loop gets thinner and collapses at $\alpha = 25°$ (in the range 25°–90°, the process of magnetization reversal is hysteresis-free). The shift also decreases, and, at $\alpha = 90°$, the "loop" becomes symmetric (the anisotropy field determined from this curve is $H_a = 15$ Oe).

Figure 2b demonstrates the variation of the hysteresis loop for the same film when permanent magnetic field $H_\perp$ is applied along the hard axis. At $H_\perp = 4$ Oe,

the loop collapses and takes the form of the magnetization reversal curve for $\alpha = 25°$. At $H_\perp = H_a = 15$ Oe, the loop is still asymmetric.

Such an observation (collapsed hysteresis loop) differs from experimental data obtained on NiFe/FeMn films [17]. Magnetization reversal curves taken of two-layer exchange-coupled structures are usually treated in terms of the model assuming that the magnetization vector of one layer is fixed, while the magnetization vector of the other spirals under the action of an external magnetic field [19, 20]. The analytical solution presented in [20] gives the following results. If magnetization reversal takes place along the easy axis ($\alpha = 0$) in films with $d_{FM} < d_{cr}$, the hysteresis loop collapses and shifts along the field axis. In films with $d_{FM} > d_{cr}$, the loop "opens up" and expands with d_{FM}. (Here, $d_{cr} = 2A/M_s H_a d_{FM}^2 > 12/\pi^2$, where A is the exchange interaction constant and M_s, H_a, and d_{FM} are, respectively, the saturation magnetization, anisotropy field, and thickness of the magnetically soft layer.)

However, in none of the numerous experiments where magnetization reversal took place along the easy axis in FM/AFM and FoM/FiM structures did the hysteresis loop collapse even for $\Delta H \gg H_C$. The reason for the discrepancy between the analytical and experimental data seems to be an inadequate estimate of d_{cr}. For an exchange-coupled structure with parameters $M_s = 800$ G and $H_a = 3$ Oe for the magnetically soft material and exchange constant $A = 10^{-6}$ erg/cm^3, the critical thickness was estimated as $d_{cr} = 260$ nm [20]. At the same time, experiments with NiFe/FeMn films showed that the exchange constant is two orders of magnitude smaller [21]; that is, $d_{cr} = 3$ nm. However, the hysteresis loop did not collapse even when magnetization reversal along the easy axis took place in structures with d_{FM} (d_{NiFe}) < 3 nm [21].

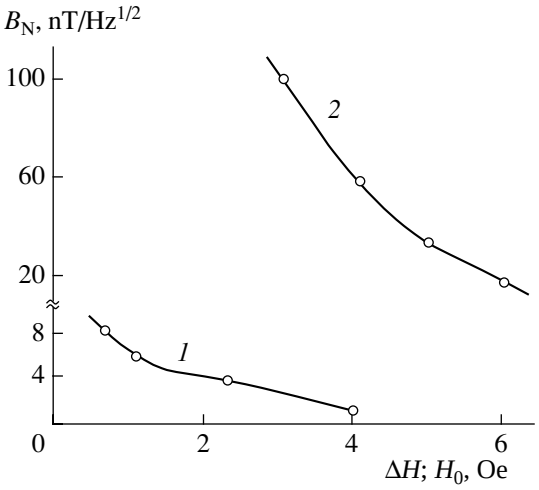

Fig. 3. Magnetic noise intensity (*1*) in the exchange-coupled DyCo/NiFe film structure vs. the amount of unidirectional anisotropy ΔH and (*2*) in the reference NiFe film vs. applied permanent magnetic field H_0.

Another model of quasi-static magnetization reversal in exchange-coupled structures that assumes coherent rotation of the magnetization in a magnetically soft layer was suggested in [17]. Here, the interaction between the layers is described in terms of specific surface energy E_s. In this case, we deal with thickness-averaged unidirectional anisotropy, the amount of which is inversely proportional to the thickness of the magnetically soft layer. Such a dependence of ΔH on the thickness of the magnetically soft layer is confirmed experimentally [9, 11]. When external magnetic field H is applied to the plane of the film at angle α to the easy axis, magnetization M of the magnetically soft layer rotates through angle β relative to the easy axis. Then, the energy of the FM layer can be written in the form

$$E = -HM\cos\varphi + E_k \sin^2\beta - \frac{E_s}{d_{FM}}\cos\beta, \qquad (2)$$

where $\varphi = \alpha - \beta$ and E_a is the unidirectional anisotropy constant.

Using the standard computational method, we derived an expression for the hysteresis loop for any α (except $\alpha = 0$ and π). It was found that the loop collapses at certain $\alpha > \alpha_{cr}$, α_{cr} depending on ratio $\Delta H/H_a$, where $\Delta H = E_s/Md_{FM}$. This model leads us to conclude that, first, magnetization reversal at an angle to the easy axis of an FM layer may proceed by rotation of vector M and, second, unidirectional anisotropy can be simulated by permanent magnetic field $H = \Delta H$. Both conclusions were corroborated in experiments, which means that the model adequately describes quasi-static magnetization reversal in exchange-coupled structures.

MAGNETIC NOISE IN FERROMAGNETIC–FERRIMAGNETIC FILM STRUCTURES

It is known that the magnetic noise in thin-film magnetic devices can be depressed, e.g., by applying a magnetic field, which makes the process of magnetization reversal more uniform. The same results can be obtained using structures with unidirectional anisotropy.

We performed special experiments to see how the external magnetic field and unidirectional anisotropy influence the magnetic noise in Permalloy films [22, 23]. The object of interest was fluctuations of the transverse emf in the presence of a constant bias (H_0, ΔH) applied along the easy magnetic axis or a high-frequency field ($H_{hf} < H_a$, H_0) applied along the hard magnetic axis.

Figure 3 shows the variation of magnetic noise B_N in the NiFe film incorporated into an exchange-coupled DyCo/NiFe structure 500 nm thick with bias field ΔH (curve *1*) and in a reference NiFe film magnetized by magnetic field H_0 (curve *2*).

As follows from Fig. 3, the magnetic noise in the exchange-coupled film structure is much lower than in the reference film. Presumably, unidirectional anisotropy is not totally equivalent (is superior) to the applied field in efficiency and exchange interaction in the structure makes the process of magnetization reversal in the magnetic layer more uniform.

APPLICATION OF EXCHANGE-COUPLED STRUCTURES

Film magnetic materials have found wide application in various fields of technology [2–4]. Here, we will concentrate on using (REE–TM)/NiFe FoM/FiM structures with unidirectional anisotropy as magnetooptic memory devices and weak-field magnetic sensors.

Memory devices. It is believed that, in this field, the film structures under consideration may decrease the power consumption and raise the speed of data writing and erasing.

Magnetooptic data writing on films with a magnetization normal to the film surface is in common use in disk storages of PCs. Data writing and erasing is accomplished by the thermomagnetic method in writing magnetic field H_3 = 400–500 Oe applied normally to the film (Fig. 4).

As materials for magnetooptic data carriers, REE–TM alloys are usually employed. Their basic disadvantages are (i) the need to apply high writing/erasing magnetic fields, which influence the electrodynamic suspension of the focusing lens holder and (ii) a large time delay between writing and erasing, which depends on the inductance of the magnetic field source winding [24].

We suggest another approach [16] to writing magnetooptic information on REE–TM/NiFe FoM/FiM structures with exchange anisotropy (see Fig. 5).Writing magnetic field $H_{wr} > H_C + \Delta H$ (10–15 Oe) is applied to a FoM/FiM structure (Fig. 5a) antiparallel to the initial magnetization in layer *3* (Fig. 5b). The magnetization of layer *3* reverses, while that of layer *2* does not. After layer *2* has been locally heated by a thermal pulse to a temperature close to Curie temperature T_C, the heated area turns into the paramagnetic state (Fig. 5c) and the magnetic state of layer *3* remains unchanged, since T_C of NiFe is much higher than T_C of DyCo. Due to exchange interaction between layers *2* and *3* (during cooling), the magnetization of the heated area of layer *2* reverses in accordance with the magnetization direction in the NiFe layer (Fig. 5d). After the thermal pulse is terminated and the writing field is switched off, the inverted state of the magnetic moment of the heated area in layer *2* persists (which corresponds to writing a bit of information), while the magnetization of the local area in layer *3* takes on a nonequilibrium (helical) structure (Fig. 5d), representing a compressed "spin spring." Data readout is accomplished using the polar Kerr effect.

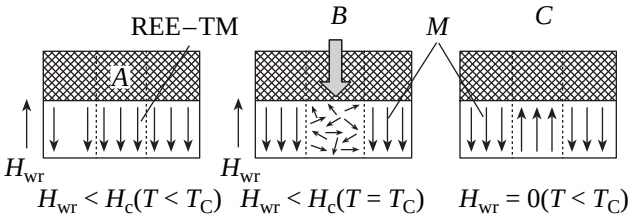

Fig. 4. Thermomagnetic data writing on REE–TM films with perpendicular magnetic anisotropy. *A*, substrate; *B*, radiation; and *C*, domain.

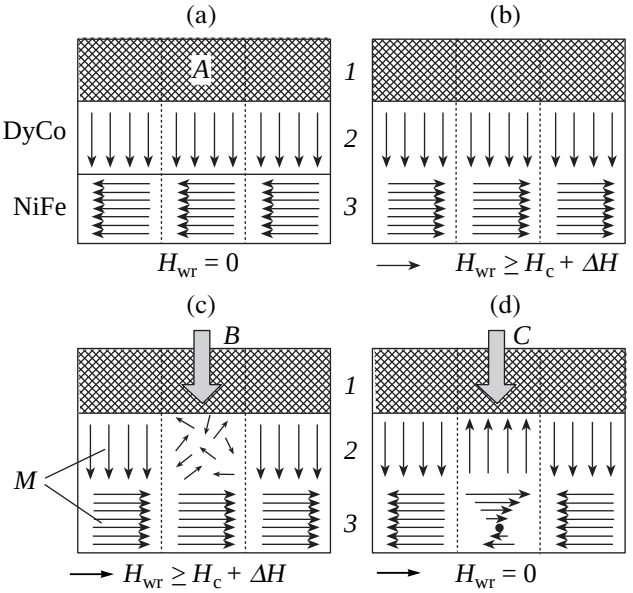

Fig. 5. Thermomagnetic data writing on exchange-coupled (REE–TM)/NiFe film structures. *A*–*C*, the same as in Fig. 4.

To erase information, it suffices to heat the same local area of layer *2* to the Curie temperature. Exchange interaction between this area and layer *3* then disappears, and the magnetization of the local area in layer *3* becomes aligned with the magnetization of the entire layer ("the helix untwists"). After the pulse is terminated and the local area of layer *2* cools, the magnetization of this area changes sense because of exchange interaction with layer *3* and the information is erased.

Thus, in our approach, writing magnetic field $H_{wr} \geq H_C + \Delta H$ is much lower than the writing field in the case of standard REE–TM films. Moreover, data erasing does not require a magnetic field at all. Accordingly, the magnetic field energy spent on data writing/erasing substantially decreases. At the same time, a low writing magnetic field, which makes it possible to generate H_3 pulses as short as several nanoseconds, and no need for switching the magnetic field at writing and/or erasing provide a higher speed of the processes. It should be emphasized that all the related advantages of REE–TM layers are retained.

Film magnetometers. FoM/FiM structures with unidirectional anisotropy were used to design a weak-field magnetic detector and study the dependence of the magnetic noise of this device on the static characteristics of the film magnetic structure and on excitation modes [22, 23]. The operating principle of this magnetometer is akin to that of a bubble magnetometer [25]. However, an exchange-coupled film structure used as a sensitive element made it possible to considerably suppress the low-frequency noise, which was found to be $\approx 2 \times 10^{-11}$ T/Hz$^{1/2}$ at a frequency of 1 Hz. The device was put to field tests, which shows that it can be applied in geophysics, specifically, in geoelectrical prospecting of shallow ore-bearing rocks and in shallow oil-and-gas prospecting [12].

CONCLUSIONS

We touched upon three issues concerning exchange-coupled FoM/FiM film structures consisting of a magnetically hard material (amorphous films of REE–TM alloys) and a magnetically soft Permalloy film. These are the mechanism of formation of exchange coupling between the layers, the magnetic properties of the structures, and application of the structures. In spite of extensive investigation, the problems considered here still need greater insight. However, wide application of these composites stimulates further effort in this field.

ACKNOWLEDGMENTS

This work was supported by the Russian Foundation for Basic Research, grant no. 04-02-16099a.

REFERENCES

1. W. H. Meiklejohn and C. P. Bean, Phys. Rev. **102**, 1413 (1956).
2. C. Tsang and R. E. Fantana, IEEE Trans. Magn. **18**, 1149 (1982).
3. A. V. Vedyaev, Usp. Fiz. Nauk **72**, 1458 (1960) [Sov. Phys. Usp. **3** (1960)].
4. K. M. H. Lenssen, A. F. M. Vierman, and J. J. T. Doukers, J. Appl. Phys. **81**, 4915 (1997).
5. J. Nogues and I. K. Shuller, J. Magn. Magn. Mater. **192**, 203 (1999).
6. A. Yelon, in *Physics of Thin Films*, Ed. by H. Francombe and R. W. Hoffman (Academic, New York, 1971; Mir, Moscow, 1973), pp. 228–333.
7. V. A. Seredkin, G. I. Frolov, and V. Yu. Yakovchuk, Pis'ma Zh. Tekh. Fiz. **9**, 1446 (1983) [Sov. Tech. Phys. Lett. **9**, 621 (1983)].
8. W. C. Cain, W. H. Meiklejohn, and M. H. Kryder, J. Appl. Phys. **61**, 4170 (1987).
9. V. A. Ceredkin, G. I. Frolov, and V. Yu. Yakovchuk, Fiz. Met. Metalloved. **63**, 457 (1987).
10. F. Hellman, R. B. Dover, and E. M. Gyorgy, Appl. Phys. Lett. **50**, 296 (1987).
11. W. C. Cain and M. H. Kryder, J. Appl. Phys. **67**, 5722 (1990).
12. A. N. Babitskiĭ, E. P. Blinnikov, A. G. Vladimirov, *et al.*, Geofiz. Apparatura, No. 94, 21 (1991).
13. V. A. Ceredkin, R. S. Iskhakov, V. Yu. Yakovchuk, *et al.*, Fiz. Tverd. Tela (St. Petersburg) **45**, 883 (2003) [Phys. Solid State **45**, 927 (2003)].
14. R. S. Iskhakov, V. A. Seredkin, S. V. Stolyar, *et al.*, Pis'ma Zh. Éksp. Teor. Fiz. **80**, 743 (2004) [JETP Lett. **80**, 638 (2004)].
15. R. S. Iskhakov, V. A. Seredkin, S. V. Stolyar, *et al.*, Pis'ma Zh. Éksp. Teor. Fiz. **76**, 779 (2002) [JETP Lett. **76**, 656 (2002)].
16. V. A. Seredkin, S. V. Stolyar, G. I. Frolov, and V. Yu. Yakovchuk, Pis'ma Zh. Tekh. Fiz. **30** (19), 46 (2004) [Tech. Phys. Lett. **30**, 820 (2004)].
17. A. A. Glazer, A. P. Potapov, R. I. Tagirov, and Ya. S. Shur, Fiz. Tverd. Tela (Leningrad) **8**, 3022 (1966) [Sov. Phys. Solid State **8**, 2413 (1966)].
18. M. Sh. Erukhimov and V. A. Seredkin, Fiz. Met. Metalloved. **44**, 757 (1977).
19. A. Ahoroni, E. H. Frei, and H. Strikman, J. Appl. Phys. **30**, 1956 (1959).
20. Yu. G. Canoyan and K. A. Egiyan, Fiz. Met. Metalloved. **38**, 231 (1974).
21. R. Jungblut, R. Coehoorn, M. T. Johnson, *et al.*, J. Appl. Phys. **75**, 6659 (1994).
22. V. V. Polyakov and G. I. Frolov, *Magnetic Materials for Radio Electronics* (Krasnoyarsk, 1982), pp. 179–185 [in Russian].
23. V. V. Polyakov, A. G. Vladimirov, and V. A. Seredkin, *Amorphous Film Alloys of Transition and Rare-Earth Metals* (Krasnoyarsk, 1988), pp. 219–223 [in Russian].
24. US Patent No. 4610009 (February 4, 1986).
25. G. Chiron and G. Delapierre, IEEE Trans. Magn. **15**, 1815 (1979).

Translated by V. Isaakyan

Technical Physics, Vol. 50, No. 12, 2005, pp. 1611–1616. Translated from Zhurnal Tekhnicheskoĭ Fiziki, Vol. 75, No. 12, 2005, pp. 76–81.

ELECTRON AND ION BEAMS, ACCELERATORS

Electron–Optical System for a Large-Orbit Gyrotron

V. L. Bratman, Yu. K. Kalynov, V. N. Manuilov, and S. V. Samsonov

Institute of Applied Physics, Russian Academy of Sciences, pr. Gagarina 23, Nizhni Novgorod, 603950 Russia

Received January 28, 2005

Abstract—An electron–optical system generating a rectilinear or helical 250 keV/4 A/10 μs electron beam with a high compression factor is developed. For the former beam, a compression factor as high as 4400 and a current density of 25 kA/cm^2 are achieved. In the process of forming the helical beam, the electrons rotating about the system's axis (paraxial beam) acquire an initial velocity in a transverse magnetic field produced by a kicker. Their pitch factor is increased to a desired (operating) value in an adiabatically growing magnetic field. In tentative experiments with the helical beam in a large-orbit gyrotron, generation was obtained at the second cyclotron harmonic (223 GHz). © *2005 Pleiades Publishing, Inc.*

INTRODUCTION

A challenging problem in microwave electronics is the development of inexpensive high-power sources of coherent sub-mm-wave radiation. Associated devices could extend the capabilities of spectroscopy, solid-state physics, medicine, and other fields of science and technology. Along with the unique sources currently available, such as traditional high-field gyrotrons [1–5] and sub-mm-wave free-electron lasers [6, 7], the so-called large-orbit gyrotrons (LOGs) [8–11], which today operate at centimeter and millimeter waves, seem to be more promising and, presumably, much simpler devices. Unlike the traditional gyrotron, the LOG employs as an active medium not a multihelix beam but a single-helix beam all particles of which, when moving along the resonator's axis, execute Larmor precession about it. In an axially symmetric electromagnetic system, such a paraxial beam is capable of exciting only those modes whose azimuth index coincides with the index of the resonance cyclotron harmonic [12–17]. This selection rule considerably thins out the mode spectrum and thereby simplifies the selective excitation of higher cyclotron harmonics compared with the traditional gyrotron. Operation at higher harmonics allows the designer to significantly decrease the intensity of the operating magnetic field.

Paraxial electron beams used in the LOG basically cannot be generated in axisymmetric magnetron injection guns, which are employed in most traditional gyrotrons. Therefore, in designing LOGs, emphasis should be on creating electron–optical systems (EOSs) generating a high-current paraxial beam with a high rotational velocity of the particles and small spreads in velocity and guiding centers. Until recently, three types of LOG have been applied. In each of them, first a rectilinear beam is formed and then the particles are imparted a rotational velocity. In early experiments [18, 19], the rotational energy was pumped in a high-frequency electromagnetic field produced by a special sweep resonator (a similar EOS is used in magnicons [20]). In such a scheme, the modulated beam is applied to the output resonator and the device operates as an amplifier. In generator circuits, a rectilinear beam is adiabatically swept in a transverse magnetostatic field. In cm-wave LOGs [15], the particles of a rectilinear tubular beam acquire a rotational velocity as they pass through the region where the guiding magnetic field abruptly reverses (the cusp of the magnetic field). In a relativistic LOG operating in the short-wave part of the millimeter-wave range at the third and fourth cyclotron harmonics [10], the rectilinear beam is formed in a thermionic EOS and the initial velocity imparted by a kicker is then raised to a desired value in an adiabatically growing magnetic field. In this work, we discuss a modified version of this EOS designed for a submillimeter generator and report the results of preliminary experiments.

DESIGN OF THE MODIFIED ELECTRON–OPTICAL SYSTEM

Theoretically [17], the LOG can selectively operate at relatively high cyclotron harmonics with indices s = 3–5 when the particle energy is higher than 30 keV provided that the spread of electron guiding centers, ΔR_0, and the offset of the beam from the axis do not exceed 0.2λ, where λ is the radiated wavelength. Also, to achieve a reasonably high electron efficiency, average electron pitch factor $g = v_\perp/v_\parallel$ must be no smaller than 1.0–1.2 for a transverse velocity spread below 20–30%.

1063-7842/05/5012-1611$26.00

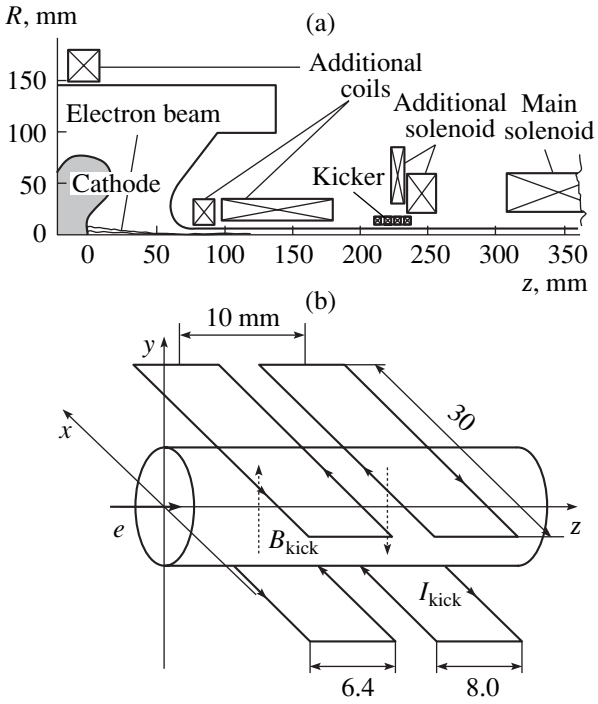

Fig. 1. Modified electron–optical system: (a) general configuration and (b) schematic of the kicker.

Here, $v_\perp$ and $v_\parallel$ are the rotational and translational components of the particle velocity. At an electron energy of 30–300 keV, the cross section of the beam in the working space has the form of a 0.2- to 0.25-λ-wide ring with an average radius of (0.1–0.5)λ. To operate at harmonics s = 3–5 with a moderate-length resonator, the LOG beam current must be on the order of several amperes. Accordingly, in the submillimeter range, such a beam will have a density as high as 3–10 kA/cm^2. If the LOG uses a thermionic cathode with a typical emission current density of $j_c < 5$ A/cm^2, such a high current density implies a high compression of the electron beam.

In this paper, we study the EOS of the relativistic 375-GHz LOG [21], which is an extension of the high-voltage device developed earlier. With that device, we succeeded in generating a 10-μs-long dense helical beam with a particle energy of 250 keV, current of 10 A, and pitch factor of 1.2 [10]. This beam was used to selectively generate the $TE_{3,2}$ mode at the third cyclotron frequency (115 GHz) and the $TE_{4,2}$ mode at the fourth cyclotron frequency (130 GHz) with an output of 100 kW and an efficiency of 4%. The EOS of this generator forms a helical electron beam in two steps. First, it creates a rectilinear beam using a quasi-Pierce diode gun with a spherical thermionic cathode (Fig. 1a). Then, the electrons are imparted a rotational velocity in the transverse magnetic field of a kicker produced by two pairs of rectangular loops placed on both sides of the beam at a distance of roughly half the Larmor pitch (Fig. 1b). Current pulses of duration about 1 ms are created by discharging a capacitor through the kicker loops. Charging voltage U_{kick} on this capacitor controls the electron transverse velocity. After passing through the kicker, the particles fall into an adiabatically growing magnetic field, where their rotational velocity is increased to a desired value. The compression factor for the beam's cross-sectional area can be as high as 1100, and the rectilinear beam current density may exceed 3 kA/cm^2. The success in generating such a dense beam allowed us to expect that, when appropriately modified, this system can also be used at shorter waves.

In order to decrease ohmic wall losses in the LOG resonator when going to a much higher frequency, one has to increase the radial index of the operating mode to a maximal value permissible for mode selection. In a traditional gyrotron resonator operating at the third cyclotron frequency, the radial index can be increased from 2 to 5–8. However, at the fourth cyclotron frequency, even the mode with a radial index of 3 has a much higher starting current and is lossy, so that an increase in the radial index may excite spurious modes. Therefore, in our design of the submillimeter LOG, the operating frequency is the third cyclotron frequency and operating modes are $TE_{3,p}$ modes with high radial indices, p = 5–8. Under these conditions and at the same particle energy as earlier (250 keV), a frequency of 375 GHz can be achieved by raising the magnetic field in the working space of the gyrotron to B_0 = 6.6 T, which is roughly four times higher than in the early version.

Our calculations show that a beam current of 3 A will suffice for the generator to efficiently operate at the above modes with electron pitch factor g = 1. At an emission current density of 4 A/cm^2 in a paraxial beam with a tolerable spread of guiding centers, such a current strength is achievable at a compression factor of about 4000. As in the early version, the magnetic field at the cathode is very weak, about 1.5 mT. Accordingly, the Larmor pitch of electrons near the cathode is several tens of centimeters and the electron cyclotron frequency is less than the plasma frequency of the beam. Under these conditions, the particles in the growing magnetic field move nonadiabatically and detailed numerical simulations with allowance for space charge forces must be carried out. To analyze the beam near the cathode, we used the EPOS program, which makes it possible to adequately calculate the particle trajectories for a given configuration of an axisymmetric EOS with regard to static electric and magnetic fields of the space charge (for more details, see [22]). As the magnetic field along the longitudinal coordinate grows, the plasma-to-cyclotron frequency ratio squared and the Larmor pitch decrease inversely with the field (with regard to the beam compression factor). Beginning with field intensity B_a at which the cyclotron frequency becomes equal to the plasma frequency and the Larmor pitch becomes several times shorter than the character-

istic scale of variation of the guiding field, the particle motion can be simulated in terms of the adiabatic theory (except for the kicker region).

At the exit from the cathode region, the nonideality of the beam can be characterized by its radial pulsations or by maximum transverse velocity $v_{\perp a}$ of peripheral electrons. In the EOS under study, the kicker is outside the cathode region; i.e., $B_k > B_a$, where B_k is the guiding field at the kicker. The relative spread of the transverse velocity of the particles after they have been swept in the kicker can be estimated by the simple formula [23]

$$\delta v_\perp = 2v_{\perp s}/v_{\perp k}, \quad (1)$$

where $v_{\perp s}$ is the maximal spurious transverse velocity of the electrons before the kicker and $v_{\perp k}$ is the transverse velocity imparted by the kicker to the electrons moving along the axis.

According to the adiabatic theory, the transverse velocity relative spread in the working space of the LOG is the same. Since the spurious transverse velocity in the kicker is given by

$$v_{\perp s} = v_{\perp a}(B_k/B_a)^{1/2}, \quad (2)$$

and operating transverse velocity $v_{\perp 0}$ is

$$v_{\perp 0} = v_{\perp k}(B_0/B_k)^{1/2}, \quad (3)$$

the relative spread can be expressed through the operating parameters and the parameters at the exit from the cathode region as

$$\delta v_\perp = \frac{2v_{\perp a}}{v_{\perp 0}}\sqrt{\frac{B_0}{B_a}}. \quad (4)$$

If parameters $v_{\perp a}$ and B_a in the cathode region remain the same when the operating field is increased by a factor of 4, the transverse velocity spread increases by a factor of 2, as follows from expression (4). Note that the position of the kicker outside the cathode region, where the magnetic field grows, does not affect the velocity spread. To decrease a necessary kicker field and increase the size of the loops, it is reasonable to place the kicker in the region where the guiding field is the weakest. In the system developed earlier, the kicker was placed near the cathode boundary, where B_0 = 0.4 T and the maximum transverse velocity is $v_{\perp a}$ = 0.06*c*. In the new EOS, the beam current was diminished to 3 A, which allowed us to decrease the emitter diameter twofold and, thereby, maintain the velocity spread at a level close to that obtained in [10].

The velocity spread of the particles swept in the kicker depends not only on the transverse velocity but also on the spread of the guiding center radii (position spread). For an adjusted paraxial beam, the spread in the radii is equal to its radius. In the presence of regular radial pulsations in a laminar beam leaving the kicker, it is reasonable to place the kicker so as to bring into coincidence a minimum of the transverse field on the system's axis (the center of the kicker) and a minimum of the beam radius. To this end, we fixed the position of the kicker and optimized the pulsation phase by slightly varying the guiding magnetic field in the cathode region.

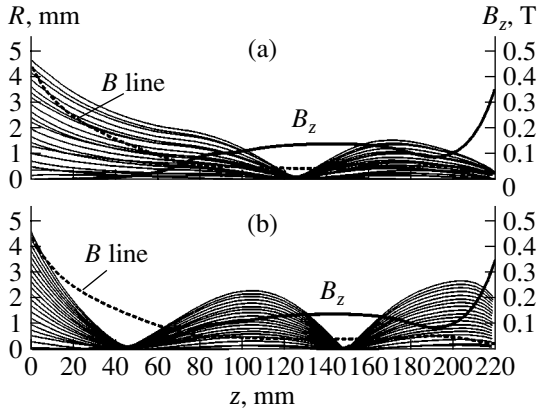

Fig. 2. Magnetic field distribution in the cathode region and analytical particle trajectories (a) at a beam current of 3 A and (b) at a vanishingly small beam current.

In accordance with the aforesaid, the magnetic system generating a field in the cathode region, the configuration of gun electrodes, the kicker, and the position of the kicker in the modified design are the same as in the earlier version of the EOS. At the same time, the diameter of the emitter is reduced by a factor of 2 (to 10 mm); the parameters of the solenoid that produces an operating magnetic field in the resonator are changed; and an additional solenoid is included, which matches the magnetic field in the gun and kicker with the operating magnetic field raised fourfold (Fig. 1a). At an emission current density of 4 A/cm^2, the rated beam current is 3 A and the gun must operate in the temperature-limited emission mode. To optimize the phase of electron spurious oscillations at the entrance to the kicker ($B < B_a$), the magnetic field in the cathode region was increased with its value immediately at the cathode remaining the same (about 1.5 mT). In this case, according to the trajectory analysis (Fig. 2a), the maximum velocity of spurious oscillations is $v_{\perp a}$ = 0.033*c* and the beam in the kicker has the smallest cross section, which reduces the effect of position spread. In the kicker region, the effect of the self-field of the beam is much weaker than in the cathode region (the plasma-to-cyclotron frequency ratio squared is 0.3); therefore, the particle motion in the kicker and then in the beam transport channel to the region of the uniform magnetic field was simulated without regard to the space charge forces. This approximation significantly simplifies the analysis and allows us to use a model based on numerical integration of equations of motion for electrons in a given three-dimensional magnetic field. As initial conditions in three-dimensional analysis, we used the results obtained from the two-dimensional trajectory

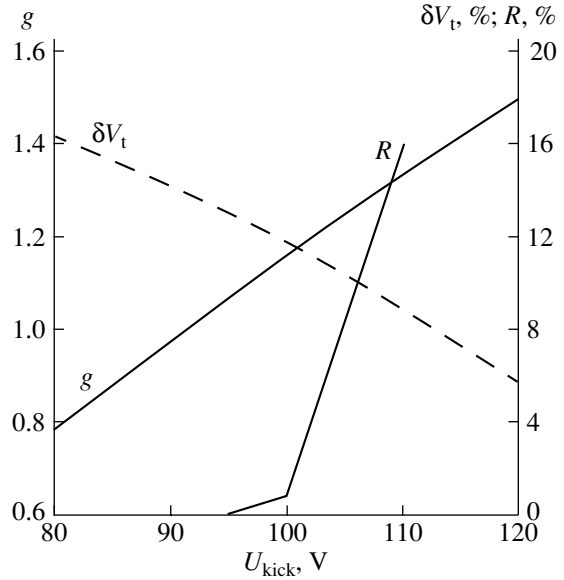

Fig. 3. Beam sweeping in the kicker: pitch factor g, transverse velocity spread δV_t, and number R of particles reflected by the magnetic mirror vs. kicker voltage.

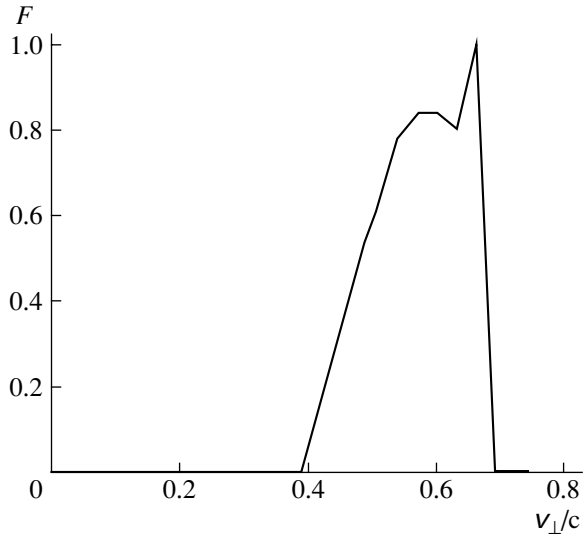

Fig. 4. Analytical particle transverse velocity distribution at kicker voltage U_{kick} = 100 V.

analysis of the EOS with the space charge considered in detail.

According to our calculations, as the current in the kicker loop increases, the absolute spread in the transverse velocity remains approximately the same (provided that the electron pitch factor also rises appropriately), while the relative spread decreases (Fig. 3). The finite value of the transverse velocity absolute spread that is determined by the cathodic part of the beam-forming region does not allow us to increase the operating pitch factor above g_{max} = 1.2. As the kicker voltage grows further, the magnetic-mirror-reflected portion of the electrons whose transverse velocity reaches a final value in the process of subsequent adiabatic compression becomes too large. At the kicker voltage corresponding to the average pitch factor (g = 1.15), when the number of reflected electrons is about 1%, the transverse velocity relative spread (the rms deviation) equals 11.5% and the relative width of the transverse velocity distribution at the base is about 50% (Fig. 4), which is in good agreement with estimate (4). The calculations show that the modified EOS can generate a beam acceptable for the 375-GHz LOG.

EXPERIMENTAL RESULTS

The modified EOS was first tested in the weak-current mode, which allows visualization of the beam's cross section on a phosphor applied on a quartz target. In this mode, the potential and magnetic field were, respectively, 2 and $2^{1/2}$ times lower than their operating values. Unlike standard simulation conditions, the electron current was reduced not by a factor of $2^{3/2}$ but to a very small value of about a milliampere that can provide the luminescence. At a higher current, the phosphor does not withstand a thermal load. If the simulation coefficient had been more than two, the magnetic field at the cathode would have been too weak (comparable to the terrestrial magnetic field).

Comparative calculations of the electron trajectories under the weak-current conditions (without the space charge, Fig. 2b) and operating conditions (at a current of 3 A, Fig. 2a) demonstrated the significant difference in the transverse velocity of the particles before the kicker and in the velocity spread after the kicker. The

Fig. 5. Luminescent spot of the helical beam on the phosphor target (the diameter of the dark inner circle is 1.5 mm).

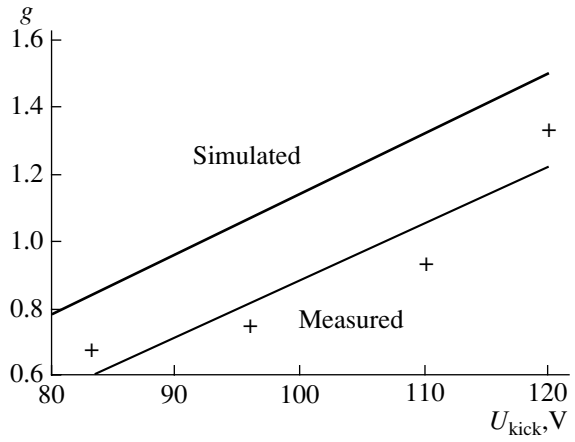

Fig. 6. Electron pitch factor measured in the simulation mode and its calculated value vs. kicker voltage.

average transverse velocities of the particles in the beam swept by the kicker in these modes were close to each other. Therefore, the weak-current mode could be used for both adjusting the beam and estimating the transverse velocity at different particle energies.

The beam was studied with the phosphor target placed at a distance of 40 mm from the center of the kicker. The pitch factor was determined from the size of the luminescent spot (Fig. 5). The quantities measured in the weak-current mode and converted to the operating mode with parameters 250 keV and 6.6 T at different kicker currents are in good agreement with the results of calculations performed for the operating mode (Fig. 6).

According to the *I–V* characteristics of the EOS obtained in the operating mode at different emitter temperatures, the maximum beam current exceeded 4 A. Thus, the maximum current density of the rectilinear beam in the resonator was found to be about 25 kA/cm^2; that of the helical beam with a pitch factor of 1.0, about 2.3 kA/cm^2.

In the experiment on excitation of the LOG resonator by the helical beam, the spurious mode at the fundamental cyclotron resonance frequency interfered with the high-radial-index $TE_{3,8}$ operating mode excited at the third cyclotron frequency. At the same time, the $TE_{2,5}$ mode at the second harmonic frequency (223 GHz) with an output of 45 kW and an efficiency of 6% was stable. The detailed comparison of the measured and analytical LOG output characteristics showed that the electron beam apparently had an appreciable transverse velocity spread (up to 60%) and was offset from the axis by about 0.2 mm. To make the radiation at the third harmonic frequency stable, it seems necessary to adjust the electron beam more finely and, presumably, to use a lower index operating mode.

CONCLUSIONS

The modified EOS forms a 250-keV/4 A/10 μs electron beam with a high compression factor (4400). The application of such a beam in the LOG provides stable excitation at the second cyclotron harmonic frequency (223 GHz) with an output of 45 kW and an efficiency of 6%. The calculations show that such an electron beam can also provide excitation at the third cyclotron frequency (375 GHz).

ACKNOWLEDGMENTS

This work was supported by the Russian Foundation for Basic Research, project nos. 03-02-17064 and 02-02-17105.

We are grateful to Yu.A. Dryagin and L.M. Kukin for assistance and to M.A. Moiseev for valuable discussion.

REFERENCES

1. N. I. Zaitsev, T. B. Pankratova, M. I. Petelin, *et al.*, Radiotekh. Élektron. (Moscow) **19**, 1056 (1974).
2. A. G. Luchinin, O. V. Malygin, G. S. Nusinovich, and V. A. Flyagin, Zh. Tekh. Fiz. **53**, 1629 (1983) [Sov. Phys. Tech. Phys. **28**, 1001 (1983)].
3. S. Spira-Hakkarainen, K. E. Kreischer, and R. J. Temkin, IEEE Trans. Plasma Sci. **18**, 334 (1990).
4. M. K. Hornstein, V. S. Bajaj, R. G. Griffin, *et al.*, in *Proceedings of the Joint 29th International Conference on Infrared and Millimeter Waves and the 12th International Conference on Terahertz Electronics, Karlsruhe (Germany), 2004*, pp. 147–148.
5. T. Idehara *et al.*, IEEE Trans. Plasma Sci. **27**, 340 (1999).
6. L. R. Elias, G. Ramian, J. Hu, and A. Amir, Phys. Rev. Lett. **57**, 424 (1986).
7. V. S. Cherkassky, B. A. Knyazev, V. V. Kubarev, *et al.*, in *Proceedings of the Joint 29th International Conference on Infrared and Millimeter Waves and the 12th International Conference on Terahertz Electronics, Karlsruhe (Germany), 2004*, pp. 567–568.
8. W. Lawson, W. W. Destler, and C. D. Striffler, IEEE Trans. Plasma Sci. **13**, 444 (1985).
9. V. L. Bratman, A. E. Fedotov, Yu. K. Kalynov, *et al.*, IEEE Trans. Plasma Sci. **27**, 456 (1999).
10. V. L. Bratman, Yu. K. Kalynov, V. N. Manuilov, *et al.*, Radiotekh. Élektron. (Moscow) **46**, 744 (2001).
11. T. Idehara, I. Ogawa, S. Mitsudo, *et al.*, IEEE Trans. Plasma Sci. **32**, 903 (2004).
12. I. I. Antakov, A. V. Gaponov, and V. K. Yulpatov, Vopr. Radioélektroniki, Ser. 1: Élektronika, No. 12, 33 (1965).
13. M. I. Petelin, in *Girotron* (IPF AN SSSR, Gor'kii, 1981), pp. 5–25 [in Russian].

14. V. K. Yulpatov, in *Girotron* (IPF AN SSSR, Gor'kii, 1981), pp. 26–40 [in Russian].
15. D. B. McDermott, N. C. Luhmann, A. Kupiszewski, Jr., and H. R. Jory, Phys. Fluids **26**, 1936 (1983).
16. G. S. Nusinovich, Int. J. Electron. **72**, 959 (1992).
17. V. L. Bratman, Yu. K. Kalynov, and A. E. Fedotov, Zh. Tekh. Fiz. **68** (10), 91 (1998) [Tech. Phys. **43**, 1219 (1998)].
18. D. B. McDermott, N. C. Luhmann, A. Kupiszewski, Jr., and H. R. Jory, Int. J. Infrared Millim. Waves **4**, 639 (1983).
19. K. R. Chu, D. S. Furuno, N. C. Luhmann, *et al.*, IEEE Trans. Plasma Sci. **13**, 435 (1985).
20. O. A. Nezhevenko, V. P. Yakovlev, S. H. Gold, *et al.*, IEEE Trans. Plasma Sci. **30**, 1220 (2002).
21. V. L. Bratman, G. G. Denisov, A. E. Fedotov, *et al.*, in *Proceedings of the 6th Workshop on High Energy Density and Higher Power RF, Berkley Springs, West Virginia, 2003*, pp. 339–348.
22. V. N. Manuilov and Sh. E. Tsimring, Izv. Vyssh. Uchebn. Zaved., Radiofiz. **24**, 491 (1981).
23. V. L. Bratman, V. N. Manuilov, and S. V. Samsonov, Zh. Tekh. Fiz. **66** (8), 190 (1996) [Tech. Phys. **41**, 846 (1996)].

Translated by A. Khzmalyan

Technical Physics, Vol. 50, No. 12, 2005, pp. 1617–1622. Translated from Zhurnal Tekhnicheskoĭ Fiziki, Vol. 75, No. 12, 2005, pp. 82–88.

SURFACE, ELECTRON AND ION EMISSION

Double Scattering Effect and Its Application in $Si_{1-x}Ge_x$ Solid Solution Diagnosis

P. Yu. Babenko, V. M. Mikoushkin, and A. P. Shergin

Ioffe Physicotechnical Institute, Russian Academy of Sciences, Politekhnicheskaya ul. 26, St. Petersburg, 194021 Russia

e-mail: babenko@npd.ioffe.ru

Received April 21, 2005

Abstract—The effect of double scattering of Ar^+ ions from the surface of C, Al, Si, Ti, Ge, and In targets is studied by the method of slow scattered ion spectroscopy. Based on this effect, a technique to estimate the cluster phase of germanium atoms in the $Si_{1-x}Ge_x$ solid solution with a small (5–10%) content of germanium is suggested. © *2005 Pleiades Publishing, Inc.*

INTRODUCTION

Diagnostics of elemental inhomogeneity (specifically, clusters) is a challenging problem in production of the $Si_{1-x}Ge_x$ solid solution, a promising material for high-speed electronics [1]. Since atoms in clusters or in regions enriched by any of the constituent elements are bound to differ in chemical state from those in the homogeneous solution, it seems natural to use X-ray photoelectron spectroscopy—the method widely used for diagnostic purposes. However, as applied to Ge clusters in the $Si_{1-x}Ge_x$ solid solution, this method is entirely unsuited. The reason is that the binding energies of core Ge levels in the bulk Ge crystal [2] (or in sufficiently high Ge clusters) and in the solid solution [3] almost coincide because of similar electronic structures of germanium and silicon. The elemental inhomogeneity can today be estimated only qualitatively by the methods of transmission and scanning electron microscopy, as well as from the plasma oscillation spectrum in the electron system of clusters [4]; direct techniques to find the fraction of clustered Ge atoms in the SiGe solid solution are absent.

In this work, we developed a method of diagnosing elemental inhomogeneity (determining the amount of Ge atoms in the cluster phase) in $Si_{1-x}Ge_x$ solid solutions. The essence of this method is picking out the contribution of ions doubly scattered by Ge atoms from the mass spectra of slow scattered ions. The double scattering effect arises in the presence of Ge clusters or Ge-enriched regions and cannot basically be observed in the low-Ge homogeneous solid solution. This method was synopsized in the proceedings of the 16th International Conference on Ion–Surface Interaction [5].

Ion double scattering is known to be the first orientation effect (discovered as early as in 1965) in experiments on scattering of medium-energy argon ions by a copper crystal [6]. The energy distribution of the scattered ions has two unequal peaks. The lower energy peak is related to quasi-single scattering of a projectile by a target atom. This statement relies on the fact that the experimental dependence of its energy position on the scattering angle agrees well with the analytical curve constructed under the assumption of single elastic scattering of ions by free atoms of the target. Namely, the run of both curves is the same and the absolute values differ by inelastic energy losses in a real experiment. The term *quasi-single scattering* here is used to reflect the fact that a few atoms of a solid target are actually involved in the scattering event but the resulting scattering angle depends largely on scattering by only one of them. In the literature, the terms *a singly scattered ion, a peak corresponding to single scattering*, etc., are usually used to describe this situation.

Under certain conditions, the high-energy part of the spectrum of ions scattered by a crystal has a peak whose energy is close to the calculated energy of ions scattered in a given direction as a result of two sequential ion–target atom collisions. The double scattering effect is considered, e.g., in [7–9]. The issue of how the atomic distance in the surface layer of solids can be determined from this effect is discussed in [10]. In most experimental works, the energy of scattered particles is found by a time-of-flight technique and both neutral and charged particles are detected. The disadvantages of time-of-flight techniques as a surface diagnostics means are (i) large dimensions of instruments that measure the time it takes for a scattered particle to fly from the target to the detector and (ii) the need to apply pulsed ion beams. The energy of scattered particles is much easier to analyze using electrostatic analyzers. However, it is impossible to detect neutrals in this case, which constitute a major fraction of the scattered particle flow (except for the case of alkali metal ion scattering). Yet, we enlarged on electrostatic analysis, which allows one to considerably simplify the setup, operate with a continuous beam of incident ions (projectiles),

1063-7842/05/5012-1617$26.00

and gain statistics in an amount making it possible to reliably discriminate the desired effect. To choose optimal experimental conditions for the technique suggested, it was necessary to see how the peaks of singly and doubly scattered ions behave depending on kinematic parameters of the process (the angle by which a projectile is scattered and the projectile-to-target mass ratio). To this end, we studied the double scattering effect on C, Al, Si, Ti, Ge, and In targets, i.e., on targets made of elements entering into most semiconductor compounds currently used.

EXPERIMENTAL

We measured the energy distributions of scattered ions after 5-keV Ar^+ ions had bombarded the surface. The measurements were taken with the high-vacuum setup described in [11]. The energy and charge of the ions scattered by fixed angle θ (relative to the primary beam direction) were analyzed by a Hughes–Rojansky analyzer with an energy resolution of 9×10^{-3}. The analyzer could be horizontally rotated in the angular range θ = 0–30°, and the angular resolution of the scattered ion collimator was 20'. The specular scattering of the ions was studied (the angle of incidence is half the scattering angle). The residual pressure in the measuring chamber was equal to 10^{-9} Torr.

RESULTS AND DISCUSSION

In the first part of this work, we studied the double scattering of positive ions; in the second one, the feasibility of using this effect for surface analysis of solids. The contribution of double scattering to the total scattered particle flow is convenient to estimate using energy peak height ratio I_d/I_s versus experimental parameters, where I_d and I_s are the intensities of double and single scattering, respectively. Monograph [9] covers experiments where ratio I_d/I_s is studied as a function of primary (incident) ion energy E_0, scattering angle θ, glancing and azimuth angles, target temperature, atomic number of a projectile, and charge of the scattered ions.

If the particle energy is analyzed with a time-of-flight technique, the experimental value of ratio I_d/I_s can be directly contrasted with the results of calculation (computer simulation), since these techniques detect both the charged and neutral components in the scattering spectrum. If only charged scattered particles are analyzed, ratio I_d^+/I_s^+ for the ion fraction is related to ratio I_d/I_s for all the scattered particles as $I_d/I_s = (p_s^+/p_d^+)(I_d^+/I_s^+)$, where p_s^+ and p_d^+ are the respective fractions of the charged particles scattered by a given angle as a result of single and double collisions with surface atoms. It is known that the charge state of a scattered particle forms away from the surface, since the particle interacts not with individual target atoms but with the surface as a whole. Accordingly, the probability that the scattered particle will be in one charge state or another depends on such parameters as the work function of the surface, ionization potential, and the velocity normal component of the particle leaving the target [12]. It is then obvious that the values of p_s^+ and p_d^+ have to equal each other when the singly and doubly scattered ions escape the surface at the same angle, since their velocities differ infinitesimally.

However, for Ar^+ ions with energies of several kiloelectron-volts scattered by a polycrystalline Au target by angle θ = 90°, ratio I_d^+/I_s^+ turns out to be smaller than I_d/I_s [13]. The same fact was indicated in [4], where Ar^+ ions were mirror-scattered by a Cu crystal by θ = 30°. This means that comparing the calculated value of I_d/I_s with the experimental value of I_d^+/I_s^+ for the charged fraction of the scattered particles may be incorrect.

In [15], it was suggested that ratio I_d/I_s be calculated by the formula

$$I_d/I_s = \frac{\sigma(\theta_1, E_0)\sigma(\theta_2, E_1)}{\sigma(\theta, E_0)d^2}, \quad (1)$$

where $\sigma(\theta, E)$ is the differential cross section of scattering an ion with energy E by angle θ, E_0 is the initial energy of the ion, E_1 is the energy of the ion scattered by the first atom, θ_1 and θ_2 are the respective angles of scattering by the first and second atoms, and d is the spacing between the first and second atoms.

In this work, we studied the energy spectra of scattered argon ions and recoil ions. For the C, Al, and Si targets, the spectra taken at angle of observation θ = 12° are presented in Fig. 1. A change in the energy width of the analyzer's window due to a change in the ion energy is disregarded. The spectra contain peaks due to single scattering (*S*) and double scattering (*D*), as well as a peak corresponding to recoil ions (*R*) (the positions of these peaks are indicated for the carbon and silicon targets).

Figure 2 shows the dependence of ratio I_d^+/I_s^+ on the target atomic mass. The energy spectra were taken in the range of scattering angles θ = 6°–27°. To trace how ratio I_d^+/I_s^+ measured at different angles depends on the atomic mass of the target, it is convenient to recalculate the values of I_d^+/I_s^+ to one angle of observation using the relationship $I_d/I_s \sim 1/\theta^{2.5}$ [15], which is valid in the small-angle approximation. The dependences of $(I_d^+/I_s^+)(\theta/12)^{2.5}$ on the atomic mass of the target (i.e., of C, Al, Si, Ti, Ge, and In) are reduced to angle θ = 12°. For these targets, the values of $(I_d^+/I_s^+)(\theta/12)^{2.5}$ fall into the range 0.4–4.0. Our results agree with those obtained

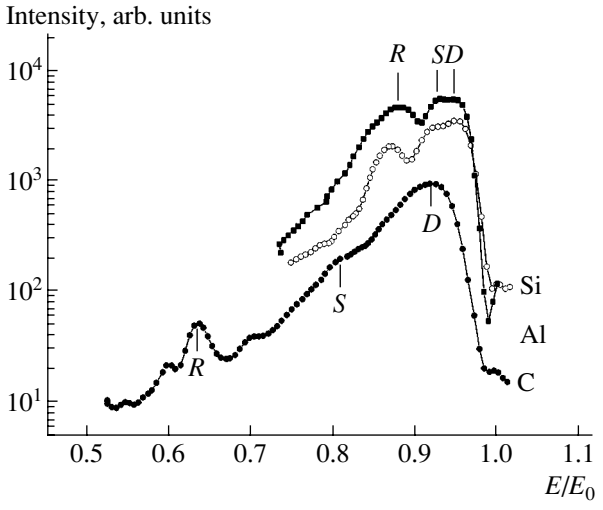

Fig. 1. Energy spectra of scattered ions and recoil ions when C, Al, and Si targets are bombarded by 5-keV Ar^+ ions. The angle of observation is $\theta = 12°$.

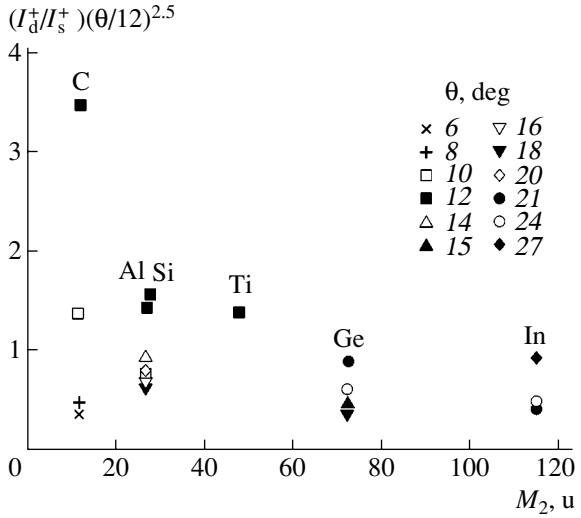

Fig. 2. Peak height ratio for singly and doubly scattered Ar^+ ions vs. the atomic mass of the target. The incident ion energy is $E_0 = 5$ keV.

in [10], where ratio I_d^+/I_s^+ for Ar^+ ions with $E_0 = 5$ keV scattered by a Cu crystal was measured. The value of $(I_d^+/I_s^+)(\theta/12)^{2.5}$ found from experimental data of [10] lies in the range 0.6–6.0 (such a wide interval is associated with the strong dependence on the target orientation).

Figure 3 demonstrates the angular dependences of I_d^+/I_s^+ (measured) and I_d/I_s (calculated by formula (1)) for Al, Ge, and In. It is seen that the data points are fitted well by the relationship $I_d/I_s \sim 1/\theta^{2.5}$ (dotted curve) [15]. Atomic spacing d of the target used in the calculation was taken from the table of lattice constants [16]. Agreement between the absolute values of experimental I_d^+/I_s^+ and I_d/I_s calculated by (1) will be achieved if d is higher by two- or threefold. Thus, formula (1) and its small-angle asymptotics, $I_d/I_s \sim 1/\theta^{2.5}$, describe well the run of the angular dependence but the absolute values of I_d/I_s disagree.

The energy dependence of I_d^+/I_s^+ for In (the angle of observation is $\theta = 27°$) is presented in Fig. 4. In the energy range 2–5 keV, I_d^+/I_s^+ equals 0.08–0.13. Figure 4 also shows the data for variously oriented Cu crystals in the case of Ar^+ projectiles with $E_0 = 5$–10 keV and $\theta = 30°$ [10]. It follows from this figure that ratio I_d^+/I_s^+ for the Cu samples monotonically grows from 0.06 to 2.60 as the energy increases from 5 to 10 keV. Our results are seen to agree with those from [10].

From the aforesaid, it follows that the effect of double scattering of the scattered particles is well pronounced in the case of the C, Al, Si, Ti, Ge, and In targets. The dependence of I_d^+/I_s^+ on experimental parameters agrees well with the data of other authors and obeys the same law as ratio I_d/I_s for the total particle flux. Thus, information gained from analysis of the charged component can be used for diagnostic purposes.

Now, let us turn to the feasibility of using this effect in diagnostics of the $Si_{1-x}Ge_x$ solid solution. The possibility of separating out the fraction of clustered Ge atoms in the SiGe solid solution is based on the difference between the energies of ions having experienced two successive collisions with similar atoms (Ge + Ge) and dissimilar atoms (Ge + Si). Consequently, the spectra of scattered Ar^+ ions for the samples with Ge clusters will differ from the spectra taken of the homogeneous solid solution: in the former case, along with the peak due to normal double scattering (Ge + Si), an additional peak associated with double scattering by Ge atoms (Ge + Ge) arises. The fraction of clustered Ge atoms can be estimated by comparing the ratio between the intensities of double (Ge + Ge) and single scattering of Ar^+ ions by Ge atoms in the solid solution with the same ratio for pure germanium.

We measured the energy distribution of Ar^+ ions with initial energy $E_0 = 5$ keV scattered by $Si_{1-x}Ge_x$ samples with $x = 5$–10, 25, 50, and 60%. The low-germanium (5–10%) samples were prepared in the Institute of Crystal Growth (Berlin, Germany); the samples with $x = 25$, 50, and 60%, in the Ioffe Physicotechnical Institute, Russian Academy of Sciences (St. Petersburg). The angles of observation (measurement) were 21° and 24°, since the double scattering peak is best visible at these angles (it is high and far apart from the single scattering peak).

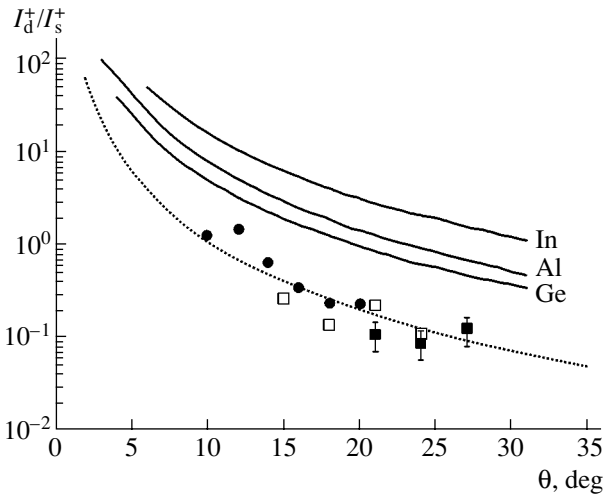

Fig. 3. Experimental values of I_d^+/I_s^+ (symbols) and calculated values of I_d/I_s (solid lines) vs. scattering angle for (●) Al, (□) Ge, and (■) In. The dotted line depicts the relationship $I_d/I_s \sim 1/\theta^{2.5}$.

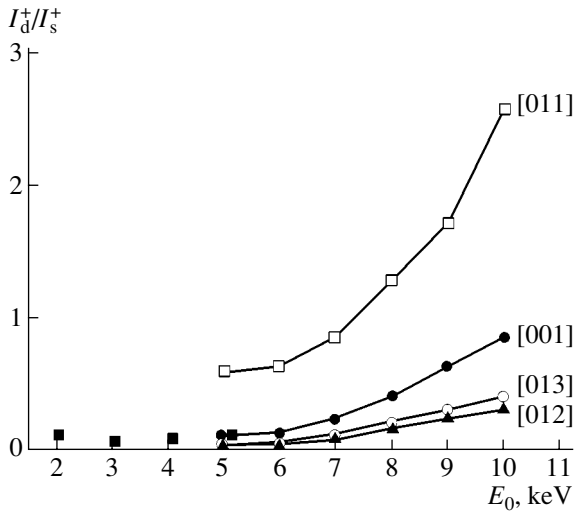

Fig. 4. Experimental value of I_d^+/I_s^+ vs. incident Ar^+ ion energy. (■) Experimental values obtained in this work for In and angle of observation θ = 27°. The lines with symbols refer to the variously oriented Cu target [10].

Figure 5 shows the energy spectra of the scattered ions and recoil atoms for the $Si_{1-x}Ge_x$ samples with x = 5, 25, and 50% at E_0 = 5 keV and θ = 24°. The spectra contain the peaks of the Ar^+ ions singly scattered by Ge atoms, *S*(Ge), and silicon atoms, *S*(Si), as well as the peak of recoil atoms, *R*(Si). A validity criterion for these measurements is the ion intensity ratio. For example, the intensity ratio for Ar^+ ions singly scattered by Ge and Si atoms in the $Si_{1-x}Ge_x$ solution must be directly proportional to the ratios between the concentrations of the respective components, differential cross sections $d\sigma/d\Omega$ of scattering by a given angle, and widths ΔE of the analyzer's energy window for the peaks measured. It is then natural to assume that probability p^+ of generation of singly charged ions, which is defined by electron exchange in the escaping ion–surface system, does not depend on whether a Ge or Si atom acts as a scatterer. In the approximation of the Ziegler–Biersack–Littmark interaction potential [17], the calculated intensity ratio of Ar^+ ions scattered by Ge and Si atoms in the $Si_{1-x}Ge_x$ samples with x = 5, 25, and 50% is 0.1, 0.6, and 1.9, respectively, for the differential cross sections estimated at an angle of observation of 24°. The accuracy of measuring the intensity ratio is not high primarily because of a poorly resolved peak of the Ar^+ ions scattered by Si (this peak overlaps with the more intense peak of Si^+ recoil ions). For the samples with x = 5, 25, and 50%, the measured intensity ratio is 0.19 ± 0.06, 1.4 ± 0.5, and 2.9 ± 1.0, respectively. Agreement between the calculation and experiment may be considered satisfactory.

On the right of single scattering peak *S*(Ge) in the spectra, a structure is observed that is related to the Ar^+ ions having experienced at least two successive collisions. At a given angle of observation, Ar^+ ions with an energy exceeding the energy of single scattering by Ge atoms may result from two processes: an Ar atom collides (i) with a Ge atom and a Si atom (the structure denoted by *D*(Ge + Si) in Fig. 5) or (ii) with two Ge atoms (this structure, which is of interest for us, is denoted by *D*(Ge + Ge) in Fig. 5), the energy of scattered ions in the former case being bound to be lower. For an angle of observation of 24° (x = 5%), the peak of double scattering by Ge and Si atoms is $\Delta E/E_0 = 0.02$ apart from the peak of single scattering by a Ge atom. For pure germanium, the peak of singly scattered Ar^+ ions is $\Delta E/E_0 = 0.03$ apart from the peak of double scattering. Thus, double scattering peak *D*(Ge + Ge) is $\Delta E/E_0 = 0.01$ apart from peak *D*(Ge + Si). This difference, while small, is sufficient to conclude that the cluster fraction in the samples with x = 5–10% is absent.

Thus, we can state that the low-germanium samples submitted for investigation are of fairly high quality: most Ge atoms in the solid solution occupy lattice sites, and the remainder are interstitials or form small clusters (clearly, Ar^+ ion scattering by small clusters makes a negligible contribution to the double scattering peak, since such is the probability that an ion having experienced a collision with a Ge atom will "find" another Ge atom to collide with in its neighborhood). The estimate of the cluster fraction, if any, could be affected by the effect of preferred sputtering of one of the solid solution components. As is known, the sputtering coefficient for pure germanium is roughly twice as high as that for pure silicon when these materials are irradiated by 5-keV Ar^+ ions. However, bombardment of the SiGe compound surface by inert gas ions leaves the surface

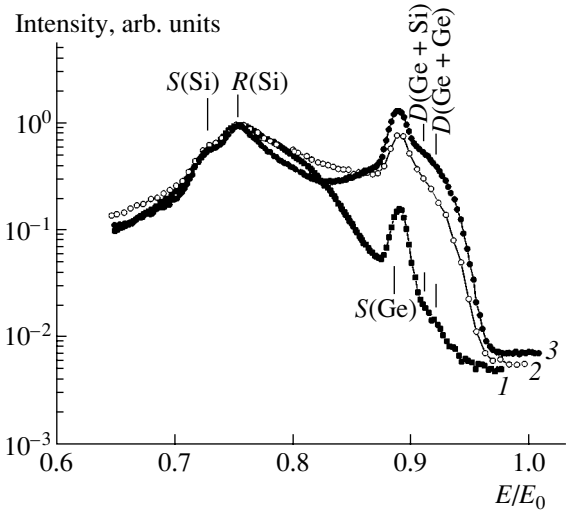

Fig. 5. Energy spectra of scattered Ar^+ ions and recoil ions in the $Si_{1-x}Ge_x$ solid solution with x = (*1*) 5, (*2*) 25, and (*3*) 50%. E_0 = 5 keV, θ = 24°.

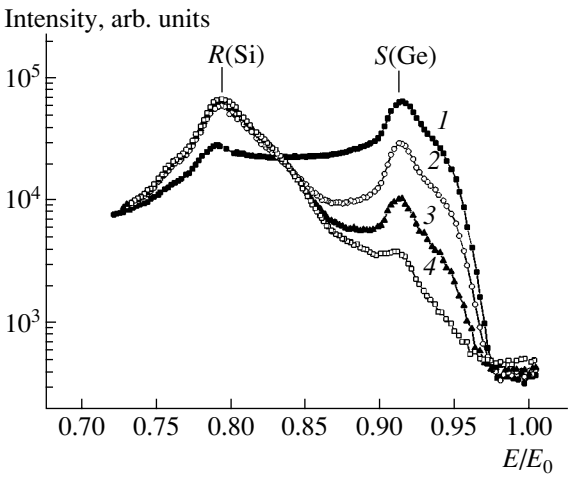

Fig. 6. Variation of the energy spectra of scattered Ar^+ ions and recoil Si^+ ions under irradiation of the $Si_{1-x}Ge_x$ target by 5-keV Ar^+ ions with etch time: (*1*) 0, (*2*) 10, (*3*) 15, and (*4*) 30 min. θ = 21°.

composition unchanged, as follows from experimental data [18].

The applicability of this approach to thin-film SiGe was tested on ≈100-nm-thick $Si_{1-x}Ge_x$ films MBE-grown on silicon in the Ioffe Physicotechnical Institute. Figure 6 shows the variation of the energy spectra obtained when one of such films (x = 60%) was etched by 5-keV Ar^+ ions with time of etching. The high-energy part of the spectra exhibits a peak of Ar^+ ions singly scattered by Ge atoms; the central part contains a peak of Si^+ recoil ions. The intensity of the former peak declines with time and almost disappears in ≈30 min. This means that the incident Ar^+ ion beam (energy E_0 = 5 keV, current density $j \approx 10$ μA/cm^2) etches off the $Si_{1-x}Ge_x$ layer and reaches the substrate. It follows from Fig. 6 that our approach provides a sufficiently high scattered ion intensity (~10^3 s^{-1}), acceptable noise-to-signal ratio (~10^2) in the energy range we are interested in, and time sufficient to carry out analysis. Hence, the method suggested can be applied for estimating the Ge cluster concentration in thin $Si_{1-x}Ge_x$ films.

Since clusters were lacking in the samples with x = 5–10%, the method of cluster concentration estimation was refined on the targets with high x (25, 50, and 60%). We proceeded from the assumption that, if the Ge concentration in the target is high, the energy spectrum will contain a collision-induced peak (Ge + Ge) resulting not from clusters but from individual Ge atoms (even if the solution is homogeneous), which are closely spaced in a high-germanium solid solution. Therefore, a collision-induced spectral feature (Ge + Ge) gives us a chance to simulate clustering in the target.

Figure 7 demonstrates the energy range of interest for the samples with x = (a) 5 and (b) 60%. The angle of observation is 21°. The estimation of the cluster con-

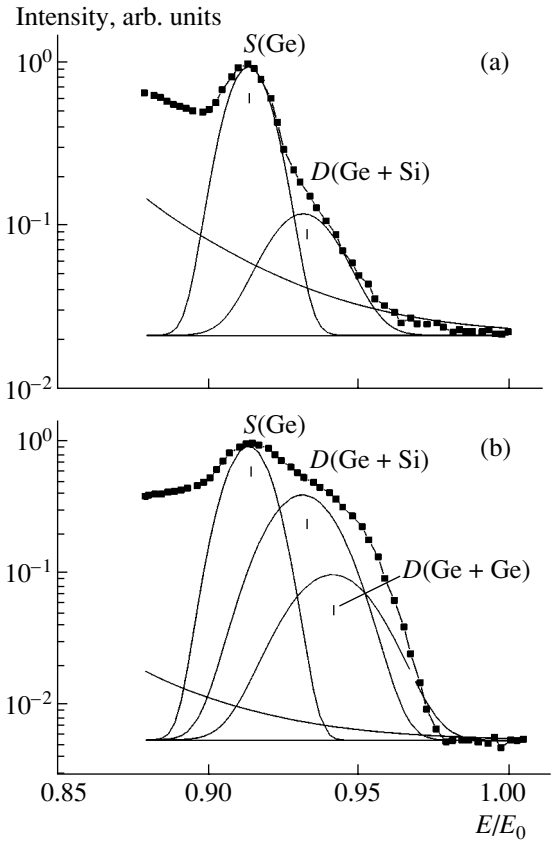

Fig. 7. Scattered Ar^+ ion spectra under irradiation of the $Si_{1-x}Ge_x$ target with x = (a) 5 and (b) 60%. θ = 21°. Symbols, data points; continuous lines, model energy distributions of components.

centration is based on the assumption that the spectrum in the given energy range consists of the following components: a peak of Ar^+ ions singly scattered by Ge atoms, a peak of Ar^+ ions doubly scattered by Ge and Si atoms, a peak of Ar^+ ions double scattered by Ge atoms, a "pedestal" associated with Ar^+ ions scattered by pure silicon, and a background due primarily to scattering of the incident beam by structure elements of the chamber. In Fig. 7, the single scattering and double scattering peaks are described by Gaussians, the substrate component is that part of the experimental spectrum described by the analytical curve, and the background is described by some constant level. Since clusters are absent in the sample with $x = 5\%$, the spectrum for this sample has four components (Fig. 7a): the background, substrate component, single scattering peak S(Ge), and double scattering peak D(Ge + Si). In simulating the spectra for the samples with a higher Ge percentage, the adjustable parameters were only the amplitudes of the Gaussians describing processes D(Ge + Ge) and D(Ge + Si) provided that these amplitudes are normalized by peak S(Ge). In describing the spectrum for the sample with $x = 60\%$, it is impossible to simulate the experimental curve without taking into account double scattering by Ge atoms, D(Ge + Ge). Comparing the intensity ratios of the Ar^+ ions singly and doubly scattered by Ge atoms in the $Si_{1-x}Ge_x$ solid solution and in a pure Ge target, one can estimate the concentration of the "clusters." In the sample with $x = 60\%$, this ratio equals ≈ 0.9. The word "clusters" is put in quotation marks, since peak D(Ge + Ge) here is associated with a decrease in the Ge atom spacing and, hence, with an increase in the double scattering probability in the high-germanium solid solution even if it is homogeneous.

CONCLUSIONS

We measured the intensity ratio for Ar^+ ions singly and doubly scattered by C, Al, Si, Ti, Ge, and In targets as a function of the atomic mass of the target (M_2 = 12–115 u), projectile energy (E_0 = 2–5 keV), and angle of observation ($\theta = 6°$–$27°$). The data obtained indicate that the double scattering effect shows up in the ionic component, which constitutes a minor part of the total particle flux and obeys the laws typical of neutrals.

This effect can be used to estimate the Ge cluster fraction in the $Si_{1-x}Ge_x$ solid solution. It is shown that slow scattered ion spectroscopy is applicable to diagnostics of elemental inhomogeneity in both thin (~100 nm) films and bulk samples of the low-germanium $Si_{1-x}Ge_x$ solid solution. The method of estimating the Ge cluster fraction in the $Si_{1-x}Ge_x$ solid solution is elaborated.

ACKNOWLEDGMENTS

The authors are indebted to D.V. Denisov (Ioffe Physicotechnical Institute, St. Petersburg) and N.V. Abrosimov (Institute of Crystal Growth, Berlin) for submitting the samples.

This work was supported by the program "Low-Dimensional Quantum Structures" at the Presidium of the Russian Academy of Sciences, project no. 6.3.

REFERENCES

1. G. Kissinger and H. G. Grimmeiss, Phys. Status Solidi A **145**, K5 (1994).
2. D. Briggs and M. P. Seah, *Practical Surface Analysis by Auger and X-ray Photoelectron Spectroscopy* (Wiley, New York, 1983; Mir, Moscow, 1987).
3. E. A. Ogryzlo, L. Zheng, B. Heinrich, *et al.*, Thin Solid Films **321**, 196 (1998).
4. Yu. S. Gordeev, V. M. Mikoushkin, V. V. Brysgalov, *et al.*, in *Proceedings of the 10th International Symposium "Nanostructures: Physics and Technology," St. Petersburg, 2002*, pp. 168–171.
5. A. P. Shergin, P. Yu. Babenko, and V. M. Mikushkin, Izv. Ross. Akad. Nauk, Ser. Fiz. **68**, 380 (2004).
6. E. S. Mashkova, V. A. Molchanov, E. S. Parilis, *et al.*, Phys. Lett. **18**, 7 (1965).
7. E. P. Th. M. Suurmeijer and A. L. Boers, Surf. Sci. **43**, 309 (1974).
8. A. L. Boers, Surf. Sci. **63**, 475 (1977).
9. E. S. Mashkova and V. A. Molchanov, *Medium-Energy Ion Scattering by Solid Surfaces* (Atomizdat, Moscow, 1980) [in Russian].
10. A. J. Algra, S. B. Luitjens, H. Borggereve, *et al.*, Radiat. Eff. **62**, 7 (1982).
11. A. P. Shergin and A. V. Shaikin, Izv. Ross. Akad. Nauk, Ser. Fiz. **66**, 467 (2002).
12. A. Arnau, P. M. Echenique, F. Aumayr, *et al.*, Surf. Sci. Rep. **27**, 113 (1997).
13. T. M. Buck, Y. S. Chen, G. H. Wheatley, *et al.*, Surf. Sci. **47**, 244 (1975).
14. S. B. Luitjens, A. J. Algra, E. P. Th. M. Suurmeijer, *et al.*, Surf. Sci. **99**, 652 (1980).
15. E. S. Mashkova and V. A. Molchanov, Fiz. Tverd. Tela (Leningrad) **8**, 1517 (1966) [Sov. Phys. Solid State **8**, 1206 (1966)].
16. C. Kittel, *Introduction to Solid State Physics* (Wiley, New York, 1976; Nauka, Moscow, 1978).
17. W. Eckstein, *Computer Simulation of Ion–Solid Interactions* (Springer, Berlin, 1991; Mir, Moscow, 1995).
18. *Sputtering by Particle Bombardment*, Ed. by R. Behrisch (Springer, New York, 1981; Mir, Moscow, 1986).

Translated by V. Isaakyan

Technical Physics, Vol. 50, No. 12, 2005, pp. 1623–1627. Translated from Zhurnal Tekhnicheskoĭ Fiziki, Vol. 75, No. 12, 2005, pp. 89–93.

SHORT COMMUNICATIONS

Electron Beam Formation in a Gas Diode at High Pressures

S. B. Alekseev*, V. M. Orlovskiĭ*, V. F. Tarasenko*, A. N. Tkachev, and S. I. Yakovlenko****

** Institute of High-Current Electronics, Siberian Division, Russian Academy of Sciences, Akademicheskiĭ pr. 4, Tomsk, 634055 Russia*

e-mail: VFT@loi.hcei.tsc.ru

*** Prokhorov Institute of General Physics, Russian Academy of Sciences, ul. Vavilova 38, Moscow, 119991 Russia*

e-mail: syakov@kapella.gpi.ru

Received January 12, 2005

Abstract—Electron beam formation in krypton, neon, helium, and nitrogen at elevated pressures are experimentally investigated. It is shown that, when the krypton, neon, and helium pressures are varied, respectively, from 70 to 760 Torr, from 150 to 760 Torr, and from 300 to 4560 Torr, runaway electrons are beamed at the instant the plasma in the discharge gap approaches the anode and the nonlocal criterion for electron runaway is fulfilled. The fast-electron simulation of discharge gap preionization is performed. The simulation data demonstrate that preionization in the discharge gap is provided if the voltage pulse rise time is shorter than a nanosecond under atmospheric pressure. © *2005 Pleiades Publishing, Inc.*

INTRODUCTION

In the studies summarized in [1], subnanosecond electron beams with a record-breaking current amplitude were produced in a gas diode under atmospheric pressure. It was shown that these beams of runaway electrons form at the instant the plasma in the discharge gap approaches the anode and the nonlocal criterion for electron runaway is fulfilled (for more details, see [1, 2]). It is of interest to study this mechanism for a wider spectrum of gases (including heavy ones) and under higher-than-atmospheric pressures. Relevant investigations at pressures far exceeding the atmospheric value have not been performed to date. Our preliminary experiments in this field were reported in [3–5].

In this study, we consider the electron beam formation at elevated pressures of different gases (krypton, neon, helium, and nitrogen), krypton being studied for the first time under these conditions.

The simulation of the propagation of bunched fast electrons has demonstrated that preionization in the discharge gap is provided at a subnanosecond voltage pulse rise time under atmospheric pressure.

EXPERIMENTAL SETUP

We used an upgraded version of the SINUS nanosecond pulser, which was described at length elsewhere [6]. The pulser (Fig. 1) was equipped with an additional built-in transmission line with a wave resistance of 40 Ω. A matched termination of 40 Ω generated a voltage pulse of amplitude ≈180 kV. At a rise time of the voltage pulse of ≈0.5 ns, its FWHM was ≈1.5 ns. As in [3–5], the cathode was composed of three coaxial cylinders (12, 22, and 30 mm in diameter) made of 50-μm-thick Ti foil and mounted on a duralumin substrate. The height of the cylinders decreased by 2 mm from the least-diameter to largest-diameter cylinder. The discharge gap width was varied from 10 to 28 mm. The plane anode through which the electron beam was extracted was made of 40- to 45-μm-thick AlBe foil or of a wire mesh. A negative voltage pulse was applied to the cathode under a krypton, neon, or helium pressure in the discharge gap varying from 1 to 760 Torr. For helium, additional measurements were taken at a pressure in the discharge gap varying from 760 to 4560 Torr (from 1 to 6 atm). Elevated-pressure measurements (from 1 to 4 atm) were also performed for nitrogen.

The beam current was measured using collectors of different diameters (from 12 to 50 mm) placed at a distance of 10 mm from the foil. Along with the electron

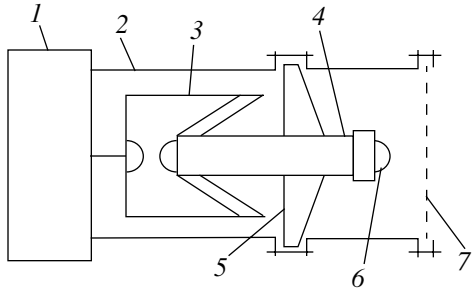

Fig. 1. Schematic of the electron accelerator with a gas diode: (*1*) pulser, (*2*) body, (*3*) sharpener, (*4*) high-voltage terminal, (*5*) insulator, (*6*) cathode, and (*7*) anode.

1063-7842/05/5012-1623$26.00 © 2005 Pleiades Publishing, Inc.

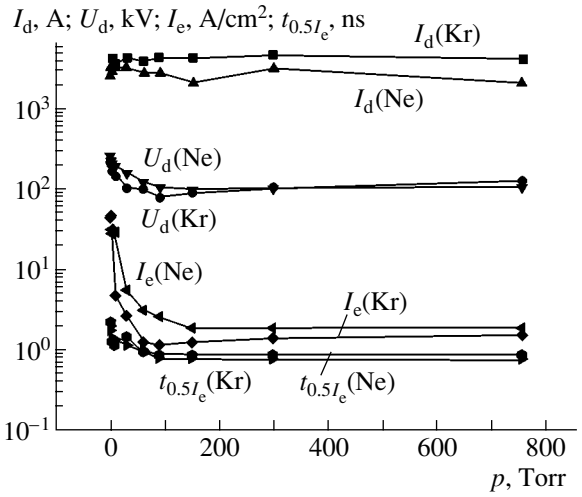

Fig. 2. Discharge current amplitude in the diode (I_d), the voltage across the gas diode (U_d), the beam current density behind the foil (I_e), and the FWHM of the beam current ($t_{0.5I_e}$) vs. the krypton and neon pressure.

beam current, we also measured the "total" current of the diode and the gap voltage. The waveforms of signals from a capacitive divider, collector, and shunt resistors were recorded by a TDS-7405 4-GHz oscilloscope with a speed of 20 GS/s (20 dots per 1 ns) and a TDS-334 0.3-GHz oscilloscope with a speed of 2.5 GS/s (2.5 dots per 1 ns). When the gas diode was filled with helium or nitrogen, the measurements were taken using the TDS-7405; when with krypton or neon, using the TDS-334. The discharge glow was photographed by a digital camera.

EXPERIMENTAL RESULTS

Figure 2 shows the pressure dependences of the amplitude of the discharge current through the diode, of the voltage across the gap, of the electron beam current density behind the foil, and of the FWHM of the beam current pulse for krypton and neon. The same dependences for helium are shown in Figs. 3 and 4. For the electron beam in helium, the measurements were taken at a time resolution of the recording system of ≈0.1 ns and a maximum pressure of 6 atm (Fig. 5). The dependences for krypton depicted in Fig. 2 are similar to those obtained by us earlier for helium and neon [3]. Note that, in krypton (the heaviest gas), the current density behind the foil, as well as the pressure at which the beam current amplitude began to increase, was the lowest.

From Figs. 2 and 3, one can separate out two main operating regimes of the diode. The first regime, which was described by us earlier [3], is observed at a helium pressure of less than 100 Torr (E/p > 0.6 kV/(Torr cm)), a neon pressure of less than 50 Torr (E/p > 1.2 kV/(Torr cm)), and a krypton pressure of less than 20 Torr (E/p >2.5 kV/(Torr cm)). This regime is characterized by a significant increase in the amplitude and duration of the electron beam current behind the foil at low helium, neon, and krypton pressures. Such behavior manifests the transition to the electron acceleration regime accomplished in [7]. Here, a critical field is reached between the electrodes of the diode or between the cathode and the excessive positive charge region in the gap. For the critical field to be reached in the first regime with increasing pressure in the diode, it is necessary to narrow the electrode gap to several fractions of a millimeter or even less. In this case, however, the electric field at the cathode rises due to explosive elec-

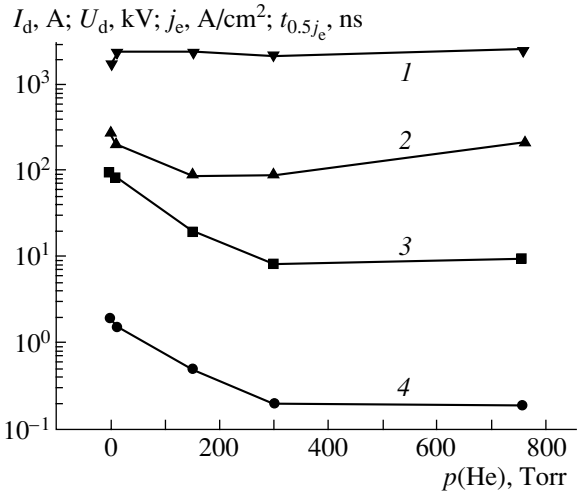

Fig. 3. (*1*) Discharge current amplitude in the diode, (*2*) voltage across the diode, (*3*) beam current density behind the foil, and (*4*) FWHM of the beam current vs. the helium pressure.

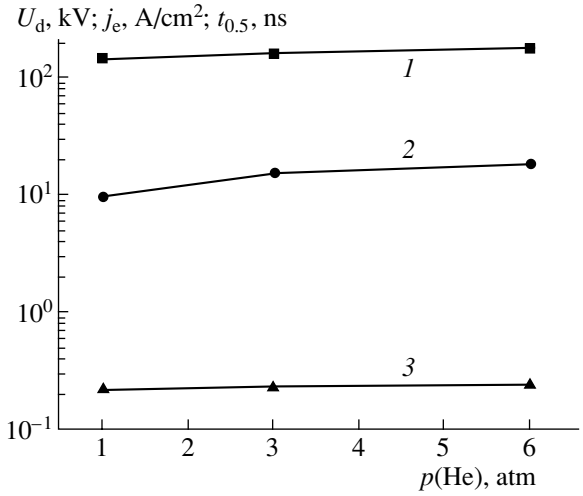

Fig. 4. (*1*) Voltage across the diode, (*2*) beam current density behind the foil, and (*3*) FWHM of the beam current vs. the helium pressure for an electrode spacing of 16 mm.

tron emission, generating a plasma. The cathodic plasma rapidly short-circuits the gap, and the beam of runaway electrons has no time to form.

Of most interest is the second regime, which was used to produce subnanosecond electron beams [1, 3–5] at a pressure of 1 atm or higher. Figures 2–4 show that, at a helium pressure exceeding 300 Torr (at neon and krypton pressures exceeding 100 and 50 Torr, respectively), the amplitude of the electron beam current, the amplitude of the gap voltage, and the amplitude of the discharge current vary insignificantly. In this case, the value of parameter E/p for all the gases becomes much smaller than critical (at which the amount of runaway electrons is considerable). In other words, a change in the krypton, neon, and helium pressures in the diode by several times has no effect on the amplitude of the electron beam current behind the foil. Such a variation of the beam current with pressure convincingly validates the assumption that the electron beam forms in the region between the anode and the plasma expanding from the cathode. As the pressure grows, the critical value of parameter E/p is attained at a proportionally decreasing distance to the anode. Note that the parameters of the electron beam will vary insignificantly under these conditions only if the discharge remains volume and its geometrical sizes remain unchanged. In helium, this condition is met; therefore, the parameters of the electron beam do not change even at a maximum pressure of 6 atm. The formation of an electron beam at still higher pressures was beyond the scope of this paper. The photos of the glow in the 16-mm-wide electrode gap at helium pressures of 1, 3, and 6 atm are shown in Fig. 6. It is seen that the discharge in the diode is of volume character and the geometry of the gas-discharge plasma remains invariable. Note that the discharge was volume in all the atomic gases under the pressures used.

Figure 7 shows the discharge glow in nitrogen at pressures of 1, 2, 3, and 4 atm. At 4 atm, the gap is short-circuited by a bright channel. As is seen on the photos taken at different pressures (Fig. 4), the channel originates at the cathode. Remarkably, when the pressure increases, the shape of the discharge changes and when the spark (channel) short-circuits the gap, the amplitude of the beam current sharply drops (Figs. 7 and 8). The pressure dependences of the gap voltage, electron beam current density behind the foil, and FWHM of the beam current under these conditions are shown in Fig. 8. The parameters of the beam current were measured with a time resolution of ≈0.1 ns. A feature of beam formation in nitrogen is that the geometrical sizes of the discharge plasma change (Fig. 7). When the pressure exceeds 1 atm, the cross section of the plasma shrinks and the amplitude of the beam current declines (Fig. 8). This decline is associated with a decrease in the capacitance of the "capacitor" made up by the anode and the plasma expanding from the cathode. It was also found that the current of the beam of runaway electrons depends on the geometrical sizes of the discharge plasma and on its homogeneity.

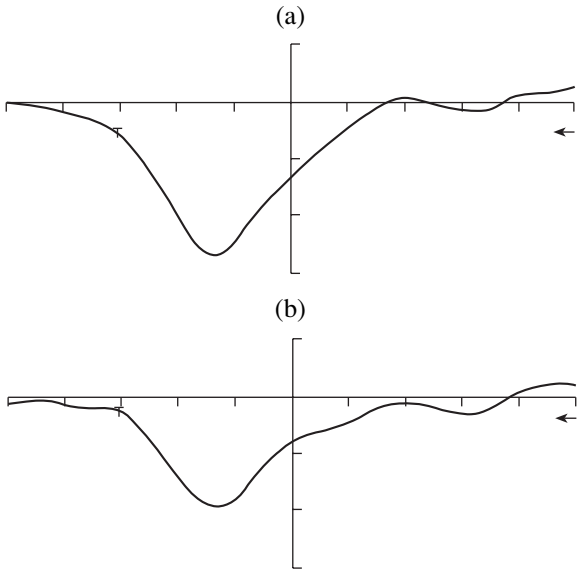

Fig. 5. Waveforms of the electron beam current pulses obtained in the diode at helium pressures of (a) 1 and (b) 3 atm. The recording surface area of the collector is 1 cm^2. The horizontal scale is 0.1 ns/div. The vertical scale is (a) 3.7 and (b) 7.8 A/div.

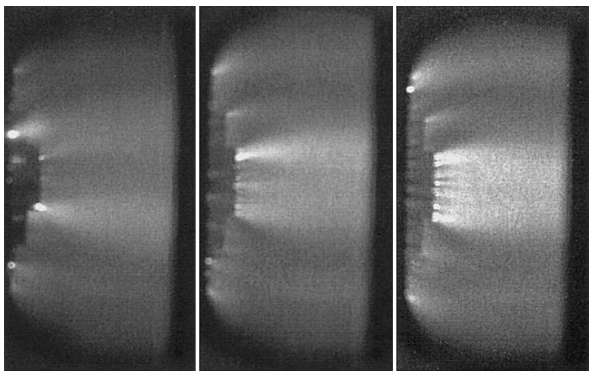

Fig. 6. Discharge glow in the diode at different helium pressures for an electrode spacing of 16 mm.

PROPAGATION OF FAST AVALANCHE ELECTRONS

According to the notions summarized in [1, 2], at the stage of electron beam formation, the discharge propagates in a dense gas by multiplication of available low-density background electrons rather than by means of electron or photon transport. The background density of electrons increases owing to the preionization of the gas by fast electrons preceding the multiplication wave. Below, we present the results of simulation for a bunch of fast electrons propagating in helium under

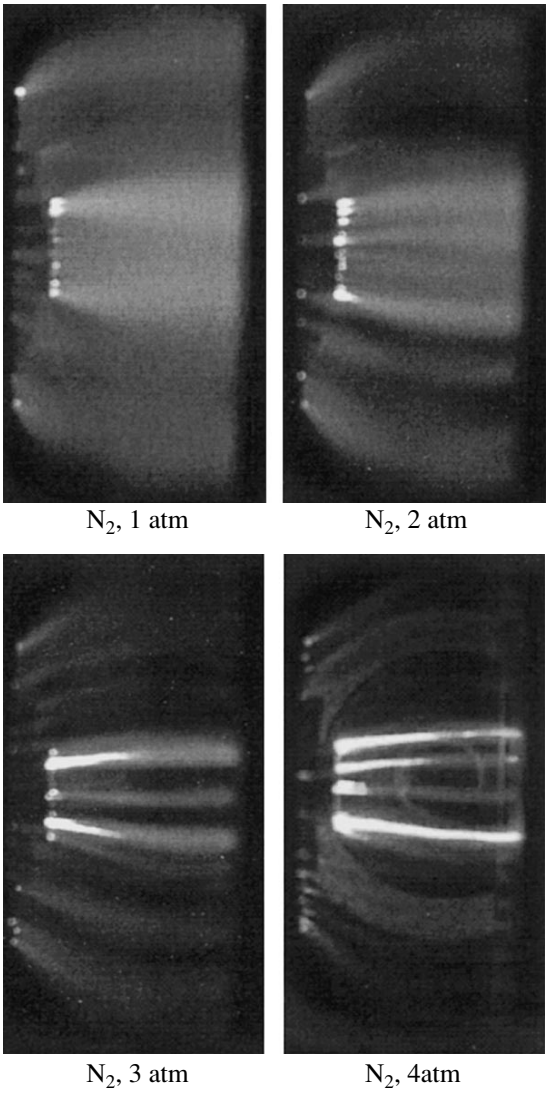

Fig. 7. The same as in Fig. 6 at different nitrogen pressures.

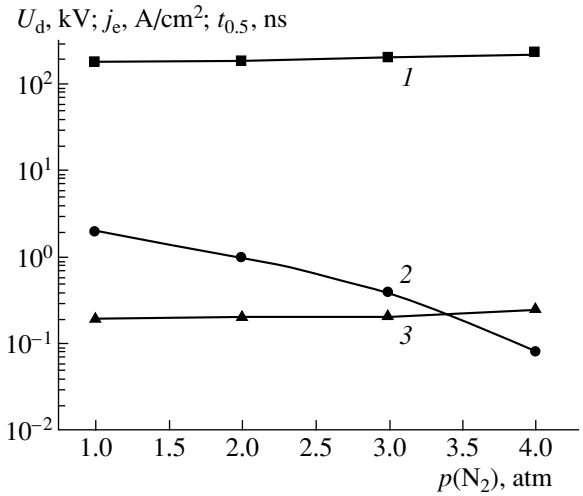

Fig. 8. (*1*) Voltage amplitude across the diode, (*2*) beam current density behind the foil, and (*3*) FWHM of the beam current vs. the nitrogen pressure for an electrode spacing of 16 mm.

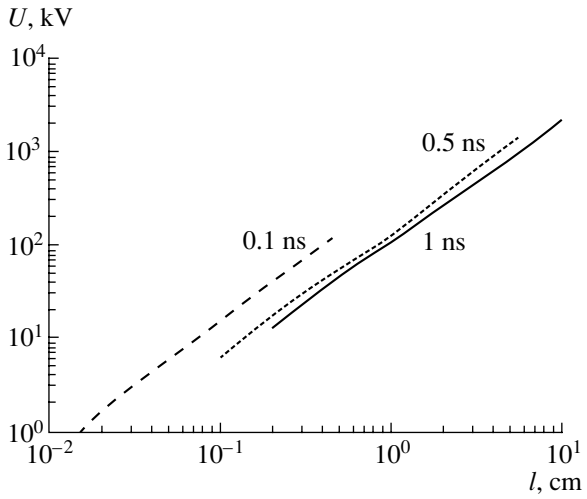

Fig. 9. Voltage drop $U = El$ over length $l = l_1 \approx l_2$ corresponding to the averaged coordinate of fast electrons vs. this length for time instants $\tau = 0.1$, 0.5, and 1 ns.

atmospheric pressure. The simulation of multiplication and runaway of electrons in helium was performed in the same manner as in [1, 2], i.e., based on a modification of the particle method (for details, see [8]). The cross sections were assumed to be relativistic [9].

We were interested in the coordinates and momenta of a bunch of the fastest electrons and also in total amount n of electrons. If this amount exceeded given amount n_{max} at a certain time step, we rejected some of the slow electrons in such a way that the number of remaining electrons was equal to n_{min} and the projections of their momenta onto the field direction were maximal. Prior to rejection, the coordinate along the field, l_1, and momentum p_1 that were averaged over all electrons were calculated and stored. After rejection, coordinate l_2 and momentum p_2 averaged over the bunch of fast electrons were calculated and stored. Next, the propagation and multiplication of these fast electrons was simulated until $n < n_{max}$.

The calculations were carried out for different electric field intensities E. Helium pressure p was assumed to be equal to 1 atm. The electron motion was traced to time instant $t = \tau = 1$ ns. We put $n_{max} = 2000$ and $n_{min} = 1000$.

It follows from the calculations that volume preionization over a given length in a given time will take place only if a voltage drop over this length is sufficiently high. This fact is illustrated in Fig. 9, which plots voltage drop $U = El$ versus length $l = l_1 \approx l_2$ (the averaged coordinate of the fast electrons) for different time instants $\tau = 0.1$, 0.5, and 1 ns. These dependences

show limiting voltage U above which fast electrons cause preionization of the gap with given electrode spacing l in a time shorter than τ. It is seen that a voltage higher than 100 kV is required for preionization of a 1-cm-wide gap filled with helium to take place in 1 ns under atmospheric pressure. This estimate is consistent with experimental findings.

However, the dependences in Fig. 9 may be treated otherwise. They show that, at a given voltage across a discharge gap of a given length, preionization will take place if the pulse rise time is shorter than time τ for which the curve in Fig. 9 was constructed.

CONCLUSIONS

Thus, we investigated the conditions under which runaway electrons are generated in krypton, neon, helium, and nitrogen at elevated pressures. For krypton, such a study was performed for the first time. Under atmospheric pressure in neon, an electron beam with a current density higher than 6 A/cm^2 was obtained. After the resolution of the recording system had been improved, the FWHM of the electron beam current in helium and nitrogen was measured to be $\approx$0.2 ns.

The electron beam formation in nitrogen demonstrates that spark channels adversely affect the beam generation conditions. This is associated with a decrease in the cross-sectional area of the volume discharge and also with the fact the spark shot-circuits the electrodes. These facts cannot be explained by assuming that the electron beam behind the foil consists of the electrons emitted from the end of the propagating spark channel [10].

The simulation of the propagation of preavalanche fast electrons showed that rapid preionization occurs if the voltage across the gap exceeds a certain value depending, in particular, on the electrode spacing. The pulse ride time must be shorter than the preionization time. In other words, a subnanosecond voltage pulse rise time under atmospheric pressure should be provided.

Thus, when the krypton, neon, and helium pressures vary, respectively, in the ranges 70–760, 150–760, and 300–4560 Torr, applying a nanosecond voltage pulse with a subnanosecond rise time generates a beam of runaway electrons. The beam forms at the instant the plasma in the discharge gap approaches the anode and the nonlocal criterion for electron runaway is fulfilled. In this case, the discharge propagates via the multiplication of background electrons. An enhanced background density of the electrons is provided by gas preionization by the fast electrons preceding the multiplication wave.

ACKNOWLEDGMENTS

We are grateful to S.D. Korovin for the aid in performing the experiments with the SINUS pulser.

REFERENCES

1. V. F. Tarasenko and S. I. Yakovlenko, Usp. Fiz. Nauk **174**, 953 (2004) [Phys. Usp. **47**, 887 (2004)].
2. A. N. Tkachev and S. I. Yakovlenko, Cent. Eur. J. Phys. (CEJP) **2**, 579 (2004); www.cesj.com/physics.html.
3. S. B. Alekseev, V. M. Orlovskiĭ, V. F. Tarasenko, *et al.*, Kratk. Soobshch. Fiz., No. 6, 10 (2004).
4. S. B. Alekseev, V. P. Gubanov, V. M. Orlovskiĭ, and V. F. Tarasenko, Pis'ma Zh. Tekh. Fiz. **30** (20), 35 (2004) [Tech. Phys. Lett. **30**, 859 (2004)].
5. S. B. Alekseev, V. P. Gubanov, V. M. Orlovskiĭ, *et al.*, Dokl. Akad. Nauk **398**, 611 (2004) [Dokl. Phys. **49**, 549 (2004)].
6. V. P. Gubanov, S. D. Korovin, I. V. Pegel', *et al.*, Izv. Vyssh. Uchebn. Zaved., Fiz., No. 12, 110 (1996).
7. P. A. Bokhan and G. V. Kolbychev, Zh. Tekh. Fiz. **51**, 1823 (1981) [Sov. Phys. Tech. Phys. **26**, 1057 (1981)].
8. A. N. Tkachev and S. I. Yakovlenko, Laser Phys. **12**, 1022 (2002).
9. A. N. Tkachev and S. I. YAkovlenko, Kratk. Soobshch. Fiz., No. 2, 43 (2004).
10. A. V. Kozyrev and Yu. D. Korolev, Zh. Tekh. Fiz. **51**, 2210 (1981) [Sov. Phys. Tech. Phys. **26**, 1303 (1981)].

Translated by Yu. Vishnyakov

Technical Physics, Vol. 50, No. 12, 2005, pp. 1628–1631. Translated from Zhurnal Tekhnicheskoĭ Fiziki, Vol. 75, No. 12, 2005, pp. 94–97.

SHORT COMMUNICATIONS

Cascade Klystron Self-Excited Oscillator with Delay

B. S. Dmitriev, Yu. D. Zharkov, V. N. Skorokhodov, P. Yu. Semenovykh, and A. A. Biryukov

Chernyshevsky State University, Saratov, 410026 Russia

e-mail: DmitrievBS@info.sgu.ru

Received April 4, 2005

Abstract—Experiments with a new type of resonance microwave self-excited system with complex dynamics, a cascade klystron self-excited oscillator with delayed feedback, are reported. The new self-excited oscillator features a low starting current and many oscillation bands; in addition, it can readily be switched into complex, including random, oscillation modes. © *2005 Pleiades Publishing, Inc.*

INTRODUCTION

When the operating current of the electron beam exceeds a threshold value by two to three times, delayed-feedback self-excited oscillators based on multiresonator klystrons break into complex, including random, oscillations [1]. Self-excited oscillators of such a type are of interest as high-power microwave sources applicable in various fields of technology [2, 3], since their frequency band in the chaotic oscillation mode is sufficiently broad. The complex dynamics of a single-klystron resonance self-excited oscillator was experimentally studied in [1].

In this work, we report experiments with a new type of such a dynamic system, a cascade self-excited oscillator built on multiresonator klystrons.

CASCADE KLYSTRON SELF-EXCITED OSCILLATOR

The device consists of two series-connected nearly identical multiresonator klystrons (the output of either of them is connected to the input of the other). The klystron stage, in turn, represents a commercial five-resonator 10-cm-range medium-power klystron. The two-gap cavities of the klystrons generate oscillations in antiphase. The parameters of the first klystron are as follows: the loaded Q factor of the input resonator is 250; that of the output resonator, 125; the unloaded Q factor, 460; and the resonance frequency, 2798 MHz. For the second klystron, the respective parameters equal 120, 112, 380, and 2800 MHz.

The accelerating and control voltages of the klystrons are applied from the same power supply. The output resonator of the first klystron is connected to the output resonator of the second one through a coaxial feedback loop. The feedback loop is connected via directional couplers to a wattmeter with a polarization attenuator, crystal detector to display the phase portrait of the signal, spectrum analyzer recording the full spectrum of the signal, a second crystal detector to display the envelope of the signal, digital frequency meter, and polarization attenuator controlling the amount of feedback. Schematically, the experimental setup is shown in Fig. 1.

The full delay time related to the feedback loop including the feedback loop length, flight time of electrons in the drift space, and Q factors of the cavities of both klystrons was measured to be 0.6 μs. As a control parameter, we used the electron beam current, damping in the feedback loop, and control voltages of the klystrons. Such a setup makes it possible to fairly accurately identify the oscillation mode, specifically the periodic modulation and random oscillation modes.

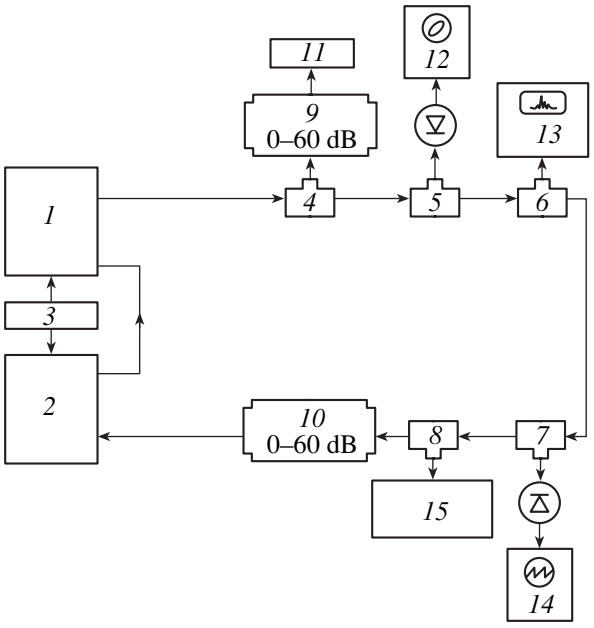

Fig. 1. Schematic of the experimental setup: (*1*, *2*) multiresonator klystrons, (*3*) power supply, (*4–8*) directional couplers, (*9*, *10*) polarization attenuators, (*11*) wattmeter, (*12*) phase portrait recorder, (*13*) spectrum analyzer, (*14*) envelope recorder, and (*15*) electronic frequency meter.

1063-7842/05/5012-1628$26.00 © 2005 Pleiades Publishing, Inc.

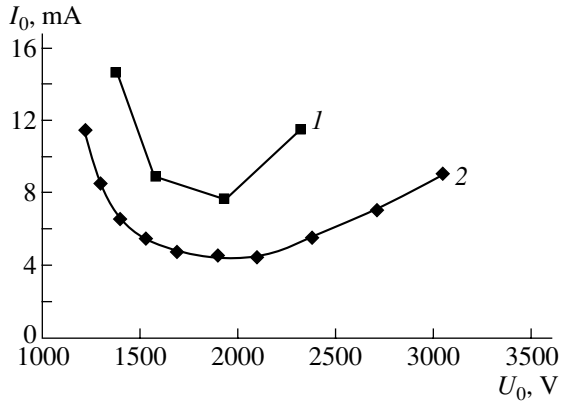

Fig. 2. Minimal starting current vs. accelerating voltage for the (*1*) single-klystron and (*2*) cascade klystron oscillators.

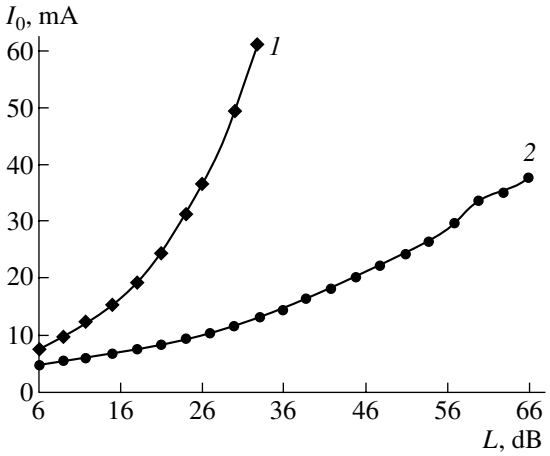

Fig. 3. Starting current vs. the damping in the feedback loop for the (*1*) single-klystron and (*2*) cascade klystron oscillators.

EXPERIMENTAL RESULTS

The performance of the cascade klystron self-excited oscillator with delay in different operating modes was thoroughly examined. The "simple-to-complex" approach was applied; that is, the operating conditions were made increasingly more complicated: from single-frequency oscillations to periodic modulation and then to random oscillations. In addition, comparison was permanently made with the performance of the oscillator based on a single five-resonator klystron [1].

To find the operating range of the control voltage, we first of all studied the dependence of the starting current of the cascade self-excited oscillator on this parameter. A cascade self-excited oscillator, as well as a single-klystron oscillator, is characterized by a set of oscillation bands.

Figure 2 plots minimal starting current I_0 for each of the bands of the cascade oscillator against accelerating voltage U_0 (curve *2*). For comparison, the same dependence is presented for the single-klystron oscillator (curve *1*). The damping in the feedback loops is identical, 6 dB. For one of the bands, Fig. 3 shows the dependence of the starting current on damping L in the feedback loop for the single-klystron (curve *1*) and cascade (curve *2*) oscillators. It is seen that the starting current of the latter device is much smaller; so, it is easier to excite and, accordingly, carry to the developed chaos mode.

The dependences of power P and oscillation frequency f on the accelerating voltage for different values of beam current I are demonstrated in Figs. 4a and 4b, respectively. As the current grows, the oscillation bands expand both in voltage and frequency and their number increases. Also, the bands deform severely; specifically, the power maxima shift toward higher voltages. The curves exhibit peaks (maximal power) followed by the sharp jump into the adjacent band. Near the peaks, power and frequency hysteresis is observed. The cascade oscillator behaves in many ways similarly to its single-klystron counterpart with the only (but essential!) difference that, for the former, the number of the bands is much larger in the same accelerating voltage range and they are excited at a much lower value of the starting current. For example, at a beam current of 10 mA in the klystron, the number of the bands is eight in

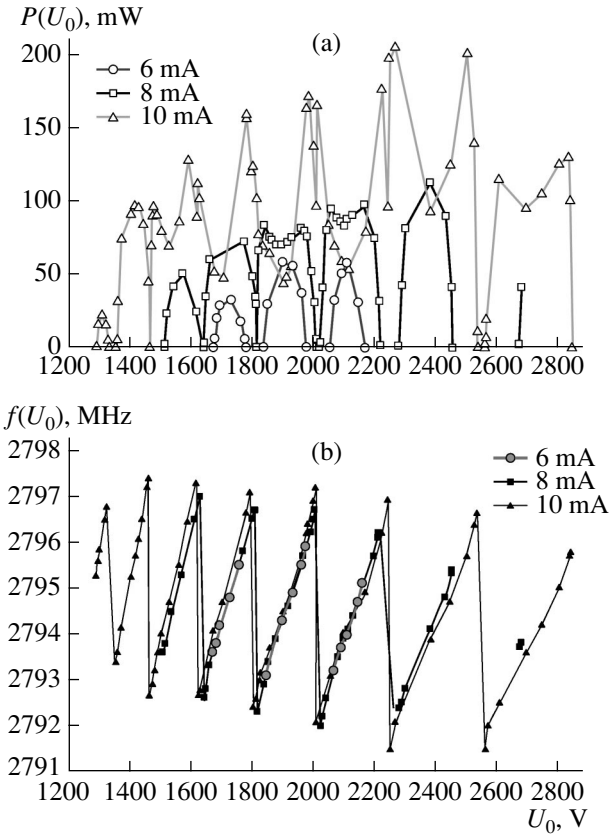

Fig. 4. (a) Power and (b) frequency vs. accelerating voltage for different beam currents.

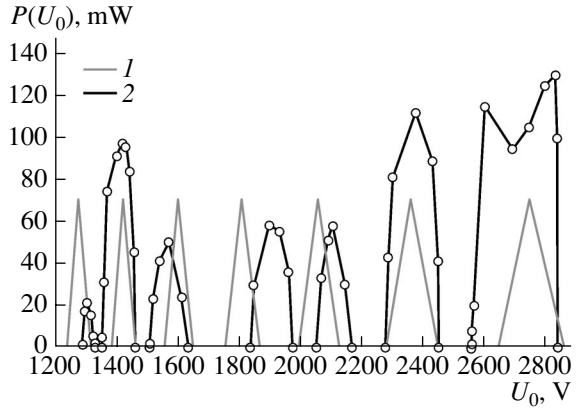

Fig. 5. (*1*) Calculated and (*2*) experimental dependences of the power on the accelerating voltage.

the cascade oscillator versus five in the single-klystron oscillator for the same accelerating voltage range.

The number of the bands, as well their positions and boundaries, can be found from the oscillation phases. Oscillations occur when the phase shift of the signal passing through the feedback loop is a multiple of 2π. If the resonators of a self-excited oscillator are tuned to synchronism, this condition is written as

$$2\theta_0 + \omega_0\delta t_1 + \omega_0\delta t_2 = 2\pi n - (k-1)\pi.$$

Here, $\theta_0 = \omega_0 l/\sqrt{2\eta U_0}$ is the undisturbed angle of flight between the initial and last resonators in each of the klystrons, $\eta = e/m$; l is the distance between these resonators, ω_0 is the eigenfrequency of the resonators, δt_1 is the time of signal propagation in the outer feedback circuit with measuring devices, δt_2 is the time of signal propagation in the circuit connecting the output resonator of the second klystron with the input resonator of the first one, k is the number of resonators per klystron, and n is an integer. The boundaries of the bands can be found from a similar relationship,

$$2\theta_0 + \omega_0\delta t_1 + \omega_0\delta t_2 = 2\pi n - (k-1)\pi \pm \frac{\pi}{2}.$$

Figure 5 compares the results obtained by these formulas with experimental data.

When the electron current in the klystrons exceeds the self-excitation threshold by two to three times, the single-frequency mode changes to the aperiodic modulation mode, in which two satellites appear that are symmetric about the basic signal in the signal spectrum and the phase portrait exhibits an ellipse-like limiting cycle. Interestingly, the self-modulation frequency in the cascade oscillator is roughly twice lower than in its single-klystron counterpart.

The self-modulation frequency of a klystron self-excited oscillator can be found from the full delay time

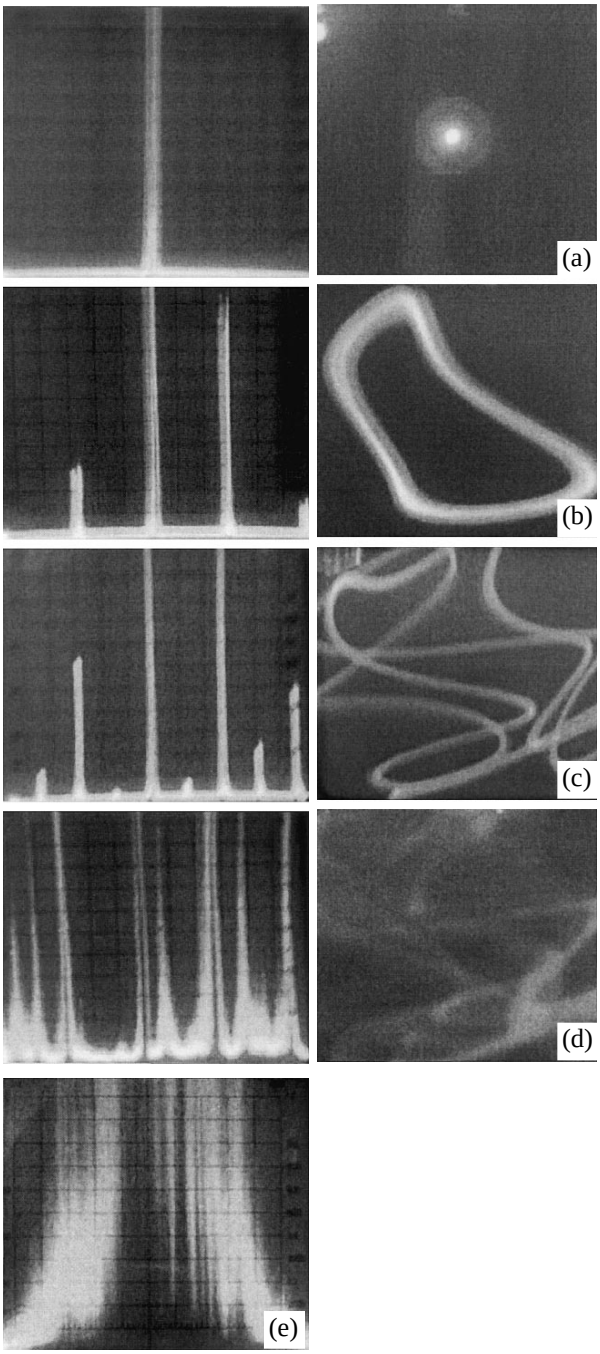

Fig. 6. (a) Single-frequency oscillation mode, A = 46 dB; (b) regular self-modulation mode, A = 37 dB; (c) double-period mode, A = 33 dB; (d) weak chaos mode, A = 32.5 dB; and (e) random oscillation spectrum under the developed chaos mode, A = 31 dB.

over the closed feedback loop,

$$\tau = \frac{L\sqrt{\varepsilon}}{c} + \frac{2l}{v_0} + \frac{2}{\omega_{01}}(3Q_{01} + Q_{in1} + Q_{out1}) + \frac{2}{\omega_{02}}(3Q_{02} + Q_{in2} + Q_{out2}).$$

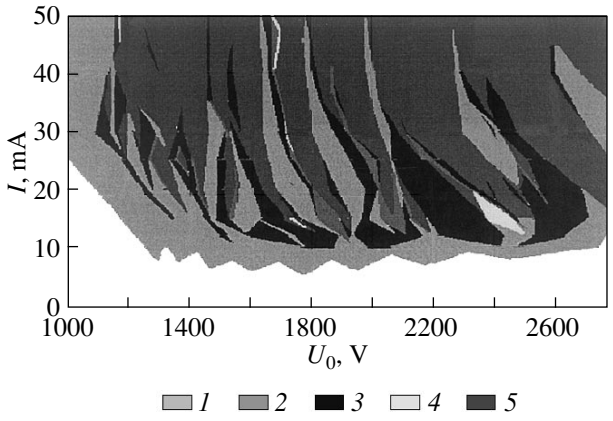

Fig. 7. Dynamic mode map on the (I_0, U_0) plane for the cascade self-excited oscillator: (*1*) single-frequency modulation, (*2*) double-period mode, (*3*) self-modulation, (*4*) quadruple-period mode, and (*5*) chaos.

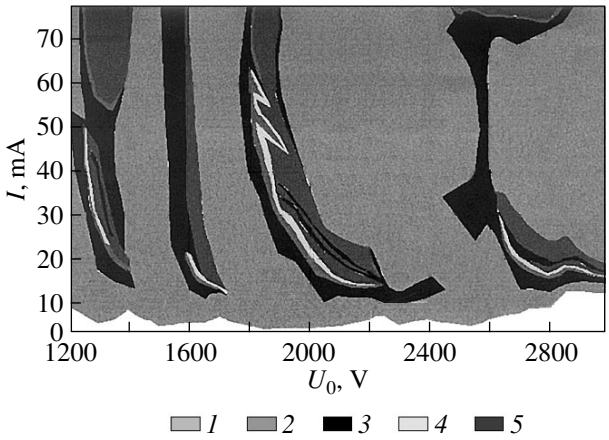

Fig. 8. Dynamic mode map on the (I_0, U_0) plane for the single-klystron self-excited oscillator. The notation is the same as in Fig. 7.

Here, L is the length of the coaxial line in the feedback loop of the klystrons, ε is the permittivity of a filler of this line, Q_0 is the unloaded Q factor of the intermediate resonators in the klystron, Q_m is the loaded Q factor of the input resonators of the klystrons, Q_{in} is the loaded Q factor of the input resonators of the klystrons, and Q_{out} is the loaded Q factor of the output resonators of the klystrons. Calculation by this formula yields self-modulation frequency f_{sm} = 2.5 MHz (cf. experimental value f_{sm} = 3.5 MHz). As in the single-klystron oscillator, self-modulation in the cascade klystron device arises in the frequency response descending portion, which is due to electron grouping, but at a much lower beam current or a much higher damping in the feedback loop.

Transition to chaos in the self-excited oscillator under study follows largely the scenario of period doubling bifurcation, as illustrated by the oscillation spectra and phase portraits taken in the case when amount of feedback A is used as a control parameter (Fig. 6).

It should be noted that transition to chaos may proceed through intermittency and quasi-periodicity, as well as directly from the single-frequency oscillation mode. The dynamic mode map on the parameter plane, beam current I, and accelerating voltage U_0 for the cascade oscillator are shown in Fig. 7. Compared with the same map for the single-klystron oscillator (Fig. 8), the developed chaos mode in the cascade occupies much more extended domains, which merge together at high currents (above 40 mA).

Remarkably, without specially selecting operating parameters for the klystrons under the developed chaos conditions, a cascade self-excited oscillator composed of almost identical resonators provides gain neither in power nor in frequency band.

CONCLUSIONS

Our experiments show that a delayed-feedback cascade klystron self-excited oscillator features a low starting current and many oscillation bands. It can be readily carried to the complex (including chaotic) oscillation mode and demonstrates various scenarios of transition to chaos. Therefore, such an oscillator is very convenient for experimental studying of the general nonlinear dynamics of distributed systems in the microwave range.

ACKNOWLEDGMENTS

This work was supported by the Russian Foundation for Basic Research (grant no. 03-02-16269) and the program “Universities of Russia: Basic Research” (project no. 01.02.021).

REFERENCES

1. V. S. Dmitriev, Yu. D. Zharkov, D. V. Klokotov, and N. M. Ryskin, Zh. Tekh. Fiz. **73** (1), 105 (2003) [Tech. Phys. **48**, 901 (2003)].
2. A. S. Dmitriev, A. I. Panas, and S. O. Starkov, Zarubezhn. Radioélektron. Usp. Sovr. Radioélektron., No. 10, 4 (1997).
3. V. D. Shalfeev, V. V. Matrosov, and M. V. Korzinova, Zarubezhn. Radioélektron. Usp. Sovr. Radioélektron., No. 11, 44 (1998).

Translated by V. Isaakyan

Technical Physics, Vol. 50, No. 12, 2005, pp. 1632–1635. Translated from Zhurnal Tekhnicheskoĭ Fiziki, Vol. 75, No. 12, 2005, pp. 98–101.

SHORT COMMUNICATIONS

On the Time Dependence of Field in the Near-Field Zone of a Nonstationary Multipole

N. S. Bukhman

Samara State Architectural and Building Academy, Samara, 443001 Russia

e-mail: buhman@ssaba.smr.ru

Received April 5, 2005

Abstract—The subject of consideration is the time dependence of the field in the near-field zone of an (acoustic or electric) dipole generating a nonmonochromatic signal smoothly varying with time. It is shown that this dependence is approximately the same at different points in the near-field zone; i.e., the smooth signal does not lag in time, as it might with regard to a finite velocity of wave propagation. The absence of delay is a result of interference between two identical but differently damped and delayed copies of one signal that are emitted from two monopoles constituting the dipole. The same is true for an arbitrary electroneutral (as a whole) set of nonstationary charges (in particular, for a nonstationary quadrupole, octupole, etc.). © *2005 Pleiades Publishing, Inc.*

Let us consider interference (superposition) of several ($i = 1, \ldots, n$) copies of one signal $A^{(0)}(t)$ with attenuation coefficients f_i and different (but positive) time delays $\tau_i > 0$. For the total signal, we have

$$\begin{aligned} A(t) &= \sum_{i=1}^{n} f_i A^{(0)}(t-\tau_i) \\ &= \left(\sum_{i=1}^{n} f_i \hat{T}(\tau_i)\right) A^{(0)}(t) = \hat{T}_{\text{tot}} A^{(0)}(t), \end{aligned} \tag{1}$$

where $\hat{T}(\tau)$ is the operator of time translation by τ ($\hat{T}(\tau)A(t) \equiv A(t-\tau)$), $\hat{T}_{\text{tot}}$ is the linear operator coupling input (initial) signal $A^{(0)}(t)$ with output (total) signal $A(t)$.

Considering transformation $A(t) = \hat{T}_{\text{tot}} A^{(0)}(t)$ as a result of passing initial signal $A^{(0)}(t)$ through a linear filter [1, 2], one can easily check that the pulsed response of this filter can be expressed as

$$g(t) = \sum_{i=1}^{n} f_i \delta(t-\tau_i),$$

and the frequency response has the form

$$K(\omega) = \int g(t)\exp(-i\omega t) = \sum_{i=1}^{n} f_i \exp(-i\omega\tau_i). \tag{2}$$

Note at once that filter (2) is (for $\tau_i \geq 0$) physically feasible (i.e., not violating the causality principle), since its pulsed response is identically zero at $t < 0$. Moreover, operator $\hat{T}_{\text{tot}}$ is not, strictly speaking, a time-translating operator (unlike operator $\hat{T}_{\text{tot}}$ ($\tau_i \geq 0$), since the pulse and frequency responses of the corresponding filter cannot be expressed as $g(t) = f\delta(t-\tau)$ and $K(\omega) = f\exp(-i\omega\tau)$, respectively, at any values of parameters f and τ. Nevertheless, linearizing the logarithm of frequency response $K(\omega)$ in frequency near the zero frequency ($\omega = 0$), i.e., using the approximation of group delay under linear filtration (well known from the theory of signals) or, which is the same thing, using the first order of the classical dispersion theory, one readily obtains the approximate formula

$$K(\omega) \approx K(0)\exp\left[\left(\frac{\partial \ln K(\omega)}{\partial\omega}\bigg|_{\omega=0}\right)\omega\right] = f\exp(-i\omega\tau), \tag{3}$$

where

$$\begin{aligned} f &= K(0) = \sum_{i=1}^{n} f_i, \\ \tau &= i(\ln K(0))' = \sum_{i=1}^{n} f_i\tau_i \Big/ \sum_{i=1}^{n} f_i. \end{aligned} \tag{4}$$

With Eq. (3), operator $\hat{T}_{\text{tot}}$ is easy to approximate by some translational operator $f\hat{T}(\tau)$ that relates parameters f and τ by Eq. (4). Then

$$A(t) = \sum_{i=1}^{n} f_i A^{(0)}(t-\tau_i) \approx f A^{(0)}(t-\tau). \tag{5}$$

Thus, in the group delay approximation [1, 2], the total signal differs from the initial one only in amplitude (f) and time shift (τ). Equation (3) is approximate and is valid at low frequencies only (when the conditions $|\omega(\tau_i - \tau)| \ll 1$; $i = 1, \ldots, n$ are satisfied). Hence,

1063-7842/05/5012-1632$26.00

Eq. (5) for signals with an arbitrary time dependence is also approximate and can be used for only smooth sufficiently long signals, $T \gg |\tau_i - \tau|$ ($i = 1, \ldots, n$).

The accuracy of approximate formula (5) depends on the form of signal $A^{(0)}(t)$, attenuation constants f_i, and delay times τ_i. It is easy to check that, in the very general case ($(\ln K(0))'' \neq 0$), formula (5) is an exact formula for any linear function ($(A^{(0)}(t) = a + bt$).Therefore, for arbitrary function $A^{(0)}(t)$ Eq. (5) may be viewed as the "inverse" formula of smooth linear interpolation [3], which differs from the "normal" formula only by permutation of the left- and right-hand sides. If the conditions $(\ln K(0))'' = \ldots = (\ln K(0))^{(m)} = 0$ are also fulfilled, formula (5) becomes an exact formula for an arbitrary mth-degree polynomial and can be viewed as the formula of smooth interpolation of the mth order. Accordingly, the accuracy of Eq. (5) for arbitrary function $A^{(0)}(t)$ rises (see below).

Importantly, Eq. (4) basically imposes no restrictions on delay time τ of the total signal. Even at positive delays τ_i of interfering copies, delay τ of the total signal may be positive, negative, or equal to zero depending on attenuation coefficients f_i. In this case, the delay of the total signal may be much different from the delays of the interfering copies of the initial signal, which constitute the total signal. For example, it may so happen that the total signal does not have a delay ($\tau = 0$), although each of the copies has ($\tau_i > 0$ at $i = 1, \ldots, n$). Such a situation should not be perceived as violation of the causality principle or the principle of the maximality of speed of light in vacuum as applied to data transfer: it is well known [2] that an infinitely smooth signal, strictly speaking, is not a signal as a data carrier and that data are transmitted through breaks in the time dependence of the signal, which appear in the high-frequency (and not in the low-frequency) part of the signal spectrum.

As an example, consider the field of an electric [1] or acoustic [4] dipole in a homogenous medium without dispersion and absorption. Designating the positions of the point oscillators as r_1 and r_2 and the distance between these oscillators and the point of observation $\mathbf{r}$ as R_1 and R_2, we have for the total field

$$A(r, t) = \frac{A^{(0)}(t - R_1/c)}{R_1} - \frac{A^{(0)}(t - R_2/c)}{R_2}. \qquad (6)$$

Here, c is the speed of light (or sound) in the medium and $A^{(0)}(t)$ is the same (up to sign) time dependence of either signal.

Equation (4) in this case yields $\tau(\mathbf{r}) = 0$ ($f_1 = 1/R_1$, $f_2 = -1/R_2$, $\tau_{1,2} = R_{1,2}/c$); i.e.,

$$A(t) \approx f A^{(0)}(t), \quad f(\mathbf{r}) = (1/R_1) - (1/R_2). \qquad (7)$$

Equation (7) applies if $\tau_{1,2} \ll T$ or $r \ll cT$. This means that we are dealing with the field of a nonstationary dipole in the near-field zone.

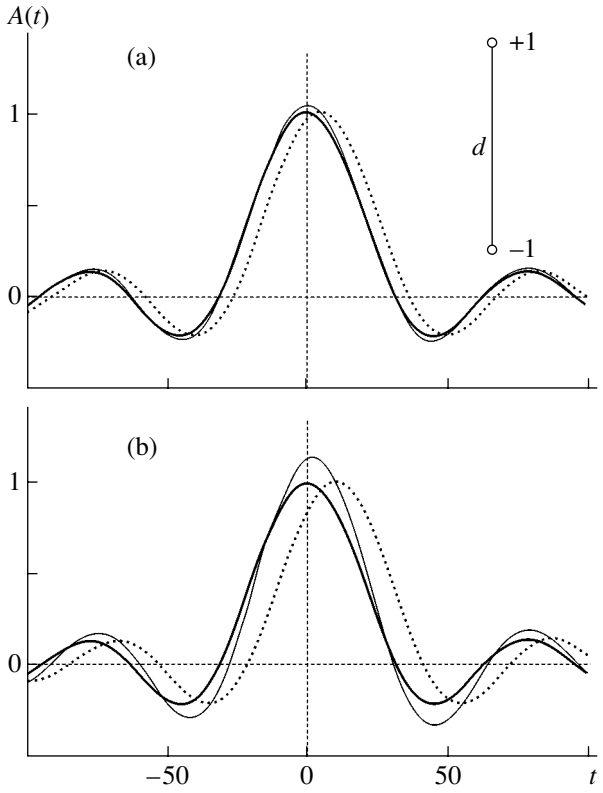

Fig. 1. Time dependence of the signal at the axis of a dipole radiator for r = (a) 5 and (b) 10.

It is seen that the total field (unlike the fields of the point sources producing this total field) has no time delay. It is easy to check that this conclusion is valid (in an absorption-free medium) for any set of point acoustic or electromagnetic oscillators provided that the total volume velocity of the acoustic monopoles (in the case of an acoustic wave) is equal to zero. The fact that the time delay is the same (zero) at each point of the near-field zone is associated with the geometric attenuation of the spherical wave field, which follows the $1/r$ law in the three-dimensional space. If the field decays with distance from the point source faster (for example, in the presence of absorption), the delay time of the total signal varies from point to point, remaining positive (while smaller than that of the signal coming from the point source nearest to the point of observation).

Let us substantiate these speculations by calculation. Figures 1a and 1b show the time dependences of the total signal at the dipole axis for point source spacing $d = 0.01$ in the medium where the wave velocity is $c = 1$. The curves are constructed at a distance from the dipole center r = (a) 5 and (b) 10. The signal is taken in the form $A^{(0)}(t) = \sin(t/T)/(t/T)$ with duration $T = 10$. Shown are (i) the time dependence of the field produced by both point sources $A^{(0)}(t - \tau_{1,2})$, two merged dotted lines; (ii) the time dependence of the signal without taking into account its delay $A^{(0)}(t)$, the solid line; and

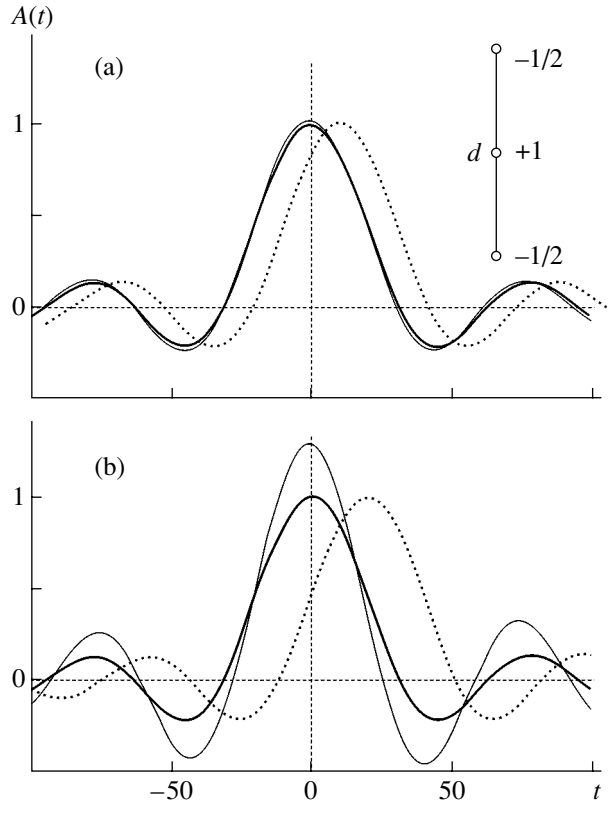

Fig. 2. Time dependence of the signal at the axis of a quadrupole radiator at r = (a) 10 and (b) 20.

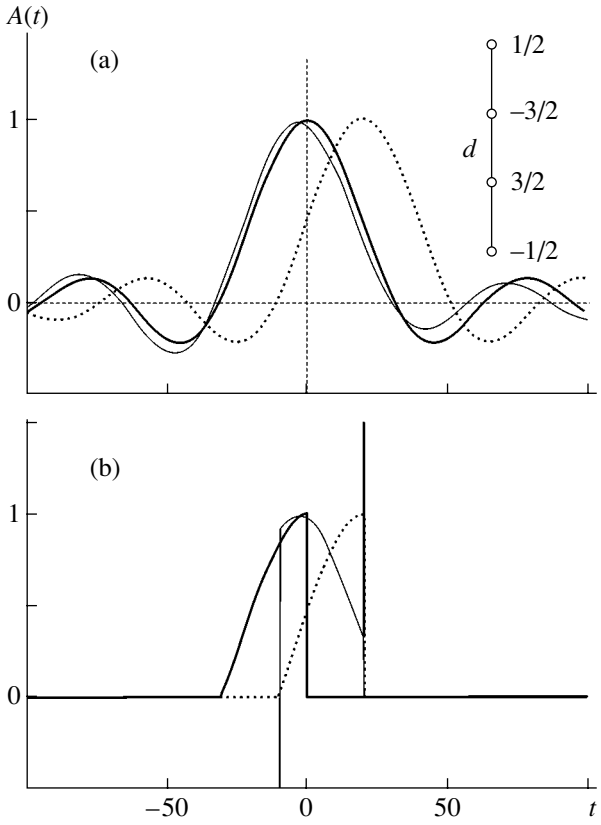

Fig. 3. Time dependence of the (a) smooth signal and (b) signal truncated from above and from below at the axis of an octupole radiator at r = 20.

(iii) the time dependence of the total field arising from interference between the fields of the point sources $A(\mathbf{r}, t)/f(\mathbf{r})$, the thin solid line. It is seen that the total field (unlike the partial fields) does "ignore" the time delay associated with the finiteness of the signal velocity: as long as the delay is small in comparison with the signal duration, the field in the near-field zone almost coincides with the "undelayed" signal. It should be emphasized that the delay ignored by the total signal is by no means beyond the calculation accuracy: it is much longer than the time taken for the signal to travel from one point source to the other (or, which is the same, greater than the difference between the delay times of the partial signals).

Figures 2a (r = 10) and 2b (r = 20) show the calculation results for a quadrupole (see Fig. 2a). Here, the accuracy of Eq. (5) turns out to be higher than in the previous case. This is because $(\ln K(0))'' = 0$ in this case, and Eq. (5) becomes exact for signals in the form $A^{(0)}(t) = a + bt + ct^2$.

Figure 3a demonstrates the results for an octupole at r = 20. In this case, $(\ln K(0))'' = (\ln K(0))''' = 0$ at the octupole axis, which improves the calculation accuracy (Eq. (5) is valid for third-degree polynomials).

Figure 3b demonstrates the results for the same signal as in Fig. 3a with the only difference that the signal is truncated: it appears stepwise at t = –30 and vanishes stepwise at t = 0. It follows from Figs. 3a and 3b that the total signal appears and vanishes synchronously with the interfering signals from the point sources (i.e., with the corresponding delay), but here its time dependence in the time "window" where the signal exists repeats the time dependence of the initial signal without delay. Practically, this means that the signal fragment being received is other than the fragment being transmitted; i.e., the time dependence of the partially transmitted signal is reconstructed (which is typical of the case when a pulse propagates with a supraluminal group velocity [5, 6]).

To conclude, we note that today the propagation of quasi-monochromatic light pulses with a supraluminal velocity in a number of dispersive media is being extensively investigated [5–12]. This effect is similar to that considered in this paper, the results of which suggest that this effect may take place not only for quasi-monochromatic signals but also for wide-band signals, not only during the propagation of waves but also when waves are emitted, and not only in a highly dispersive (or nonlinear) medium but also in a vacuum.

REFERENCES

1. M. B. Vinogradova, O. V. Rudenko, and A. P. Sukhorukov, *Theory of Waves* (Nauka, Moscow, 1979) [in Russian].
2. L. A. Vaĭnshteĭn, Usp. Fiz. Nauk **118**, 339 (1976) [Sov. Phys. Usp. **19**, 189 (1976)].
3. A. A. Amosov, Yu. A. Dubinskiĭ, and N. V. Kopchenova, *Computational Methods for Engineers* (Vysshaya Shkola, Moscow, 1994) [in Russian].
4. M. A. Isakovich, *General Acoustics* (Nauka, Moscow, 1973) [in Russian].
5. N. S. Bukhman, Zh. Tekh. Fiz. **72** (1), 136 (2002) [Tech. Phys. **47**, 132 (2002)].
6. N. S. Bukhman, Kvantovaya Élektron. (Moscow) **31**, 774 (2001).
7. S. V. Sazonov, Usp. Fiz. Nauk **171**, 663 (2001) [Phys. Usp. **44**, 631 (2001)].
8. A. N. Oraevsky, Usp. Fiz. Nauk **168**, 1311 (1998) [Phys. Usp. **41**, 1199 (1998)].
9. L. J. Wang, A. Kuzmich, and A. Dogariu, Nature (London) **406**, 277 (2000).
10. B. Macke and B. Segard, Eur. Phys. J. D **23**, 125 (2003).
11. A. M. Akulshin, A. Cimmino, A. J. Sidorov, *et al.*, Phys. Rev. A **67**, 011801 (2003).
12. G. D'Aguanno, M. Centini, M. J. Bloemer, *et al.*, Opt. Lett. **27**, 176 (2002).

Translated by M. Astrov

Technical Physics, Vol. 50, No. 12, 2005, pp. 1636–1639. Translated from Zhurnal Tekhnicheskoĭ Fiziki, Vol. 75, No. 12, 2005, pp. 102–105.

SHORT COMMUNICATIONS

Kinetics of Localized Plasticity Macrodomains at the Prefracture Stage in Metals

L. B. Zuev and V. I. Danilov

Institute of Strength Physics and Materials Science, Siberian Division, Russian Academy of Sciences, Akademicheskiĭ pr. 2/1, Tomsk, 634021 Russia

Received April 19, 2005

Abstract—The behavior of localized plasticity macrodomains is experimentally studied at the final stage of the plastic flow in going to necking and ductile fracture in fcc, bcc, and hcp materials. General features of the localization process at the stage of prefracture are found. They are a constant velocity of domains and their tendency to consistently move toward the focus of a bundle of straight lines in space–time diagrams. A correlation between the type of fracture and the kinetics of localized plasticity domains is established. © *2005 Pleiades Publishing, Inc.*

INTRODUCTION

In the previous studies [1, 2], we revealed specific features in the behavior of the domains (centers) of localized plastic strain at the final stage of the plastic flow in single-crystalline and polycrystalline Fe–3wt% Si alloys (siliceous iron). At this stage, the stress–strain dependence is known to obey a parabolic law, $\sigma \sim \varepsilon^n$ [3]. For $n < 1/2$, localized strain domains were found to move along the sample with velocity V, which depends on n as [4]

$$V(n) = V_0(n - q)^2, \quad (1)$$

where $q \approx 1/2$. For strain hardening in the form $\sigma \sim \sqrt{\varepsilon}$ predicted by Taylor [3], i.e., when $n \approx 1/2$, localized strain domains are immobile ($V_{n = 1/2} = 0$), in accordance with (1). This fact has been confirmed in many experiments [1, 2, 4, 5]. For $n = 1$, formula (1) describes the stage of linear hardening, when plasticity domains have the same constant velocity $V_{n = 1}$.

During the plastic flow, parabolicity exponent n in the relationship $\sigma \sim \varepsilon^n$ decreases. This circumstance has made it possible to separate out a number of parabolic substages with different parabolicity indices n [4, 5]. In the range $n < 1/2$, localized plasticity domains become mobile [1, 2]. An important and interesting feature of the motion of the domains at this stage of deformation is the self-consistency of their velocities, which spontaneously arises in the stressed material.

The essence of such a self-consistent motion is illustrated in Fig. 1a, which shows the kinetics of localized strain domains in submicrocrystalline aluminum produced by the method of equichannel angular pressing[1] [6]. In this case, the domain trajectories at the final stage of the process plotted in the space–time diagram (X is the domain position and t is the time) appear as a bundle of straight lines converging to some point (focus) with coordinates X^* and t^*.

EXPERIMENTAL RESULTS

The data obtained in this work complement those for bcc siliceous iron [1, 2]. We carried out similar experiments with pure submicrocrystalline (grain size D lies between 30 and 100 nm) fcc aluminum and with hcp magnesium and bcc vanadium alloys (their compositions are presented in the table). The methods of determining parabolicity exponent n, as well as of visualizing and quantitatively describing localized plastic-strain domains, are described in [4, 5, 7].

Figures 1a–1d summarize the results obtained for the alloys. Along with the conventional analysis of the flow curve $\sigma(\varepsilon)$ and dependence $d\sigma/d\varepsilon = \theta(\varepsilon)$, we constructed associated X–t diagrams. They show three well-defined stages of strain hardening: linear hardening (V = const, $n = 1$), Taylor hardening ($V = 0$, $n \approx 1/2$), and the stage of prefracture ($V \neq 0$, $n < 1/2$).

It follows from Fig. 1 that, at the stage of prefracture, the domains have different velocities, which, however, remain constant throughout the domain lifetime. Similar results were obtained previously [2] for Fe–3% Si single crystals. It was found that the velocity depends only on the site of birth of a domain: the closer this site to the region of subsequent fracture, the lower the domain velocity. At the prefracture stage, new domains may start to consistently move from one (Figs. 1a and 1c) or both (Figs. 1b and 1d) sides of a stationary domain.

It can be shown that extrapolating the portions of the straight lines $X(t)$ where $n < 1/2$ to intersection yields a bundle of lines for each of the materials. It turns out that

[1] The authors thank N.M. Rusin for the preparation of submicrocrystalline aluminum samples.

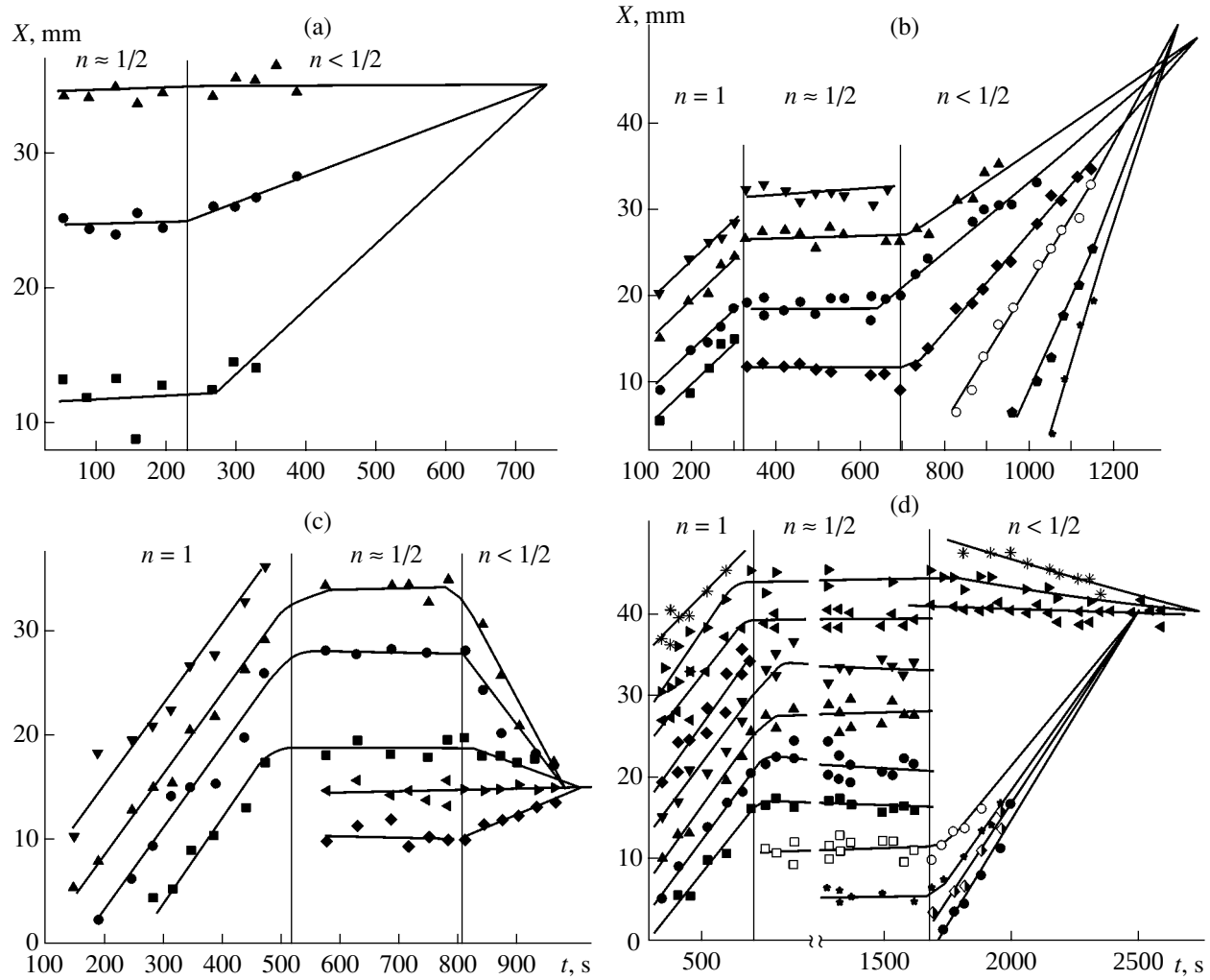

Fig. 1. Kinetics of localized plasticity domains in (a) submicrocrystalline aluminum, (b) magnesium alloy, (c) vanadium alloy, and (d) siliceous iron.

the time and space coordinates of the focuses of these bundles, X^* and t^*, are close to the coordinates of fracture. This means that the velocities of the domains synchronize from the very beginning of this stage so that the domains simultaneously arrive at the focus. To determine X^* and t^*, extrapolation of the dependence $X(t)$ to long times is often needed, as can be seen from Figs. 1a and 1c. Therefore, the site of fracture and the time to fracture of the sample are predetermined early in the stage of plastic flow. Note that, actually, the domains moving at the last stage of the process may collapse at a certain time instant, as it is well seen in Figs. 1a and 1c for Al and Mg. As time passes, only one domain "survives," namely, the one that emerges at the site of subsequent macroscopic necking and ductile fracture [4]. Usually, having appeared at the stage of

Coefficients of the equation for the domain velocity and the coordinates and times of fracture

Parameter	Pure Al	Mg (≈2.0 wt % Mn, ≈0.25 wt % Ce)	V (≈2.3 wt % Zr, ≈0.4 wt % C)	Fe–Si (≈3 wt % Si)
α, s^{-1}	1.13×10^{-3}	4.64×10^{-3}	7.24×10^{-3}	1.32×10^{-3}
α_0, m s^{-1}	6.7×10^{-3}	1.7×10^{-2}	-6.1×10^{-4}	-1.27×10^{-3}
$X^* = \alpha_0/\alpha$, mm	6.2	3.7	-8×10^{-3}	1.0
$t^* = t_0 + 1/\alpha$, s	1174	1265	980	2560

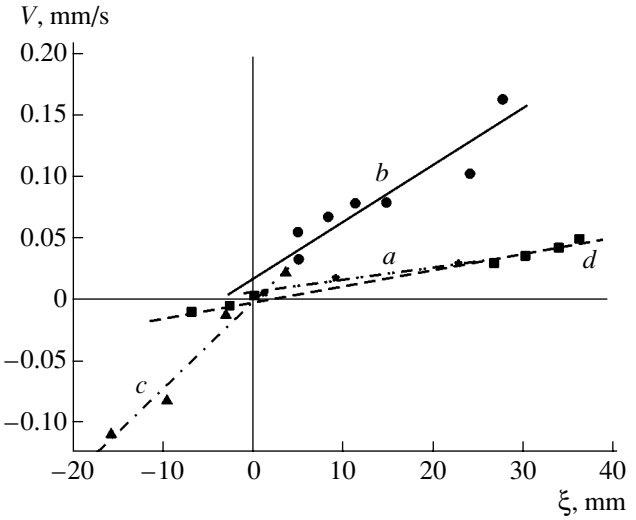

Fig. 2. Dependence $V(\xi)$ in (*a*) submicrocrystalline aluminum, (*b*) magnesium alloy, (*c*) vanadium alloy, and (*d*) siliceous iron.

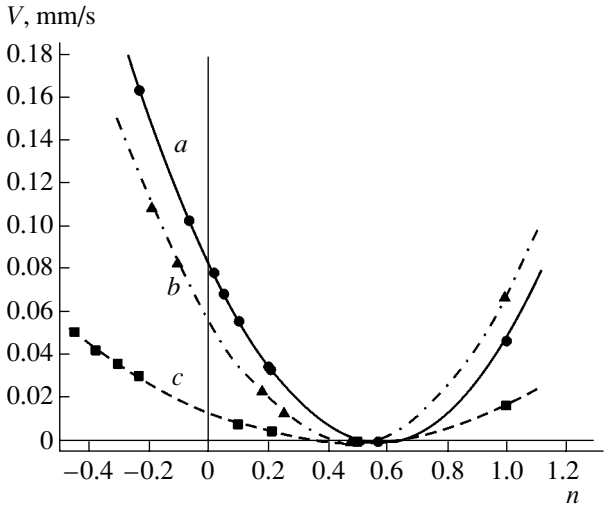

Fig. 3. Domain velocity V vs. parabolicity exponent n in (*a*) magnesium alloy, (*b*) vanadium alloy, and (*c*) siliceous iron.

Taylor hardening at $n \approx 1/2$, such a domain remains almost immobile up to fracture but becomes progressively strained as the flow decays in other domains.

DISCUSSION

Let us consider the formation conditions for the bundles of straight lines $X(t)$ shown in Fig. 1. It is known [8] that these lines intersect if the domain velocities linearly depend on coordinates ξ of the site of birth at time instant $t = t_0$, i.e., if $V(\xi) = \alpha\xi + \alpha_0$. Here, α and α_0 are empiric constants. Coordinate ξ is convenient to measure from the stationary domain, as is shown in Fig. 1a. The dependences $V(\xi)$ for the materials studied are plotted in Fig. 2, and corresponding constants α and α_0 are listed in the table. The domain velocity as a function of the domain's initial position was determined from the slopes of the lines in Fig. 1. As follows from Fig. 2, the curve $V(\xi)$ is actually linear for all the samples. The coefficient of parabolic strain hardening, $\theta = d\sigma/d\varepsilon \sim n\varepsilon^{n-1}$, decreases with decreasing parabolicity exponent n. Then, the velocity of the localized strain fronts, $V \sim 1/\theta$, is bound to grow with a decrease in n and, accordingly, in θ [5, 7]. At $n < 1/2$, the velocity also grows by virtue of Eq. (1).

The coordinates of the focal point, which correspond to the site and time of fracture,

$$X^* = \alpha_0/\alpha, \quad t^* = t_0 + 1/\alpha,$$

were calculated in the same way as in [8] (see table). Since the focus was found for all the materials, one may suggests that it is a general sign of localization at the stage of prefracture and associate the convergence of the domains in the X–t coordinates with the automatic fulfillment of condition $V(\xi) = \alpha\xi + \alpha_0$ in the samples under tension at the prefracture stage with $n < 1/2$.

As was mentioned above, localized plasticity domains may originate on both sides of the site of subsequent fracture (V, Fe–3% Si alloys) and on one side (Al, Mg alloy). The domains originating on both sides of the stationary domain make angles of unlike signs with the axis of tension. This may be a reason for the different type of ductile fracture in low-plasticity (bcc) and high-plasticity (fcc and hcp) materials [9]. This conjecture is supported by the different structure of fracture surfaces. More plastic materials (Al and Mg alloy) exhibit a typical pattern of shear ductile fracture, while fracture in vanadium and Fe–3% Si alloy is more brittle [1].

Next, using Eq. (1) and normalizing the quadratic dependence $V(n)$ by the experimental values $V_{n=1}$ and $V_{n=1/2} = 0$ corresponding to the stages of linear and Taylor strain hardening ($n = 1$ and $n \approx 1/2$, respectively), we estimated the values of n for each of the mobile domains in all the materials, except for the submicrocrystalline aluminum.[2] The results of such processing (Fig. 3) indicate an intriguing property of the dependence $V(n)$: the parabolicity exponent is negative ($n < 0$) for the fastest domains of localized plasticity. A negative value of the exponent corresponds to the descending branch of the conditional stress–strain diagram [9, 10]; however, the parabolicity exponent for a sample as a whole remains positive at this stage. It is worth noting that the domains for which $n < 0$ spontaneously appear at the stage of prefracture and are geometrically unrelated to the regions of localization aris-

[2] In the submicrocrystalline aluminum, the stage of linear hardening was absent and so the velocity corresponding to $n = 1$ could not be measured.

ing at the stage of Taylor hardening and remaining stationary as long as $\sigma \sim \sqrt{\varepsilon}$, i.e., at $n \approx 1/2$.

The dependences observed can be explained by supposing that parabolicity exponent n may take different, including negative, values in every localized plasticity domain moving at the stage of prefracture. Then, one has to admit that the deformability of separate domains in a material may be different and the ability of the material for strain hardening under the plastic flow conditions may vary during this stage. It was shown [11] that the dislocation structure inside plasticity domains at various stages of deformation develops ahead of the dislocation substructure between the domains, which confirms this viewpoint.

CONCLUSIONS

Important points concerning the behavior of materials at the stage of prefracture preceding macroscopic necking can be summarized as follows.

(1) According to the evolution patterns that show localized deformation zones immediately before the onset of macroscopic necking, the site of fracture can be found early in the process [4]. The stage of the stable parabolic (Taylor) hardening ($n \approx 1/2$) is followed by the transition stage with $n < 1/2$, which ends in the formation of a macroscopic neck with subsequent ductile fracture. Such a change in n may correspond to the instant the plastic flow becomes unstable [12–14].

(2) The patterns observed at the stage of prefracture indicate that macroscopic necking shortens the zone of intense plastic flow and suppresses the plastic flow in the rest of the sample. As the sample elongates, the wavelength of local deformation decreases.

(3) It seems that localized strain domains appearing at the stage of prefracture evolve (in the sense of strain hardening/softening) independently. In other words, hardening domains ($n > 0$, $\theta > 0$) may coexist with softening ones ($n < 0$, $\theta < 0$) in the same sample. Each of the domains moves with its own constant velocity, which is a linear function of the start point coordinates.

(4) Necking and the fracture zone nucleation start long before fracture and result from the consistent motion of plastic flow domains concentrating at the site of subsequent ductile fracture. Its position is fixed early in the process by a domain arising at the end of Taylor hardening. The time of fracture is defined by the consistent motion of all the domains.

REFERENCES

1. V. I. Danilov, G. V. Shlyakhova, L. B. Zuev, *et al.*, Fiz. Met. Metalloved. **98** (3), 107 (2004).
2. S. A. Barannikova, V. I. Danilov, and L. B. Zuev, Zh. Tekh. Fiz. **74** (10), 52 (2004) [Tech. Phys. **49**, 1296 (2004)].
3. J. Friedel, *Dislocations* (Pergamon, Oxford, 1964; Mir, Moscow, 1967).
4. T. M. Poletika, G. M. Narimanova, S. V. Kolosov, and L. B. Zuev, Prikl. Mekh. Tekh. Fiz. **44**, 132 (2003).
5. L. B. Zuev, V. I. Danilov, T. M. Poletika, and S. A. Barannikova, Int. J. Plast. **20**, 1227 (2004).
6. V. M. Segal, V. I. Reznikov, V. I. Kopylov, and D. A. Pavlik, *Processes of Structure Formation in Metals* (Navuka i Tekhnika, Minsk, 1994) [in Russian].
7. L. B. Zuev and V. I. Danilov, Philos. Mag. A **79**, 43 (1999).
8. Ya. B. Zel'dovich and A. D. Myshkis, *Elements of Mathematical Physics* (Nauka, Moscow, 1973) [in Russian].
9. F. McClintock and A. Argon, *Mechanical Behavior of Materials* (Reading, New York, 1966; Mir, Moscow, 1970).
10. V. V. Struzhanov and V. I. Mironov, *Strain Softening of Structure Materials* (Inst. Mashinoved. UrO RAN, Yekaterinburg, 1995) [in Russian].
11. L. B. Zuev, T. M. Poletika, and G. M. Narimanova, Pis'ma Zh. Tekh. Fiz. **29** (12), 74 (2003) [Tech. Phys. Lett. **29**, 519 (2003)].
12. E. C. Aifantis, Int. J. Non-Linear Mech. **31**, 797 (1996).
13. G. A. Malygin, Fiz. Tverd. Tela (St. Petersburg) **47**, 236 (2005) [Phys. Solid State **47**, 246 (2005)].
14. G. A. Malygin, Fiz. Tverd. Tela (St. Petersburg) **47**, 870 (2005) [Phys. Solid State **47**, 896 (2005)].

Translated by A. Sidorova